

On the
Characteristics and Stability
of the Wakes of Cylinders
with a **Triangular Cross-Section**

by

Zhi Yuen Ng



A thesis submitted to Monash University
for the degree of
Doctor of Philosophy

June 2019

Department of Mechanical and Aerospace Engineering
Monash University

Copyright Notice

On the Characteristics and Stability of the Wakes of Cylinders with a Triangular Cross-Section.

© Zhi Yuen Ng (2019).

I certify that I have made all reasonable efforts to secure copyright permissions for third-party content included in this thesis and have not knowingly added copyright content to my work without the owner's permission.

Abstract

This thesis investigates the properties of the wake of a cylinder with a triangular cross-section as its inclination is varied, and the associated symmetry-breaking bifurcations which occur as the Reynolds number of the flow is increased. Two-dimensional flow solutions are computed numerically using a high-order spectral-element method in conjunction with a third-order-accurate multistep time-integration scheme. Three-dimensional flow solutions are computed using the same spectral-element discretisation in the two-dimensional base plane but with discretisation of the flow variables in the out-of-plane direction through Fourier expansion basis functions, all while using the same time-integration scheme. Work is first reported to demonstrate the resolution independence of the two-dimensional mesh through the convergence of global properties of the two-dimensional flow. The resolution dependence of the three-dimensional flows is addressed subsequently.

Using the equations of motion of the fluid for a two-dimensional flow, the steady recirculation region is shown to develop through a detached eddy at inclinations where the cylinder presents itself asymmetrically to the flow. At these Reynolds numbers, the lift forces induced on the cylinder are low, and the dominating drag forces are shown to increase at a rate approximately proportional to $Re^{-0.6}$. The primary flow instability is shown to be affected by the cylinder inclination primarily through the width of the steady recirculation region and the formation of small regions of flow reversal prior to the transition. Variations in the spatial form of the vortex street at higher Reynolds numbers of the two-dimensional flow are also described. Specifically, the familiar Kármán vortex street observed beyond the primary instability changes in form at higher Reynolds numbers ranging $100 < Re \leq 200$ to either a secondary vortex street, a 2P mode vortex pattern, or a P+S mode vortex pattern depending on the cylinder inclination. The 2P and P+S modes here resemble those in the wakes of oscillating circular cylinders. In addition, the lift and drag forces induced on the cylinder along with the Strouhal numbers of the unstable wakes are quantified. Within the range of cylinder inclinations considered in this study, the shedding frequencies were found to be related to the Reynolds number through two quadratic functions depending on the cylinder inclination.

The stability of the two-dimensional wakes are evaluated through a global Floquet stability analysis. The properties of the three-dimensional perturbation eigenmodes

which destabilise the wakes, found to be modes A and C depending on the cylinder inclination, are described, and a connection between the occurrence of the subharmonic mode and the degree of asymmetry of the flow in the two-dimensional wake is drawn. Specifically, mode C can be predicted from the stability analysis when the base flow possesses an asymmetry that varies strongly in the wake. The streamwise perturbation vortices for mode C also appear to grow in regions where the local asymmetry variation is greatest. For mode A, these local asymmetry measures do not necessarily have to be negligible, but are required to remain equally asymmetric throughout the wake. The stability of the two-dimensional time-mean wakes to two-dimensional perturbations are also assessed to investigate the potential sources of the variations in the vortex street. The sensitivity of these perturbations to localised force-velocity feedback is investigated to determine the core of these instabilities, and the energetics of the perturbation eigenmodes evaluated to determine the terms contributing most to the instability growth. The regions in the wake responsible for the production of perturbation kinetic energy coincides with the wavemaker of the instability in most cases.

The properties of the three-dimensional flow transition through modes A and C at near-critical Reynolds numbers (to three-dimensional perturbations) are evaluated under the assumption that these modes are weakly nonlinear to determine if the bifurcation is sub- or supercritical. The evolution of the flow at higher Reynolds numbers and within an extended spanwise domain are then reported, elucidating the effects of nonlinearities in altering the growth of three-dimensional disturbances in the wake leading to its saturation as well as the onset of turbulent-like states in the wake. The forces induced on the cylinder and the vortex shedding frequencies of the wake are finally quantified to demonstrate the extent of the variation of these properties derived from a two-dimensional flow from those obtained from full three-dimensional flow computations.

Statement of Originality

This thesis is an original work of my research and contains no material which has been accepted for the award of any other degree or diploma at any university or equivalent institution and that, to the best of my knowledge and belief, this thesis contains no material previously published or written by another person, except where due reference is made in the text of the thesis.

Zhi Yuen Ng

13 June 2019

Publications from this project

Journal articles

NG, Z. Y., VO, T., HUSSAM, W. K. & SHEARD, G. J. 2016 Two-dimensional wake dynamics behind cylinders with triangular cross-section under incidence angle variation. *J. Fluids Struct.* **63**, 302–324.

NG, Z. Y., VO, T. & SHEARD, G. J. 2018 Stability of the wakes of cylinders with triangular cross-sections. *J. Fluid Mech.* **844**, 721–745.

Conference papers

NG, Z. Y., HUSSAM, W. K., & SHEARD, G. J. 2015 Wake structures of unsteady two-dimensional flows past cylinders with triangular cross-sections. *In proceedings of the Eleventh International Conference on Computational Fluid Dynamics in the Minerals and Process Industries*, Melbourne Convention and Exhibition Centre, Melbourne, Australia, December 2015.

NG, Z. Y., VO, T., HUSSAM, W. K. & SHEARD, G. J. 2016 Linear instabilities in the wakes of cylinders of triangular cross-sections. *In proceedings of the 20th Australasian Fluid Mechanics Conference*, The University of Western Australia, Perth, Australia, December 2016.

NG, Z. Y., VO, T., HUSSAM, W. K. & SHEARD, G. J. 2018 Energetics of instability modes in the cylinder wake. *In proceedings of the 21st Australasian Fluid Mechanics Conference*, Adelaide Convention Centre, Adelaide, Australia, December 2018.

Acknowledgements

This project has benefited from a generous level of support and assistance, culminating in this dissertation.

I am particularly indebted to Prof. Greg Sheard for his direction and enthusiasm in the project. The attention to detail and elocution, and approachability and patience amongst other qualities he reflected as project advisor are qualities I strive to espouse. I am also indebted to Dr. Tony Vo for his support and guidance in this project, and also for trusting me enough with tutoring opportunities. Helping with ENG1060 has been an incredible experience, and worked wonderfully to toggle off from PhD work. I also have to thank Drs. Lizi Sironic and Tom Simko for also trusting me with ENG1001. Working as the lead tutor and subsequently as co-lecturer to develop the unit impacted my approach to-, and perspective on the research project.

The moral support and camaraderie between research and teaching groups have also been helpful. I extend my appreciation to (a) research group members Tony V., Oliver C., Tzekih T., amongst others, (b) NH campers Caitlin L., Sam M., Jason B., Lachlan S., Saab D., Dave S., Paco, Sean L., Bill C., Noemie O., Dave G., Bradyn P. amongst many others, and (c) fellow ENG1060 and ENG1001 teaching associates. The support from family and friends during this period cannot be overstated.

Finally, support from several organisations or bodies are also acknowledged. This research was supported by an Australian Government Research Training Program (RTP) Scholarship. Financial support in the form of an Engineering Research Living Allowance (ERLA) followed by a Monash Departmental Scholarship (MDS) from the Faculty of Engineering and Department of Mechanical and Aerospace Engineering at Monash University are gratefully acknowledged. This research was undertaken with the assistance of resources from the National Computational Infrastructure (NCI), which is supported by the Australian Government. We acknowledge the use of Rapid Response imagery from the Land, Atmosphere Near real-time Capability for EOS (LANCER) system operated by NASA's Earth Science Data and Information System (ESDIS) with funding provided by NASA Headquarters.

Nomenclature

Accents and symbols

Symbol	Description
$\bar{\square}$	Time mean of a field or signal
$\langle \square \rangle$	Spatial mean of a field or signal
\S	Thesis section
∇	Vector gradient operator (grad)
∇^2	Laplacian operator

Scripts

Symbol	Description
\mathcal{A}	Forward evolution operator for the linearised Navier–Stokes equation
\mathcal{D}	Dissipation term in the perturbation kinetic energy equation
$\mathbf{DN}(\mathbf{u})$	Linearised advection term for the linearised Navier–Stokes equation
$\mathcal{F}[\square]$	Fourier transform of term \square
\mathcal{L}_N	Legendre polynomial function
\mathcal{L}'_N	Derivative of the Legendre polynomial function
$\mathbb{L}(u)$	Linear differential operator on u for the spectral-element method
$\mathbf{L}(\mathbf{u})$	Terms linear in \mathbf{u} in the Navier–Stokes equation
$\mathbf{N}(\mathbf{u})$	Nonlinear advection term in the Navier–Stokes equation
\mathcal{P}	Production term in the perturbation kinetic energy equation
\mathcal{T}	Transport term in the perturbation kinetic energy equation
\mathcal{V}	Computational domain
$E_{\mathcal{D}}$	Volume integral of \mathcal{D}
$E_{\mathcal{P}}$	Volume integral of \mathcal{P}
$E_{\mathcal{T}}$	Volume integral of \mathcal{T}

Greek characters

Symbol	Description
α	Cylinder inclination angle, presented in $^\circ$
δ	Unit tensor
ϵ	Distance parameter from the bifurcation: $(Re - Re_k)/Re_k$
$\epsilon_\Gamma(x)$	Measure of the net circulation imbalance at a streamwise plane x
$\epsilon_t(x)$	Measure of the shedding phase imbalance over a period at a streamwise plane x
$\epsilon_\Omega(x)$	Measure of the peak vorticity imbalance at a streamwise plane x
λ	Wavelength
λ_A	Critical wavelength of the mode A secondary instability
λ_B	Critical wavelength of the mode B secondary instability
λ_C	Critical wavelength of the mode C secondary instability
λ_I	Critical wavelength of the mode I secondary instability of the 2P wake
λ_{II}	Critical wavelength of the mode II secondary instability of the 2P wake
λ_{III}	Critical wavelength of the mode III secondary instability of the 2P wake
$ \Lambda $	Complex signal amplitude of an evolving flow
$ \Lambda _{\text{lim}}$	Cubic order prediction of the complex signal amplitude at mode saturation
$ \Lambda _{\text{sat}}$	Complex signal amplitude at mode saturation
μ	Dynamic viscosity of the fluid,
	Floquet multiplier from the Floquet stability analysis.
ν	Kinematic viscosity of the fluid
ξ	Local spatial dimension within an element of the computational domain for the spectral-element method
ξ_q	Nodes of the tensor-product-polynomial
Π	Computational domain
Π_b	Boundary planes of the computational domain
Π_e	Domain of the spectral element
Π_z	Spanwise plane in the computational domain

Continued on the next page.

Continued from previous page.

Symbol	Description
ρ	Density of the fluid
σ	Growth rate of the linear/weakly nonlinear instability
$\boldsymbol{\tau}$	Stress tensor
ϕ	Instantaneous phase of the complex signal of an evolving flow, Spanwise shift of the signal for the autocorrelation
ϕ_q	Expansion basis function about ξ_q
ω	Angular frequency of the complex signal at mode saturation
$\boldsymbol{\omega}$	Vorticity field such that $\boldsymbol{\omega} = (\omega_x, \omega_y, \omega_z)(x, y, z)$
$\boldsymbol{\omega}'$	Perturbation vorticity field such that $\boldsymbol{\omega} = (\omega'_x, \omega'_y, \omega'_z)(x, y, z)$
$\hat{\boldsymbol{\omega}}$	Perturbation vorticity field of the eigenmode of the linearised system
$\boldsymbol{\Omega}$	Vorticity field of the two-dimensional flow such that $\boldsymbol{\Omega} = \Omega_z(x, y)$

Latin characters

Symbol	Description
c	Landau constant
c_d	Drag coefficient
$c_{d,p}$	Pressure contribution to c_d
$c_{d,v}$	Viscous contribution to c_d
c_l	Lift coefficient
$c_{l,p}$	Pressure contribution to c_l
$c_{l,v}$	Viscous contribution to c_l
$-c_{pb}$	Base suction coefficient
d	Cylinder side length
E_k	Total (volume integrated) kinetic energy of the flow
f	Frequency
\boldsymbol{f}	Body force acting on the fluid
f_0	Fundamental frequency of a signal obtained from an FFT
F_d	Drag force acting on the cylinder (streamwise)
F_l	Lift force acting on the cylinder (cross-flow)
h	Projected height of the cylinder on the uniform flow

Continued on the next page.

Continued from previous page.

Symbol	Description
l	Sensitivity field / Spectral norm of the sensitivity tensor
J	Order of the time integration's multistep scheme
k'	Perturbation kinetic energy
l	Landau coefficient / Cubic saturation term in the Landau equation
L_R	Length of the recirculation region in steady wake
L'_R	'Half' length of the recirculation region in the steady wake
m	Wavenumber
m_A	Critical wavenumber for mode A
m_B	Critical wavenumber for mode B
m_C	Critical wavenumber for mode C
m_I	Critical wavenumber for mode I
m_{II}	Critical wavenumber for mode II
m_{III}	Critical wavenumber for mode III
N_F	Number of Fourier modes
N_p	Order of the tensor-product-polynomial shape function
p	Pressure
P	Pressure field of the two-dimensional flow
$ P(f) $	Normalised power spectral density from the FFT
\mathbf{q}	State variable such that $\mathbf{q} = \{\mathbf{u}, p\}$
\mathbf{q}'	Perturbation state variable such that $\mathbf{q}' = \{\mathbf{u}', p'\}$
\mathbf{q}^+	Adjoint state variable such that $\mathbf{q}^+ = \{\mathbf{u}^+, p^+\}$
\mathbf{q}_b	Base state variable such that $\mathbf{q}_b = \{\mathbf{u}_b, p_b\}$
$R(u)$	Residual function of variable u
$R(\phi)$	Autocorrelation function
t	Time
T	Vortex shedding period
\mathbf{u}	Velocity field such that $\mathbf{u} = (u, v, w)(x, y, z)$
\mathbf{u}'	Perturbation velocity field such that $\mathbf{u}' = (u', v', w')(x, y, z)$
\mathbf{u}^+	Adjoint velocity field such that $\mathbf{u}^+ = (u^+, v^+, w^+)(x, y, z)$

Continued on the next page.

Continued from previous page.

Symbol	Description
\mathbf{u}^\dagger	First intermediate velocity solution of the time integration
\mathbf{u}^\ddagger	Updated intermediate velocity solution of the time integration
$\hat{\mathbf{u}}$	Perturbation velocity field of the eigenmode of the linearised system
\hat{u}	Coefficients of the expansion basis functions
u^δ	Approximated solution variable from the Galerkin method of weighted residuals
\mathbf{U}	Velocity field of the two-dimensional flow such that $\mathbf{U} = (U, V)(x, y)$
U_0	Uniform inlet velocity
v_q	Test function for the Galerkin method of weighted residuals
w^*	Normalised w -velocity signal such that $ w^* (t) \leq 1$
w_q	Nodal weights of the Gauss–Lobatto quadrature
\mathbf{x}	Spatial dimensions $\mathbf{x} = (x, y, z)$
$y_c(x)$	Wake centreline at a position x

Dimensionless groups and text variables

Symbol	Description
Re	Reynolds number
Re_{2P}	Transition Reynolds number for the onset of the 2P vortex street
Re_A	Transition Reynolds number for the mode A secondary instability
Re_B	Transition Reynolds number for the mode B secondary instability
Re_c	Critical Reynolds number for the primary wake instability
$Re_{c,d}$	Re_c rescaled by the cylinder side length d
Re_C	Transition Reynolds number for the mode C secondary instability
Re_d	Reynolds number rescaled by the cylinder side length d
Re_E	Energy Reynolds number below which all disturbances decay
Re_I	Transition Reynolds number for the mode I secondary instability
Re_{II}	Transition Reynolds number for the mode II secondary instability
Re_{III}	Transition Reynolds number for the mode III secondary instability
Re_s	Reynolds number for the onset of flow separation
$Re_{s,d}$	Re_s rescaled by the cylinder side length d

Continued on the next page.

Continued from previous page.

Symbol Description

Re_{t1}	Reynolds number where the <i>Sec</i> mode becomes unstable in the time mean wake
Re_{t2}	Reynolds number where the <i>Sec</i> mode overtakes the <i>BvK</i> mode as the dominant instability in the time mean wake
Ro	Roshko number
St	Strouhal number
2P	2P form of the vortex street in the two-dimensional flow
<i>Bil</i>	Time-mean wake instability mode responsible for the separated vortex street in two-dimensional flows
<i>BvK</i>	Time-mean wake instability mode responsible for the near wake vortex shedding in two-dimensional flows
<i>Sec</i>	Time-mean wake instability mode responsible for the secondary vortex street in two-dimensional flows
P+S	P+S form of the vortex street in the two-dimensional flow
DSV	Dual secondary vortex shedding pattern
FFT	Fast Fourier transform
MS	Main separation vortex shedding pattern
SSV	Single secondary vortex shedding pattern
VM	Vortex merging shedding pattern
PKE	Abbreviation for “perturbation kinetic energy”

Contents

Introduction	1
Motivation and overview	1
Fundamental concepts	4
Kinematics of a fluid element	5
Transitions between flow states	6
Dimensionless groups	8
Constraints of the study	8
Structure of the thesis	9
1 A Review of the Literature	11
1.1 Wakes of circular cylinders	11
1.2 The wakes of cylinders having non-circular cross-sections	33
1.3 Project aims	45
2 Methodology	47
2.1 Governing equations	48
2.2 Numerical formulation	50
2.2.1 Spatial discretisation: the spectral-element method	50
2.2.2 Temporal evolution	54
2.2.3 Three-dimensional flows: the spectral-element–Fourier method	57
2.3 Analytical tools	59
2.3.1 Linear/Floquet-type global stability analysis	59
2.3.2 Perturbation kinetic energy analysis	62
2.3.3 Receptivity and structural sensitivity analysis	65
2.3.4 Stuart–Landau equation	67
2.3.5 Force calculations	69
2.4 Validation of the solver and the analytical tools	70
2.4.1 Two-dimensional flow: spectral-element (SE) solver	70
2.4.2 Three-dimensional flow: SE–Fourier solver	72
2.4.3 Validation of the time-integration scheme	74
2.4.4 Validation of the Floquet stability analysis	77
Circular cylinder wake stability	78

	Square cylinder wake stability	80
2.4.5	Validation of the structural sensitivity analysis	81
2.5	Problem setup	84
3	Two-dimensional flow characteristics	95
3.1	Steady flow regime	96
3.1.1	Wake characteristics	96
3.2	Unsteady flows	105
3.2.1	Transition to periodic flow	106
3.2.2	Variations of the two-dimensional vortex street	111
	Regime I: The Kármán vortex street	113
	Regime II: Decay or re-arrangement to a dual layer wake	114
	Regime III: Secondary vortex street wake	116
	Regime IV: The 2P mode	119
	Regime V: The P+S mode	123
	Further discussion on the 2P and P+S modes	126
3.3	<i>St-Re</i> variations with cylinder inclination	128
3.4	Flow induced forces	132
3.5	Chapter summary	138
4	Stability of the cylinder wake	141
4.1	Stability of two-dimensional time-periodic wakes	142
4.1.1	Instability growth rates and neutral stability	143
4.1.2	Mode structure and symmetry	148
4.1.3	Quantifying deviations from the Kármán vortex street symmetry	150
	4.1.3.1 Deviation of the wake centreline	151
	4.1.3.2 Measures of global asymmetry	154
4.1.4	Linear instability modes in the 2P mode base flow	161
4.2	Stability of the time-averaged wakes	164
4.3	Chapter summary	173
5	Structural sensitivity and energetics of wake instabilities	175
5.1	Structural sensitivity of the linear instability modes	176
5.2	Perturbation kinetic energy budget of the linear instability modes	180
5.3	Chapter summary	193
6	Three-dimensional flows past the inclined cylinder	197
6.1	Three-dimensional flow transition via the linear instability modes	198
6.2	Three-dimensional flow dynamics in extended systems	207
6.2.1	Modal growth, nonlinearities, and turbulence	208
6.2.2	Flow induced forces and shedding frequencies	221

6.3 Chapter summary	235
7 Conclusions	237
7.1 Two-dimensional flow past an inclined cylinder	238
7.2 Stability of the cylinder wake	240
7.3 Perturbation characteristics of the instability modes	242
7.4 Three-dimensional flows past the cylinder	245
Bibliography	249

Introduction

This thesis presents the findings from a project looking into the characteristics and stability of flows past a cylinder with a triangular cross-section. Over the following sections, the motivation behind this investigation will be introduced along with some fundamental concepts, followed by an outline of the aims of the project. Finally, the structure of this thesis will be explained.

Motivation and overview

The wakes of flows past bluff bodies have, over the past century, held a prominent place in the field of fluid mechanics, continuing to fascinate and inspire further studies with an aim to unravel the complex physics behind them. The vortex shedding phenomenon and its cascade to turbulence are ubiquitous in nature, developing various forcing profiles on the solid body from which the wake is produced depending on the incident flow, and bears continued importance from an engineering perspective. For example, at sufficiently high wind speeds, the wake of the body can be observed to oscillate, which may either be desirable or detrimental depending on the application. Beneficial effects of these unsteady wakes include heat transfer enhancement where the unsteady flow potentially promotes convective heat transfer in the system, as well as in renewable energy concepts such as tidal or wave energy devices or even in wind energy devices (see vortexbladeless.com) where the vibrational energy associated with these wake oscillations or that induced on the body may be harvested. Conversely, oscillations in the flow can be detrimental to static structures such as buildings which generally possess prismatic geometries, and bridge pylons amongst other examples by introducing fatigue from the vibrations, noise generation, and resonant effects. An infamous example of a structural failure induced by undesirable aerodynamic effects is the collapse of the Tacoma Narrows Bridge in 1940. It is thus clear that an understanding of the causes of any transition in these flows, while fundamental in nature, is pivotal to develop a



FIGURE I: Kármán vortex street formation in the clouds past the Beerenberg Volcano on Jan Mayen Island in the North Atlantic Ocean. The image was acquired by NASA’s MODIS instrument on April 4, 2012. Credit: NASA/GSFC, Rapid Response.

deeper understanding in this field and is of broad engineering relevance.

Figure I shows an example of the wake forms to be considered in this thesis. The dual rows of counter-rotating patches of fluid (vortices) make up the Kármán vortex street, which was investigated chiefly by Henri Bénard in his experiments at the University of Lyon (Bénard, 1908). In an experiment where a knife was placed at an angle into a water tank, he noted that he, quoting a translation by Wesfreid (2017), *“was surprised to discover two splendid lines of alternate vortices, a phenomenon that many people can see every day without noting it”*. The phenomenon itself borrows its name from Theodore von-Kármán who derived that the arrangement of point vortices in an array is unstable for all but one arrangement. Lord Rayleigh then demonstrated the role of this phenomenon in causing the Aeolian tones investigated by Strouhal (von Kármán, 1954). The Kármán street is the most well known of the wake patterns this thesis investigates. Despite the many years of investigation in this field, one finds that there is still much to be uncovered. The complexity of these flows was well described by Roshko:

“It is ironic that in the light of experience it has become clear that the complex flow past a circular cylinder could hardly be less suitable as a starting place to develop understanding of bluff-body flow dynamics. The variability of the separation-point position adds a degree of freedom for complexity which has its most spectacular manifestation at the “critical” Reynolds number and which may also play a role in other changes...”

Roshko, 1993.

While much attention has been paid to investigating the flows and transitions in the wake of a cylinder with a circular cross-section, the characteristics and associated transitions of the wakes of other bluff bodies possessing sharp corners over which flow separation may be fixed have received far less attention. Additionally, a systematic study on the relations between the transition modes which manifest in the wakes generated by various cylindrical bodies is lacking. Besides this, the effects of gradually altering the flow symmetry through forced flow separation on the wake is largely unknown. The cylinder possessing a triangular cross-section is interesting in this respect since this cross-section features sharp corners, which are common features in structural design, vortex generators, heat exchangers and flow measurement devices among other applications. The triangular cross-section cylinder shows a stronger lack of geometric symmetry to the oncoming flow since, with the exception of two orientations, the cylinder always presents an unequal number of faces to the upstream and downstream directions of the flow. The degree of geometric asymmetry about the streamwise direction can be controlled solely through the inclination of the cylinder, thus allowing for the effects of flow asymmetry on the wakes of the cylinder and its properties to be studied systematically. The shape also naturally fixes the point of flow separation at the triangle corners, unlike the circular cylinder where separation points are free to drift on the cylinder surface.

The findings from this thesis may help better inform flow control strategies by exploiting the properties of these wakes, illustrate the effects of geometric sharp corners on the aerodynamics of structures, or to augment the scalar transport properties of a flow as exemplified by vortex promoters in heat exchangers, amongst other applications.

This study thus connects two extremes of cylindrical geometries investigated in the past, from the circular cross-section cylinder whose surface is continuous and symmetric over which the flow separation points may vary and so its dynamics are hard to predict, to the wake of the flat plate which presents sharp separation points to the flow without a bluff geometric profile.

Fundamental concepts

Before proceeding further, a brief introduction into relevant fundamental concepts is first covered here to provide context into the problem as well as to introduce terminology used extensively hereafter. This section begins with a definition of a fluid.

By definition, a fluid is a medium which deforms continuously under the action of an applied shear stress. Solid media, on the other hand, exert a restoring force under the action of an applied stress, deforming permanently only when the stress applied exceeds a certain threshold. Following this definition, liquids and gases commonly encountered in everyday life generally conform to this definition, with water and air respectively being the two most recognisable examples. Different types of fluids are then distinguished by their intrinsic properties such as density and viscosity, amongst many others. Such a definition of a fluid encompasses a large class of media whose behaviour can still vary quite drastically, and as such, subsequent classifications of different types of fluids are necessary.

One such classification is based on how the fluid itself reacts to applied stresses. Fluids whose shear strain rate is proportional to the applied shear stress are classed as Newtonian fluids, the proportionality constant being the fluid viscosity. Fluids behaving otherwise fall under the non-Newtonian class, examples of which include honey, toothpaste, many polymer melts, etc. Given their myriad engineering applications, this project restricts itself to Newtonian fluid flows.

The next assumption made in this study is that fluid motion is dictated by continuum mechanics from where the relations in the following section are derived although the primary equations governing the motion will be introduced in a subsequent chapter. A more detailed elaboration may be found in fluid mechanics texts such as Munson *et al.* (2009), White (2011), Anderson (2011), amongst others.

Kinematics of a fluid element

To aid these explanations, consider a unit volume fluid element moving at a velocity $\mathbf{u}(\mathbf{x}) = (u, v, w)(x, y, z)$. In general, the motion or deformation of the fluid element arise from actions of the strain-rate tensor $\nabla \mathbf{u}$, which is given as

$$\nabla \mathbf{u} = \mathbf{S} + \mathbf{A} = \begin{bmatrix} \partial_x u & \partial_y u & \partial_z u \\ \partial_x v & \partial_y v & \partial_z v \\ \partial_x w & \partial_y w & \partial_z w \end{bmatrix},$$

where

$$\mathbf{S} = \frac{1}{2} \begin{bmatrix} 2\partial_x u & \partial_y u + \partial_x v & \partial_z u + \partial_x w \\ \partial_x v + \partial_y u & 2\partial_y v & \partial_z v + \partial_y w \\ \partial_x w + \partial_z u & \partial_y w + \partial_z v & 2\partial_z w \end{bmatrix},$$

$$\mathbf{A} = \frac{1}{2} \begin{bmatrix} 0 & \partial_y u - \partial_x v & \partial_z u - \partial_x w \\ \partial_x v - \partial_y u & 0 & \partial_z v - \partial_y w \\ \partial_x w - \partial_z u & \partial_y w - \partial_z v & 0 \end{bmatrix}.$$

Alternately, $\mathbf{S} = (\nabla \mathbf{u} + (\nabla \mathbf{u})^T) / 2$ and $\mathbf{A} = (\nabla \mathbf{u} - (\nabla \mathbf{u})^T) / 2$, each being the symmetric and anti-symmetric decomposition of the strain-rate tensor, and the notation $\partial_b a$ corresponds to the partial derivative $\partial a / \partial b$.

Translation

The first obvious motion of the element is its own translation, which is simply quantified through the rate of change of its displacement $d\mathbf{x}/dt$, and acts through its centre of mass without deforming the element. Under a uniform velocity field aligned with the fluid element, the motion is purely translational, but the action of velocity gradients about the fluid element will introduce additional effects on the motion as follows.

Rotation

The rotation of a fluid element is quantified through the anti-symmetric part of the strain-rate tensor, and is associated with the curl of the velocity field

$$\begin{aligned} \boldsymbol{\omega} &= \nabla \times \mathbf{u} \\ &= \begin{pmatrix} \partial_y w - \partial_z v \\ \partial_z u - \partial_x w \\ \partial_x v - \partial_y u \end{pmatrix}. \end{aligned}$$

The resultant field $\boldsymbol{\omega}$ is called the vorticity field, and can be shown to be twice the magnitude of the angular velocity of the fluid element's rotation. This measure is

useful to quantify localised rotations in flow fields, crudely identifying flow features such as vortices, shear layers, or boundary layers (more accurate identification methods are, of course, available).

Dilatation

The dilatation of a fluid element is a deformation incurred through the actions of normal stresses applied on the element. This deformation is described through the trace of the symmetric component of the strain-rate tensor which is simply the divergence of the velocity field, and is given as

$$\begin{aligned}\text{Tr}(\mathbf{S}) &= \partial_x u + \partial_y v + \partial_z w, \\ &= \nabla \cdot \mathbf{u}.\end{aligned}$$

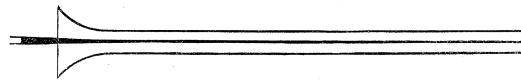
Here, the fluid element is either volumetrically expanding or contracting, and so it incurs a volumetric change. For an incompressible flow, the divergence of the velocity field $\nabla \cdot \mathbf{u} = 0$ as will be shown in a later chapter, and so such deformations are not permitted.

Shear strain

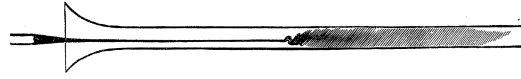
The last of these deformations arise through shearing of the fluid element, and can be quantified through the off-diagonal components of the symmetric part of the strain-rate tensor \mathbf{S} . Here, the fluid element deforms when unequal shear stresses are applied about the fluid element, causing it to skew.

Transitions between flow states

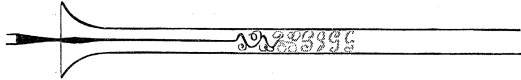
Amongst the significance of Reynolds' pipe flow experiments (Reynolds, 1883) was the reconciliation of the often differing friction factors from previous studies — Reynolds demonstrated that the friction factor changed from varying proportionally to the flow rate U to one proportional to $U^{1.723}$, the former range agreeing with Poiseuille's results in capillary tubes, and the latter range generally in agreement with Darcy's experiments. A crucial part of the result was in relating the change in the law of the friction to the various types of fluid motion in the pipe through the Reynolds number. Below a critical Reynolds number, the fluid flow appeared smooth and continuous as visualised through a stream of dye, and upon a certain speed, the stream of dye would spontaneously mix



(a) Undisturbed colour streak at low velocities.



(b) Disturbed colour streak at sufficiently high flow rates.



(c) Same as in (b), but at an instant illuminated by an electric spark.

FIGURE II: Reynolds' sketch of the ink dye visualisation of the flow through a pipe demonstrating the laminar and turbulent motions observed. These images are reproduced from Reynolds (1883) with permission conveyed through Copyright Clearance Centre, Inc.

with the rest of the fluid flowing through the pipe. Reynolds then reported the presence of distinct eddies when the diffused ink flow was viewed through a flash. While such fluid motions had already been observed by that period, this was the first to provide clear evidence that the different fluid motions occur past a certain threshold of the Reynolds number.

Another significant contribution of the paper was in the introduction of a dimensionless parameter relating the fluid's density ρ , viscosity μ , flowrate U and the pipe's diameter c :

“This is a definite relation of the exact kind for which I was in search.” ... “It seemed, however, to be certain if the eddies were owing to one particular cause, that integration would show the birth of eddies to depend on some definite value of $\frac{c\rho U}{\mu}$ ”

Reynolds, 1883.

This dimensionless parameter is now known as the Reynolds number. The Reynolds number can be read as a measure of the ratio of the inertial to viscous forces acting within the fluid, and is arguably the single most important parameter in fluid mechanics.

The low flow speed regime where the stream of ink remained smooth and continuous is now termed laminar flow, the higher speed regime where the stream of ink completely mixed with the rest of the flow in the pipe is generally termed turbulent flow, and the state bridging both regimes is the transitional state.

“The Reynolds number is now generally used in hydrodynamics, aerodynamics, hydraulics, and other sciences which have to do with fluid flow. It works in some cases almost like black magic.”

von Kármán, 1954.

These results find relevance in a large spectrum of fluid flows, a particular example drawn from von Kármán (1954) describes how the discrepancies in the drag forces on a sphere measured by Prandtl in Göttingen and Eiffel in Paris led to the finding of a critical Reynolds number about which the drag force appeared to decrease. Such an example is of direct relevance to the work undertaken in this thesis. This project is primarily interested in the transitional states of the flow past a cylinder as it gradually becomes turbulent, investigating (through numerical experiments as opposed to physical experiments) the states of the wake associated with these transitions and any associated changes in the dynamics and flow properties.

Dimensionless groups

Other dimensionless parameters are also important, and may be derived from dimensional analysis of the relevant variables in a particular flow system. Besides the Reynolds number, another parameter used extensively in this study is the Strouhal number which quantifies the frequency response of an oscillatory flow,

$$St = \frac{fd}{U},$$

where f is the flow frequency, d is some characteristic length, and U is the flow speed.

Constraints of the study

Several constraints are placed on the fluids and flows investigated in this study. As mentioned previously, this study restricts itself to Newtonian flows where the fluid strain rate is proportional to the applied shear stress. Many fluids behave in a similar

manner (air and water being the two most common examples), and so such a constraint is not overly restrictive. Besides that, this study restricts itself to flows which are incompressible. Anderson (2011) explains that most homogeneous liquids, and also gases moving at speeds of less than 30% the speed of sound in the medium may be treated as incompressible without any detrimental loss of accuracy. Examples of the speed limits where this constraint becomes weak are approximately 435 m/s (1566 km/h) for water at room temperature where the speed of sound is approximately 1450 m/s, or speeds of approximately 102 m/s (367 km/h) for air where the speed of sound is approximately 340 m/s, both of which are of fairly large magnitudes. Another assumption made in this project is that the flows are isothermal, and so the constant temperature here would not incur the need to solve the energy equation or apply any thermodynamical relations. Considering that no thermal forcing is to be applied anywhere in this system, thermal fluctuations remain small, and so its effect may be assumed to be negligible, justifying the assumption.

Structure of the thesis

The remainder of this thesis is structured as follows. Chapter 1 provides a review of the existing literature on the wakes of flows past canonical cylindrical bodies, building up a picture of the state of knowledge in the field and highlighting some persisting questions motivating the present investigation. In chapter 2, the numerical scheme underpinning the solver utilised to compute the solutions of the flow throughout this project is briefly described. The chapter then introduces the various analytical tools utilised in this study, validating each approach against existing results where available to verify their implementation for the system under investigation.

The results chapters then follow, and are communicated in order of increasing dimensional consideration. The first of these is chapter 3 which investigates the various regimes observable for a two-dimensional flow and their associated characteristics. The flow frequency responses and structural forces induced on the cylinder by the two-dimensional flow are also presented. Chapter 4 then details the results from stability analyses performed on the two-dimensional flows as the basic state, describing first the stability of the two-dimensional time-periodic wakes to three-dimensional perturbations, followed by a discussion of the stability of the time-mean two-dimensional wakes to two-dimensional perturbations. Results from further investigations into the characteristics

of the dominant eigenmodes obtained from the stability analysis are then presented in chapter 5, covering the structural sensitivity of the eigenmodes as well as the sources of the instability growth as quantified through the evolution of the perturbation kinetic energy equation. Chapter 6 then presents the results for the three-dimensional flows computed, first discussing the weakly nonlinear aspects of the transitions through the dominant eigenmodes predicted from the stability analysis. Then, the flows at increasing Reynolds numbers are presented, elucidating the action of nonlinear mode interactions on the wake. The forces and wake frequencies are then reported for select cylinder inclinations as the Reynolds number is increased up to an upper limit of $Re = 300$ considered for this project. At the conclusion of this thesis in chapter 7, chapter-wise summaries of the key findings are presented.

Chapter 1

A Review of the Literature

Solid cylindrical structures are found throughout the physical world, and so the flows about these structures are just as ubiquitous. To very crude approximation, these can range from flows past buildings, bridge supports, network towers to undersea cables, and the wakes generated by such structures can at times be disruptive, if not destructive. Several examples of these have been covered in the preceding introduction.

This chapter provides a review of the results and key findings from relevant past studies into the wakes of bluff bodies and their stability. The literature review will first cover the transitions in the wakes of the circular cylinder in § 1.1, followed by those of canonical non-circular cross-sections such as the square cylinder in § 1.2 and flat plates and elliptical cylinders in § 1.2 to introduce the rich dynamics of wake instabilities. Literature for the triangular cylinder is then reviewed in § 1.2, demonstrating the stark contrast in efforts to understand its dynamics compared to the other cross-sections despite rising interests. The chapter finally concludes by outlining the aims of this project in § 1.3.

1.1 Wakes of circular cylinders

Considering its ubiquity in engineering, and the mathematical simplicity of its geometric form, the flows past a circular cylinder has attracted much interest in research. The simple mathematical representation of its geometry invites theoretical treatment, though analytical solutions remain scarce. Some early treatises on the subject can be found in Stokes (1851) and Lamb (1932), and more recent reviews of the subject are given by Berger & Wille (1972) and Williamson (1996b). The coverage to follow is structured in such a way as to present the wakes in order of increasing complexity.

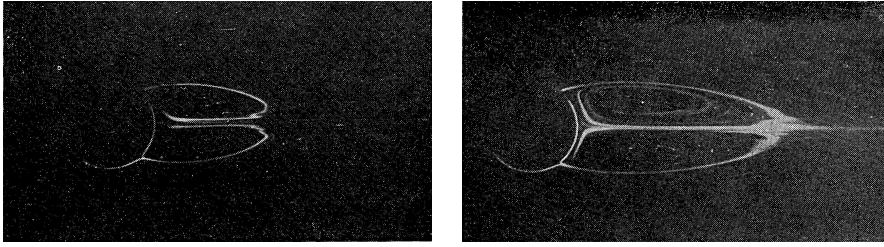


FIGURE 1.1: The steady symmetric eddies in the cylinder wake at $Re = 28.4$ and 41 illuminated by reflections from aluminium dust. The images are reproduced from Taneda (1956) with permission from The Physical Society of Japan.

Steady flows in the cylinder wake

Amongst the first to consider the problem was Stokes (1851) who attempted to derive an expression for the resistance of the fluid exerted on a pendulum (sphere). Several assumptions were made to simplify the equations of viscous fluid motion. Amongst them is the assumption that inertial effects are negligible such that the force on the sphere (drag) is derived purely from viscous forces. From this, the drag force was found to be expressed by $F_d = -6\pi\nu\rho rU$, where r and U are the radius of the sphere and the speed of the flow in which the sphere is immersed, respectively, and ν and ρ are the fluid's kinematic viscosity and density, respectively. Flows at such conditions are termed Stokes flows, the assumptions made implying that the flow is reversible, thus restricting the realisability of the solution to flows at Reynolds numbers $Re \rightarrow 0$. An equivalent expression of the drag force on an infinitely long cylinder was later derived by Lamb (1911). Several extensions to the Stokes flow solution by Oseen (1910), Lamb (1911), and Proudman & Pearson (1957), amongst others, incorporated corrections to partially account for the inertial term over subdomains in the flow where necessary. The solutions from these corrections then become physically realisable, albeit at small Reynolds numbers.

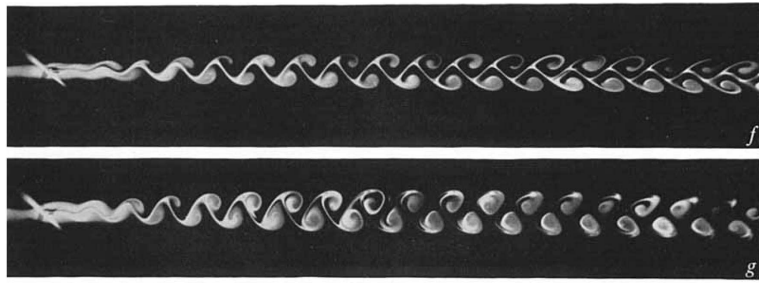
By gradually increasing the Reynolds number of the flow, Taneda (1956) observed that the twin recirculation vortices forming in the cylinder wake emerges and grows beyond a separation Reynolds number of $Re_s = 5$. Images of the steady symmetric eddies in the cylinder wake reproduced from Taneda (1956) are shown in figure 1.1. Coutanceau & Bouard (1977) showed that the length of the steady recirculation region (L) increases linearly with the Reynolds number, and that extrapolation of this

length to zero finds $Re_s \approx 4.4$ (after correcting for blockage effects arising from the experimental setup). They also reported that the velocity profile within the recirculation region of the steady flow is self-similar when the streamwise velocity profiles are normalised by their local maximum (u/u_{\max}) and the streamwise positions by the recirculation wake length (x/L). Various other verifications of these measures and values have also been performed, but a more recent prediction obtained from highly resolved numerical computations of the flow by Sen *et al.* (2009) estimates the separation Reynolds number as $Re_s = 6.29$, and shows that blockage effects on the separation Reynolds numbers diminish rapidly with decreasing blockages, the effect being negligible at blockage ratios below 0.01 (the blockage ratio being the transverse domain height to cylinder diameter ratio). These flows are steady-state and two-dimensional (they are invariant in both time and the spanwise direction).

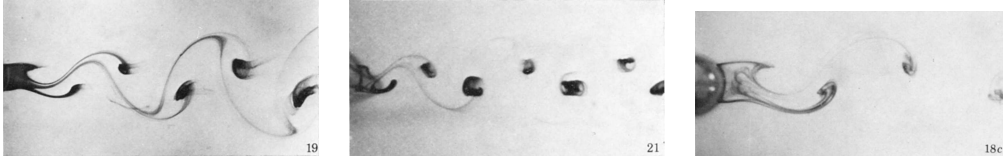
Transition to, and characteristics of, two-dimensional time-periodic flow

Taneda (1956) conducted a systematic experimental investigation into the states of the wake and its associated transitions, amongst which is the emergence of unsteady flow via the vortex street. Their results report that the wake begins to oscillate sinusoidally without shedding any vortices at Reynolds numbers of $Re = 30 - 45$, and that vortex shedding is observed at $Re > 45$. A subsequent report by Zdravkovich (1969) on smoke visualisations of the wakes at low Reynolds numbers ($30 \leq Re \leq 90$) described the development of the wake from an initially weakly distorted state, through one where the wake oscillates sinusously, to one where the shear layers of the wake roll up alternately to generate the staggered arrangement of counter-rotating vortices characteristic of the Kármán vortex street, which at the time provided some of the first strikingly detailed visualisations of the entire process. Further careful experiments by Gerrard (1978) found wake oscillations at $Re = 34$ similar to the experimental results of Coutanceau & Bouard (1977), and vortex shedding to manifest at about $Re \approx 55 - 70$. Images of the vortex streets reproduced from Zdravkovich (1969) and Gerrard (1978) are shown in figure 1.2.

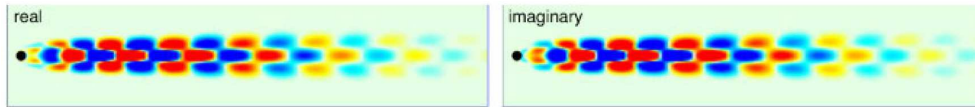
Taneda (1956) mentioned the sensitivity of the wake to external excitation where slight disturbances caused oscillations in the wake to begin at $Re < 30$ in his experiments. Taneda investigated this idea further in his 1963 paper to determine the Reynolds number below which all disturbances will decay. This threshold is essentially



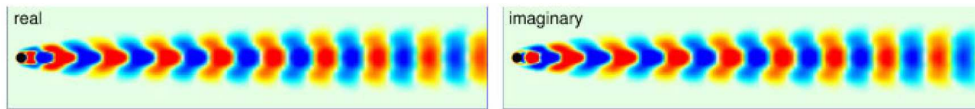
(a) Smoke visualisation of the vortex street by Zdravkovich (1969)



(b) Dye visualisation of the vortex shedding at $Re = 77$, 106, and 150 by Gerrard (1978)



(c) Eigenmodes of the steady flow by Mittal (2008)



(d) Eigenmodes of the time-averaged flow by Mittal (2008)

FIGURE 1.2: The images in panel (a) are reproduced from Zdravkovich (1969) with permission from Cambridge University Press. The images in panel (b) are reproduced from Gerrard (1978) with permission conveyed through Copyright Clearance Centre, Inc. The figures in panels (c, d) are reproduced from Mittal (2008) with permission from John Wiley & Sons, Ltd.

the energy Reynolds number (Re_E) albeit without measure or reference to the disturbance kinetic energy, which, for the circular cylinder wake, Taneda finds a value of approximately $Re_E = 1$ experimentally and about $Re_E = 3.2$ theoretically using the Orr–Sommerfeld equations under a parallel flow assumption. Indeed, transient growth analysis of the global mode responsible for the primary wake instability by Cantwell & Barkley (2010) finds that these excitations can effect responses in the wake at subcritical thresholds as low as $Re_E = 2.2$. These values of Re_E ranging around 1–3 reported

by Taneda (1956) and Cantwell & Barkley (2010) are below even those where the steady symmetric wake exists naturally.

Chomaz *et al.* (1988) and Monkewitz (1988) describe the nature of the growth of a disturbance in a flow, in which one finds the explanations behind global or local modes, each of which potentially being convectively or absolutely unstable. In an absolutely unstable flow, a disturbance introduced into the flow will grow unidirectionally from the source and ultimately contaminate the entire flow. In a convectively unstable flow, a similar disturbance introduced into the flow grows only as its advected by the flow, and so the disturbance grows away from its source. Chomaz *et al.* (1988) provides various descriptions of these, but the pertinent point made is that local absolute instability is a necessary but insufficient condition to incite a global instability. Monkewitz (1988) computed the local stability of various wake profiles, finding that local absolute instabilities manifest in the wake at low Reynolds numbers of $Re \approx 25$, which is below the value of $Re = 47$ at which the flow is globally unstable. These results, in addition to the threshold for unstable convective modes at $Re_E \approx 2$ from prior studies, follow exactly the local-to-global bifurcation sequences explained by Chomaz *et al.* (1988). A review on the concepts of global absolute and convective instabilities can be found in Huerre & Monkewitz (1990).

The mechanics of the primary wake instability as a global mode in its entirety has also been investigated through the linearised flow equations. While being significantly more computationally expensive than the local approach described earlier, this approach has the advantage of fully accounting for nonparallel effects in the wake. Jackson (1987) performed a global linear stability analysis of the steady wakes of the circular cylinder (and for various other cylinder cross-sections as well). The results showed that the steady wake becomes linearly unstable at a predicted critical Reynolds number of $Re_c = 46.2$, agreeing exceedingly well with the experimental results of Mathis *et al.* (1984) (which will be discussed shortly).

Barkley (2006) reported the results of a global linear stability analysis of the time mean and (forced) steady wakes of the circular cylinder, showing that the eigenmodes of the mean flows have wavelengths and frequencies that agree well with the unsteady two-dimensional flows computed compared to those estimated from the eigenmodes of the steady flows. A similar investigation was performed independently by Mittal (2008) who reported the same benefits of using the time averaged flows for stability analyses.

Examples of the eigenmodes of the steady and mean wakes reproduced from Mittal (2008) are shown in figure 1.2.

Mathis *et al.* (1984) demonstrated that the amplitudes of the transverse velocity fluctuations measured 5 cylinder diameters (d) downstream of the cylinder varied with the square root of a distance parameter ϵ through a power law where $\epsilon = Re - Re_c$ and Re_c is the predicted critical Reynolds number for the primary wake instability which they showed to be $Re_c = 47$. This relation enabled the pointwise velocity in the near wake to be described through the Stuart–Landau equation (Landau & Lifshitz, 1976) which models the response of a nonlinear complex oscillator. A significant outcome from relating the wake to the Landau model was proving the linear relation between the dimensionless frequency group Ro ($Ro = St Re$) and the Reynolds number Re . This was exactly the relation which Rayleigh (1915) and Roshko (1954) suggested to relate the shedding frequencies and the Reynolds number, Rayleigh deriving the expression through a similarity law and Roshko obtaining the relation empirically from extensive wind tunnel experiments.

Provansal *et al.* (1987) extended on this work to show that the Stuart–Landau equation also applied to the transient response of the wake, and that nonlinearities in the wake only influence the saturating amplitudes of the wake and have a negligible effect on the frequencies.

Sreenivasan *et al.* (1987) verified (independent to Provansal *et al.*, 1987) that the primary wake transition is through a supercritical Hopf bifurcation, and also that the transition can be described by the Stuart–Landau equation. Their experiments also find that the growth rate of the primary wake instability is constant through the wake, demonstrating the global and absolute nature of the unstable wake.

Goujon–Durand *et al.* (1994) demonstrated that the spatial variation of oscillation amplitudes in the wakes, when rescaled by the maximum amplitude and its position, have a universal form. The square of the wake oscillation amplitude was also shown to be proportional to the distance parameter $(Re_c - Re)/Re_c$, consistent with the results demonstrated by Mathis *et al.* (1984), and also that the position of the maximum amplitudes in the wake approaches the cylinder with increasing Reynolds number such that the position is inversely proportional to the square root of $(Re_c - Re)/Re_c$.

Zielinska *et al.* (1997) showed that the decrease in the length of the recirculation region at supercritical Reynolds numbers is due to mean flow corrections for nonlinear

interactions in the wake, and so nonlinearities in the wake strongly affects the flow even at moderate Reynolds numbers. Linear and weakly nonlinear theory are thus only applicable near the onset of the primary wake instability.

Thompson & Le Gal (2004) demonstrated the utility of the lift coefficient as an amplitude measure for the Stuart–Landau equation, showing all measured constants and coefficients to match almost exactly those found using the transverse velocity fluctuations in the near wake, the benefits being that the lift coefficient is a global measure of the wake instability as opposed to the velocity fluctuations which only describe the instability growth locally.

Regarding the properties of the unsteady two-dimensional wake, Perry *et al.* (1982) elucidated the effects of the observer speed on the perceived streamlines, and so the determination of the critical points in the flow at different spatial positions (since the unsteady wake varies spatially) require careful consideration. The authors also provide a clear explanation of the vortex shedding process.

Henderson (1995) computed the solutions of the two-dimensional flows and reported the details of the drag- and base pressure coefficients at increasing Reynolds numbers up to $Re = 1000$. Both coefficients register a gradient change about the onset of the primary wake instability, and the base pressure coefficients agree with available experimental data only up to a Reynolds number of $Re \approx 150$.

Stability of the vortex street

Historically, the vortex street imaged by Bénard (1908) was the first to clearly elucidate the formation of two alternate rows of vortices, showing that the wavelength of the structure (the distance between two successive vortices on one of the rows) increases with distance from the cylinder, and also with the viscosity of the fluid. A biography of Bénard by Wesfreid (2017) describes the extensive amount of research Bénard invested into the vortex shedding phenomenon (and myriad other fluid instabilities), amongst which it is noted that his early work demonstrates that the convection speed of the vortices and also the vortex street remains constant (for a distance) within the wake, and that this convection speed is distinct from and always lower than the constant towing speed of the cylinder (or the uniform flow velocity for a static cylinder).

The stability of the arrangement of an array of inviscid point vortices when only one vortex was free to move while the other vortices remained fixed in their relative

positions was analysed by von Kármán (1911), who found that a reflection symmetric arrangement of vortices is always unstable (and so the vortex will always drift), and that a staggered arrangement of vortices is similarly unstable except for when the (latitudinal-to-longitudinal) vortex spacing ratio is at a value of $\pi^{-1} \cosh^{-1} \sqrt{3} \approx 0.365$, at which spacing the arrangement itself is stable. Improving on this analysis and allowing all inviscid point vortices in the array to be free to move found the same stability characteristics, only that the vortex spacing ratio where the staggered arrangement of vortices is stable occurs at a slightly lower value of $\pi^{-1} \cosh^{-1} \sqrt{2} \approx 0.281$.

Hooker (1936) investigated the action of viscosity on the ideal vortex street derived by von Kármán (1911) motivated by a lack of agreement between experimental data and the theoretical result. Generally, prior experiments showed that the vortex spacing ratios were always much larger than the value of 0.281 derived by von Kármán (1911). These experiments also show that the vortex spacing ratio increases with distance from the cylinder, usually stemming from increases in the latitudinal distances between the two rows of the vortices while the longitudinal distances between vortices remain approximately constant, implying that the group velocity of the vortices comprising the street is approximately constant. Several crucial deductions were made in their study. First, the size of the vortex is shown to be affected by viscous effects such that the radius of the eddy increases in time (and also space since the vortices advect downstream in the wake over time). The center of vorticity is also deduced, from linear assumptions, to remain in its original position, and so from this the vorticity distribution within a vortex in the vortex street must be biased towards the street centreline to preserve the circulation. The vorticity is thus not symmetrically distributed within the vortex about its apparent center of rotation. Accounting for all these effects, Hooker showed that although the center of rotation of the vortices in the vortex street appeared to drift noticeably (and with it causing the vortex spacing ratio to increase to large excesses of the stable value predicted by von Kármán), the center of vorticity of the vortices in the near wake tend to follow quite closely the ideal vortex street spacing when accounting for viscous effects.

Saffman & Schatzman (1982) extended the analysis of von Kármán (1911), focusing on the effects of vortices of finite sizes as opposed to the point vortices considered by von Kármán (1911). The authors showed that accounting for the finite sizes of the vortices broadens the range of values of vortex street spacings where the array of vortices remain

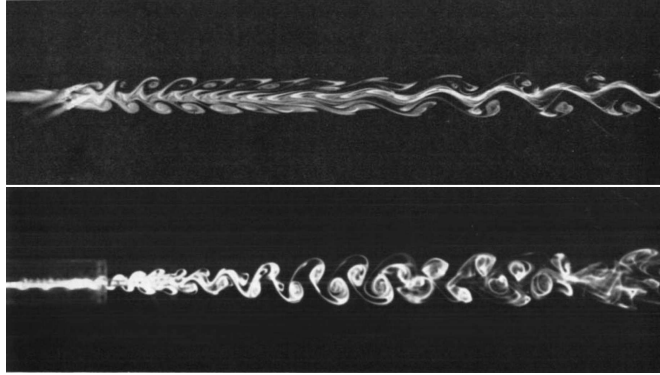


FIGURE 1.3: Visualisation of the secondary vortex street in the wakes generated by a group of three cylinders at approximate Reynolds numbers of 100 and 200, respectively. The images are reproduced from Zdravkovich (1968) with permission from Cambridge University Press.

stable, the vortex spacing ratio generally increasing with the vortex sizes.

Ponta (2010) systematically investigated the vortex shedding process in detail, and clearly elucidated that the vortices in the street at a Reynolds number $Re = 100$ are elliptical in shape in the near wake with a Gaussian vorticity distribution, slowly relaxing back into a circular shape downstream. The decay of the vorticity as the vortices advect downstream is also shown to vary hyperbolically with position.

As a counterpart to Ponta's findings, the vortex street can be perturbed in such a way that circular vortices within the vortex street would strain into an elliptical form. Durgin & Karlsson (1971) demonstrated this from experiments decelerating the vortex street by placing a large obstruction some distance downstream in the wake. Their results showed that the deceleration affected the vortex spacing ratio, which in turn caused the convection of vorticity within a vortex about its centre due to induced velocities from neighbouring vortices. Specifically, the vortex can only remain circular at a critical vortex spacing ratio value of 0.365, and on either side of this threshold the vortex will begin to stretch and rotate into an elliptical form. Considering that the ideal spacing ratio of inviscid point vortices is approximately 0.281, and that the lateral spacing of the vortices generally increases with distance from the cylinder, it is almost inherent that the vortices in the vortex street will adopt such deformation modes. The motivation behind this study was to understand the vortex street breakdown phenomena where the array of vortices generally diffuse into two shear layers, which can subsequently be unstable to a secondary vortex street.

Indeed, visualisations by Taneda (1959) and Williamson & Prasad (1993) amongst others have shown complex structures forming in the far wake of the circular cylinder. Taneda (1959) visualised these developments into a secondary vortex street in the far wake of the cylinder experimentally, and suggested that it develops from a hydrodynamic instability of the mean flow. Zdravkovich (1968) also showed that a similar larger scaled vortex street forms in the wake of a group of three cylinders. Some images of the secondary vortex street reproduced from Zdravkovich (1968) are shown in figure 1.3.

Cimbala *et al.* (1988) focused on the formation of the secondary vortex street in the far wake, and performed a local stability analysis on the time mean wakes (assuming a parallel flow which was admittedly approximate). One of the outcomes of the investigation was in demonstrating that smoke visualisation methods used extensively in past flow visualisations retain a memory effect in the streaklines due to a mismatch in the vorticity and dye diffusion rates. The experiments showed that the onset of the secondary vortex street may actually commence much further downstream in the far wake than previous studies had suggested owing to this effect, and also that the decay of the Kármán vortex street may actually occur much more rapidly. Spectral analysis of the fluctuating velocities in the wake show that the shedding frequencies in the spectra decrease in amplitude to negligible levels with increasing distance from the cylinder (the dominant Kármán shedding frequency decaying exponentially up to 125 cylinder diameters downstream), but at sufficiently large distances downstream in the wake, specific non-harmonic frequencies are found to be selectively amplified. A pseudo spatial local stability analysis of the two dimensional time mean wake profiles showed a very approximate agreement with the results from the spectral analysis, showing that the experimentally measured secondary wake frequencies remain approximately constant until a distance where it matches the locally neutral frequency, at which point it begins to follow the secondary frequency curve predicted by the stability analysis. The authors then suggested that the secondary vortex street manifests from an instability of the mean wake as suggested by Taneda (1959) (as opposed to another popular hypothesis that the secondary vortex street arises from vortex amalgamation put forward by Matsui & Okude, 1983) since the frequencies in the far wake can be approximately predicted from stability analyses of the time mean wake which does not see any of the secondary vortices.

Karasudani & Funakoshi (1994) showed both numerically and experimentally the

evolution of the vortex street from the Kármán street, through the vortex street breakdown, and finally to a secondary vortex street of larger scale, also showing that the vortex spacing ratio increases as the vortices move downstream in agreement with past findings by Taneda (1959), Hooker (1936), and Cimbala *et al.* (1988). A subsequent study by Inoue & Yamazaki (1999) on the effects of time periodic flow forcing on the vortex street shows that a similar secondary vortex street forms. The formation of the secondary vortex street in this case was shown to be due to vortex merging processes only when the forcing was applied, with the authors explicitly stating that no such interactions were found in the unforced cases. This provides further support for the hydrodynamic instability scenario suggested by Taneda (1959) over the vortex pairing mechanism by Matsui & Okude (1983). Further investigations by Vorobieff *et al.* (2002) on the occurrence of the secondary vortex street using soap film visualisation for the wake (which essentially reflects the two-dimensional flow) and also two-dimensional flow simulations demonstrated that the position at which the secondary vortex street develops approaches the cylinder proportionally to $Re^{-0.5}$.

Various other techniques have also been applied to further understand the formation of the secondary vortex street. Kumar & Mittal (2012) conducted a global stability analysis of the time-mean wakes of the cylinder at $Re = 150$, investigating the convective nature of the two-dimensional perturbation field. The analysis reveals that the mode is convective for the $Re = 150$ wake of the circular cylinder, but remains asymptotically stable in a static reference frame. This agrees with their flow visualisation of the unsteady wake in which the $Re = 150$ case saturates without the secondary vortex street becoming dominant in the wake, the disturbance packets remaining at low magnitudes as they are advected by the flow. The study also demonstrated that the secondary vortex street was strongly sensitive to excitation levels, showing that the amplitudes of the far wake disturbances decrease significantly when the temporal resolution was increased by an order of magnitude as well as when the inlet velocity excitation was decreased. Further to these results, the study also discussed the structural sensitivity of the dominant convective eigenmode at $Re = 150$, and also showed that the (forced) steady wakes do not produce any eigenmodes relevant to the secondary vortex street (see Verma & Mittal, 2011 for the stability characteristics of the steady wake), supporting the time mean wake instability hypothesis. While the investigation demonstrated that the secondary vortex street manifests through a convective mode at $Re = 150$, it would

be interesting to compare it with the wake at $Re = 200$, considering that their results showed that the secondary vortex street develops in the far wake of the asymptotic solution, indicating that it is potentially a global absolutely unstable mode following the bifurcation path from Chomaz *et al.* (1988). The transition mechanisms between these convective and absolute states are of interest.

An interesting study by Dynnikova *et al.* (2016) demonstrated that the secondary vortex street emerges from a region of high dipole moment density, before which the vortex street decays and beyond which the far wake disturbances begin to amplify. Within such a region, two perturbation modes may manifest: one acting to alternately stretch and compress the street both axially and transversally (referred to as the varicose wave), and the other inducing a waviness in the street (referred to as the sinuous wave). The varicose wave was then shown to be capable of (conditionally) propagating disturbances upstream toward the cylinder body and is thus relevant in sustaining far wake disturbances for an absolute instability, while the sinuous wave always propagates disturbances downstream indicating that it is at most capable of supporting only a convective mode. Mismatch between the upwinding varicose wave velocity and the downstream vortex street group velocity causes the dipole cluster to move to a stable position where the velocity mismatch is reconciled and so the position of this dipole cluster remains at an approximately constant distance from the cylinder.

At Reynolds numbers where the vortex street breakdown or the secondary vortex street is observed on the two-dimensional solution branch, the wake is usually already three-dimensional. The following section introduces and discusses these three-dimensional flows.

Three-dimensionality of the vortex street

Roshko (1954) systematically quantified the properties of the wake of the circular cylinder such as the shedding frequencies and drag coefficients over an extensive range of Reynolds numbers. The data obtained suggests that the flow can be broadly be classed in to three ranges: the stable range extending through $40 < Re < 150$, the transition range through $150 < Re < 300$, and the irregular range for larger Reynolds numbers. The rapid decay of the Kármán vortex street was also quantified through the decay of the wake energy (as mentioned in an earlier section); the vortex street being indistinguishable at a distance of approximately 100 cylinder diameters downstream at a

Reynolds number of $Re = 100$. Another crucial result from this report is in the agreement that Roshko found between the linear variation of the dimensionless shedding frequency parameter $St Re$ (called the Roshko number Ro) with the Reynolds number Re and the similarity law that Rayleigh (1915) found. This section focuses only on the stable range, discussing the three-dimensional form of the vortex street and the mechanism behind its formation.

Amongst the first to enter this debate was Tritton (1959), whose experiments found a discontinuity in the Strouhal–Reynolds number relation at $Re \approx 90$ about which a transition was argued to occur, and from this it was suggested that the Roshko–Reynolds number relation fits to a quadratic function better than it does to a linear function to account for changes incurred by this transition. A low speed mode manifests at Reynolds numbers below this threshold and was associated with an instability originating in the wake. The high speed mode, on the other hand, manifests at Reynolds numbers beyond this threshold and was associated with an instability caused by the vortex street forming very close to the cylinder. From this, Tritton suggested that the discontinuity in the Ro – Re curve was associated with a movement of the wavemaker between these two positions.

Tritton’s result drew a considerable amount of interest as it was the first three-dimensional mode of the vortex street to be clearly elucidated, and several other papers on this feature followed, amongst which Berger & Wille (1972) suggested that these modes were due to freestream turbulence levels. Gerrard (1978) explained that the two branches in the St – Re curve (also the Ro – Re curve) in the stable region are associated with the low- and high- speed modes, describing that the ends of the finite length cylinder in the experiments cause the initially parallel lines of vortices (the parallel vortices being characteristic of the low speed mode) to ‘bow’. This ultimately contaminates the frequency of the initially parallel vortex street as the high speed mode (characterised by the bowing and ‘knotting’ effects on the spanwise vortices) dominates the wake. Gerrard (1978) finally suggested that this transition possibly marks the end of the Reynolds number range where vorticity diffusion is significant.

This discontinuity in the St – Re relation was finally reconciled by Williamson (1988a) in a short report followed by an extensive article on its occurrence in 1989. Using the idea by Gerich & Eckelmann (1982) on the effects of angled end plates fixed to the cylinder on the wake, Williamson (1988a) showed that it was possible to force the high

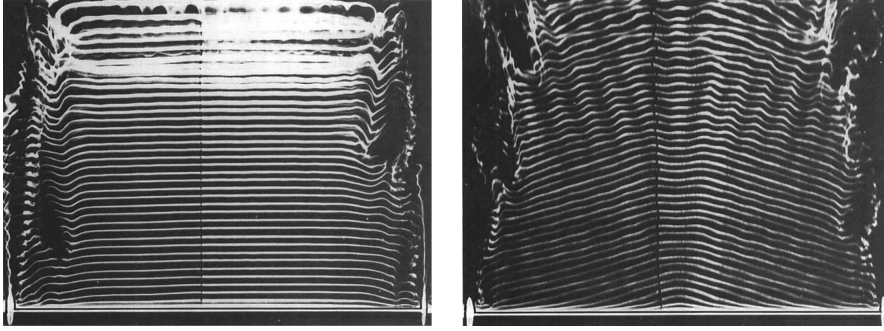
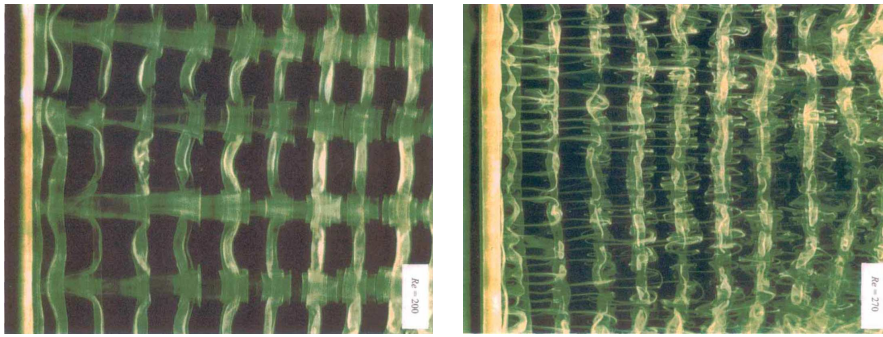


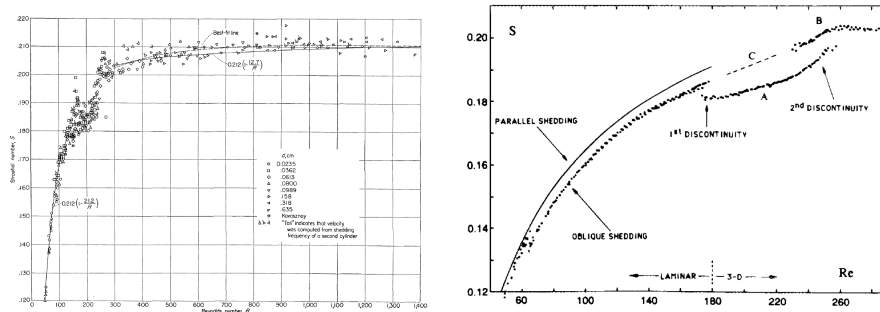
FIGURE 1.4: Visualisation of (left) the parallel vortex shedding mode at the initial stages of the shedding, and (right) the oblique shedding mode as its final state, both in the wake of the cylinder at a flow of $Re = 95$. The images are reproduced from Williamson (1989) with permission from Cambridge University Press.

speed mode (hereafter referred to as the oblique shedding mode) back into a parallel shedding state, and in doing so, causing its associated lower $St-Re$ branch to shift upwards in continuation with that of the parallel shedding mode. At about the same time, Eisenlohr & Eckelmann (1989) conducted almost identical experiments to show that the oblique shedding mode can be manipulated and reverted back to a parallel shedding mode, but focused on the effects and control of vortex splitting through a forced breakline. The outcomes were again similar to Williamson (1988a). Williamson (1989) explained that the frequency differences between the oblique- and parallel shedding modes are related to a velocity mismatch between that at the central span of the cylinder to that found at the cylinder ends. Several additional experiments using flat-plate-like bodies also showed the oblique shedding mode, and can also be corrected in the same way, and so these effects are expected to be generic to all experiments on bluff body wakes. Images of these parallel and oblique shedding modes by Williamson (1989) are reproduced in figure 1.4.

Having resolved the issue of the discontinuity in the $St-Re$ curve, it was clear that the oblique shedding mode was a three-dimensional effect induced by the experimental setup, and not an inherent three-dimensional instability of the wake itself. This established the next direction of focus in the field to investigate the three-dimensional instabilities through which the wake transitions.



(a) Visualisation of the three-dimensional transition modes by Williamson (1996a). (Left) Mode A at $Re = 200$, (right) mode B at $Re = 270$.



(b) Strouhal–Reynolds number relations by (left) Roshko, 1954, and (right) Williamson, 1988a.

FIGURE 1.5: The images in panel (a) are reproduced from Williamson (1996a) with permission from Cambridge University Press. The left plot in panel (b) is reproduced from Roshko (1954), while the right plot in (b) is reproduced from Williamson (1988a) with the permission of AIP Publishing.

Three-dimensional transition of the parallel vortex street

The focus is next redirected to the transition range in the $St-Re$ plot by Roshko (1954), which has been reproduced in figure 1.5(b). The reasoning behind the classification of the transition range is in the noticeable spread of the data found only at these Reynolds numbers. The extensive set of experiments conducted by Gerrard (1978) included few visualisations at Reynolds numbers within this range. In these cases, the wakes at lower Reynolds numbers in the transition range formed coherent streamwise structures that continuously extend back towards the cylinder as the vortex is shed, forming at the same spanwise position in succession — no such streamwise structures were noticed at Reynolds numbers within the stable range, although the Kármán vortices were observed to ‘knot’. The generation site of these ‘fingers of dye’ were said to appear at random

positions along the span, which in hindsight, was either an unfortunate composition of the inherent streamwise structure and the oblique shedding mode, and/or the natural dislocations which form in the vortex rollers of mode A which will be discussed next.

Following from their correction of the oblique shedding mode to the parallel shedding mode, Williamson (1988b) reported that the suppression of oblique shedding had remarkably removed the spread of the data in Roshko’s transition range, revealing distinct branches on the $St-Re$ curves with two clear discontinuities, each being associated with the onset of spanwise periodic three-dimensional structures of different scales developing on the spanwise vortex rollers. Images of these three-dimensional coherent structures by Williamson (1996a) are reproduced in figure 1.5(a). These streamwise structures originate from deformations of the primary vortex loops themselves, the first of which was associated with the $St-Re$ branch A, measured as possessing a spanwise wavelength of $3d$, and the transition being hysteretic. Visually, the streamwise structures observed by Gerrard (1978) were consistent with this pattern. The flow structures associated with the $St-Re$ branch B instead possessed a characteristic wavelength of about $1d$, and the associated transition was not hysteretic. The letter by Williamson (1988b) was followed by a comprehensive report (Williamson, 1996a), discussing in detail the dynamics of modes A and B (each being associated with the A and B branches in the $St-Re$ curve in Williamson, 1988a). Several results from the latter publication to note are the parameters associated with the transition: the critical Reynolds numbers for modes A and B are predicted here as 194 and 260, respectively, and the wavelengths of each mode are approximately $3-4d$ and $1d$, respectively. The temporal symmetries of both modes also differ, with mode A structures describing an out-of-phase symmetry each half-cycle while mode B describes an in-phase symmetry. The self-sustaining pattern of mode A from fixed positions along the cylinder span as well as its out-of-phase symmetry was also explained to be assisted through Biot–Savart induction of the existing streamwise vortices on the forming vortex roller. The in-phase symmetry of mode B was due to the proximity of the vortices, causing the existing streamwise vortex to ‘imprint’ its streamwise vorticity on the newly forming braid shear layer. A final observation made in this paper was that the mode A streamwise structures would inherently induce dislocations in the vortex roller, and is a state Williamson denoted mode A*.

Linear stability theory has been applied with great success to examine the stability

characteristics of these flows. The basic state of the flow is time-periodic, and so the linearised problem is of a Floquet type. The first attempt at a global stability analysis of the two-dimensional time-periodic vortex street to three-dimensional perturbations was conducted by Noack *et al.* (1993) who predicted a critical Reynolds number of 170 and a critical wavelength of $1.8d$, respectively. These predictions did not lie in agreement with the experimental results.

A subsequent attempt at a global stability analysis of the two-dimensional vortex street by Barkley & Henderson (1996) predicted two distinct modes to become unstable, the critical parameters for both being remarkably similar to the values found experimentally by Williamson (1996a). The symmetries of these two modes confirm that each were precisely the modes A and B reported by Williamson (1996a), with mode A predicted to become critical at a Reynolds number of 189 with a wavelength of $3.96d$, and mode B at a Reynolds number of 260 with a wavelength of $0.82d$. Besides the two synchronous modes corresponding to the mode A and mode B branches in the eigen-spectra from the stability analysis, a third quasiperiodic branch was also predicted. This branch remained stable within the range of Reynolds numbers investigated in the study, and was not explored further at the time.

Blackburn *et al.* (2005) investigated the characteristics of the quasiperiodic mode, predicting its criticality at a Reynolds number of 377 with a wavelength of $1.8d$. In applying the results from Marques *et al.* (2004), the paper explains that the symmetry properties of the vortex street in the circular cylinder wake only permits three generic bifurcations: two synchronous modes wherein one preserves the underlying symmetry of the base flow (which in this case corresponds to mode A which retains the half-period-flip map) while the other breaks the symmetry (corresponding to mode B), and a quasiperiodic mode which may manifest as either a modulated travelling wave or a modulated standing wave. This mode, however, would be difficult to observe in the circular cylinder wake since a broad spectrum of linear eigenmodes are already unstable when this quasiperiodic mode becomes critical.

Full three-dimensional computations of these flows have also been reported, showing that similar structures observed experimentally and through global stability analyses can be resolved, thus providing a reliable alternative to investigate these transitions. Amongst the first to compute these three-dimensional flows was the study by Karniadakis & Triantafyllou (1992) whose results suggested that the wake first becomes

three-dimensional at a Reynolds number within $Re = 200\text{--}210$. These flows were primarily computed on a volume extending through πd in the cylinder spanwise direction, with some additional computations at a longer span of $2\pi d$. A contour of the streamwise velocity in the wake centreplane provided for an $Re = 225$ flow suggests that the three-dimensional mode possessed a wavelength of $\pi d/2 \approx 1.57d$, lacking agreement with the experimental work by Williamson (1988b). In another report, Mittal & Balachandar (1995) computed the flows at $Re = 525$ within a computational volume with a spanwise extent of $1d$, showing the presence of coherent span- and streamwise structures in the wake, the latter being subharmonic to the vortex shedding. Thompson *et al.* (1996) later successfully captured modes A and B in the cylinder wake in their numerical simulations, showing that the predicted streamwise structures visually match those reported by Williamson (1988b).

Zhang *et al.* (1995) conducted both experiments and numerical simulations of the flow with large spanwise domains. Their numerical simulations find modes A, B, and A* in agreement with experimental data, but also finds an additional mode they coined ‘mode C’ which possesses a wavelength of approximately $2d$. Within the large computational domain, the wakes were found to become unstable at Reynolds numbers of $Re > 180$ for mode A and $Re > 230$ for mode B. The authors also mentioned that mode B could be observed from both experiments and numerical simulations to persist at Reynolds numbers of at least $Re = 1000$. Another interesting finding from this study was in the observation of mode C. This mode was only observed when a small trip wire (diameter = $0.006d$) was placed proximate to the cylinder. Besides the different wavelength it possessed compared to modes A and B, a distinguishing feature of this mode was its subharmonic nature (that is, the three-dimensional structure had a period twice that of the two-dimensional vortex street). This was consistent with the mode which Noack *et al.* (1993) reported from their stability analysis and experiments. The influence of a trip wire placed in proximity to the cylinder on effecting mode C was further investigated by Yildirim *et al.* (2013a) and Yildirim *et al.* (2013b) who demonstrated the reliance of mode C on the trip wire being placed asymmetrically about the wake centreplane, and also the rapid decay of the strength of the streamwise vorticity.

Henderson (1997) computed the three-dimensional flows using a spectral-element–Fourier method and showed from normal mode analysis that the mode A transition is subcritical causing the dominant frequency of the basic flow to drop when the three-di-

dimensional mode saturates, and that the mode B transition is supercritical. The study also demonstrated that the amplitude equation expanded to cubic-order is sufficient to model the saturating amplitudes of the supercritical bifurcation, but not the subcritical bifurcation. When the flow at $Re = 265$ was computed in a domain with a spanwise length in excess of the predicted unstable modes, the flow saturated to a state of spatio-temporal chaos arising from complex mode interactions. This suggests that the onset of three-dimensionality in the flow can lead to irregular states and fast transition to turbulence. An estimation of the dissipation scales of such an extended system was made, and from this the approximate number of Fourier modes (for spectral-element–Fourier methods) required to resolve these scales is suggested to be $N_F \approx 2\pi Re^{0.5}/L_z$ (L_z being the spanwise length of the computational domain).

The numerical study by Braza *et al.* (2001) for a flow at $Re = 220$ again found coherent streamwise structures in the wake with inherent vortex dislocations consistent with mode A*, and suggested similarly to Williamson (1996a) that vortex dislocations are a natural feature of the saturated mode A flow. A subsequent study by Akbar *et al.* (2011) demonstrated that nonlinear effects in the wake are strong even at the onset of mode A, suggesting that the subcriticality of the mode greatly diminishes the relevance of the linear predictions. This is in large part due to the vortex dislocations which naturally develop in the wake as mode A saturates, showing that the lower transition Reynolds number of the bistable range can occur as low as 170 in extended systems, whereas smaller domains prohibiting such vortex dislocations show a smaller bistable bracket where the lower threshold was at a Reynolds number of approximately 188 (mode A becomes linearly unstable at a Reynolds number of 189). Further flow computations by Behara & Mittal (2010) and Jiang *et al.* (2016) arrive at the same conclusions: the former study further showing that mode B flows saturate to a state without vortex dislocations.

Characteristics of the instabilities

With the literature having established the transition scenario, this section now considers the developments towards our understanding of the properties associated with these instability modes. The hysteretic nature of the transitions and the natural tendency for vortex dislocations to develop in mode A but not in mode B have already been reviewed. However, several results from various other works have also provided insight

into these transitions.

Williamson (1996a) and Leweke & Williamson (1998) suggested that the physical origin of mode A is one of a cooperative elliptic instability mechanism, a mechanism associated with the strain of a circular vortex into an elliptic shape. The elliptic streamlines in the near wake arises from the flow being subjected to an approximate uniform strain field and an approximate uniform rotation field within which region inertial waves may become unstable. A review of the elliptical instability mechanism can be found in Kerswell (2002), and a review of the instabilities in vortex pairs (drawing some similarities to the vortex arrays found in this system) is given by Leweke *et al.* (2016). Williamson (1996a) and Leweke & Williamson (1998) showed that such an instability mechanism would generate spanwise structures with wavelengths of approximately $3d$ after accounting for the action of viscosity, agreeing with mode A wavelengths of $3\text{--}4d$ found from the experiments. A subsequent analysis by Thompson *et al.* (2001) later suggested that both the elliptical and hyperbolic regions of the two-dimensional flow contribute to the mode A instability, and by decomposing the Floquet mode into these two regions, they concluded that the elliptical instability mechanism accounts for approximately two-thirds of the mode A transition, the remaining one-third coming from hyperbolic means.

In the numerical study by Braza *et al.* (2001), the authors investigated the relevance of a Craik–Leibovich instability mechanism as a means through which the instability is instigated. The mechanism is based on Stokes drift and the application of small spanwise periodic perturbations. Stokes drift arises in periodic wavy flows through a discrepancy between the Lagrangian and Eulerian mean flow velocities. The analysis predicted a dominant spanwise wavelength of approximately $3.4d$ at a Reynolds number of $Re = 220$, which is within the band of unstable wavelengths at this Reynolds number as reported in Barkley & Henderson (1996). The authors also noted that this analysis is complementary to the elliptical instability and Floquet analyses, all working towards understanding the mechanism behind the generation of axial (spanwise) undulations in the vortex loops in the two-dimensional time-periodic wake.

Another interesting feature of these instabilities is the localisation of the source where the disturbances appear to emerge from, drawing from the concept of a wave-maker owing to successful applications of weakly nonlinear theory in modelling the flow transition as a complex oscillator. This was investigated by Barkley (2005) by

means of, first, projecting the two-dimensional time-periodic base flow solution onto computational domains with progressively shorter outflow lengths past the cylinder, and then subjecting these flows in the truncated domains to a global stability analysis. The results for flows at $Re = 190$ and 260 corresponding to near neutral stability of modes A and B, respectively, remarkably showed that the eigenspectrum is faithfully reconstructed at outflow lengths as small as $3d$, and that by an outflow length of $1.5d$ the eigenspectrum becomes irrelevant to the actual problem. These results strongly allude to the existence of such a wavemaker, and that its position for modes A and B lie very close to the cylinder such that its exclusion essentially suppresses the instability.

In a separate study investigating the primary wake instability (transition from a steady flow to an unsteady flow), Giannetti & Luchini (2007) proposed a method to determine the position of the wavemaker, and hence also the sensitivity of the wake to perturbation force-velocity feedback. The method utilises the stability properties of both the linearised flow and its corresponding adjoint system to determine the response of the perturbation field to localised forcing, quantified through the eigenvalue drift. The spectral norm of the resulting tensor maps the sensitivity of the eigenvalues in the domain to perturbation force-velocity feedback in which the force is oriented in the worst possible direction. Applying this structural sensitivity analysis to the primary wake instability showed that the sensitive regions were concentrated to two regions in the near wake symmetrically distributed about the wake centreline. This map very approximately agreed with the regions reported by Sreenivasan *et al.* (1987) whose focus was on controlling and suppressing the instability. Giannetti *et al.* (2010) extended the analysis to these secondary instabilities in the wakes, and reported that the period averaged sensitivity fields were concentrated close to the cylinder and are also symmetrically distributed about the wake centreline as anticipated. For mode A at $Re = 190$, the most sensitive region in the wake (anticipated to be the wavemaker) extends from the cylinder to approximately 2 cylinder diameters downstream, while for mode B at $Re = 260$, the sensitive region extends from the cylinder to some position 1.5–2 cylinder diameters downstream. These results completely justify the observations made by Barkley (2005) — the stability analysis performed on domains whose outflow length interfered with or truncated the wavemaker showed a complete lack of semblance to the expected eigenspectrum. The results from these studies imply that most of the disturbances are excited only in the immediate vicinity of the cylinder despite the eigenmodes

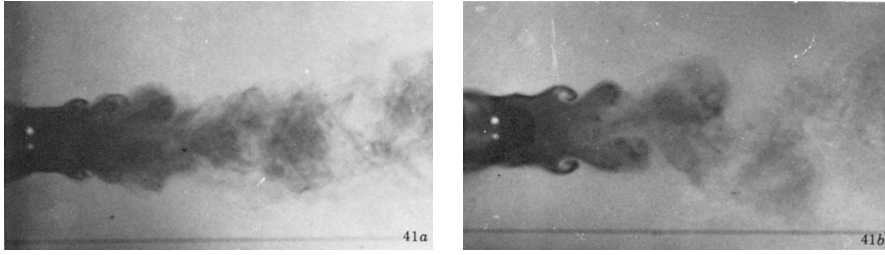


FIGURE 1.6: Visualisation of the shear layer instability in the cylinder wake at $Re = 1968$. The images are reproduced from Gerrard (1978) with permission conveyed through Copyright Clearance Centre, Inc.

showing the disturbances to persist over large distances in the wake.

The transient growth of these secondary instabilities in the cylinder wake was also investigated by Abdessemed *et al.* (2009), finding that transient growth only acted over the initial few shedding cycles before the disturbance energy amplification of the dominant mode approached the growth rate predicted by the Floquet analysis. The amplification rates in these cases also asymptote to the growth rates predicted by the Floquet modes, and so no significant bypass transitions are predicted. The optimal disturbances obtained from the analysis also evolve rapidly to match that given by the linear modes.

After all this work, it would be immensely useful to determine the measurements of the wake which are sensitive to the various flow regimes. The first obvious candidate is the shedding frequency as demonstrated by Roshko (1954) for the stable (unsteady two-dimensional) and irregular ranges, and also from Williamson (1988a) for the transition range. The shedding frequency across these ranges show two discontinuities at the transitions to modes A and B as described earlier, with a third discontinuity possible at the low Reynolds number range associated with the onset of oblique shedding which might be observed in experiments. Another of these measures that should be mentioned is the base pressure coefficient. Roshko (1993) shows that this measure behaves remarkably differently at different flow regimes and can thus provide initial information on underlying transitions. The paper also provides an analysis into why the measure works as well as it does.

Instability of the shear layer

At even higher Reynolds numbers, irregularities in the wakes emerge from the structured three-dimensional modes. Bloor (1964) investigated the development of these irregular high frequency fluctuations, terming them *transition waves*. These were shown to commence at some distance downstream in the wake and approaches the cylinder as the Reynolds number is increased. When these transition waves form close to the cylinder (well within the formation region), the transition to turbulence in the flow was observed to change from one forming in the wake due to the distortion of the vortices (consistent with the secondary instabilities discussed prior) to one forming in the shear layer before the vortices roll up. The latter form is attributed to the generation of two-dimensional Tollmien–Schlichting waves in the separated shear layer, and is the primary focus of this section. Gerrard (1978) observed such transition waves in his experiments to become noticeable at $Re > 350$. Some images of the fully developed instability in the shear layer from Gerrard (1978) is reproduced in figure 1.6. Wei & Smith (1986) showed that immediately after the formation of the secondary vortices from the shear layer instability, the secondary vortices undergo strong three-dimensional distortion and become three-dimensional. Two-dimensional flow computations by Braza *et al.* (1986) also observed this breakdown of the free shear layer, demonstrating the nominally two-dimensional nature of the onset of this instability as suggested by Bloor (1964).

1.2 The wakes of cylinders having non-circular cross-sections

The literature covered thus far has focused solely on the transitions found in the wake of a circular cylinder. As mentioned earlier, the simplicity of the geometry having a simple mathematical form in the cross-section and also a homogeneous span has invited much attention to the problem with the allure that a simple flow solution might also exist. This, however, is not the case. Roshko (1993) highlights that the continuous cylinder surface permits a variability in the point of flow separation which adds to the complexity of the problem being considered.

From an engineering perspective, the circular cylinder is not the only cylindrical structure to be commonly used. Prismatic structures or cylinders with polygonal sections are easier to manufacture or build across a large variety of applications, and so an idealisation of the structures as simple geometries such as square or elliptical section

cylinders are useful. In this section, the literature coverage of flow transitions in the wakes of common non-circular cross-sections are summarised.

Introducing corners: wakes of square cylinders

Numerical computations of the two-dimensional flow past a square cylinder by Sen *et al.* (2011) with its sides aligned parallel to the flow investigated the properties of the steady wake and the onset of flow separation. The study predicted steady flow separation from the cylinder to occur at a separation Reynolds number of $Re_s = 1.15$, and that the length of the steady recirculation region in the wake increased linearly with increasing Reynolds number even up to $Re = 40$. The steady recirculation region was also shown to comprise two symmetric eddies about the wake centreline, both emerging from the center of the leeward surface of the cylinder instead of the sharp corners, and so the scenario here follows that found for the circular cylinder. The drag coefficient within this regime was also shown to vary with Reynolds number according to a power law with an exponent of -0.66 .

Sohankar *et al.* (1997) simulated the unsteady flows at $Re \leq 200$ past rectangular cylinders of aspect ratios ranging over 1–4, and varying the cylinder inclination through $0 - 90^\circ$, quantifying parameters of the wake such as the Strouhal numbers, drag coefficients, and lift coefficients. Sohankar *et al.* (1998) investigated this in further detail, focusing on the square cylinder for flows at Reynolds numbers ranging over $45 \leq Re \leq 200$, and varying the cylinder inclination from 0° to 45° . The study utilised the Stuart–Landau equation to predict the onset of the primary wake instability across these cylinder inclinations, finding that the critical Reynolds number decreases with increasing cylinder inclination, and that the transition is supercritical. The study further quantified various parameters of the wake, showing that the shedding frequency, mean drag coefficient, fluctuating lift coefficient, and base pressure coefficient generally increase with the cylinder inclination.

Another numerical study by Yoon *et al.* (2010) investigated these wakes, placing more emphasis on the vortex shedding process. Similar to Sohankar *et al.* (1998), the study modelled the transition using the Stuart–Landau equation to predict the critical parameters of the transition, finding a similar trend where the critical Reynolds number decreased as the cylinder inclination was increased from 0° to 45° , but at lower magnitudes than those predicted by Sohankar *et al.* (1998) owing to the larger computational

domain used and spatial resolution afforded for the computations. Besides quantifying the forces, this study elucidated the subtle differences in the vortex shedding topology, categorising them into two broad categories — the main separation pattern (MS) and the vortex merging pattern (VM), with the MS pattern having two further subcategories of the single- and double secondary vortex patterns (SSV and DSV, respectively). Analogous patterns to these are illustrated in figure 1.8 for the triangular cylinder discussed in a later section, and are reproduced from Tu *et al.* (2014).

Robichaux *et al.* (1999) studied the stability of the wakes of the square cylinder, utilising a power-type method to solve for the magnitude of the leading eigenvalue of the system dictating its linear stability. The study predicted three secondary instabilities to develop in the wakes at increasing Reynolds numbers. The first two correspond to modes A and B in the wake of the circular cylinder and occur at Reynolds numbers of 162 and 190, respectively. The third instability mode predicted was characterised as a subharmonic mode which becomes unstable at an approximate Reynolds number of 200, and possesses a wavelength intermediate to those found for modes A and B. A subsequent study by Blackburn & Lopez (2003) investigated the occurrence of this subharmonic mode further and demonstrated that the mode was actually quasiperiodic instead of subharmonic; the earlier misidentification stemming from the use of a one-dimensional power method along with the new finding that the eigenvalue of the quasiperiodic mode in this case behaves increasingly subharmonically when the Reynolds number is increased past the bifurcation. This mode is in fact analogous to the quasiperiodic mode in the wake of the circular cylinder.

The results from these stability analyses agree with past experimental and numerical results. Computations of the three-dimensional flow by Sohankar *et al.* (1999) at Reynolds numbers ranging from 150 at increments of 50 up to 500 found that the flow was two-dimensional at $Re = 150$, and three-dimensional at $Re = 200$ with vortical structures that resembling mode A (in fact the structures were more consistent with mode A* given that the simulations detected low frequency modulations induced by vortex dislocations). The authors also observed streamwise structures consistent with mode B for flows at $Re \geq 250$. Saha *et al.* (2003) reported similar findings from their numerical simulations, refining the range of Reynolds numbers where mode A can be observed to within $175 \leq Re \leq 240$. Jiang *et al.* (2018) repeated this exercise, their numerical simulations finding mode A to occur at $Re = 165.7$, and that the mixed

mode region where energy is gradually transferred from mode A to mode B extending through $185 \leq Re \leq 210$. Mode B was then predicted to become the dominant global mode at Reynolds numbers of $Re > 201.4$. The Jiang *et al.* (2018) study also showed that predictions of hysteresis in these wakes are sensitive to the computational domain size, similar to those found for the wake of the circular cylinder by Akbar *et al.* (2011), and so the mode A transition here is subcritical.

Luo *et al.* (2003) conducted experiments to verify the transitions predicted from these flow computations, reporting that mode A becomes unstable at a Reynolds number of approximately 160 with a wavelength of approximately $5.2d$ (d here corresponds to the cylinder side length), and mode B at a Reynolds number of approximately 200 with a wavelength of approximately $1.2d$, both in approximate agreement with Robichaux *et al.* (1999) and Sohankar *et al.* (1999). The experiments here found that the transitions were both non-hysteretic. This was repeated by Luo *et al.* (2007), finding that mode A was actually hysteretic unlike their previous prediction, and suggests that hysteresis phenomena in these wakes may be sensitive to the experimental setup.

In a variation to the square cylinder, Park & Yang (2016) investigated the effects of rounding the sharp corners of the square cross section on the wake it produces. The three generic bifurcations, modes A and B and the quasiperiodic mode, were predicted as expected owing to the base flow's symmetry. The critical wavelengths of each mode varied with the rounding ratio as well, decreasing from approximately $5d$ to $4d$ for mode A, $2.6d$ to $1.8d$ for the quasiperiodic mode, and $1.2d$ to $0.8d$ for mode B as the rounding ratio was increased from a square cross section to a circular one. The critical Reynolds numbers for each of these modes were, interestingly, highest for a cross-section with a rounding ratio exactly midway between the square and cylinder cross-sections, with those for mode A varying between approximately $150 \lesssim Re \lesssim 200$, mode B between $200 \lesssim Re \lesssim 260$, and the quasiperiodic mode between $220 \lesssim Re \lesssim 380$.

Several interesting observations have also been made when introducing the square cylinder inclination as an additional variable parameter. The experimental investigation by Tong *et al.* (2008) measured the dominant frequencies in the wakes of the cylinder as its inclination was varied from 0° to 45° , and demonstrated the existence of modes A and B. The authors concluded that the transition scenario for the inclined cylinder was the same as that found for the circular cylinder, although their properties vary with the cylinder inclination.

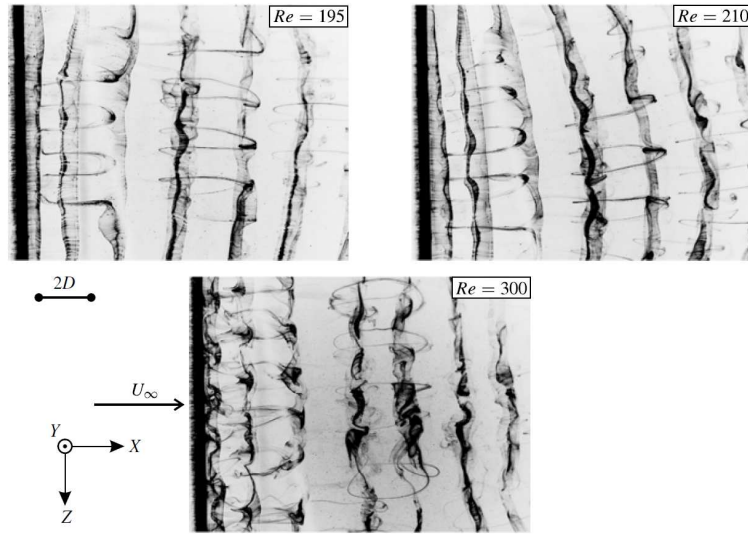


FIGURE 1.7: Visualisation of the three-dimensional mode C in the wake of a circular cylinder with a trip wire in proximity at Reynolds numbers of $Re = 195, 210$ and 300 , clockwise. The images are reproduced from Yildirim *et al.* (2013b) with permission from Cambridge University Press.

A subsequent numerical study by Sheard *et al.* (2009) investigating the stability of the wakes of an inclined square cylinder found that a different mode manifests in these wakes. The mode emerges as the first three-dimensional mode at cylinder inclinations within $12^\circ \lesssim \alpha \lesssim 26^\circ$ (α being the cylinder inclination angle) with a critical wavelength of approximately $2d$, and was reported to be subharmonic to the periodic base flow. This mode is consistent with mode C reported by Zhang *et al.* (1995) in the wake of a circular cylinder with a trip wire placed in proximity, and also by Sheard *et al.* (2003) and Sheard *et al.* (2005) in the wakes of toroidal bodies. Visualisation of mode C in the wake of a circular cylinder with a trip wire by Yildirim *et al.* (2013b) is reproduced in figure 1.7. Indeed, Tong *et al.* (2008) did not provide any visualisation of the flow between cylinder inclinations of 10° and 45° where mode C becomes dominant, and had thus incorrectly generalised their observations of modes A and B across the cylinder inclination range. An interesting feature of mode C is its emergence only in flows which have some perceived asymmetry — the trip wire near the cylinder in Zhang *et al.* (1995) and also the curvature of the torus in Sheard *et al.* (2003) provide such asymmetries. Sheard *et al.* (2009) further investigated the weakly nonlinear characteristics of the secondary bifurcation using the Stuart–Landau equation, finding the transition of mode A

at $\alpha = 0^\circ$ and mode C at $\alpha = 22.5^\circ$ to be supercritical, while the mode A bifurcation at $\alpha = 45^\circ$ is subcritical. As mentioned earlier, Jiang *et al.* (2018) demonstrated that the mode A transition at all inclinations where it is unstable is subcritical when the same analysis is applied on the flows computed in domains with an extended span. The three-dimensional flows at $Re = 300$ computed in an extended spanwise domain for cylinder inclinations of 0° , 22.5° and 45° by Sheard *et al.* (2009) reveals mode B structures in the wake, consistent with the predictions from the stability analysis of the wakes of the cylinder inclined at 0° . The study also shows that the streamwise vortices decay rapidly within 4 shedding cycles downstream, and that the spanwise vortex rollers develop dislocations in the far wake consistent with those found in the wake of the circular cylinder by Henderson (1997). Further investigations by Yoon *et al.* (2010) and Sheard (2011) refine the cylinder inclination at which mode C replaces mode A as the first-occurring three-dimensional mode.

Studies by Blackburn & Sheard (2010) and Sheard (2011) demonstrated the strong dependence of the quasiperiodic mode on the symmetry of the wake, showing that the multiplier locus migrates towards the negative real axis with increasing cylinder inclination (increasingly deviating from the half-period-flip map of the wake), coalescing on the negative real axis and subsequently bifurcating into two distinct real modes on further increasing the inclination — one becoming increasingly stable while the other becomes unstable through a negative real multiplier. The quasiperiodic- to subharmonic mode changeover is predicted to occur between cylinder inclinations of 2° and 3° . This demonstrates that the quasiperiodic mode in this wake system *becomes* the subharmonic mode once the spatiotemporal symmetry of the wake is sufficiently broken.

Wakes behind flat plates and elliptical cylinders

For an elliptical cylinder, computations by Park *et al.* (1989) showed that the wake transitions are similar to that for the circular cylinder, traversing through steady and unsteady states with increasing Reynolds numbers.

Sen *et al.* (2011) later investigated numerically the effects of flattening the cylinder from a circular cross-section to an elliptical cross-section on the steady wakes by decreasing the (width-to-height) aspect ratio of the cylinder cross-section, showing that the steady recirculation region forms at Reynolds numbers which decrease with the aspect ratio. The study also demonstrated the movement of the separation points of

the flow as the aspect ratio was varied, showing that the separation points in the steady wakes of the elliptical and circular cylinders tend towards $\pm 90^\circ$ on the cylinder surface relative to the oncoming flow in contrast to the separation angles of $\pm 135^\circ$ found for the square cylinder wake (separation at the leeward edges of the cylinder) even at low Reynolds numbers.

A subsequent computational study by Paul *et al.* (2014) investigated the effects of varying the inclination and aspect ratio of an elliptical cylinder on the two-dimensional wakes it produces. For the steady wakes, the study quantifies the separation Reynolds numbers Re_s and shows that it decreases with the aspect ratio similar to that reported by Sen *et al.* (2011), and also that Re_s decreases as the inclination is increased from a streamlined orientation to a normally inclined cylinder. The study also determined the critical Reynolds numbers Re_c for the primary wake instability through the Stuart–Landau equation, finding that it decreases with increasing inclination angle and aspect ratio.

In another study by Zhang *et al.* (2008), the two-dimensional wakes of an inclined flat plate were computed across a range of inclinations and Reynolds numbers. The study finds that the Kármán vortex street becomes unstable to a subharmonic excitation at high Reynolds numbers when the flat plate is inclined within $20^\circ \lesssim \alpha \lesssim 30^\circ$ relative to the oncoming flow. Increasing the Reynolds number further past the onset of this subharmonic excitation rapidly excited quasiperiodic frequencies and structures in the wake, prior to any observation of shear layer instabilities in these wakes. Similar complex states were observed in the vortex streets in a numerical study by Yang *et al.* (2012).

Johnson *et al.* (2004) investigated numerically the occurrence of the secondary vortex street in the wake of a normally inclined elliptical cylinder as the aspect ratio was varied, and demonstrated that the primary wake frequency decays rapidly downstream in the wake and also that select frequencies are amplified in the far wake characteristic of the development of the secondary vortex street. A similar study for an approximate flat plate by Saha (2007) and Mizushima *et al.* (2014) finds the same results. The latter study also performed a linear stability analysis of the steady symmetric wakes and found that the evolution of the eigenmodes do not converge to the secondary vortex street, and so it cannot be responsible for the formation of the secondary vortex street (this result is consistent with Kumar & Mittal, 2012). Thompson *et al.* (2014) again

investigated the wakes of elliptical cylinders, varying the aspect ratio from one where the cylinder cross-section was circular to one where the cross-section was approximately a flat plate similar to Johnson *et al.* (2004). Although the primary focus of the study was on three-dimensional wake instabilities (which will be reviewed subsequently), the secondary vortex street in the two-dimensional flows were given some consideration. The study showed that the increasing prominence of the secondary vortex street with decreasing aspect ratios (tending to a flat plate) can be attributed to an increased vorticity flux generated on the cylinder fed into the wake per shedding cycle. This can then be viewed in conjunction with the studies by Hooker (1936), Durgin & Karlsson (1971) and Dynnikova *et al.* (2016) as a means through which the secondary vortex street forms.

For the stability of the wakes of inclined flat plates to three-dimensional perturbations, Yang *et al.* (2013) reported that flat plates at inclinations of 20° , 25° , and 30° become unstable through mode C at chord Reynolds numbers of approximately 400, 266, and 182, respectively. Two further modes are predicted from the stability analysis at even higher Reynolds numbers past the secondary bifurcation, one being a quasiperiodic mode with a wavelength of approximately 2.5 times the chord length of the plate, and another called mode D being a regular mode identical to the subharmonic mode C except that it is unstable on the period-doubled ($2T$) baseflow reported by Zhang *et al.* (2008) and Yang *et al.* (2012) (that is mode D has an orbital period matching the $2T$ -periodic baseflow in contrast to mode C which has an orbital period twice that of the T -periodic baseflow).

The stability of the wakes of a normal elliptical cylinder with (minor-to-major axis) aspect ratios decreasing from a circular cross-section to an approximate flat plate was investigated by Thompson *et al.* (2014), finding three-dimensional wake transitions in these wakes to be associated with mode A except for the flat plate where a quasiperiodic mode is predicted. The mode A transition Reynolds numbers predicted decrease from $Re = 190$ to $Re = 88.5$ while the critical wavelengths range between $3.92h \leq \lambda \leq 5.34h$ for aspect ratios decreasing from 1 to 0.25 (h here being the projected height of the cylinder on the uniform flow). The quasiperiodic mode in the wake of the flat plate is predicted to become critical at a Reynolds number of 116 with a wavelength of $5h$. Several further secondary bifurcations were also observed from further computations of the three-dimensional flow. At certain aspect ratios, the wake is observed to re-twodim-

ensionalise as mode A is suppressed, agreeing with the experimentally measured wake frequencies by Radi *et al.* (2013). This two-dimensional state is subsequently unstable again at a higher Reynolds number through a new patterned mode termed mode AA whose spatiotemporal symmetry is consistent with mode A but possesses a different perturbation structure within the base flow vortices.

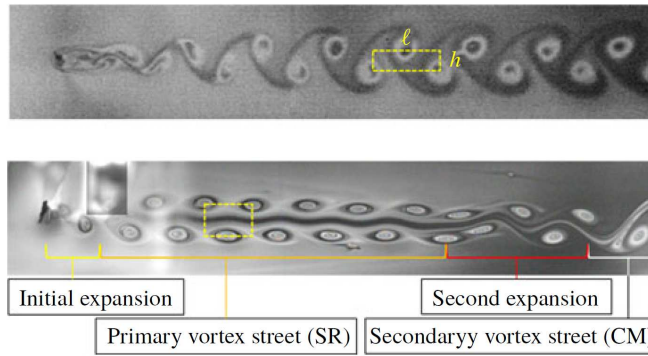
The results from the stability analysis by Thompson *et al.* (2014) are also consistent with the experimental visualisation by Mizushima *et al.* (2014), who investigated the far wake structures of a rectangular cylinder with a width-to-height aspect ratio of 0.2. Clear three-dimensional distortions of the vortex loops were observed to form by a Reynolds number of 90, close to the predicted Reynolds number of 88 for the mode A transition in the wake of the normal elliptical cylinder with an aspect ratio of 0.25 (both cylinders being not too dissimilar as both are thin and normally oriented).

Three-dimensional flow computations of the flat plate wake by Najjar & Balachandar (1998) at a Reynolds number of 250 reported a three-dimensional mode with a wavelength of approximately $1.2h$, which the authors stated was reminiscent of mode B. The drag force induced on the cylinder by this flow exhibits a low-frequency modulation similar to mode A*; the modulation being similarly associated with spanwise vortex dislocations. Three-dimensional flow computations of the flat plate wake at a high Reynolds number of $Re = 1000$ have also been reported by Najjar & Vanka (1995), finding that the drag coefficients predicted from these three-dimensional computations differ from the two-dimensional predictions owing to the strong three-dimensionality of the wake.

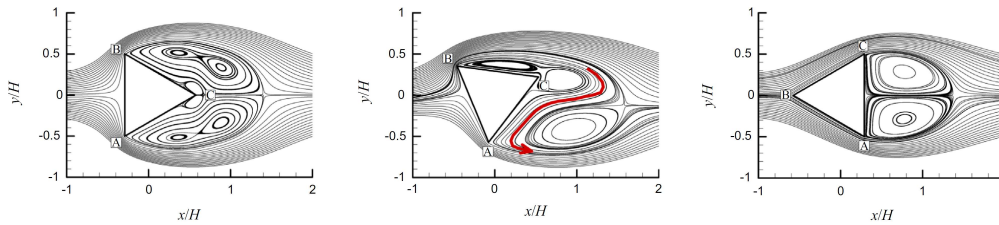
Further studies by Leontini *et al.* (2015) investigating the stability of the wakes of a streamlined elliptical cylinder of varying aspect ratios, and also by Rao *et al.* (2017) on the effects of varying the inclination and also the aspect ratio of the streamlined elliptical cylinder finds, on top of the list of canonical modes A, B, QP and C, various new modes termed modes \hat{A} , \hat{B} , QPL, QPA, and E which become unstable at various combinations of the aspect ratio and inclination. It should suffice to say at this stage that the wakes in this system are rich in linear instabilities.

Wakes of triangular cylinders

A review of the literature reveals that a much smaller body of work has been dedicated to the wakes of a triangular cylinder. Amongst the earlier works, Zielinska & Wesfreid



(a) Secondary vortex street forming in the triangular cylinder wake by Kim (2019).



(b) Mean flow streamlines describing vortex shedding topology variations by Tu *et al.* (2014)

FIGURE 1.8: The images in panel (a) are reproduced from Kim (2019) with permission from Cambridge University Press. The figures in panel (b) are reproduced from Tu *et al.* (2014) with permission from Elsevier.

(1995) investigated the unsteady two-dimensional flows near the transition for an equilateral triangular cylinder with its apex directed upstream using numerical simulations. They predicted the primary wake instability to become unstable at a critical Reynolds number of $Re_c = 39.6$, which very crudely agrees with the value of $Re_c = 34.9$ interpolated from the results reported by Jackson (1987) who used a significantly smaller computational domain for the stability analysis. The study also found that the spectral amplitudes of the transverse velocity fluctuations in the wake increase proportionally with $(Re - Re_c)^{0.5}$ while the streamwise position of the amplitude maxima approaches the cylinder inversely proportional with $(Re - Re_c)^{0.5}$. Appropriate re-scaling of the spectral amplitudes and streamwise lengths showed that the amplitude response in the wake collapses to a universal curve, demonstrating the global nature of the instability. The study also suggested that nonlinear effects might play an important role in the transition, a point which the authors investigated further using the circular cylinder wake (Zielinska *et al.*, 1997) as discussed earlier in this chapter.

De & Dalal (2006) computed the two-dimensional flows of the same system at Reynolds numbers ranging from 10 to 250. The study showed that the steady wake length increases linearly with increasing Reynolds numbers similar to that found for the circular cylinder, and predicted the primary wake instability to manifest at $Re_c = 39.9$. This value is in good agreement with that reported by Zielinska & Wesfreid (1995). The drag coefficient induced by the steady flow on the cylinder is shown to decrease in magnitude with increasing Reynolds numbers approaching Re_c , and the mean drag coefficient ($\overline{c_d}$) and root-mean-squared lift coefficient (c'_l) increases with Reynolds number in the unsteady regime.

Experiments by Iungo & Buresti (2009) investigated the effects of finite span of the cylinder on the forces induced on it at a Reynolds number of 1.2×10^5 . At the (span-to-sidelength) aspect ratios of 1–3 tested in the study, the mean force coefficients show little dependence on the aspect ratio, decreasing only slightly with the aspect ratio. The mean drag coefficient was found to be lowest when the cylinder was oriented with the triangle apex pointing upstream and largest in the opposite orientation where the triangle apex was pointing downstream. The mean lift coefficients ($\overline{c_l}$) increase in magnitude with geometric asymmetry relative to the uniform flow, showing an approximately zero magnitude at symmetric angles where the triangle apex pointed up- and downstream and was largest when the cylinder apex pointed perpendicular to the flow direction / in the cross-flow direction. The study also included sketches of the flow around the cylinder drawn qualitatively from their experimental observations, describing the wake as being significantly broader at an inclination where the triangle apex was directed downstream compared to that when the apex was directed upstream, thus influencing the magnitude of the drag force induced on the cylinder. These results demonstrate the effects of afterbody shape on the wake.

Bao *et al.* (2010) investigated the two-dimensional flows at $Re = 100$ and 150 but at varying cylinder inclinations primarily as a validation of their numerical scheme. This study utilised the cylinder side length d as the characteristic length scale. The Strouhal number quantified from this study showed that the values obtained at $Re = 150$ were larger than those obtained at $Re = 100$, and that the Strouhal number decreases as the inclination was varied from one where the apex pointed upstream to one where the apex pointed downstream. $\overline{c_d}$ and c'_l were again larger in magnitude at the higher Reynolds number, and showed a smooth variation with the cylinder inclination such

that the lowest $\overline{c_d}$ and largest c'_l were found at an inclination where the cylinder apex pointed perpendicular to the oncoming flow. The variation of the mean drag coefficient with cylinder inclination angle for these two-dimensional flows also appear qualitatively similar to the results from wind tunnel experiments by Iungo & Buresti (2009) at much higher Reynolds numbers.

Tu *et al.* (2014) later reported that the vortex shedding process for two-dimensional flows past the triangular cylinder followed the main separation (MS), single secondary vortex (SSV), and vortex merging (VM) patterns depending on the cylinder inclination and Reynolds number of the flow, missing the double secondary vortex (DSV) pattern reported for the square cylinder by Yoon *et al.* (2010) for reasons purely geometric. The streamlines of the mean flow characteristic of these patterns reported by Tu *et al.* (2014) are reproduced in figure 1.8. The remainder of the paper then focused on the response of the wake to forced oscillatory rotational motions of the cylinder.

In another study by Ganga Prasath *et al.* (2014), the wakes produced by triangular cylinders or wedges with varying aspect ratios were computed from the two-dimensional flow equations. The study showed that the steady flow separation was delayed as the streamwise length of the cylinder was increased. The Reynolds number (scaled by the cylinder height h) where the primary wake instability manifests also decreased with increasing aspect ratios, the effect being significantly more pronounced for the cylinder oriented with its apex pointing downstream and that for the cylinder pointing upstream.

To the best of the author's knowledge, one of the only attempts at investigating the transition to three-dimensional flow in the wake of the triangular cylinder was performed by Luo & Eng (2010) who conducted ink-dye visualisations at low Reynolds numbers for the wake of an isosceles triangular cylinder (the cross-section fitted into a square of side length d) oriented with its apex pointing downstream. The study reported the first three-dimensional instability as mode A which becomes unstable at a Reynolds number of approximately 164, and the transition is predicted to be hysteretic. Curiously, mode B was not observed within the range of Reynolds numbers the study investigated (approximately $Re \lesssim 230$).

A recent paper by Kim (2019) investigated the onset of a form of the vortex street the authors denoted as the 'separated rows' structure using soap film visualisations. Flow visualisation of this structure, reproduced from their work, is shown in figure 1.8. This

form is essentially characterised by like-signed vortices in the vortex street aligning into two distinct rows, and are stretched elliptically along the streamwise direction without fully diffusing or merging with the other vortices in the row. The cross-flow distance between these two separated rows of vortices is also large with a sheet of irrotational fluid between the rows preventing interactions between the rows of vortices. The authors find that this two-dimensional structure forms when the boundary layer on the cylinder thinner than 40% of the row separation distance, but exceeding this threshold, the canonical Kármán vortex street forms (their ‘conventional mushroom’ structure).

Several other studies using the triangular cylinder in various applications and setups demonstrates the perceived benefits of using such geometries with sharp corners and asymmetries. Such strong geometric asymmetry presumably causes the cylinder to be susceptible to vibrations and rotations. The vortex-induced-vibrations on the cylinder confined within a channel and its wake responses have been investigated using two-dimensional flow computations by Alawadhi (2013), and flow-induced-vibrations and its wake responses using two-dimensional flow computations by Wang *et al.* (2015) and experimentally by Seyed-Aghazadeh *et al.* (2017). Abbassi *et al.* (2001) and Srikanth *et al.* (2010) investigated the heat transfer enhancement attained using the triangular cylinder as a vortex promoted confined in a heated channel using two-dimensional flow computations. An experimental study by Srigrarom & Koh (2008) investigated the free rotation response of the cylinder pivoted about its axis showing that the cylinder is capable of auto-rotations (drawing from aeroelastic flutter). A subsequent study using two-dimensional flow computations by Wang *et al.* (2011) for two freely rotatable triangular cylinders placed in tandem at $Re = 200$ investigated the effects of the distance between these cylinders on the wake responses, finding that the cylinder rotation can be broadly categorised by antiphase synchronised-, autorotation-, and chaotic regimes. Most of these phenomena were investigated numerically assuming a two-dimensional flow although at such Reynolds numbers, the wakes were presumably three-dimensional. The lack of a thorough investigation concerning the stability of these wakes is apparent.

1.3 Project aims

An outline of the aims of the project is as follows. First, aspects of the two-dimensional flow past the cylinder at varying inclinations are to be understood, and will be achieved through numerical simulations of such flows. Of particular interest are the

features of the wake in the lead-up to any changes in flow topology or any transitions. The responses of the wake without any three-dimensional effects are to be measured to determine the role of the cylinder inclination in affecting these responses. Proceeding from these computations, the stability of the two-dimensional flows to infinitesimal three-dimensional perturbations are to be assessed, and the dominant modes through which the transition is agitated is to be identified. For this, a global Floquet stability analysis of the flow system is employed. To further understand the dynamics of these instability modes and its interaction with the base flow, the structural sensitivity of these instabilities are to be derived. Besides that, the perturbation kinetic energy budget of the unstable modes are to be determined. In all cases, the effect of cylinder inclination variation on the stability properties and the characteristics of the eigenmodes are to be assessed. Finally, this project will investigate the extent of the role of nonlinearities in the developing flow as three-dimensional effects begin to grow and then saturate. In particular, the weakly nonlinear flow approximation will be applied to determine the nature of the three-dimensional flow transition. The temporal development of turbulent states in the wake as well as common wake properties will also be investigated to determine the effects of three-dimensionality on the wake.

Chapter 2

Methodology

In this chapter, pertinent concepts and methodologies underpinning the work reported throughout this thesis will be introduced, and results from verification and validation studies will be presented to demonstrate that the solver and computational setup employed has been properly implemented. Specifically, § 2.1 first introduces the governing equations of fluid motion, followed by § 2.2 which outlines concepts and the numerical formulations implemented in the solver used throughout this project. Here, a brief recount of the two-dimensional nodal spectral-element discretisation scheme is first provided followed by that of the third-order multistep temporal advancement scheme. The section then concludes with the introduction of the Fourier method for discretisation of the flow in the out-of-plane direction — the historical aspects of the development of these spectral-element schemes, their theory and implementation are comprehensively expounded in the Karniadakis & Sherwin (2005) textbook. § 2.3 then introduces the theories behind the different analyses utilised in this project. In particular, the concepts of linear instabilities and their adjoint modes are introduced, followed by weakly non-linear analysis approaches. The numerical tools are then tested, with results journalled in § 2.4. Finally, § 2.5 introduces the system of interest, detailing the computational setup used to obtain a physical flow solution, and concludes with results from preliminary computations testing the sensitivity of the flow solutions to resolution and domain truncation effects.

2.1 Governing equations

The equations governing the motions of a fluid element in a continuum are the Navier–Stokes equations, which comprise mass and momentum conservation equations, and their derivation can be found in numerous texts prescribed for introductory courses on fluid dynamics. Specific assumptions are made on the fluid and flows in the present project which permits several simplifications to the general form of the Navier–Stokes equations. A brief summary and explanation of these equations as well as some underlying assumptions are described in this section, making reference to the *Fundamentals of Aerodynamics* textbook by Anderson (2011) most extensively which beautifully articulates the derivation of these equations.

An easy approach to the derivation of the continuity equation which embodies the conservation of mass is to use an Eulerian control volume approach — this conservation means that the net mass transfer across the surface of the fixed volume must offset any time rate of change of mass within this control volume. The final differential/elemental form of the continuity equation can be expressed as

$$\frac{\partial \rho}{\partial t^\star} + \nabla^\star \cdot (\rho \mathbf{u}^\star) = 0, \quad (2.1)$$

where ρ is the density of the fluid, t is time, \mathbf{u} is the velocity of the fluid, ∇ is the del operator (e.g. $\nabla = (\partial/\partial x, \partial/\partial y, \partial/\partial z)$ in Cartesian coordinates), and terms with a superscripted \star denotes that the variables are in dimensional form. For a flow where the fluid density does not vary significantly either over space or time (such as those with negligible temperature gradients and flow speeds far below that of sound), ρ may be assumed to be constant which results in the incompressibility constraint on equation (2.1), reducing it to

$$\nabla^\star \cdot \mathbf{u}^\star = 0. \quad (2.2)$$

Proper treatment of the conservation of momentum through a differential approach is provided in chapter 15 of the Anderson (2011) text in addition to that by the control-volume approach they derived in chapter 2. Considering the actions of viscous and pressure stresses along the surfaces of a generic fluid element, the conservation of momentum can be derived as

$$\rho \frac{\partial \mathbf{u}^\star}{\partial t^\star} + \rho (\mathbf{u}^\star \cdot \nabla^\star) \mathbf{u}^\star = -\nabla^\star p^\star + \nabla^\star \cdot \boldsymbol{\tau}^\star + \rho \mathbf{f}^\star,$$

where p is the scalar pressure field, $\boldsymbol{\tau}$ is the stress tensor, and $\rho \mathbf{f}$ is a generic term to include any additional body forcing (for example, a weight force commonly imposed on the vertical y -direction can be expressed through $\mathbf{f}^* = g \mathbf{e}_y$). A crucial assumption underpinning further simplification of the momentum equation is to use the generalisation of Newton's Law of Viscosity for the inclusion of the bulk viscosity coefficient, such that

$$\boldsymbol{\tau}^* = \mu (\nabla^* \mathbf{u}^* + (\nabla^* \mathbf{u}^*)^T) + \left(\lambda - \frac{2}{3} \mu \right) (\nabla^* \cdot \mathbf{u}^*) \boldsymbol{\delta},$$

where μ is the dynamic viscosity of the fluid, terms with a superscript T denotes a transpose operation, λ is commonly denoted the bulk viscosity coefficient, and $\boldsymbol{\delta}$ is the unit tensor (analogous to the application of the Kronecker delta in tensorial index notation). For incompressible flows which this project is concerned with, the term containing the bulk viscosity is identically zero due to equation (2.2). Thus the final momentum equation for an incompressible Newtonian flow can be written as

$$\frac{\partial \mathbf{u}^*}{\partial t^*} + (\mathbf{u}^* \cdot \nabla^*) \mathbf{u}^* = \frac{1}{\rho} \nabla^* p^* + \nu \nabla^{2,*} \mathbf{u}^* + \mathbf{f}^*, \quad (2.3)$$

where ν is the kinematic viscosity of the fluid $\nu = \mu/\rho$, and ∇^2 is the Laplacian operator which can be expressed as $\nabla^2 = \partial^2/\partial x^2 + \partial^2/\partial y^2 + \partial^2/\partial z^2$ in Cartesian coordinates. For the flows considered in this project, no body forces are applied, and so the body force term is omitted.

Careful selection of appropriate characteristic scales representing the system of interest permits the nondimensionalisation of the continuity and momentum equations in (2.2) and (2.3). For this project, the following characteristic scales were chosen

$$\begin{aligned} \mathbf{x}^* &= (h) \mathbf{x}, \\ \mathbf{u}^* &= (U_0) \mathbf{u}, \\ t^* &= (h/U_0) t, \\ p^* &= (\rho U_0^2) p. \end{aligned}$$

These reference scales for nondimensionalisation purposes will be defined and explained subsequently in § 2.5 where it is more relevant, so they may be considered as arbitrary constants for now. The nondimensionalised governing equations solved in this project is thus the incompressible Navier–Stokes equations for a Newtonian fluid, expressed as

$$\begin{aligned} \nabla \cdot \mathbf{u} &= 0, \\ \frac{\partial \mathbf{u}}{\partial t} + (\mathbf{u} \cdot \nabla) \mathbf{u} &= -\nabla p + \frac{1}{Re} \nabla^2 \mathbf{u}, \end{aligned} \quad (2.4)$$

where Re is the Reynolds number $Re = U_0 h / \nu$, $\partial \mathbf{u} / \partial t$ and $(\mathbf{u} \cdot \nabla) \mathbf{u}$ represent the temporal and spatial contributions to the acceleration of the fluid, ∇p represents the pressure force, and $\nabla^2 \mathbf{u} / Re$ represents the viscous diffusion of the flow.

2.2 Numerical formulation

Analytical solutions to the governing equations described in the previous section are rare, and its application to complex fluid systems generally require severe limiting assumptions (such as those for Stokes flow — see Stokes, 1851) which may find a lack of utility in engineering. The advent and advancement of numerical approximation techniques along with the rapid evolution of microprocessing units/CPU’s established the field of computational fluid dynamics (CFD) wherein complex flow systems can be broken down into simpler domains over which the governing equations are solved. This project capitalises on this advantage to solve for the flows in complex systems.

For this project, the flow was numerically evolved using an in-house flow solver which employs a nodal spectral-element method for spatial discretisation of flow variables in a two-dimensional domain — the use of polynomial basis functions for spectral methods were first introduced by Gottlieb & Orszag (1977), with flow variables in the third spatial-dimension discretised through a Fourier expansion method in conjunction with the spectral-element discretisation as described by Karniadakis & Triantafyllou (1992). The temporal advancement of the flow is achieved through the implementation of a third-order-accurate multistep scheme based on backwards differentiation detailed by Karniadakis *et al.* (1991). Readers interested in to learn more about these spectral/ hp element methods are directed to the Karniadakis & Sherwin (2005) text, but a summary of the pertinent concepts and formulations used in the present code are described in the following sections for convenience.

2.2.1 Spatial discretisation: the spectral-element method

Following Karniadakis & Sherwin (2005) and references therein, first consider a linear differential equation $\mathbb{L}(u)$ described within an elemental domain Π_e with a dimension ξ such that

$$\begin{aligned} \mathbb{L}(u) &= 0, \\ \mathbb{L}(u^\delta) &= R(u^\delta), \end{aligned} \tag{2.5}$$

where $u(\xi)$ is the exact solution satisfying $\mathbb{L}(u) = 0$, $u^\delta(\xi)$ is the approximated solution, and $R(u^\delta)$ is the residual function. The approximate solution $u^\delta(\xi)$ can be formed through the expansion

$$u^\delta(\xi, N) = u_0(\xi) + \sum_{q=0}^N \hat{u}_q \phi_q(\xi),$$

$$\lim_{N \rightarrow \infty} u^\delta(\xi, N) = u(\xi), \quad (2.6)$$

where u_0 is the set of functions enforcing prescribed boundary conditions and initial conditions, $\phi_q(\xi)$ is the q^{th} local expansion basis function, \hat{u}_q is the set of coefficients of the q^{th} expansion base which is to be solved for, and N is the number of expansion basis functions to be used. The choice of the expansion basis function affects the numerical formulation in multiple ways as described in Karniadakis & Sherwin (2005). The solver used in this project utilises high-order Lagrangian polynomial expansion basis functions about the roots of the Legendre polynomials, which permits the use of quadrature rules for efficient integration. For nodal polynomial expansion basis functions of order N along a local dimension ξ such that $-1 \leq \xi \leq 1$, the local expansion basis $\phi_q(\xi)$ is given by

$$\phi_q(\xi) = \begin{cases} 1 & \text{for } \xi = \xi_q, \\ \frac{(\xi - 1)(\xi + 1) \mathcal{L}'_N|_\xi}{N(N + 1) \mathcal{L}_N|_{\xi_q} (\xi_q - \xi)} & \text{otherwise,} \end{cases} \quad q = 0, 1, \dots, N, \quad (2.7)$$

where ξ_q are the nodes of the expansion basis ϕ_q corresponding to the roots of the function

$$g(\xi) = (1 - \xi)(1 + \xi) \mathcal{L}'_N|_\xi,$$

and $\mathcal{L}_N(\xi)$ is the Legendre polynomial function of order N and consequently \mathcal{L}'_N its derivative. In the present solver, the coefficients of $\mathcal{L}_N(\xi)$ is evaluated through the recursive relation

$$\mathcal{L}_N(\xi) = \begin{cases} 1 & \text{for } N = 0, \\ \xi & \text{for } N = 1, \\ \frac{1}{N} \left[(2N - 1)\xi \mathcal{L}_{N-1} - (N - 1)\mathcal{L}_{N-2} \right] & \text{for } N = 2, 3, \dots \end{cases}.$$

An alternative approach to generate the Legendre polynomial is to apply Rodrigues' formula which involves computing the N^{th} derivatives of an N^{th} order polynomial expansion, which is more inefficient from a computational perspective.

Drawing back to equations (2.5) and (2.6), it is the treatment of the residual function R which distinguishes collocation methods from the method of weighted residuals in approximating the solution of $\mathbb{L}(u)$ — the former optimises the solution by enforcing

the residual to be exactly zero at the nodal points of the expansion, whereas the latter enforces that the weighted residual over the domain is zero such that

$$(v_q, R(u^\delta)) = \int_{\Pi_e} v_q \mathbb{L}(u^\delta) d\xi = 0, \quad (2.8)$$

where the notation (f, g) is the inner product g with respect to f , and v_q is the test or weighting function. The Galerkin method is used in the present formulation, wherein the expansion basis functions are chosen as the weighting functions itself:

$$v_q = \phi_q(\xi).$$

Integrating equation (2.8) for the exact solution ($u^\delta = u$) by parts results in the weak (integral) form approximating the differential equation $\mathbb{L}(u)$, and so the solution to the differential equation can be approximated using high-order quadrature methods. In the present solver, integrals are approximated using the Gauss–Lobatto quadrature rule via

$$\int_{-1}^1 f(\xi) d\xi = \sum_{q=0}^{N-1} w_q f(\xi_q) + R(f), \quad (2.9)$$

where $f(\xi)$ is the integrand to be evaluated within the elemental domain $-1 \leq \xi \leq 1$, and w_q are the nodal weights of the integration determined through

$$w_q = \frac{2}{N(N-1) \mathcal{L}_{N-1}^2|_{\xi_q}} \text{ for } q = 0, 1, \dots, N-1.$$

A crucial distinction of the Gauss–Lobatto rule from conventional Gaussian quadrature is the inclusion of the nodal points affixed at the limits of the elemental domain, $\xi_q \in \{-1, 1\}$, which is critical to the enforcement of continuous solutions across element interfaces in more complex multi-element domains. Gauss–Lobatto quadrature is exact for polynomials up to degree $2N-3$, where N is the number of quadrature points/expansion basis function employed.

Extending these concepts to a two-dimensional formulation (as employed in the present solver), the weak form of the differential equation from the Galerkin method of weighted residuals utilises the divergence theorem to solve for the inner product $(v_q, \mathbb{L}(u))$, and the solution within each local element $\Pi_e \in \{\xi_1, \xi_2\}$ where $-1 \leq \xi_1, \xi_2 \leq 1$ simply considers the tensor products of the one-dimensional formulations such that the expansion basis can now be formed as

$$\phi_{pq}(\xi_1, \xi_2) = \phi_p(\xi_1)\phi_q(\xi_2), \text{ for } p, q = 0, 1, \dots, N-1,$$

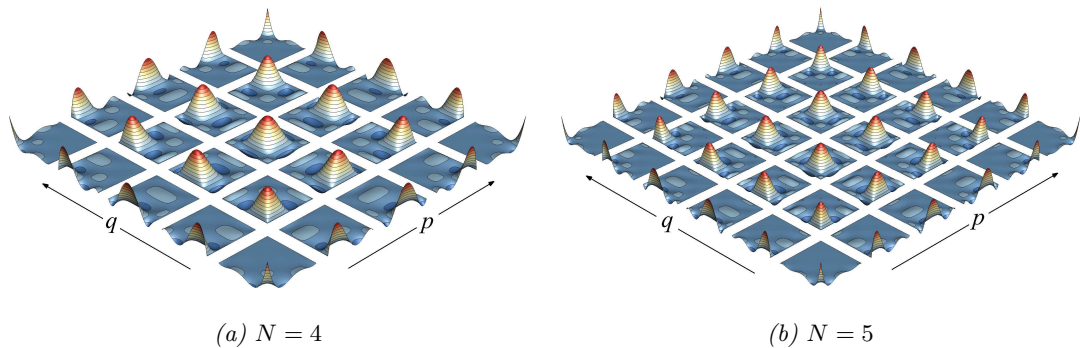


FIGURE 2.1: Shape of the two-dimensional expansion basis functions ϕ_{pq} using a 4th and 5th order polynomial expansion, the former replicated from Karniadakis & Sherwin (2005, chap. 3, figure 3.1*b*).

as an extension to the one-dimensional form in equation (2.7) — examples are shown in figure 2.1, and the integration can be formed as

$$\begin{aligned} \int_{\Pi_e} f(\xi_1, \xi_2) d\xi &= \int_{-1}^1 \left(\int_{-1}^1 f(\xi_1, \xi_2) |_{\xi_2} d\xi_1 \right) d\xi_2, \\ \int_{\Pi_e} f(\xi_1, \xi_2) d\xi &= \sum_{p=0}^{N-1} w_p \left\{ \sum_{q=0}^{N-1} w_q f(\xi_p, \xi_q) \right\}, \end{aligned}$$

as an extension to the Gauss–Lobatto–Legendre rule in equation (2.9). Note that the number of expansion bases ϕ_p and ϕ_q along ξ_1 and ξ_2 do not necessarily have to be the same, but are set as so in the present solver to facilitate element connectivity in generalised domains. The solution of the integration over a complex multi-elemental domain $\Pi(\mathbf{x})$ is simply the incorporation of the local solutions in $\boldsymbol{\xi} \in \{\xi_1, \xi_2\}$ mapped onto the global coordinate system $\mathbf{x} \in \{x, y\}$, with the solutions along coincident elemental boundaries for adjacent elements matched to enforce continuous solutions, and so

$$u^\delta(\mathbf{x}) = \sum_{e=1}^{N_{\text{el}}} \left(\sum_{q=0}^N \hat{u}_{pq}^e \phi_{pq}^e \right),$$

where N_{el} is the number of elements in the system, and the superscript e denotes elemental operations.

Threading these concepts specifically for the incompressible Navier–Stokes equations, this spectral element discretisation scheme is applied in conjunction with the operator splitting time-integration scheme, which ultimately defines the differential equations $\mathbb{L}(u)$ to be solved. A summary of these are as described by Sherwin &

Karniadakis (1996) which discretises the various terms in the Navier–Stokes equations in conjunction with the temporal advancement scheme into a linear advection equation (interpreting the nonlinear advection term as a linear convective operator with an instantaneous wavespeed) and groups of Poisson or Helmholtz equations. The discretisation of each of these terms lead to globally assembled matrices of the flow variables across the computational domain which are to be solved for at each time step. The next section describes the time integration scheme employed.

2.2.2 Temporal evolution

To evolve the governing equations forward in time, a third-order accurate multistep scheme based on backwards differentiation is implemented. The formalisation of the scheme is provided by Karniadakis *et al.* (1991). A brief overview of the pertinent concepts are outlined here.

For an equation of the form

$$\frac{\partial \mathbf{u}}{\partial t} = L\mathbf{u},$$

where L is some operator that can be written as a sum of m pieces, we can approximate the solution as

$$L\mathbf{u} = \sum_{q=1}^m L_q\mathbf{u},$$

allowing the contribution of each term to be computed separately, with the total effect on the solution \mathbf{u} being the sum of the contributions of each individual term. Here, the governing equations can be re-written as

$$\frac{\partial \mathbf{u}}{\partial t} = -\nabla p + \mathbf{L}(\mathbf{u}) - \mathbf{N}(\mathbf{u}),$$

where linear term $\mathbf{L}(\mathbf{u})$ contains only the viscous diffusion term ($\nabla^2\mathbf{u}/Re$), and non-linear term $\mathbf{N}(\mathbf{u})$ contains only the nonlinear advection term ($\mathbf{u} \cdot \nabla \mathbf{u}$). Integrating this equation from times n to $n + 1$ results in the approximation

$$\mathbf{u}^{n+1} - \mathbf{u}^n = \int_n^{(n+1)} -\nabla p + \mathbf{L}(\mathbf{u}) - \mathbf{N}(\mathbf{u}) dt, \quad (2.10)$$

for the flow in the computational domain Π . The solver here implements a multistep method based on backwards-differentiation which utilises the field solutions at multiple previous time steps $\{n - (J - 1) : n\}$ to evolve the solution to time $n + 1$, as opposed to single-step approaches such as the Runge–Kutta methods which evolve the solution

(iteratively) from a single previous solution at time n . For the multistep scheme, the semi-discrete system is given as

$$\frac{\gamma_0 \mathbf{u}^{n+1} - \sum_{q=0}^{J-1} \alpha_q \mathbf{u}^{n-q}}{\Delta t} = -\nabla \bar{p}^{n+1} + \mathbf{L}(\mathbf{u}^{n+1}) - \sum_{q=0}^{J-1} \beta_q \mathbf{N}(\mathbf{u}^{n-q}), \quad (2.11)$$

where J is the order of the integration scheme. The solution of the velocity field at time $n+1$ is evaluated in separate substeps, each solving for the nonlinear advection-, pressure-, and diffusion terms as

$$\frac{\mathbf{u}^\dagger - \sum_{q=0}^{J-1} \alpha_q \mathbf{u}^{n-q}}{\Delta t} = -\sum_{q=0}^{J-1} \beta_q \mathbf{N}(\mathbf{u}^{n-q}), \quad (2.12)$$

$$\frac{\mathbf{u}^\ddagger - \mathbf{u}^\dagger}{\Delta t} = -\nabla \bar{p}^{n+1}, \quad (2.13)$$

$$\frac{\gamma_0 \mathbf{u}^{n+1} - \mathbf{u}^\ddagger}{\Delta t} = \mathbf{L}(\mathbf{u}^{n+1}), \quad (2.14)$$

at each stage obtaining an intermediate/updated velocity field denoted by \mathbf{u}^\dagger and \mathbf{u}^\ddagger , and so by the end of the diffusion substep, the solution reflects the final field \mathbf{u}^{n+1} . The values of the coefficients α_q , β_q , and γ_q for the third-order-accurate scheme ($J = 3$) implemented here are given as

q	α_q	β_q	γ_q
0	3	3	11/6
1	-3/2	-3	
2	1/3	1	

The first substep involves solving the nonlinear advection term $\mathbf{N}(\mathbf{u})$ to obtain the intermediate velocity field \mathbf{u}^\dagger . The nonlinear term has several representations which, although all are identical in a continuum, suffer from discretisation of the governing equations (Zang, 1991). These are the divergence form $\nabla \cdot (\mathbf{u}\mathbf{u})$, convective form $(\mathbf{u} \cdot \nabla)\mathbf{u}$, rotational form $(\nabla \times \mathbf{u}) \times \mathbf{u} + \nabla |\mathbf{u}|^2/2$, and skew-symmetric form $(\mathbf{u} \cdot \nabla)\mathbf{u}/2 + \nabla \cdot \mathbf{u}\mathbf{u}/2$. In the inviscid limit, the form of the nonlinear advection term chosen affects the conservational properties of the discretisation scheme. Specifically, the rotational and skew-symmetric forms conserve both linear momentum and kinetic energy, the divergence form conserves only linear momentum, while the convective form conserves neither. The disadvantages of the different forms are in the costly number of derivative operations required by the skew-symmetric form of the advection operator, and in the

aliasing errors that the rotational form is strongly susceptible to. The present solver utilises the convective form which has been shown to exhibit a higher convergence rate than the skew-symmetric form with increasing spatial resolution (Blackburn & Sherwin, 2004), while retaining a similar accuracy to the other forms.

The nonlinear term $\mathbf{N}(\mathbf{u})$ on the right hand side is extrapolated to time $n + 1$ via equation (2.12). This substep for the implementation of the third-order scheme thus requires the velocity field solutions of the three previous time steps \mathbf{u}^{n-2} , \mathbf{u}^{n-1} and \mathbf{u}^n to predict the intermediate solution \mathbf{u}^\ddagger .

The second substep involves computing the contribution of the pressure field to the velocity solution, and thus obtains an updated intermediate velocity field \mathbf{u}^\ddagger . First, consider the divergence of equation (2.13)

$$\frac{\nabla \cdot \mathbf{u}^\ddagger - \nabla \cdot \mathbf{u}^\dagger}{\Delta t} = -\nabla^2 \bar{p}^{n+1}.$$

Enforcing the incompressibility constraint on \mathbf{u}^\ddagger causes $\nabla \cdot \mathbf{u}^\ddagger = 0$, producing a Poisson equation for the pressure \bar{p}^{n+1} . At this stage also, a high-order pressure boundary condition is enforced on the outward normal gradient of pressure without which time-differencing errors may accumulate and propagate within the solution thus affecting the overall accuracy of the scheme, as described by Karniadakis *et al.* (1991), and Dirichlet boundary conditions on pressure are also enforced. The incompressibility constraint on the divergence equation and the Neumann pressure boundary conditions are given respectively by

$$\begin{aligned} \nabla^2 \bar{p}^{n+1} &= \nabla \cdot \left(\frac{\mathbf{u}^\ddagger}{\Delta t} \right), \\ \frac{\partial \bar{p}^{n+1}}{\partial n} &= -\mathbf{n} \cdot \left[\sum_{q=0}^{J-1} \beta_q \mathbf{N}(\mathbf{u}^{n-q}) + \frac{1}{Re} \sum_{q=0}^{J-1} \beta_q (\nabla \times (\nabla \times \mathbf{u}^{n-q})) \right], \end{aligned} \quad (2.15)$$

where \mathbf{n} is the unit normal vector along defined boundaries Π_b in the computational domain. The Poisson equation is solved with $\partial \bar{p}^{n+1} / \partial n$ weakly enforced to obtain the pressure solution \bar{p}^{n+1} . The updated intermediate velocity field (\mathbf{u}^\ddagger) is then computed from equation (2.13).

The third substep then involves solving the diffusion term in equation (2.10) to provide the final corrected velocity field solution \mathbf{u}^{n+1} . The solution to the diffusion term can be approximated using equation (2.14) which can be recast into an inhomogeneous Helmholtz equation as

$$\left(\nabla^2 - \frac{\gamma_0 Re}{\Delta t} \right) \mathbf{u}^{n+1} = -\frac{Re}{\Delta t} \mathbf{u}^\ddagger.$$

Dirichlet velocity boundary conditions are enforced during these Helmholtz solves. The solution sought for this equation is the final velocity field at time $n + 1$, and this substep completes the time-stepping algorithm.

2.2.3 Three-dimensional flows: the spectral-element–Fourier method

The extension of the two-dimensional solver described up to this stage to the third spatial dimension is achieved through a Fourier expansion of the flow variables in the third (out-of-plane) spatial dimension. This method is extensively described in Karniadakis & Sherwin (2005) and elsewhere.

For a system with a homogeneous geometry in the out-of-plane direction (such as that for the infinite span cylinder or those with an axisymmetry such as a toroidal duct), the flow variables in the out-of-plane (z -) direction can be expressed through a Fourier expansion as

$$\begin{Bmatrix} \mathbf{u}(x, y, z, t) \\ p(x, y, z, t) \end{Bmatrix} = \sum_{k=0}^{N_F-1} \begin{Bmatrix} \mathbf{u}_k(x, y, t) \\ p_k(x, y, t) \end{Bmatrix} \exp(imkz),$$

where $\{\mathbf{u}, p\}$ are the full three-dimensional expression of the flow variables, $\{\mathbf{u}_k, p_k\}$ are the coefficients of the k^{th} Fourier mode, N_F is the number of Fourier modes used for the expansion, and m is the out-of-plane wavenumber of the z -domain defined as $m = 2\pi/l_z$ where l_z is the length of the domain in the out-of-plane direction. This expansion basis naturally enforces a periodicity condition in the out-of-plane direction over l_z . Substituting this expansion of \mathbf{u} into the governing equations in (2.4) results in the following z -discretised form,

$$\begin{aligned} \frac{\partial \mathbf{u}_k}{\partial t} + \mathcal{F}_k[\mathbf{N}(\mathbf{u})] &= -\tilde{\nabla}_k p_k + \frac{1}{Re} \tilde{\nabla}_k^2 \mathbf{u}_k, \\ \tilde{\nabla}_k \cdot \mathbf{u}_k &= 0, \end{aligned} \tag{2.16}$$

where the \mathcal{F}_k operator is the k^{th} component of the Fourier transform of the nonlinear term within the parenthesis, and $\tilde{\nabla}_k$ and $\tilde{\nabla}_k^2$ are the modified gradient and Laplacian operators which exploit the periodicity of each Fourier mode in z such that

$$\begin{aligned} \tilde{\nabla}_k &= \left\langle \frac{\partial}{\partial x}, \frac{\partial}{\partial y}, imk \right\rangle, \\ \tilde{\nabla}_k^2 &= \left(\frac{\partial^2}{\partial x^2} + \frac{\partial^2}{\partial y^2} - (mk)^2 \right). \end{aligned} \tag{2.17}$$

The efficiency gain in the Fourier discretisation approach becomes obvious when considering the form of equation (2.16) — computation of the governing equations for

each Fourier mode in the expansion is almost fully decoupled except through the nonlinear term $\mathbf{N}(\mathbf{u})$, and the introduction of the operators $\tilde{\nabla}_k$ and $\tilde{\nabla}_k^2$ reduces the three-dimensional problem to a series of two-dimensional problems solvable in a two-dimensional domain identical to $\Pi(x, y)$ as described in § 2.2.1.

From this, the only substep in the temporal discretisation scheme that is affected by the Fourier expansion basis is the advection substep in equation (2.12) since the nonlinear advection term is coupled across the Fourier modes. The substep can be re-written for each Fourier mode to incorporate the Fourier expansion such that

$$\frac{\mathbf{u}_k^\dagger - \sum_{q=0}^{J-1} \alpha_q \mathbf{u}_k^{n-q}}{\Delta t} = - \sum_{q=0}^{J-1} \beta_q \mathcal{F}_k \left[\mathbf{N}(\mathbf{u}^{n-q}) \right].$$

In this substep, the Fourier coefficients \mathbf{u}_k for each mode is first forward extrapolated from time n to $n+1$ in Fourier space. These coefficients are then inverse transformed to physical space to evaluate the nonlinear operator, after which they are transformed back into Fourier space where the remainder of the substeps in the temporal advancement scheme are solved. Specifically, the pressure substep is now re-written for each Fourier mode as

$$\frac{\mathbf{u}_k^\dagger - \mathbf{u}_k^\dagger}{\Delta t} = -\tilde{\nabla}_k \bar{p}_k^{n+1},$$

where \bar{p}_k is the solution of the pressure of the k^{th} Fourier mode incorporating incompressibility through

$$\tilde{\nabla}_k^2 \bar{p}_k^{n+1} = \tilde{\nabla}_k \cdot \left(\frac{\mathbf{u}_k^\dagger}{\Delta t} \right),$$

as well as enforcing the high-order pressure boundary condition described by Karniadakis *et al.* (1991), and the diffusion substep is posed as

$$\frac{\gamma_0 \mathbf{u}_k^{n+1} - \mathbf{u}_k^\dagger}{\Delta t} = \frac{1}{Re} \tilde{\nabla}_k^2 \mathbf{u}_k^{n+1},$$

wherein the Dirichlet velocity conditions are enforced when solving the Helmholtz equation.

Since the solver substeps for each Fourier mode are almost fully decoupled, this scheme benefits significantly from parallelised multi-CPU computations. This is implemented in the present solver through the *Open MPI* (Open Message Passing Interface) library where an $N_F - 1$ mode Fourier expansion distributes the computations of each

mode $k \in \{0, 1, \dots, N_F - 1\}$ across multiple processing cores (ideally $N_F - 1$ cores so that each mode is computed on a single core in parallel thus reducing bottleneck effects), with the MPI library facilitating communication of solutions of variables across the independent cores necessary for the transformation of variables back to physical space to compute the nonlinear term or for various calculations and interpolations.

2.3 Analytical tools

Having established the numerical formulation underpinning the flow computations in this project across the previous section, this section now provides a brief overview of several analytical tools and calculations applied extensively across this project.

2.3.1 Linear/Floquet-type global stability analysis

A common method in the study of flow transitions is the application of a stability analysis of a basic state. The goal of such an analysis is to reduce the dimensionality of a complex problem sufficiently to enable further investigations probing the mechanism behind any underlying transitions in the flow. This project considers global instabilities extensively, and so a brief summary of its formulation will be provided here.¹ The interested reader is referred to the thorough coverage on this topic given in Schmid & Henningson (2001) and examples of directly relevant applications such as Barkley & Henderson (1996) amongst others.

The starting point of such an analysis is to assume that the flow possesses a basic state $\mathbf{q}_b = \{\mathbf{u}_b, p_b\}$, and that a small perturbation $\mathbf{q}' = \delta\{\mathbf{u}', p'\}$ is applied on the basic flow such that the total flow $\mathbf{q} = \{\mathbf{u}, p\}$ can be described by

$$\mathbf{q} = \mathbf{q}_b + \mathbf{q}', \quad (2.18)$$

where δ is a small perturbation scalar. Substitution of this decomposition into the Navier–Stokes equations (2.4) and decomposing into terms of order δ^0 and δ^N ; $N \geq 1$ results in the base flow evolution equations

$$\begin{aligned} \frac{\partial \mathbf{u}_b}{\partial t} + \mathbf{N}(\mathbf{u}_b) &= -\nabla p_b + \frac{1}{Re} \nabla^2 \mathbf{u}_b, \\ \nabla \cdot \mathbf{u}_b &= 0, \end{aligned} \quad (2.19)$$

¹Local stability analysis of flows are also common but requires a parallel flow assumption which is very rarely observed in bluff body wakes, and so its methodology is not discussed here.

and the perturbation evolution equations

$$\begin{aligned}\delta \frac{\partial \mathbf{u}'}{\partial t} + \delta \mathbf{DN}(\mathbf{u}') + \delta^2 \mathbf{N}(\mathbf{u}') &= -\delta \nabla p' + \frac{\delta}{Re} \nabla^2 \mathbf{u}', \\ \delta \nabla \cdot \mathbf{u}' &= 0,\end{aligned}\tag{2.20}$$

where $\mathbf{DN}(\mathbf{u}')$ is the linearised advection term given by

$$\mathbf{DN}(\mathbf{u}') = (\mathbf{u}_b \cdot \nabla) \mathbf{u}' + (\mathbf{u}' \cdot \nabla) \mathbf{u}_b.$$

For an infinitesimally small disturbance, terms of order δ^2 may be assumed to be negligible relative to the other terms of $\mathcal{O}(\delta)$, so retaining only terms of $\mathcal{O}(\delta)$ results in the linearised Navier–Stokes equations

$$\begin{aligned}\frac{\partial \mathbf{u}'}{\partial t} &= -\mathbf{DN}(\mathbf{u}') - \nabla p' + \frac{1}{Re} \nabla^2 \mathbf{u}', \\ \nabla \cdot \mathbf{u}' &= 0.\end{aligned}\tag{2.21}$$

Note here the critical assumption that the perturbation field \mathbf{u}' is very small compared to the base flow for this linearisation to be valid. Each term on the right hand side of the momentum equation in (2.21) is now linear with respect to the perturbation field \mathbf{q}' , which can be compactly written as

$$\frac{\partial \mathbf{u}'}{\partial t} = \mathbf{L}(\mathbf{u}').\tag{2.22}$$

For a two-dimensional basic flow $(\mathbf{u}_b(x, y, t))$ becoming unstable to a three-dimensional perturbation field $\mathbf{u}'(x, y, z, t)$, the problem can be further simplified by representing \mathbf{u}' through its Fourier expansion

$$\mathbf{u}'(x, y, z, t) = \int_{-\infty}^{\infty} \hat{\mathbf{u}}(x, y, m, t) \exp(imz) dm,$$

where m is the wavenumber which is related to the mode wavelength through $\lambda = 2\pi/m$, and $\hat{\mathbf{u}}$ are the corresponding coefficients of each Fourier mode. Substituting this representation into equation (2.21), the linearised perturbation equations decouple for each mode and so the solutions of \mathbf{u}' can be expressed as

$$\begin{Bmatrix} u'(x, y, z, t) \\ v'(x, y, z, t) \\ w'(x, y, z, t) \\ p'(x, y, z, t) \end{Bmatrix} = \begin{Bmatrix} \hat{u}(x, y, t) \cos(mz) \\ \hat{v}(x, y, t) \cos(mz) \\ \hat{w}(x, y, t) \sin(mz) \\ \hat{p}(x, y, t) \cos(mz) \end{Bmatrix}.$$

This permits the stability of the flows at different wavenumbers to be computed independently since each mode is coupled only to the base flow itself.

The differential equation in (2.22) may be posed as a Floquet type problem by assuming that the differential equation is T -periodic through the base flow, and so the solution of $\mathbf{L}(\mathbf{u}')$ is of the form $\hat{\mathbf{u}}\exp(\sigma t)$, where σ is the Floquet exponent which can be obtained through the complex Floquet multiplier μ through $|\mu| = \exp(\sigma T)$. For time-independent / steady base flows, the period T can be arbitrarily set.

In the present solver, the Floquet multipliers μ are determined as the eigenvalues of the evolution operator \mathcal{A} which is constructed from the solutions of the linearised perturbation fields on the linearised Poincaré map of the T -periodic base flow such that

$$\mathbf{u}'(x, y, m, t_0 + nT) = \mathcal{A}\mathbf{u}'(x, y, m, t_0).$$

The eigenvalues are determined using the implicitly restarted Arnoldi method based on the use of a Krylov subspace projection (Lehoucq *et al.*, 1998, implemented in ARPACK). In this manner, full construction of the evolution operator \mathcal{A} is avoided, and is thus beneficial from a memory savings perspective. Here, the base flow and linearised perturbation evolution equations are evolved simultaneously, and discrete time solutions are supplied as component vectors forming the Krylov subspace. QR factorisation is then performed orthonormalising using the Gram–Schmidt process, and the set of eigenvalues are then computed from the resulting upper Hessenberg matrix using a multishift QR algorithm. The iteration then proceeds until the norm of the residual vector becomes small, and the Ritz approximations of the corresponding eigenvectors are then extracted.

Within this method, solutions of the base flow and perturbation evolution equations are obtained using the spectral-element method for spatial discretisation in conjunction with the time-integration scheme described in § 2.2.1 and § 2.2.2. The out-of-plane derivatives ($\partial^n/\partial z^n$) in the linearised flow system are treated in the same way as described in equation (2.17) for the spectral-element–Fourier method since the solutions of these linearised modes are necessarily periodic in the out-of-plane direction. The ARPACK solver (Lehoucq *et al.*, 1998) is then called to solve the leading eigenvalues of \mathcal{A} which are the Floquet multipliers μ_m . The stability the linearised system is determined by the eigenmode having $\max(|\mu_m|)$, thus maximising σ . Specifically, the stability of the basic solution $\mathbf{u}_b(x, y, t)$ to a perturbation mode $\hat{\mathbf{u}}(x, y, m, t)$ can be deduced from the outcome of the exponent σ where stable solutions are described through $\sigma < 0$, unstable solutions through $\sigma > 0$, and the neutrally stable solution existing precariously at $\sigma = 0$. For a periodic base flow $\mathbf{u}_b(x, y, t_0) = \mathbf{u}_b(x, y, t_0 + nT)$ where n is an

integer, the complex Floquet multiplier further divulges the nature of the instability — a positive real multiplier ($\text{Re}(\mu) > 0$) indicates that the instability mode possesses an orbit synchronous with the base flow, a negative real multiplier ($\text{Re}(\mu) < 0$) indicates that the instability mode possesses an orbit which is subharmonic to that of the base flow and so the instability is period-doubled, while simultaneous conjugate multipliers with an imaginary component ($\text{Im}(\mu) \neq 0$) indicate that the instability mode possesses an orbital period nonharmonic to that of the base flow. For a steady base flow, the period $T \rightarrow \infty$ and so $\text{Re}(\mu)$ eigenvalues indicate a translation of the fixed point from one stable node to another, whereas the presence of $\text{Im}(\mu)$ eigenvalues indicate a fixed point bifurcation to a limit cycle.

For the remainder of this thesis, the notations adopted for the base flows are $\overline{\mathbf{U}}$ which corresponds to either a steady or time-averaged base flow on which a two-dimensional ($m = 0$) perturbation field is imposed, and \mathbf{U} which corresponds to a T -periodic base flow on which the perturbation field is imposed ($m \geq 0$). In both cases, the base flows are two-dimensional in nature, and so the base flow evolution equations in (2.19) are just the two-dimensional form of the incompressible Navier–Stokes equations.

2.3.2 Perturbation kinetic energy analysis

A complementary study to the instability modes predicted from the Floquet stability analysis is to consider the sources contributing to the instability growth through the Reynolds–Orr equation, which is an evolution equation of the perturbation kinetic energy. The derivation provided here can also be found in more details in the text by Schmid & Henningson (2001). The remainder of the derivation in this section uses the index notation with the summation convention for brevity, i.e. $\mathbf{u} = u_i$ where $u_1 = u$, $u_2 = v$, and $u_3 = w$ in Cartesian coordinates.

The perturbation evolution equations shown in (2.20) can be expressed in index notation as

$$\begin{aligned} \frac{\partial u'_i}{\partial t} + u'_j \frac{\partial U_i}{\partial x_j} + U_j \frac{\partial u'_i}{\partial x_j} + u'_j \frac{\partial u'_i}{\partial x_j} &= -\frac{\partial p'}{\partial x_j} \delta_{ij} + \frac{1}{Re} \frac{\partial^2 u'_i}{\partial x_j^2}, \\ \frac{\partial u'_i}{\partial x_i} &= 0, \end{aligned}$$

where j is the free index of the system, and δ_{ij} is the Kronecker delta, and also recalling that the uppercase $\{U_i, P\}$ denote base flow variables. To arrive at the perturbation

kinetic energy evolution equation (PKE), the scalar product of the perturbation velocity field u'_i with the perturbation momentum equation above is formed, noting that the perturbation kinetic energy $k' = u'_i u'_i / 2$. The resulting equation presents as

$$\begin{aligned} \frac{\partial k'}{\partial t} = & - U_j \frac{\partial k'}{\partial x_j} - u'_i u'_j \frac{\partial U_i}{\partial x_j} - \frac{2}{Re} \mathbf{s}'_{ij} \mathbf{s}'_{ij} + \dots \\ & \dots \frac{\partial}{\partial x_j} \left(-\frac{1}{\rho} p' u'_i \delta_{ij} + u'_i u'_i u'_j + \frac{2}{Re} u'_i \mathbf{s}'_{ij} \right), \end{aligned} \quad (2.23)$$

where \mathbf{s}'_{ij} is the strain-rate tensor

$$\mathbf{s}'_{ij} = \frac{1}{2} \left(\frac{\partial u'_i}{\partial x_j} + \frac{\partial u'_j}{\partial x_i} \right),$$

which in Cartesian coordinates can be expanded as,

$$\mathbf{s}'_{ij} = \begin{bmatrix} 2 \frac{\partial u'}{\partial x} & \frac{\partial u'}{\partial y} + \frac{\partial v'}{\partial x} & \frac{\partial u'}{\partial z} + \frac{\partial w'}{\partial x} \\ \frac{\partial v'}{\partial x} + \frac{\partial u'}{\partial y} & 2 \frac{\partial v'}{\partial y} & \frac{\partial v'}{\partial z} + \frac{\partial w'}{\partial y} \\ \frac{\partial w'}{\partial x} + \frac{\partial u'}{\partial z} & \frac{\partial w'}{\partial y} + \frac{\partial v'}{\partial z} & 2 \frac{\partial w'}{\partial z} \end{bmatrix},$$

and $\mathbf{s}'_{ij} \mathbf{s}'_{ij}$ is the double dot product of second order tensor \mathbf{s}'_{ij} . The spatial periodicity in the out-of-plane direction of the eigenmodes \hat{u}_i obtained from the Floquet stability analysis ultimately provides the impetus for one final simplification by considering the out-of-plane average of the equation. The PKE equation in (2.23) thus simplifies significantly to

$$\frac{\partial \langle k' \rangle}{\partial t} = -U_j \frac{\partial \langle k' \rangle}{\partial x_j} - \langle u'_i u'_j \rangle \frac{\partial U_i}{\partial x_j} - \frac{2}{Re} \langle \mathbf{s}'_{ij} \mathbf{s}'_{ij} \rangle, \quad (2.24)$$

where the final group of terms in equation (2.23) contributes equally zero through an integration in the out-of-plane direction. The angled braces $\langle \cdot \rangle$ in equation (2.24) denote that the quantity is averaged in the out-of-plane direction, and the perturbation terms \mathbf{q}' hereafter denote a specific eigenmode obtained from the stability analysis $\mathbf{q}' = \hat{\mathbf{q}}(x, y, m, t)$. The first term on the right hand side of equation (2.24) represents the mean rate of transport of PKE by the base flow, the second term represents the mean rate of PKE production by the base flow, and the last term quantifies the mean rate of PKE dissipation. Observe here that the nonlinear perturbation advection term, even if retained, integrates to zero, and so although the system is initially seeded with the global instability modes of the linearised governing equations, this equation shows that the nonlinear perturbation terms are energy preserving and do not alter the energy growth.

Since the stability analysis described in § 2.3.1 predicts exponentially growing eigenmodes, the instability growth rate σ (through the Floquet exponent) can be related to the PKE evolution through

$$\sigma = \frac{1}{2E_k} \int_{\Pi} \frac{\partial \langle k' \rangle}{\partial t} d\Pi,$$

where $E_k = \int_{\Pi} \langle k' \rangle d\Pi$ is the total PKE within the computational domain. This thus directly correlates the global instability growth rate to the PKE production and dissipation within the domain, and ultimately provides further insight into the instability mechanism. Specifically, for the system under investigation, the volume integral of equation (2.24) in Cartesian coordinates can be written as

$$\frac{dE_k}{dt} = \int_{\Pi} \frac{\partial \langle k' \rangle}{\partial t} d\Pi = E_{\mathcal{T}} + E_{\mathcal{P}} + E_{\mathcal{D}}, \quad (2.25)$$

with each term on the right hand side of the equation being defined as

$$E_{\mathcal{T}} = \int_{\Pi} \mathcal{T} d\Pi = \int_{\Pi} -U \frac{\partial \langle k' \rangle}{\partial x} - V \frac{\partial \langle k' \rangle}{\partial y} d\Pi, \quad (2.26)$$

$$E_{\mathcal{P}} = \int_{\Pi} \mathcal{P} d\Pi = \int_{\Pi} -\langle u'u' \rangle \frac{\partial U}{\partial x} - \langle u'v' \rangle \frac{\partial U}{\partial y} - \langle u'v' \rangle \frac{\partial V}{\partial x} - \langle v'v' \rangle \frac{\partial V}{\partial y} d\Pi, \quad (2.27)$$

$$E_{\mathcal{D}} = \int_{\Pi} \mathcal{D} d\Pi = \int_{\Pi} -\frac{2}{Re} \langle \mathbf{s}'_{ij} \mathbf{s}'_{ij} \rangle d\Pi. \quad (2.28)$$

Here, $\{\mathcal{T}, \mathcal{P}, \mathcal{D}\}$ are the local distributions of the transport, production, and dissipation terms of the PKE equation, and $\{E_{\mathcal{T}}, E_{\mathcal{P}}, E_{\mathcal{D}}\}$ are the domain integrated quantities normalised by E_k . This final integral form shown in equation (2.25) is the Reynolds–Orr equation as described by Schmid & Henningson (2001), which primarily finds utility in the literature as the basis for energy stability analyses.

The numerical implementation of this analysis evolves both the linearised Navier–Stokes equations in (2.21) and its base flow equations in (2.19) simultaneously following the same spectral-element discretisation scheme discussed in § 2.2.1 in conjunction with the time-integration scheme described in § 2.2.2. The assumption of an infinitesimal perturbation for the linearised system is crucial here since it decouples the base flow and perturbation evolution equations, the total flow being a simple superposition of both the base flow and disturbance fields. This then permits the evaluation of each component of the PKE evolution equation in (2.25) to be performed independently. This analysis has been implemented in the solver, with further details available through Sheard *et al.* (2016)

2.3.3 Receptivity and structural sensitivity analysis

Another perspective from which one may investigate the source of instability growth in a given flow system is the consideration of the receptivity and structural sensitivity of the problem. Giannetti & Luchini (2007) provide a brief summary of the derivation of the adjoint linearised Navier–Stokes equations, but extend the problem to determine the location which most significantly alters the stability of the base flow by drawing on the concept of a localised ‘wavemaker’. A review of the adjoint equations, the structural sensitivity analysis, and some of its applications is provided by Luchini & Bottaro (2014), and a brief revision of these concepts is provided below.

First, recall the linearised Navier–Stokes equations given in (2.21), which are rearranged to produce the homogeneous system $\mathcal{H}\mathbf{q}'$ such that

$$\mathcal{H}\mathbf{q}' = \mathbf{0} = \begin{cases} \frac{\partial \mathbf{u}'}{\partial t} + \mathbf{U} \cdot \nabla \mathbf{u}' + \mathbf{u}' \cdot \nabla \mathbf{U} + \nabla p' - \frac{1}{Re} \nabla^2 \mathbf{u}' \\ \nabla \cdot \mathbf{u}' \end{cases},$$

where $\mathbf{q}' = \{\mathbf{u}', p'\}$ is the solution of the linearised system $\mathcal{H}\mathbf{q}'$, both compactly summarised in row vector form. This system of equations will be referred to as the direct/forward linearised system. To derive the adjoint linearised Navier–Stokes equations (hereafter referred to as the adjoint system for convenience) whose solutions are the adjoint modes $\mathbf{q}^+ = \{\mathbf{u}^+, p^+\}$, consider the dot product of the adjoint solution with the forward system such that

$$\mathbf{q}^+ \cdot \mathcal{H}\mathbf{q}' = \mathbf{u}^+ \cdot \left(\frac{\partial \mathbf{u}'}{\partial t} + \mathbf{U} \cdot \nabla \mathbf{u}' + \mathbf{u}' \cdot \nabla \mathbf{U} + \nabla p' - \frac{1}{Re} \nabla^2 \mathbf{u}' \right) + p^+ \cdot (\nabla \cdot \mathbf{u}').$$

Applying the product rule to manipulate the arrangement of the variables in this system results in the following expanded equation

$$\begin{aligned} & \left(\mathbf{u}^+ \cdot \left(\frac{\partial \mathbf{u}'}{\partial t} + \mathbf{U} \cdot \nabla \mathbf{u}' + \mathbf{u}' \cdot \nabla \mathbf{U} + \nabla p' - \frac{1}{Re} \nabla^2 \mathbf{u}' \right) + p^+ \cdot (\nabla \cdot \mathbf{u}') \right) - \dots \\ & \dots \left(\mathbf{u}' \cdot \left(-\frac{\partial \mathbf{u}^+}{\partial t} - \mathbf{U} \cdot \nabla \mathbf{u}^+ + \nabla \mathbf{U} \cdot \mathbf{u}^+ - \nabla p^+ - \frac{1}{Re} \nabla^2 \mathbf{u}^+ \right) + p' \cdot (-\nabla \cdot \mathbf{u}^+) \right) \\ & = \frac{\partial (\mathbf{u}' \cdot \mathbf{u}^+)}{\partial t} + \nabla \cdot \mathbf{J}, \end{aligned} \quad (2.29)$$

where \mathbf{J} is the bilinear concomitant given by

$$\mathbf{J} = \mathbf{U} (\mathbf{u} \cdot \mathbf{u}^+) + p^+ \mathbf{u}' + p' \mathbf{u}^+ + \frac{1}{Re} (\nabla \mathbf{u}^+ \cdot \mathbf{u}' - \nabla \mathbf{u}' \cdot \mathbf{u}^+).$$

This abides by Lagrange’s identity, and so the adjoint operator to the forward system,

$\mathcal{H}^+ \mathbf{q}^+$, can be extracted as

$$\mathcal{H}^+ \mathbf{q}^+ = \mathbf{0} = \begin{cases} -\frac{\partial \mathbf{u}^+}{\partial t} - \mathbf{U} \cdot \nabla \mathbf{u}^+ + \nabla \mathbf{U} \cdot \mathbf{u}^+ - \nabla p^+ - \frac{1}{Re} \nabla^2 \mathbf{u}^+ \\ -\nabla \cdot \mathbf{u}^+ \end{cases}, \quad (2.30)$$

subject to the application of appropriate boundary conditions satisfying J . The eigenmodes \mathbf{q}^+ of the adjoint system are the receptivity modes of the system which satisfies the form $\mathbf{q}^+ \exp(-\sigma t)$ (the negative growth rate owing to the stable reverse time evolution of the adjoint system)

To arrive at the structural sensitivity tensor, consider again the forward system (Floquet problem described in § 2.3.1) whose solutions were expressed as $\mathbf{q}' = \hat{\mathbf{q}}' \exp(\sigma t)$, but the system is now further perturbed by a disturbance δ such that

$$\begin{aligned} \tilde{\mathbf{u}}' &= \hat{\mathbf{u}}' + \delta \hat{\mathbf{u}}', \\ \tilde{p}' &= \hat{p}' + \delta \hat{p}', \\ \tilde{\sigma} &= \sigma + \delta \sigma, \end{aligned}$$

where σ is the Floquet exponent (also the instability growth rate), terms with a circumflex denote the Fourier coefficients of the mode, and terms accented with a tilde are the perturbed solutions. The forward system under such a perturbation can thus be expressed as

$$\begin{aligned} 0 &= \left(\sigma(\delta \hat{\mathbf{u}}') + (\delta \sigma) \hat{\mathbf{u}}' + \mathbf{U} \cdot \nabla(\delta \hat{\mathbf{u}}') + (\delta \hat{\mathbf{u}}') \cdot \nabla \mathbf{U} + \nabla(\delta \hat{p}') - \frac{1}{Re} \nabla^2(\delta \hat{\mathbf{u}}') \right) + \dots \\ &\dots \left(\sigma \hat{\mathbf{u}}' + \mathbf{U} \cdot \nabla \hat{\mathbf{u}}' + \hat{\mathbf{u}}' \cdot \nabla \mathbf{U} + \nabla \hat{p}' - \frac{1}{Re} \nabla^2 \hat{\mathbf{u}}' \right), \\ 0 &= \nabla \cdot (\delta \hat{\mathbf{u}}') + \nabla \cdot \hat{\mathbf{u}}'. \end{aligned}$$

In both equations, the second group of terms are those of the forward system $\mathcal{H} \hat{\mathbf{q}}'$ which equates to $\mathbf{0}$. This perturbed system can thus be reduced to show that

$$\mathcal{H} \delta \hat{\mathbf{q}}' = \mathbf{0} = \begin{cases} \sigma(\delta \hat{\mathbf{u}}') + (\delta \sigma) \hat{\mathbf{u}}' + \mathbf{U} \cdot \nabla(\delta \hat{\mathbf{u}}') + (\delta \hat{\mathbf{u}}') \cdot \nabla \mathbf{U} + \nabla(\delta \hat{p}') - \frac{1}{Re} \nabla^2(\delta \hat{\mathbf{u}}') \\ \nabla \cdot (\delta \hat{\mathbf{u}}') \end{cases}.$$

Taking the spatial inner product between the adjoint mode and the perturbed forward mode $(\hat{\mathbf{q}}^+, \delta \hat{\mathbf{q}}')$ and applying Lagrange's identity again as proven in the derivation of equation (2.29), the term $\int \nabla \cdot \mathbf{J} d\Pi = 0$ under appropriate boundary conditions through the application of the divergence theorem and also recalling that the adjoint system $\mathcal{H}^+ \hat{\mathbf{q}}^+ = \mathbf{0}$ as derived in equation (2.30). The property of interest here is the drift of

the eigenvalue of the instability, $\delta\sigma$, under an applied structural perturbation, and so a rearrangement of the resulting equation leads to

$$\delta\sigma = \frac{(\hat{\mathbf{q}}^+, \mathcal{H} \delta\hat{\mathbf{q}}')}{(\hat{\mathbf{u}}', \hat{\mathbf{u}}^+)},$$

where the notation (\mathbf{a}, \mathbf{b}) is the spatial inner product $\int_{\Pi} \mathbf{a} \cdot \mathbf{b} \, d\Pi$. Giannetti & Luchini (2007) then showed that the maximum bounds of the eigenvalue drift $|\delta\sigma|$ is proportional to the function

$$l(\mathbf{x}) = \frac{\|\hat{\mathbf{u}}^+\| \|\hat{\mathbf{u}}'\|}{(\hat{\mathbf{u}}^+, \hat{\mathbf{u}}')}, \quad (2.31)$$

where l is the spectral norm of the sensitivity tensor which maps the regions of maximum coupling between both the forward and adjoint mode velocity fields. In broad terms, this sensitivity tensor finds utility in flow control applications where these regions may locate ideal actuator placements for control strategies. In contrast, and specifically to this study where no external forcing is applied on the flow, regions of high sensitivity may be interpreted as the wavemaker location which ideally encompasses the core of the instability.

For the numerical implementation of this analysis, the adjoint eigenmode $\hat{\mathbf{q}}^+$ is computed using the same method described for the forward system in § 2.3.1, with appropriate modification to the terms being solved. The sensitivity field $l(\mathbf{x})$ and its associated norms can then be computed manually.

2.3.4 Stuart–Landau equation

Further complexities in the flow system can be considered by accounting for the effects of nonlinear interactions in the flow as it starts from an initially basic state, to one where unstable modes begin to grow beyond the linear regime. An equation describing the evolution of the amplitude of the mode is given in Landau & Lifshitz (1976, chap. 5, § 29–30) following their initial proposal in 1944, and has been re-derived and summarised across the literature, amongst which are those by Schmid & Henningson (2001) and Drazin & Reid (2004) from where most of the explanations here are drawn (see also Henderson, 1997). If one perceives a complex flow state as a basic stationary state (\mathbf{u}_b) compounded with a large number of unstable multi-scale modes such that

$$\mathbf{u} = \mathbf{u}_b + \sum_{j=0}^{j \rightarrow \infty} \mathbf{u}'_j(x, y, z, t),$$

where \mathbf{u}'_j represents individual perturbation fields of varying length scales, then a critical bifurcation parameter, say, the critical Reynolds number Re_c , can be defined such that all perturbation fields decay when $Re < Re_c$, and only a single perturbation mode m is marginally stable at $Re = Re_c$. For small increments of Re past Re_c such that only mode m is unstable while all other modes remain stable, then the growth rate of the instability mode (σ) can be expanded about Re_c such that

$$\sigma(Re) = \sigma(Re_c) + (Re - Re_c) \frac{d\sigma}{dRe} + \frac{1}{2}(Re - Re_c)^2 \frac{d^2\sigma}{dRe^2} + \mathcal{O}(\sigma^{(3)}).$$

The neutrally stable first term on the right is zero by definition of the critical bifurcation parameter, and retaining only terms linear in order of Re leaves an expression describing a simple relation between the instability growth rate and a distance parameter $Re - Re_c$. To estimate this instability growth rate, Landau proposed that a small-amplitude oscillation Λ might evolve through

$$\frac{d|\Lambda|^2}{dt} = 2a_1|\Lambda|^2 - a_2|\Lambda|^4 + \dots, \quad (2.32)$$

where $\Lambda(t) = |\Lambda|(t) \exp(i\phi(t))$ is the complex amplitude quantifying the instability,² $|\Lambda|$ is the magnitude/envelope of the complex amplitude response, ϕ is the phase of the complex amplitude, and both a_1 and a_2 are complex coefficients such that $a_1 = \sigma + i\omega$ and $a_2 = l(1 + ic)$. Truncating the amplitude evolution equation up to the terms shown in (2.32), then re-arranging the equation and decomposing terms into their real and imaginary components yields evolution equations for the amplitude's magnitude and phase as

$$\begin{aligned} \frac{d \log |\Lambda|}{dt} &= \sigma - \frac{1}{2}l|\Lambda|^2, \\ \frac{d\phi}{dt} &= \omega - \frac{1}{2}lc|\Lambda|^2. \end{aligned} \quad (2.33)$$

Note that this is the cubic-order truncation of the amplitude evolution equation $d|\Lambda|/dt$ shown in (2.32). Some crucial information on the bifurcation dynamics can be obtained from these complex coefficients following Drazin & Reid (2004) and Schmid & Henningson (2001). Firstly, the sign of $\text{Re}(a_1) = \sigma$ determines the stability of the system where a positive coefficient indicates instability to a small perturbation. Further, the sign of $\text{Re}(a_2) = l$ describes the nature of the bifurcation at the critical point such that

²The symbol used for the complex amplitude is usually A in most prescribed texts, but this thesis replaces this with Λ to avoid any confusion with references to the mode A instability used extensively in this thesis.

positive values of l indicates that the transition is supercritical (and so the truncated equation shown in equation 2.33 should fairly represent the equilibrium dynamics of the flow), while negative values of l indicates that the transition is subcritical. Note that if $l = 0$, the amplitude evolution equation shown in (2.33) matches that of the exponential growth form of the linearised disturbances shown earlier in § 2.3.1 and so it describes the dynamics of the linearised flow system. For the supercritical case, the long time evolution of the flow ($t \rightarrow \infty$) predicted from this equation shows that the amplitude saturates as predicted by the amplitude evolution equation ($d \log |\Lambda|/dt \rightarrow 0$, $|\Lambda| \rightarrow \sqrt{2\sigma/l}$) regardless of the initial amplitude of the disturbance. For subcritical bifurcations where $l < 0$, the amplitude evolution equation for long time evolution ($t \rightarrow \infty$) of flows with $\sigma > 0$ produces no real solution and so it fails to predict the equilibrium dynamics of the flow. This is indicative that higher order terms in the expansion of equation (2.32) is required to estimate the equilibrium solution.

2.3.5 Force calculations

While not a complex analysis in its own right, computation of the forces acting on the cylinder is performed extensively throughout this thesis as validation and also for results and discussions in almost all chapters, and so it is pertinent that the calculation of the forces exerted on a body or boundary is formally introduced.

To solve for the forces on a solid body at a time instant t_0 for which the flow solutions $\mathbf{q} = \{\mathbf{u}, p\}$ are known, the actions of the pressure and shear stresses along the boundaries defining the body are first computed through

$$\begin{aligned} F_p &= \oint_{\Pi_o} p \, d\mathbf{n}, \\ F_v &= \oint_{\Pi_o} \tau \, d\mathbf{n}, \end{aligned}$$

where Π_o are the boundaries defining the cylinder body, \mathbf{n} is the outward normal unit vector to the boundary Π_o , and τ is the shear stress on the surface given by $\tau = \mu \partial \mathbf{u} / \partial \mathbf{n}$. Since the lift and drag forces (F_l and F_d , respectively) are the streamwise and cross-stream components of the forces induced on the cylinder, they can be directly computed as the sum of the projection of the pressure and viscous components in these directions such that

$$\begin{aligned} F_d &= F_{d,p} + F_{d,v} = F_p \mathbf{e}_x + F_v \mathbf{e}_x, \\ F_l &= F_{l,p} + F_{l,v} = F_p \mathbf{e}_y + F_v \mathbf{e}_y, \end{aligned}$$

where \mathbf{e}_x and \mathbf{e}_y are unit vectors in the streamwise and cross-stream directions, respectively.

These forces can then be non-dimensionalised as the lift and drag force coefficients c_l and c_d , respectively, through

$$c_d = \frac{2F_d}{\rho U_0^2 A_f},$$

$$c_l = \frac{2F_l}{\rho U_0^2 A_f},$$

where A_f is the area of the surface projected by the cylinder on the oncoming flow. For the cylinder of interest here (as will be introduced subsequently in § 2.5), $A_f = hl_z$, where h is the height of the cylinder, and l_z is the span length of the cylinder. This is further generalised in this thesis owing to the homogeneous geometry of the cylinder in the spanwise direction, and so these coefficients are derived for the forces per unit span such that

$$c_d = \frac{2f_d}{\rho U_0^2 h},$$

$$c_l = \frac{2f_l}{\rho U_0^2 h}.$$

2.4 Validation of the solver and the analytical tools

In this section, the implementation of the numerical scheme and the analytical tools described above are tested and validated against analytical solutions available or against existing published data. Further validation specific to the system under investigation is provided in a subsequent section.

2.4.1 Two-dimensional flow: spectral-element (SE) solver

The implementation of the spatial discretisation scheme is first evaluated by evolving the case of a steady laminar flow past a wire grid. The analytical solution to this problem was derived by Kovaszny (1948) as

$$U(x, y) = 1 - \exp(\lambda x) \cos(2\pi y),$$

$$V(x, y) = \frac{\lambda}{2\pi} \exp(\lambda x) \sin(2\pi y), \quad (2.34)$$

where the parameter λ is given by

$$\lambda = \frac{Re}{2} - \left(\frac{Re^2}{4} + 4\pi^2 \right)^{0.5}. \quad (2.35)$$

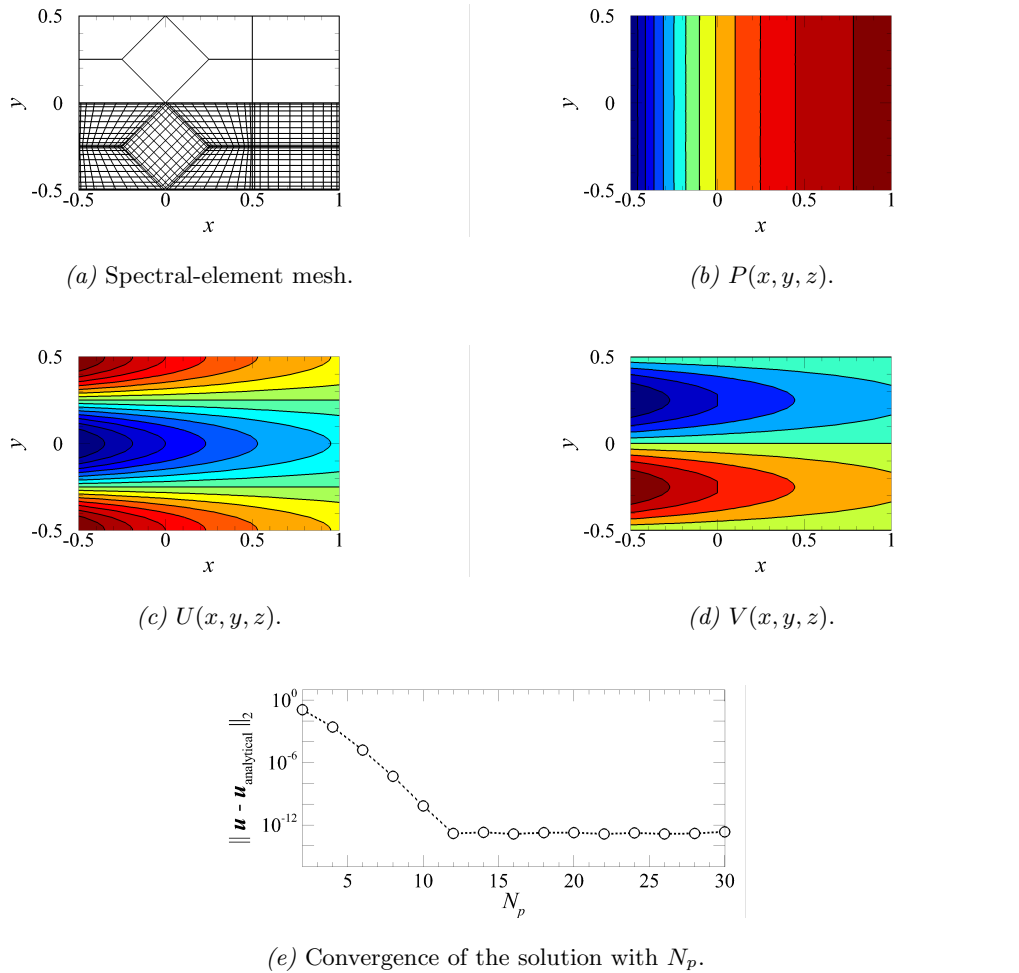


FIGURE 2.2: Results from computations of the two-dimensional Kovaszny flow solutions. In (a), the upper half of the total computed domain shows the mesh elements used, while the lower half shows the spectrally discretised elements. Plots in (b-d) then shows the coloured contours of the computed solution, while the lines in the same images are drawn from the analytical solution. Finally, (e) plots the convergence with increasing N_p of the computed solutions to the analytical solutions in equation (2.34) measured through the 2-norm of the difference.

A simple exercise to recover the pressure field from the governing equations in (2.4) yields

$$P(x) = P_i - \frac{1}{2} (\exp(2\lambda x) - \exp(2\lambda x_i)), \quad (2.36)$$

where P_i is the pressure at a point x_i in the domain to be used as the reference level and can be arbitrarily set. The derivation of the Kovaszny flow solution made no assumptions for the pressure boundary conditions, and so these do not necessarily need to be explicitly enforced (which is the case used in this study, and the pressure

field resulting from the computations will be shown to agree with the expression in equation 2.36).

For this case, the computational domain was set up to span $\Pi_x \in \{-0.5, 1\}$ and $\Pi_y \in \{-0.5, 0.5\}$ as shown in figure 2.2, matching the case reported by Kovasznyay. The flow was computed at a Reynolds number $Re = 40$, imposing velocity boundary conditions as described by the analytical solution. The flow variables were discretised using polynomial shape functions of a range of orders, and these were each evolved until the asymptotic solutions were obtained. The results, shown in figure 2.2, show that the total deviation between the computed flow solution and the analytical solution converges to the limits of machine precision by a polynomial shape function order of $N_p = 12$, exceeding which the two-norm error of the velocity field ($\|\mathbf{u} - \mathbf{u}_{\text{analytical}}\|_2$) remains at $\sim \mathcal{O}(10^{-13})$, almost perfectly agreeing with the results in Blackburn & Sherwin (2004)³. The computed pressure field (coloured contours) is also shown to match the analytical solution (contour lines) exceedingly well, demonstrating the efficiency of the high order Neumann pressure boundary condition.

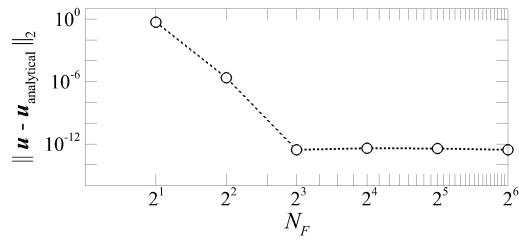
2.4.2 Three-dimensional flow: SE–Fourier solver

The implementation of the SE–Fourier code is also assessed using a variation of the flow past a wire grid. Here, the two-dimensional Kovasznyay flow (U, V) in (x, y) , again at $Re = 40$, was solved in a computational domain that is obliquely projected in the out-of-plane direction through the coordinate transformation:

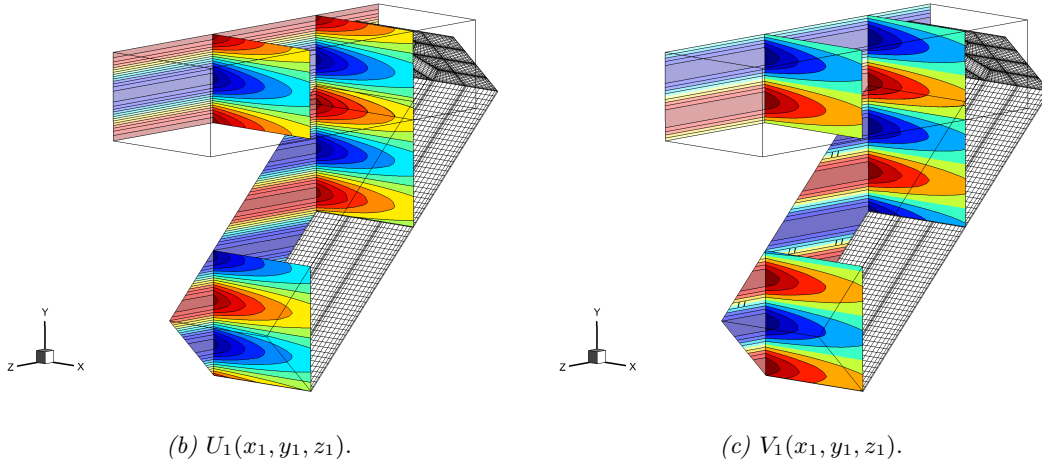
$$\begin{aligned}x_1 &= x_2, \\y_1 &= y_2 \cos(\alpha) - z_2 \sin(\alpha), \\z_1 &= y_2 \sin(\alpha) + z_2 \cos(\alpha),\end{aligned}$$

where $\mathbf{x}_1 = (x_1, y_1, z_1)$ is the base/global coordinate system for which the two-dimensional solution derived by Kovasznyay (1948) applies (and so the flow solution here is homogeneous in z_1), and $\mathbf{x}_2 = (x_2, y_2, z_2)$ are the coordinates transformed through a rotation of α about the x_1 -axis. The computational domain in \mathbf{x}_2 ensures that the nonzero modes in the Fourier expansion were excited and non-trivial. The flow was

³This agreement was expected since the spectral-element mesh employed here was identical to that used by Blackburn & Sherwin (2004)



(a) Convergence of the solution with N_F .



(b) $U_1(x_1, y_1, z_1)$.

(c) $V_1(x_1, y_1, z_1)$.

FIGURE 2.3: Three-dimensional solutions of the Kovasznay flow computed using the spectral-element–Fourier method using $N_F = 32$. In (a), the convergence of the solutions to its analytical form shown in equation (2.37) with increasing number of Fourier modes is shown. Plots in panels (b,c) then shows the solutions of the velocity fields for both $\alpha = 0^\circ$ and 45° .

evolved until the asymptotic solution was obtained, subject to the boundary conditions

$$\begin{aligned}
 U_2(x_2, y_2, z_2) &= 1 - \exp(\lambda x_2) \cos\left(2\pi(y_2 \cos(\alpha) - z_2 \sin(\alpha))\right), \\
 V_2(x_2, y_2, z_2) &= \frac{\lambda}{2\pi} \exp(\lambda x_2) \sin\left(2\pi(y_2 \cos(\alpha) - z_2 \sin(\alpha))\right) \cos(\alpha), \\
 W_2(x_2, y_2, z_2) &= -\frac{\lambda}{2\pi} \exp(\lambda x_2) \sin\left(2\pi(y_2 \cos(\alpha) - z_2 \sin(\alpha))\right) \sin(\alpha), \\
 P_2(x_2) &= P_i - \frac{1}{2} (\exp(2\lambda x_2) - \exp(2\lambda x_i)), \tag{2.37}
 \end{aligned}$$

where x_i and P_i for the pressure boundary condition were set to zero for simplicity. Here, the oblique projection angle was chosen as $\alpha = \pi/4 \text{ rad} = 45^\circ$, with the domain in \boldsymbol{x}_2 extending by a length of $l_z = n/\cos(\alpha)$ with $n = 3$. A polynomial shape function of order $N_p = 12$ was utilised for the spectral-element discretisation of the flow variables (see figure 2.2e), and the number of Fourier modes (N_F) used to discretise the flow

variables in the out-of-plane direction was gradually varied to observe the convergence rate. Implementation of the pressure boundary condition in this case was necessary for numerical stability in contrast to the previous two-dimensional case. The results from these computations are shown in figure 2.3.

In panels (b,c) , the solution computed for the non-oblique projection of the domain ($\alpha = 0^\circ$) was included to aid with visualisation of the problem, and the velocity contours shown in both domains at $\alpha = 0^\circ$ and $\alpha = 45^\circ$ are the solutions in \boldsymbol{x}_1 for consistency. A remarkable agreement was again obtained for the three-dimensional flow computed in the inclined domain, as demonstrated by the closeness in the computed solution (shown as coloured contours) and the analytical solution (shown as the line contours). The plot of the two-norm error between the computed solution and the analytical solution (given in equation 2.34) with increasing number of Fourier modes shows that the deviation limit is capped at an order of $\sim \mathcal{O}(10^{-13})$, which is achieved with just $N_F = 8$. The convergence of the two- and three-dimensional steady flows computed here to the analytical solution validates the implementation of the spectral-element and spectral-element–Fourier schemes in the present solver.

2.4.3 Validation of the time-integration scheme

A further test to assess the implementation of the time integration scheme was conducted for the case of the flow past a circular cylinder. The aim here was to, as a secondary measure, replicate the visualisation of the onset of three-dimensional flow past a circular cylinder as reported in Williamson (1996a), Barkley & Henderson (1996), and Thompson *et al.* (1996), but primarily to identify that the growth of the most unstable wavenumber matches the results obtained from the Floquet stability analysis, which is validated in a following subsection by comparing the results against those reported by Barkley & Henderson (1996). The two-dimensional computational mesh utilised for this purpose was replicated from Blackburn & Lopez (2003), and the distribution of the macro-elements in this mesh is shown in figure 2.4. A towing tank type setup was simulated through the application of the following boundary conditions:

$$\begin{aligned}\Pi_{\text{in}} &: \boldsymbol{U} = \langle 1, 0 \rangle, \\ \Pi_{\text{t}} &: \boldsymbol{U} = \langle 1, 0 \rangle, \\ \Pi_{\text{out}} &: P = 0, \partial\boldsymbol{U}/\partial x \approx 0, \\ \Pi_{\text{o}} &: \boldsymbol{U} = 0,\end{aligned}$$

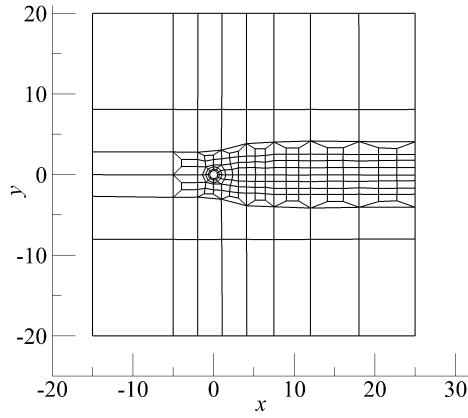


FIGURE 2.4: Spectral-elements in the mesh employed in this validation study, replicating that used by Blackburn & Lopez (2003).

where Π_{in} , Π_{t} , Π_{out} , and Π_{o} are the inlet- (left edge), transverse- (top and bottom edges of the domain), outflow- (right edge), and solid body boundaries, respectively. A high order Neumann boundary condition for pressure (equation 2.15) is also enforced on all boundaries here.

The first case considered here is the two-dimensional flow at a Reynolds number of $Re = 190$, testing the convergence through the non-dimensional Strouhal number (St) and force coefficients (\bar{c}_d, c'_d, c'_l) , and then subsequently validating it against the values published by Barkley & Henderson (1996). A grid convergence test demonstrates that an $N_p = 7$ order polynomial shape function in the spectral-element discretisation produces sufficiently small variation in Strouhal number when using this mesh, the results being shown in table 2.1. The base suction coefficients $(-c_{pb})$ and Strouhal numbers (St) of the two-dimensional flow computed over a range of Reynolds numbers from 50 to 150 were then compared against published experimental and numerical data, the results (shown in figure 2.5) demonstrating a good agreement in the values obtained. This validates the reliability of the two-dimensional flow solver which is utilised extensively throughout this thesis. For the three-dimensional flow computations at the same Reynolds number, the grid converged two-dimensional asymptotic flow solution using an $N_p = 7$ polynomial function for the spectral-element discretisation is imposed as the initial condition into the fundamental Fourier mode used in the out-of-plane discretisation of variables. The spanwise extent of the computational domain in this

	N_p	St	\bar{c}_d	c'_d	c'_l
Present results	5	0.19516 (0.36%)	1.36919 (0.97%)	0.02592 (11.94%)	0.45931 (1.42%)
	7	0.19597 (0.05%)	1.34977 (0.07%)	0.02947 (0.10%)	0.46639 (0.10%)
	10	0.19587 (< 0.01%)	1.34890 (< 0.01%)	0.02944 (< 0.01%)	0.46594 (< 0.01%)
	12	0.19588 (< 0.01%)	1.34886 (< 0.01%)	0.02944 (< 0.01%)	0.46592 (< 0.01%)
	14	0.19587 (< 0.01%)	1.34885 (< 0.01%)	0.02944 (< 0.01%)	0.46592 (< 0.01%)
	16	0.19587	1.34885	0.02944	0.46592
Barkley & Henderson (1996)	10	0.1954	1.3442	0.0293	0.4656

TABLE 2.1: Shedding frequency, mean and fluctuating drag coefficient, and the fluctuating lift coefficient measured for the flow at $Re = 190$, with the values in the parentheses describing the error of the quantity relative to the solution at $N_p = 16$. The results reported by Barkley & Henderson (1996) is also shown here for comparison.

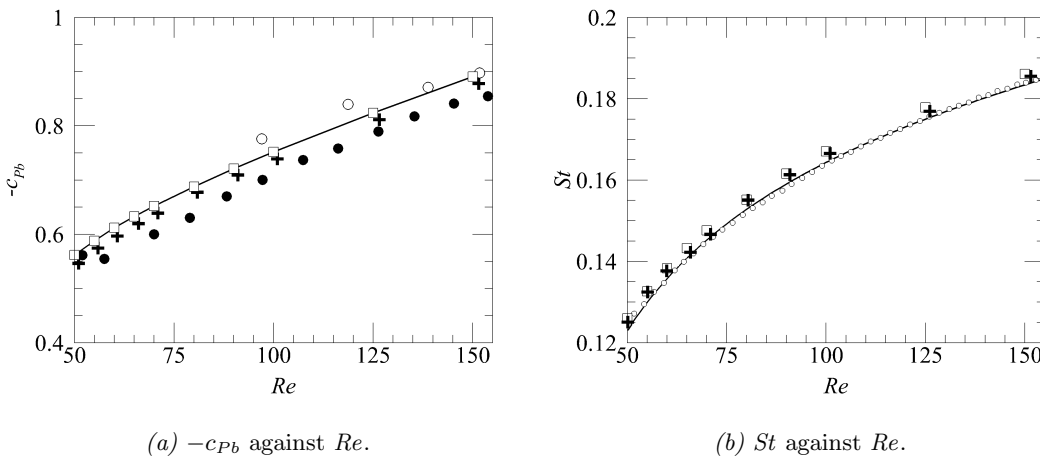
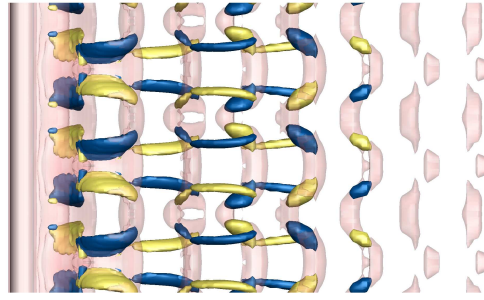
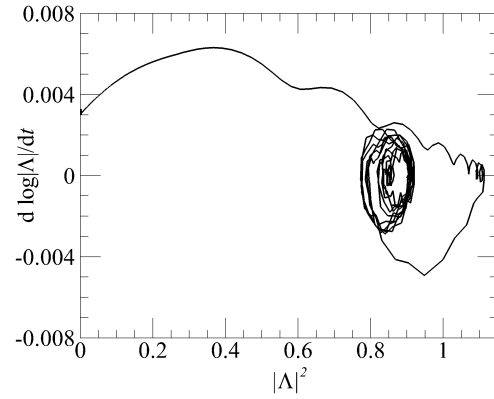


FIGURE 2.5: Variation of (a) the base suction coefficient, $-c_{Pb}$, and (b) the Strouhal number St with increasing Reynolds number. Here, $c_{Pb} = 2(p_b - p_\infty)/\rho U_{in}^2$, where p_b is the base pressure of the cylinder (taken at the rear of the cylinder) and p_∞ is the static pressure of the free stream flow at the inlet. In (a), + data markers correspond to the results of Barkley & Henderson (1996), o from Norberg (1994), • from Williamson & Roshko (1990), and the □ data markers with a connecting line showing the present results. In (b), o data markers are the results obtained from Williamson (1989), + from Barkley & Henderson (1996), while □ markers denote present results. The solid line in (b) is the quadratic function $St = -3.3265/Re + 0.1816 + 1.600 \times 10^{-4}Re$ suggested by Williamson (1989) in fitting the experimental results shown in o.



(a) Flow visualisation.



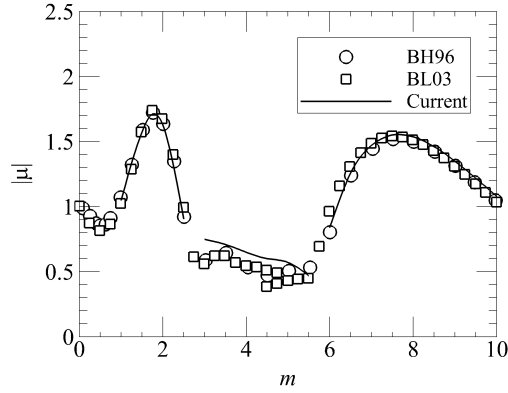
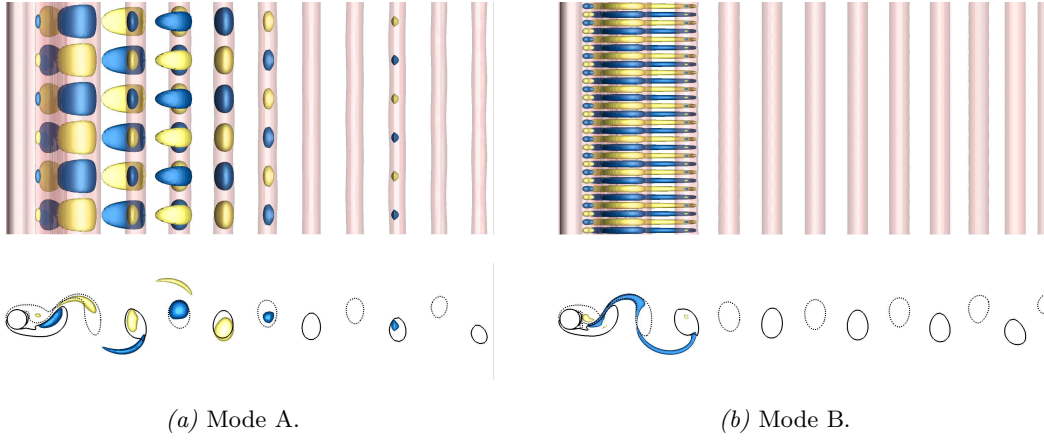
(b) $d|\Lambda|/dt$ against $|\Lambda|^2$.

FIGURE 2.6: (a) Visualisation of the saturated flow unstable through mode A at $Re = 190$. Here, the blue/yellow isosurfaces represent the streamwise vortices at equal magnitudes but opposite signs, while the translucent red isosurface shows the deformed spanwise vortex rollers. (b) Deviation of the instability growth rate and its amplitude over time as the instability saturates to a nonlinear state. The positive gradient at the vertical axis intercept indicates a negative l coefficient, and so the transition here is subcritical.

case is chosen to span $\Pi_z/d \in \{0, 2\pi/1.5879\}$ (d being the cylinder diameter which is chosen as the characteristic length scale), corresponding to the wavelength of the most dominant mode for the mode A instability (obtained from the validation case reported in the following section), and is discretised using $N_F = 32$ Fourier modes. As shown in figure 2.6, the streamwise vortical structures of the saturated solution corresponds strongly with that of the mode A instability structure (showing several repetitions of the mode) as shown by and Henderson (1997). The figure also includes results from the amplitude evolution equation shown in (2.33) demonstrating the subcritical nature of the transition, using the kinetic energy of the dominant Fourier mode as the complex amplitude measure similar to Henderson (1997).

2.4.4 Validation of the Floquet stability analysis

Several of the results chapters in this thesis investigates the stability characteristics of the wakes of an inclined triangular cylinder, and utilises the dominant linearised modes extensively to understand the characteristics of the wakes at the onset of the transition. In this section, the global stability analysis tool is validated using two different cylinder geometries to demonstrate the reliability of the linearised Navier–Stokes solver (see



(c) Floquet multiplier spectrum.

FIGURE 2.7: (a,b) Plan- and side views of the streamwise perturbation vortices of modes A and B, each being obtained at near-critical parameters of ($Re_A = 189$, $m_A = 1.585$) and ($Re_B = 259$, $m_B = 7.616$), respectively, but repeated over a domain of $l_z \approx 12d$ to aid with visualisation of the instability structure. Colours are as described for the three-dimensional case shown in figure 2.6. (c) Eigenspectra of the Floquet multipliers in wake of the cylinder at $Re = 280$. Here, circular markers (\circ) are the results obtained from Barkley & Henderson (1996), square markers (\square) are those from Blackburn & Lopez (2003), while the solid line represents the results obtained from present computations.

§ 2.3.1) and its integration with the ARPACK eigenvalue solver (Lehoucq *et al.*, 1998).

Circular cylinder wake stability

The first of these cases is again that of the flow past a circular cylinder (details of the two-dimensional setup is provided in the previous section, § 2.4.3). In this case, the stability of the wakes of the circular cylinder at several Reynolds numbers were computed to determine the parameters for which the instability modes A and B become

neutrally stable, the results then being compared to those published by Barkley & Henderson (1996), whose eigenmodes and stability results demonstrated a remarkable agreement to the coherent structures observed experimentally by Williamson (1988b). In both cases, a polynomial shape function of order $N_p = 7$ was used to discretise the governing equations (see § 2.4.3). The boundary conditions imposed on the linearised system are the homogeneous velocity boundary conditions along the inlet, transverse and solid body boundaries, $\mathbf{u}_{\Pi_b} = \mathbf{0}$ where Π_b are the specified boundaries, while homogeneous Dirichlet pressure and Neumann velocity boundary conditions are applied on the outflow boundary.

Overall, the predicted critical parameters show a strong agreement with the values published by Barkley & Henderson (1996), with mode A here becoming unstable at a transition Reynolds number of $Re_A = 188.7$ with a wavelength of $\lambda_A = 3.969d$, and mode B at $Re_B = 258.8$ and $\lambda_B = 0.825d$ (the corresponding values reported by Barkley & Henderson are $Re_A = 188.5 \pm 1.0$, $Re_B = 259$, $\lambda_A = 3.96d \pm 0.02d$, and $\lambda_B = 0.822d$). For the flow at $Re = 280$, the reproduced eigenspectrum demonstrates a close agreement between the results obtained for the Floquet multipliers with those reported by Barkley & Henderson (1996) and Blackburn & Lopez (2003). The quasi-periodic mode branch, however, shows a slight discrepancy in the magnitude of the eigenvalues predicted although it extends through a similar range of wavenumbers as those reported in the cited studies. The following subsection will demonstrate that the quasi-periodic branch of solutions observed in the wakes of a square cylinder describes a much better agreement. The cause of this discrepancy in the quasi-periodic mode branch is uncertain, but one speculates that it might have been derived from the method in which the time-periodic base flow is evolved in conjunction with the linearised Navier–Stokes equations — the computations reported by Barkley & Henderson utilised a Fourier reconstruction of the time-periodic two-dimensional base flow whereas the present study evolves this base flow concurrently with the perturbation fields, potentially introducing a difference in temporal fidelity between the two studies. Since this does not resolve or justify the issue of the difference, the authors have taken precaution in the analysis of any quasi-periodic eigenmodes, which is not the dominant mode branch in any case investigated for the periodic wake, nor does it become unstable within the range of Reynolds numbers where the stability of the periodic wakes are computed.

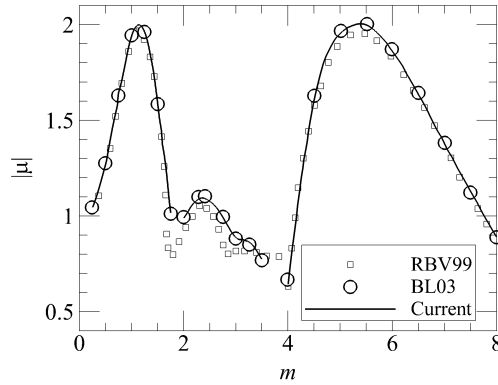


FIGURE 2.8: Eigenspectra of the Floquet multipliers in wake of the square cylinder at $Re = 205$. Here, square markers (\square) are the results obtained from Robichaux *et al.* (1999), circular markers (\circ) are those from Blackburn & Lopez (2003), while the solid line represents the results obtained from present computations.

Square cylinder wake stability

The second of the validation tests for the stability analysis concerns the case of a uniform flow past a square cylinder at a Reynolds number of $Re = 205$. This case was chosen specifically to validate against the results reported by Robichaux *et al.* (1999) and Blackburn & Lopez (2003). For this case, the mesh utilised was again a reconstruction of that used by the cited references (as shown in figure 2.8), with spatial discretisation of flow variables in the governing equations achieved through a 15th order polynomial shape function. The boundary conditions imposed on the flow computations in these cases are similar to those used for the circular cylinder flow setup, which for the base flow are a uniform streamwise flow on the left, top, and bottom boundaries, a no-slip condition on the boundaries outlining the square cylinder surfaces, and a zero reference pressure in conjunction with a zero outward normal gradient of velocity for the outflow boundary on the right edge, while the corresponding boundaries for the linearised flow system applies appropriate boundary conditions such that the boundary conditions for the base flow satisfies that of the total flow. The eigenspectrum obtained from the Floquet stability analysis of this flow case demonstrates a strong agreement between the results obtained from the present work and those reported in Robichaux *et al.* (1999) and Blackburn & Lopez (2003). Note in particular the agreement of the magnitudes of the complex Floquet multipliers between the present study and those published by Blackburn & Lopez (2003) (as labelled).

2.4.5 Validation of the structural sensitivity analysis

For this analysis, the numerical implementation was validated against those reported in several prior studies on flows past the circular cylinder. In all cases, appropriate boundary conditions were derived and applied on all boundaries when evolving the adjoint equations (Barkley *et al.*, 2008, see). The first case tested here was the steady flow at $Re = 50$ for comparison with Giannetti & Luchini (2007). Since the primary instability in the circular cylinder wake occurs at about $Re_c \approx 47$, and that the numerical solver used evolves the unsteady governing equations, the ‘steady’ base flow solution for this $Re = 50$ flow was forced through the application of a symmetry boundary condition applied along the wake centreline such that

$$V(y = 0) = 0, \quad \partial U / \partial y(y = 0) = 0.$$

This assumption is based on results that the wake centreline can be found at a constant level of $y = 0$ for all x owing to the symmetry of the system, and has been applied in several prior studies such as in the mean wake stability analyses by Barkley (2006). The results for the two-dimensional base flow streamlines, velocity field moduli of the direct and adjoint modes, and the sensitivity field are shown in figure 2.9, each comparing exceedingly well against those reported by Giannetti & Luchini (2007). Specifically, the streamlines of the two-dimensional base flow from present computations shown in panel (a) shows a recirculation bubble length of $L_R = 2.92d$ where Giannetti & Luchini (2007) reported a recirculation bubble length of $L_R \approx 3d$ at the same Reynolds number (figures 5 and 6 of their paper), the flooded contours of the direct and adjoint mode’s velocity modulus in panels (b,c) coincides exceedingly well with those shown in figures 8 and 10 of their paper, and the sensitivity field shown in panel (d) shows a strong agreement to their figure 17.

The structural sensitivity tensor was also calculated for the unsteady flow at $Re = 190$ with a three-dimensional perturbation mode of wavenumber $m = 1.585$ past the circular cylinder which corresponds to the mode A instability to validate the calculations of the instantaneous sensitivity field of an unsteady flow against those reported by Giannetti *et al.* (2010). This was crucial to ensure the correctness of the calculations since the instabilities associated with three-dimensional perturbation modes are amongst the key foci of this thesis. The spatial distribution of the sensitivity field $l(x, y)$ at 4 time instances spaced at a phase of $\pi/4$ rad apart are shown in figure 2.10,

the sensitivity field at each phase showing the same distribution as that in figure 3 of Giannetti *et al.* (2010), thus validating the numerical procedure for this study.

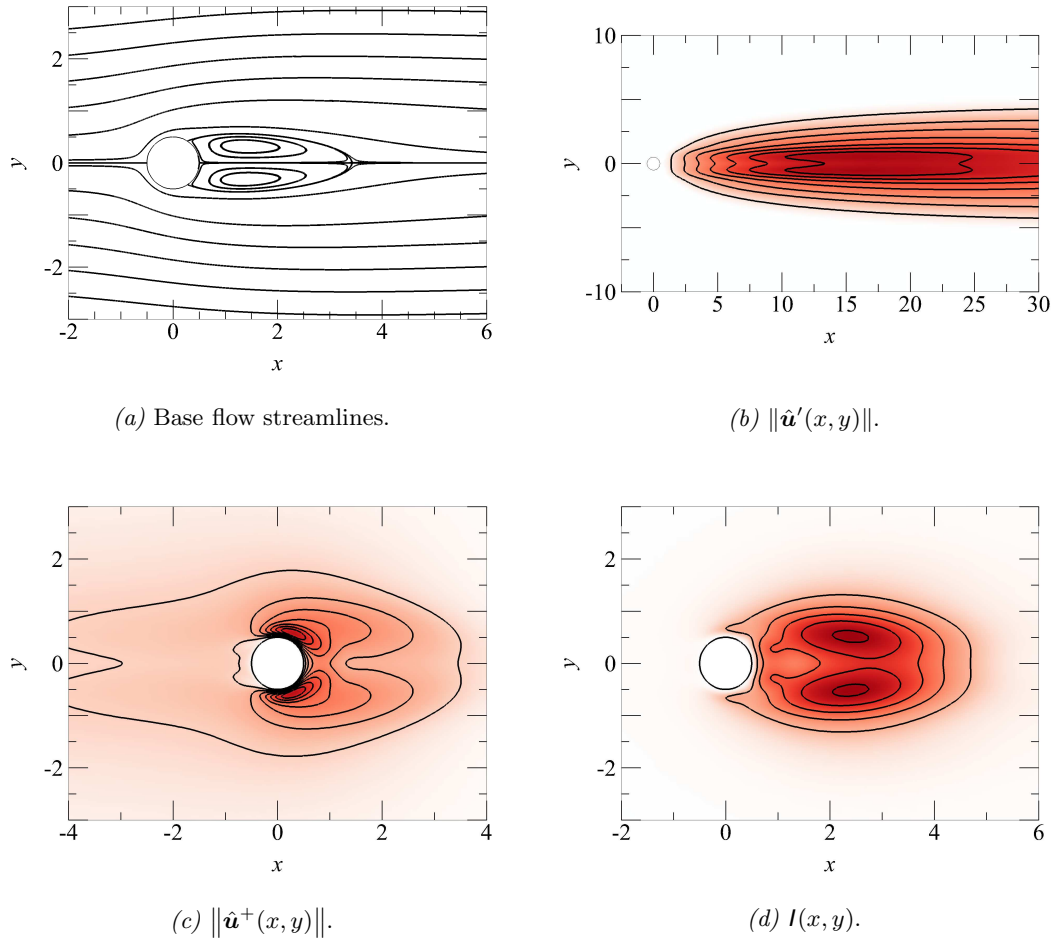


FIGURE 2.9: Computations of the (forced) steady flow past the cylinder at $Re = 50$. In particular, panel (a) shows the streamlines of the base flow in the vicinity of the cylinder, (b) shows the modulus of the velocity of the direct eigenmode, (c) shows that for the adjoint eigenmode, and (d) shows the structural sensitivity field. These results compare exceedingly well with those reported by Giannetti & Luchini (2007).

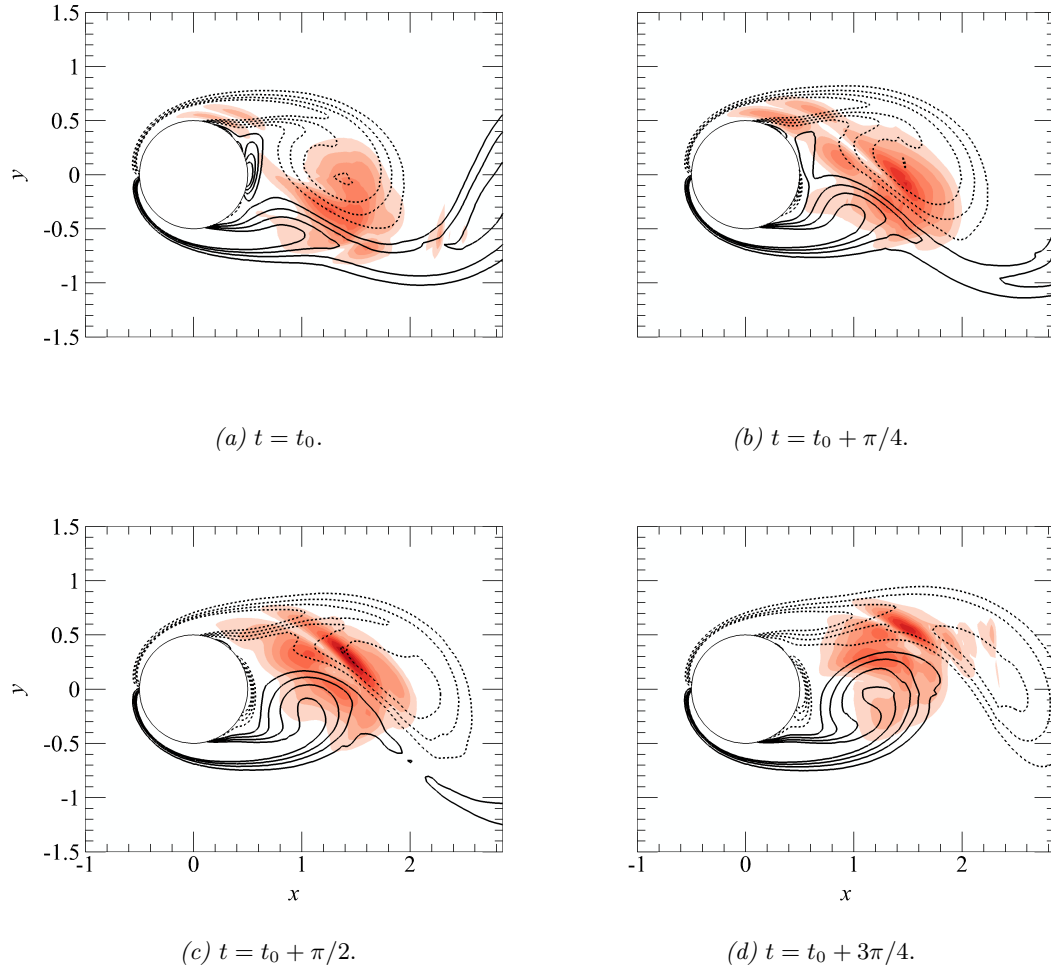


FIGURE 2.10: Plots of the sensitivity field of mode A in the wake of the cylinder at parameters ($Re = 190$, $m_A = 1.585$) at 4 equispaced time-instances $t = t_0 + nT/8$ where $n = 0, 1, \dots, 3$, with the remainder of the period being a reflection of the phases shown owing to the spatio-temporal symmetry of the flow field. The shaded regions map the sensitivity field while the solid and dashed contour lines depict positive and negative vorticity at arbitrary levels to indicate the positions of the vortices being shed. These results again agree with those reported by Giannetti *et al.* (2010).

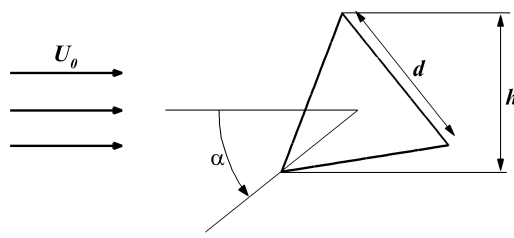


FIGURE 2.11: Schematic of the system under investigation. The equilateral triangle cross-section cylinder here has a side length of d and is immersed in a uniform flow field U_0 . As the cylinder inclination α is increased in the counter-clockwise direction, the cylinder obstructs the flow through a projected height of h as indicated in the figure. Further examples showing the inclined cylinder system are provided in figure 2.13.

2.5 Problem setup

Here, the flow system of interest is introduced along with the computational setup, followed by preliminary results from a grid dependence (p -refinement) study and a domain dependence study. Some results are then validated, comparing against limited available data in the literature.

The system under investigation comprises a cylinder with an equilateral triangular cross-section (hereafter referred to as ‘cylinder’ for brevity) immersed in a uniform flow with velocity U_0 perpendicular to the cylinder span, producing a wake region whose dynamics and stability characteristics are sought. A schematic diagram of this system is shown in figure 2.11 with specific examples of the inclined cylinder shown in figure 2.13. The cylinder inclination is gradually varied within $0^\circ \leq \alpha \leq 60^\circ$ (increasing in the counter-clockwise direction), generally at an increment of $\Delta\alpha = 6^\circ$, with all inclinations outside this range being either reflection symmetric about the horizontal centreline, or identical to the geometries contained within the initial range. Specifically, $\alpha = 0^\circ$ corresponds to the case with the triangle cross-section pointing directly upstream, $\alpha = 30^\circ$ corresponds to the case where the triangle is pointing vertically upwards, $\alpha = 60^\circ$ describes the triangle pointing directly downstream, and $\alpha = 90^\circ$ which is outside the computed range of angles is simply the cylinder at $\alpha = 30^\circ$ reflected about the horizontal centreplane. The projected height of the cylinder (h) is thus related to the cylinder side length (d) and the inclination angle (α) through

$$\frac{h}{d} = \sin(60^\circ - |\alpha - 30^\circ|) + \sin(|\alpha - 30^\circ|). \quad (2.38)$$

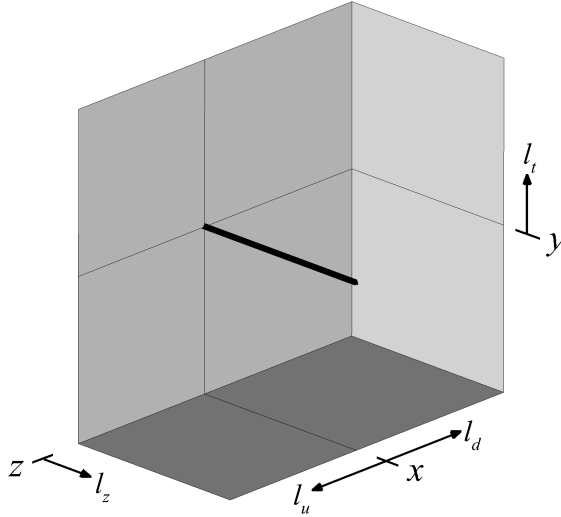


FIGURE 2.12: View of the three-dimensional computational domain, introducing the domain lengths l_u , l_d , l_t , and l_z which will be varied in a subsequent domain dependence study. The solid lines on the planes in the projected view indicate the axes $\boldsymbol{x} = 0$. The cylinder here is highlighted by the dark shaded surfaces, its cross-section center being affixed to the coordinate origin, and the flow moves in the positive x direction extending down l_d .

Choosing h as the characteristic length scale and U_0 as the velocity scale, the Reynolds number in this system can thus defined as

$$Re = \frac{U_0 h}{\nu}, \quad (2.39)$$

where ν is the fluid kinematic viscosity (the Reynolds number scaled by the cylinder side length, Re_d , can be recovered by dividing equation 2.39 by equation 2.38). This results in a time and pressure scaling of $t^* = t h/U_0$ and $p^* = p \rho U_0^2$, respectively, recalling that the starred (*) terms denote dimensional variables. Note that the convective time-scale is used here in preference to the alternative diffusive time scale ($t^* = t_d h^2/\nu$) owing to the focus of this project on moderate to higher Reynolds number flows — the latter finding utility at low Re where diffusive effects are dominant.

An example of the computational domain is shown in figure 2.12. The nomenclature adopted for the remainder of this thesis is such that $\Pi_x \in \{l_u, l_d\}$ describes a boundary plane along the (y, z) -axis, $\Pi_y \in \{-l_t, l_t\}$ describes a boundary plane along the (x, z) -axis, and $\Pi_z \in \{0, l_z\}$ describes a boundary plane along the (x, y) -axis, with l_u , l_d , l_t , and l_z being the upstream, downstream, transverse, and spanwise domain lengths, respectively, as shown in figure 2.12. To capture the physics of a uniform flow past the cylinder, the boundary conditions for two-dimensional flow computations are chosen as

follows:

$$\begin{aligned}
\Pi_{\text{in}} &: \mathbf{U} = \langle 1, 0 \rangle, \\
\Pi_{\text{t}} &: V = 0, \partial \mathbf{U} / \partial y = 0, \\
\Pi_{\text{out}} &: P = 0, \partial \mathbf{U} / \partial x \approx 0, \\
\Pi_{\text{o}} &: \mathbf{U} = 0,
\end{aligned}$$

where Π_{in} describes the inflow boundary plane at $x = -l_u$, Π_{t} describes the transverse boundary planes at $y = \pm l_t$, Π_{out} describes the outflow boundary plane at $x = l_d$, and Π_{o} describes the three surfaces that make up the triangular cylinder whose centroid is affixed at the origin of the computational domain. On all boundaries assigned with a Dirichlet velocity condition, the high-order Neumann pressure boundary condition derived by Karniadakis *et al.* (1991) (ref. equation 2.15) was enforced to maintain the overall third-order accuracy in time. Note that a towing tank type boundary condition may alternatively be applied on the transverse boundaries (Π_{t}) of the domain (similar to those applied in the validation cases of the wakes of the circular and square cylinders in § 2.4.4), in lieu of the impermeable stress-free/symmetry boundary condition imposed in this study — several prior studies such as that by Posdziech & Grundmann (2007) have mentioned that the choice of the towing tank- (Dirichlet) and symmetry (Neumann) boundary conditions on these transverse (‘farfield’) edges are similarly effective in emulating an unbounded flow provided that the domain blockage is not too severe, a point which was methodically examined in Sen *et al.* (2009). In the latter study, Sen *et al.* showed that applying the towing tank boundary condition on the farfield boundaries ($\Pi_{\text{t}} : \mathbf{U} = \langle 1, 0 \rangle$) in a domain with a large blockage ratio artificially accelerated the flow about the cylinder amongst other effects, producing misleading predictions of the separation Reynolds numbers, and so the stress-free impermeable boundary condition performs more satisfactorily in computational domains with high blockage ratios. Otherwise, it appears from most prior studies that the choice of either boundary condition type was a matter of convenience — notably, domains with a curved/circular inlet boundary edge preferentially apply the towing tank condition since the inlet boundary smoothly connects to the transverse edges (for example, Johnson *et al.*, 2004; Posdziech & Grundmann, 2007; Thompson *et al.*, 2014), while rectangular computational domains are more flexible with their choice of boundary conditions, the minor drawback being the higher number of degrees-of-freedom in the discretised

system for a similar domain size $\Pi \in \{\Pi_x, \Pi_y\}$. The stress-free impermeable boundary condition was opted for the farfield in this project because it is less susceptible to domain blockage effects as demonstrated by Sen *et al.* (2009). For three-dimensional flow computations, the decomposition of flow variables in the out-of-plane direction through a Fourier expansion naturally imposes a periodic boundary condition on the boundary edge planes (Π_z) such that

$$\{\mathbf{u}, p\}(z = 0) = \{\mathbf{u}, p\}(z = l_z).$$

The remainder of this chapter describes the development of the two-dimensional spectral-element mesh — details of the mesh resolution in the out-of-plane (z -) direction will be presented in chapter 6. The development of the two-dimensional mesh used throughout this project proceeded through several stages to exploit the benefits of the spectral/ hp element method. The initial h -refinement stage designs the spectral element domain, ensuring that sufficient resolution (number of spectral elements) is afforded to regions of the domain where the flow is anticipated to be subjected to large shear or fluctuations. This is prudent for the reliability of the discretisation scheme since the sharp vertices or corners about the triangular cross-section cylinder subjects the adjacent flow to significant pressure and velocity gradients, and that derivatives are known to become unbounded under such curvature in the meshes, ultimately eroding the performance of the scheme. Readers are directed to the corresponding discussion on non-smooth domains, section 5.5 of Karniadakis & Sherwin (2005), for a thorough description of the problem. Several means of minimising this effect are known, the most straightforward approach being to simply increase the resolution of the discretised domain about these non-smooth regions using either radical or geometrically refined elements. The other solutions described require a modification to the spectral discretisation code. We have adopted the former approach, and the significant resolution afforded about these cylinder corners can be seen in figure 2.13. Once a satisfactory distribution of spectral-elements was obtained in the computational domain, a p -refinement study was performed to determine the optimal polynomial shape function order which produces sufficient grid convergence. Finally, a domain dependence study is performed to determine if the initial computational domain size chosen was sufficient, and if so, what the domain truncation uncertainty levels are.

For this purpose, and without any knowledge *a priori* of the flow dynamics associated with the wakes of the triangular cylinder, test parameters of $\alpha = 30^\circ$ for the

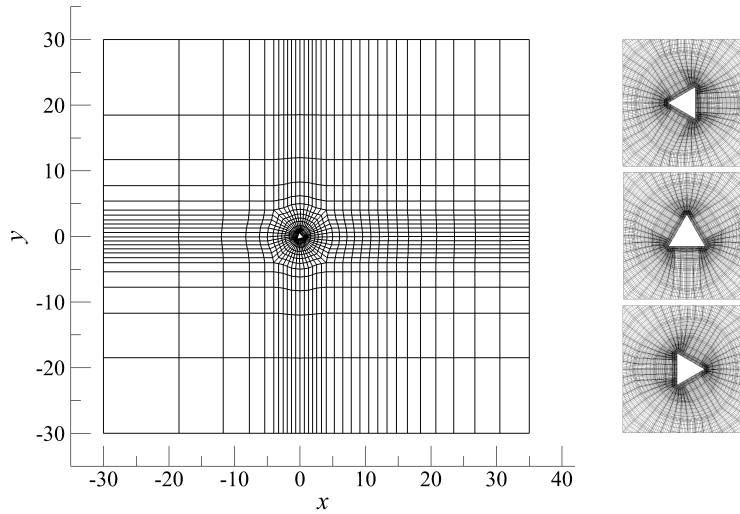


FIGURE 2.13: The two-dimensional macro-element mesh distribution in the test domain M_0 is shown in the left panel, while the three images on the right panel demonstrates the high resolution afforded in the near wake of the cylinder (particularly about the cylinder vertices) after an 8th order polynomial shape function discretisation, each corresponding to cylinder inclinations of $\alpha = 0^\circ$, 30° , and 60° , respectively.

cylinder inclination and $Re = 200$ for the flow were chosen, anticipating that the flow at this cylinder inclination would produce the most asymmetric flow field about the cylinder and hence the most interesting dynamics, and also because of the nature of the design of the spectral element mesh where the quadrilateral nodal elements in the vicinity of the cylinder were scaled by the cylinder side length d (the function d/h in equation 2.38 is maximised at $\alpha = 30^\circ$, and so it possesses the largest spectral elements amongst the other cylinder inclinations). The Reynolds number of $Re = 200$ was chosen since flow three-dimensionality was expected to occur below this level, and that this Reynolds number was expected to be among the highest to be computed in this project. A two-dimensional spectral-element domain was designed such that $l_u = 30h$, $l_d = 35h$ and $2l_t = 60h$, which was amongst the larger sized domains commonly used in previous studies on bluff body wake flows. The blockage of the present test domain thus quantifies as $\beta = h/2l_t = 1/60$, as shown in figure 2.13. The convergence of the properties of the two-dimensional flow from the p -refinement study was monitored through the shedding frequency as quantified by the nondimensional Strouhal number (St), the time-mean and root-mean-squared values of the lift coefficient (\bar{c}_l and c'_l), and the time-mean drag coefficient (\bar{c}_d). In addition to these measurements, Floquet

stability analysis was performed on the asymptotic two-dimensional flow solutions to determine the peak Floquet multiplier magnitude ($|\mu|_{\text{peak}}$) and its corresponding dominant wavenumber (m_{peak}), the results of which have direct bearing on the reliability of most of the work underpinning this thesis. These results are presented in table 2.2, with the decrease in the errors with increasing N_p being further elucidated in figure 2.14.

N_p	St	\bar{c}_d	$ \bar{c}_l $	c'_l	m_{peak}	$ \mu _{\text{peak}}$
4	0.1701 (0.08%)	1.9928 (0.12%)	1.5030 (1.08%)	1.1680 (0.62%)	1.3212 (0.06%)	1.5922 (18.17%)
5	0.1702 (0.46%)	1.9952 (0.30%)	1.4868 (0.29%)	1.1609 (0.51%)	1.3220 (2.06%)	1.9458 (1.48%)
6	0.1694 (0.40%)	2.0011 (0.18%)	1.4912 (0.35%)	1.1668 (0.23%)	1.2954 (0.08%)	1.9174 (1.30%)
7	0.1688 (0.10%)	1.9975 (0.05%)	1.4859 (0.06%)	1.1640 (0.10%)	1.2944 (0.18%)	1.9426 (0.12%)
8	0.1686 (0.04%)	1.9986 (0.04%)	1.4868 (0.08%)	1.1652 (0.07%)	1.2921 (0.07%)	1.9403 (0.25%)
9	0.1685 (0.04%)	1.9994 (0.05%)	1.4880 (0.07%)	1.1660 (0.07%)	1.2912 (0.02%)	1.9453 (0.08%)
10	0.1685 (0.02%)	2.0004 (0.05%)	1.4890 (0.06%)	1.1669 (0.06%)	1.2910 (0.02%)	1.9468 (0.05%)
11	0.1684 (0.01%)	2.0014 (0.04%)	1.4899 (0.05%)	1.1675 (0.05%)	1.2907 ($< 0.01\%$)	1.9478 (0.02%)
12	0.1684	2.0021	1.4907	1.1681	1.2907	1.9473

TABLE 2.2: Grid convergence data obtained from the p -refinement study. The values in the parentheses are the relative errors of the measurements with increasing N_p . A summary of these results is shown in figure 2.14.

As shown in figure 2.14, all parameters from the two-dimensional flow computed show a convergence to better than 0.1% for $N_p \geq 8$, which is generally smaller than most experimental uncertainty thresholds. The relative error of the peak Floquet multiplier, however, increases to $\epsilon_{|\mu|} \approx 0.26\%$ between $N_p = 7$ and $N_p = 8$ but remains at approximately the same order of magnitude and subsequently decreases with increasing N_p . Errors computed relative to $N_p = 12$ (highest polynomial order tested) clarifies this issue by showing a monotonic decrease for $N_p \geq 8$, with the largest error at $N_p = 8$ being $\epsilon_{|\mu|} = 0.36\%$. A polynomial order of $N_p = 8$ is thus applied for all computations in this study since most parameters of the flow are shown to change quite negligibly with increasing resolution, and the larger magnitudes of $\epsilon_{|\mu|}$ are justifiable considering

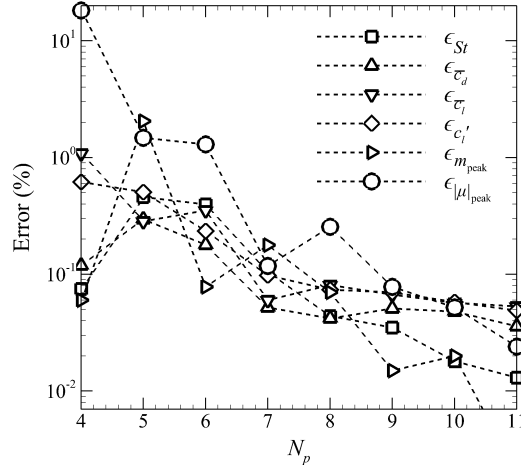


FIGURE 2.14: Relative errors (ϵ) with increasing N_p for the Strouhal number (\square), mean drag coefficient (\triangle), mean lift coefficient (∇), r.m.s. of the lift coefficient (\diamond), and the leading instability mode wavenumber (\triangleright) and its corresponding Floquet multiplier (\circ). This figure summarises the data tabulated in table 2.2.

that the stability analysis applied to derive $|\mu|$ would compound the underlying resolution errors from the two-dimensional base flow itself. The discretised mesh resolution in the near wake of the cylinder using an $N_p = 8$ polynomial order discretisation was also included in figure 2.13, showing the cylinder inclined at incidence angles of $\alpha = 0^\circ$, 30° , and 60° , respectively.

Another source of error in computing solutions of the flow past an immersed cylinder in the present configuration arises from the truncation to a finite domain where ideally the domain should extend infinitely in all directions. Extensively sized domains are impractical from a numerical standpoint as their computational expense can severely outweigh the gain in the qualitative understanding of the physics of the flow, and so an appropriate compromise between the accuracy of the solution and the computational efficiency is sought. The application of appropriate boundary conditions can aid in reducing such artificial forcing imposed on the flow due to the truncation as discussed earlier in this section (demonstrated by Sen *et al.* amongst other works), but cannot completely eliminate the issue. It is thus imperative that such domain related uncertainties are assessed and quantified to show that the flow solutions reported in this thesis do not suffer significantly from such a finite domain.

To this end, the domain lengths l_u , l_d , and l_t were independently varied from the test domain utilised in the p -refinement study, and the flow solutions for the same case

of an $Re = 200$ flow past the cylinder inclined at $\alpha = 30^\circ$ were computed. For brevity, the base mesh used in the p -refinement study shall be referred to as mesh M_0 here, while the meshes with the varied lengths are denoted with subscripted u , d , and t to indicate which lengths l_u , l_d , or l_t have been modified, the remaining lengths being kept consistent with the base mesh M_0 . A summary of the lengths tested and the results from the flow computations are tabulated in table 2.3. Knowing that the flow computations will produce unphysical results if any of l_u , l_d , or l_t are set to zero given the prescribed boundary conditions, and also that flow measurements should necessarily converge to a single solution as these domain lengths tend to very large values ($\{l_u, l_d, l_t\} \rightarrow \infty$), the variation of these flow measurements with increasing domain lengths may be crudely approximated using an inverse power law type function. In this case, the function form

$$g(l) = \frac{a_0}{l^{a_1}} + a_2, \quad (2.40)$$

where a_0 , a_1 , and a_2 are the nonlinear regression coefficients, satisfies such constraints, thus permitting the estimation of the asymptotic solutions for large domain lengths. The nonlinear regression was performed using the `cftool` curve fitting application in MathWorks[®] MATLAB[®] version R2015b which implements a nonlinear least-squares fitting procedure using the Trust-Region algorithm for iterative optimisation. The small dataset was extrapolated to crudely estimate the asymptotic solution for an infinite domain length (denoted with the subscript ∞ in table 2.3), and these are reported along with their 95% confidence interval limits. The values in the parentheses are the percentage differences between the M_0 results and its corresponding M_∞ estimation. These results show that the blockage effects from the transverse domain size (l_t) in the present setup affects the flow solutions most severely with deviations of up to a modest level of $\approx 3\%$, while the truncation errors introduced by finite l_u and l_d domain lengths are estimated to be within 1% of the solutions obtained for M_0 .

The final spectral-element meshes employed throughout this project thus possesses 1016 quadrilateral elements constructed from 1082 vertices which are further discretised through $N_p = 8$ order tensor-product polynomial shape functions, resulting in 150738 degrees-of-freedom for each two-dimensional flow computation. The computational domain Π extends through $\Pi_x \in \{-30, 35\}$ and $\Pi_y \in \{-30, 30\}$, consistent with mesh M_0 since the estimated uncertainty level appeared at an acceptable level of 3%. This domain size of $\langle \Pi_x, \Pi_y \rangle$ is also among the larger sets compared to previous works on unbounded flows past cylinders with triangular cross-sections such as those used by

	l_u/h	l_d/h	$2l_t/h$	St	\bar{c}_d	$ \bar{c}_l $	c'_d	c'_l
M_{u1}	9	35	60	0.1738	2.0878	1.5498	2.1023	1.7126
M_{u2}	15	35	60	0.1704	2.0310	1.5094	2.0456	1.6711
M_{u3}	20	35	60	0.1694	2.0137	1.4963	2.0283	1.6583
M_{u4}	25	35	60	0.1688	2.0047	1.4901	2.0194	1.6519
M_0	30	35	60	0.1686	1.9993	1.4874	2.0140	1.6484
$M_{u\infty}$	∞	35	60	0.1676 ± 0.0015	1.9810 ± 0.0039	1.4754 ± 0.0220	1.9968 ± 0.0021	1.6359 ± 0.0100
				(0.61%)	(0.92%)	(0.81%)	(0.86%)	(0.77%)
M_{d1}	30	15	60	0.1626	1.9092	1.4118	1.9236	1.5700
M_{d2}	30	20	60	0.1659	1.9624	1.4560	1.9772	1.6167
M_{d3}	30	25	60	0.1672	1.9794	1.4709	1.9942	1.6318
M_{d4}	30	30	60	0.1681	1.9924	1.4817	2.0071	1.6427
M_0	30	35	60	0.1686	1.9993	1.4874	2.0140	1.6484
$M_{d\infty}$	30	∞	60	0.1699 ± 0.0018	2.0104 ± 0.0596	1.4973 ± 0.0433	2.0258 ± 0.0584	1.6584 ± 0.0435
				(0.75%)	(0.55%)	(0.66%)	(0.59%)	(0.60%)
M_{t1}	30	35	15	0.1729	2.1041	1.5632	2.1203	1.7351
M_{t2}	30	35	20	0.1716	2.0701	1.5388	2.0857	1.7071
M_{t3}	30	35	30	0.1702	2.0393	1.5167	2.0546	1.6820
M_{t4}	30	35	40	0.1695	2.0231	1.5048	2.0381	1.6686
M_{t5}	30	35	50	0.1690	2.0106	1.4956	2.0255	1.6580
M_0	30	35	60	0.1686	1.9993	1.4874	2.0140	1.6484
$M_{t\infty}$	30	35	∞	0.1660 ± 0.0026	1.9453 ± 0.1067	1.4455 ± 0.0865	1.9594 ± 0.1096	1.6009 ± 0.1021
				(1.57%)	(2.77%)	(2.90%)	(2.79%)	(2.97%)

TABLE 2.3: Results obtained from computations of the two-dimensional flow using various domain sizes. The domain lengths being varied at each stage are indicated by the bolded font. The asymptotic ‘domain independent’ results estimated from the regression model are shown under the M_∞ data rows along with the 95% confidence level limits. The values in the parenthesis are the percentage differences between the results obtained from the M_0 mesh and those estimated for M_∞ .

α	Source	St	\bar{c}_d	c'_l
0°	De & Dalal (2006)	0.1966	1.7607	0.2968
	Wang <i>et al.</i> (2015)	0.196	1.710	0.285
	Present study	0.1946	1.7041	0.2840
60°	Tu <i>et al.</i> (2014)	0.154	2.122	0.742
	Wang <i>et al.</i> (2015)	0.154	2.097	0.733
	Present study	0.1529	2.0550	0.7307

TABLE 2.4: Comparison of the results obtained from the present configuration against those reported in the various cited studies, validating the present mesh and problem set-up.

Zielinska & Wesfreid (1995); De & Dalal (2006); Bao *et al.* (2010); Tu *et al.* (2014); Wang *et al.* (2015), amongst others.

As a conclusion, several additional simulations were performed to validate the mesh, boundary conditions, and the problem set up. Here, attempts to replicate the results published in various studies is made, but using the meshes generated for this project as described in the earlier part of this section. Specifically, the solutions for a flow at $Re = 100$ at cylinder inclinations $\alpha = 0^\circ$ and $\alpha = 60^\circ$ are computed, and the asymptotic solutions obtained are as detailed in table 2.4 which are presented along with results from various studies (as cited) for comparison. The results in table 2.4 compare well with the most recent study by Wang *et al.* (2015), where the results differed by less than 1% except for the drag force coefficient at $\alpha = 60^\circ$. Presumably, the small discrepancies observed arise from restrictions from the different domain sizes used, and the different numerical methods and boundary conditions employed — where the previous studies implemented finite-volume approaches, the current study utilises a high-order spectral-element technique. As will be also be presented later in this thesis, the critical Reynolds number for the transition to a time-periodic flow obtained using the present mesh and set-up for the cylinder inclined at $\alpha = 0^\circ$ is $Re_c = 40.45$, comparing well against the values reported by Zielinska & Wesfreid (1995)—39.6, De & Dalal (2006)—39.9, and Prhashanna *et al.* (2011)—40.4, the minor discrepancies likely arising from the different computational domain sizes employed.

Chapter 3

Two-dimensional flow characteristics

This chapter discusses the results obtained from evolving the two-dimensional Navier–Stokes equations, elucidating the various wake regimes encountered and describing their characteristics. For the two-dimensional framework, the flow is assumed to possess no out-of-plane velocity, $W(\mathbf{x}, t) = 0$, and a spanwise invariance, $\partial \mathbf{Q} / \partial z$, where $\mathbf{Q} = \{\mathbf{U}, P\}$. The upper bound of Reynolds numbers investigated in this chapter extends primarily to $Re = 200$, exceeding this value at times only to test a hypothesised change in the wake regimes. Without knowing *a priori* the transition to three-dimensional flow behind a triangular cylinder, this upper bound of Reynolds numbers is chosen based on knowledge of similar transitions in the wakes of circular and square cylinders. The aim here is to first characterise the various wake regimes and build the parametric space over which the stability analyses will be conducted in the next chapter.

This chapter is structured as follows. First, § 3.1 presents the observations and measurements obtained for flows that saturate to a time-invariant state, exploring the emergence of the steady recirculation region, as well as characteristics of the steady wake affecting the onset of the primary wake instability. In § 3.2, the critical Reynolds numbers of the bifurcation are quantified, and the spatial variations of the vortex street subsequently described. The Strouhal number and force coefficients’ dependence on the cylinder inclination and Reynolds number are then presented and discussed in § 3.3 and § 3.4, respectively. Some of the results in this chapter have been included in Ng *et al.* (2016).

3.1 Steady flow regime

The first of the two-dimensional flow regimes encountered with increasing Reynolds number is the steady flow regime. Here, the flow exhibits a temporal invariance ($\partial\mathbf{U}/\partial t = 0$), and serves as a good starting point for detailing the series of impending bifurcations and transitions in these flows.

3.1.1 Wake characteristics

At low Reynolds numbers increasing from a stationary state ($Re = 0$), the wake is initially that of a boundary layer attached to the cylinder surface, separating as the flow exceeds a threshold Reynolds number which will be referred to as the separation Reynolds number, Re_s . At such low Reynolds numbers, viscous forces in the flow act comparably to inertial forces. Historically, the potential flow solution past a sphere derived by Stokes (1851) and subsequent workers assumed the inertial forces to be negligible, and so its validity lies only at $Re \rightarrow 0$ for real systems. Beyond this, the flow may remain attached to the cylinder despite non-negligible inertial effects from finite small Reynolds numbers before it subsequently separates from the cylinder, as observed by Taneda (1956). Note that the transition from the attached- to separated flow does not incur significant changes in the trends of flow-induced forces on the cylinder (being dominated by the effects of viscous drag, and as such flow reversal along the surface induces little change), the difference only being topologically felt. For the circular cylinder, steady flow separation has been reported to occur at values as low as $Re_s = 6.29$ (Sen *et al.*, 2009), exceeding which a reflection-symmetric pair of eddies form in the cylinder wake. The formation of the steady recirculation region in the wakes of cylinders with a non-reflection-symmetric cross-section however, such as those for the inclined elliptical cylinder (Park *et al.*, 1989; Paul *et al.*, 2014), have been shown to develop differently in that flow separation first manifests through a single steady recirculation vortex instead of the symmetric eddies. The formation of the recirculation region introduces inviscid critical points into the flow streamlines (curiously, while the flow is highly viscous, at these points the viscous contributions cancel — see Perry & Fairlie, 1975 and Perry *et al.*, 1982), the only two which are permissible in this case are the centre and saddle points through the enforcement of continuity. Centres (degenerate focal points) correspond to fixed points in the flow where the trajectory of the fluid element becomes undefined, which for a two-dimensional flow field correspond

approximately to the center of a vortex. Saddle points on the other hand are the hyperbolic fixed points of the flow, and are observed at points where the streamlines or separatrices bifurcate. For steady flows, these critical points remain stationary. These concepts will be useful to help quantify the observations to follow for the steady wakes of the triangular cylinder.

As expected, the wakes of cylinders at reflection symmetric inclinations ($\alpha = 0^\circ$ and 60°) develop similarly to those of the circular cylinder where increasing the Reynolds number of the flow eventually leads to two steady symmetric eddies forming about the cylinder half-plane. It is prudent to clarify here that flow separation observed in these cases still occurred at about the centre of the leeward surface(s) of the cylinder at these symmetric inclinations similar to that for the square cylinder Sen *et al.* (2009). It is conceded that flow separation may also occur at the sharp cylinder vertex edges where the flow faces an intense adverse pressure gradient, and may exhibit even a miniscule separation for any finite Reynolds number; these regions were not observed in the present simulations of the flow. Closer examination of the stages of development of the steady recirculation region in the wake of the symmetrically oriented cylinder shows that the wake of the $\alpha = 60^\circ$ case was the only inclination where symmetric counter-rotating vortices were observed to develop simultaneously from the onset of flow separation — the wake of the $\alpha = 0^\circ$ case showed flow separation to occur through the single eddy scenario found in the wakes of asymmetric cylinder inclinations (which will be described in further detail shortly), but rapidly develops a counter-rotating eddy that is visually symmetrical as expected of the wakes of symmetric cylinder orientations. To address the doubt as to whether this occurrence was due to a lack of resolution, this $\alpha = 0^\circ$ case was recomputed with a higher resolution of $N_p = 13$ (compared to the default $N_p = 8$), the results showing the same lack of symmetry during the forming stages. While this does not definitively rule out a lack of resolution causing this asymmetry, it strongly supports the conclusion that such asymmetric formations can naturally occur in real flows.

The wakes of non-symmetric cylinder inclinations instead show the recirculation region to initiate through a single steady eddy, similar to those observed in Park *et al.* (1989) and Paul *et al.* (2014) for flows past elliptical cylinders, and occurs over the leeward cylinder surface for cylinder inclinations $0^\circ \leq \alpha \leq 30^\circ$, and over the leeward cylinder surface presenting a steeper angle to the uniform flow for cylinder inclina-

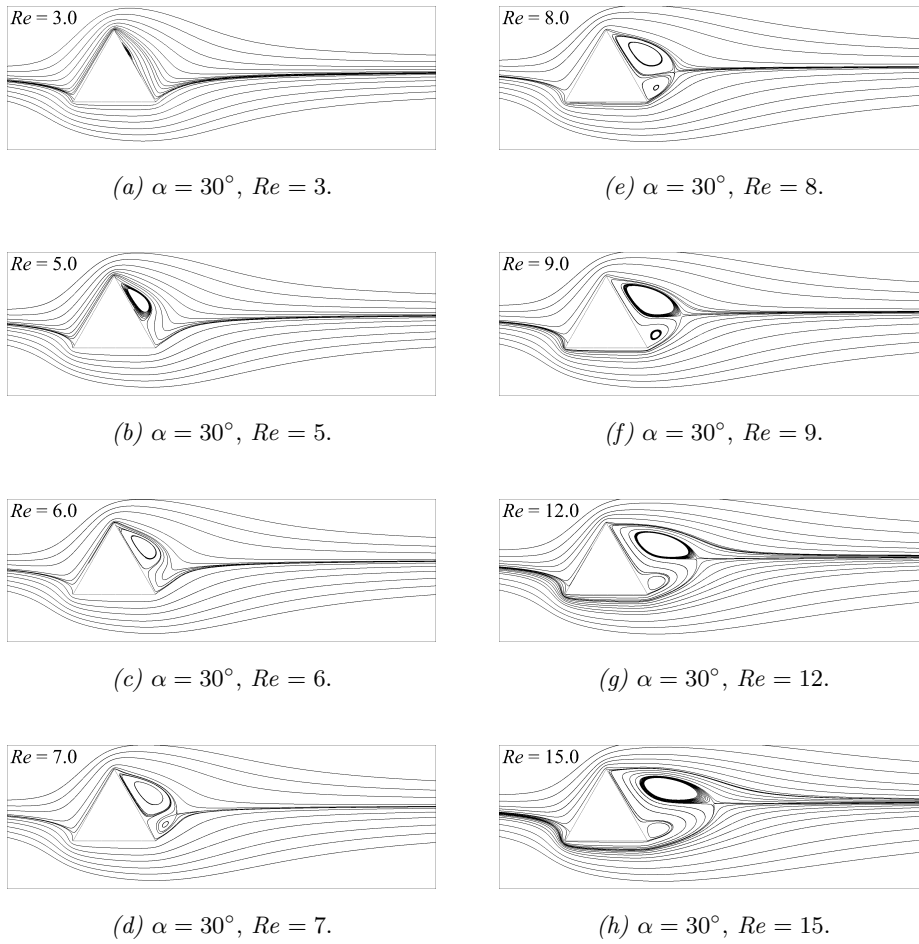


FIGURE 3.1: Streamlines of the separated flow past the cylinder inclined at $\alpha = 30^\circ$ at Reynolds numbers as labelled.

tions $30^\circ < \alpha \leq 60^\circ$ which in this study was always the upper leeward surface. At such low Reynolds numbers, these flows are analogous to the flow on a flat plate and sees flow separation to occur due to an adverse pressure gradient experienced by the attached flow, largely exacerbated by the suction of the fluid in the downstream direction (nonparallel to the surface) due to the bulk flow. The recirculation eddy is then characterised by a region of flow reversal within the boundary layer and, for cylinder inclinations presenting two cylinder surfaces to the downstream flow, a subsequent reattachment to the cylinder surface — the streamlines on the upper leeward cylinder surface reconnects smoothly with the stagnation streamline at the rear vertex of the cylinder. With increasing Reynolds number, this primary recirculation eddy increases in strength until the flow streamlines external to- and about the eddy are sufficiently

deformed to form a cusp-point eventually causing a secondary steady eddy to develop inwards from the cusp towards the cylinder surface. This process is shown in figures 3.1 and 3.2. The ‘closed’ recirculation region appears only over a narrow range of Reynolds numbers, exceeding which the wake develops differently for different ranges of cylinder inclinations. The general scenario is such that the secondary eddy dislodges the primary eddy from the cylinder surface, creating an ‘alleyway’ flow which separates the two eddies. Figure 3.1 elucidates the evolution of this recirculation region for the wake of the cylinder inclined at $\alpha = 30^\circ$ with increasing Reynolds numbers. In the figure, the primary vortex is shown to be present through all images (predicted $Re_s = 2.73$), and that the secondary vortex begins to form only at $6 < Re < 7$. The primary vortex then detaches from the cylinder surface at $Re \approx 8$, initiating the alleyway flow feature. Further increasing the Reynolds number then increases the width of the alleyway flow. This alleyway flow is found to be present in the steady wakes of cylinders lacking a reflective symmetry about the horizontal centreline, not just in the wakes of the triangular cross-section cylinder in this study but also in those for bluff rings (Sheard *et al.*, 2003), square cylinders (Yoon *et al.*, 2010), and elliptical cylinders (Park *et al.*, 1989; Paul *et al.*, 2014). This feature can also be observed in the mean wakes of the flow at higher Reynolds numbers where the flow is unsteady, examples of which are shown in figure 3.10. Therefore, such asymmetric development of the steady wake is expected to be universal in flows past bluff bodies lacking a geometric reflection symmetry to the flow. While for circular cylinders the symmetric recirculation region in the ‘cavity’ flow classically defines the extent of the recirculation, the steady flows past asymmetrically aligned bodies show a mass transfer across the recirculation region of the wake.

The steady recirculation region for the wakes of cylinders inclined at $42^\circ \lesssim \alpha < 60^\circ$ develops differently to the aforementioned scenario. In these cases, the secondary eddy that initially forms at low Reynolds numbers opens up to form an alleyway flow immediately after wedging the primary eddy away from the cylinder surface. The new secondary eddy that eventually establishes itself develops over the underside of the cylinder due to the adverse pressure gradients decelerating the flow. Figure 3.2 elucidates this new scenario for the cylinder inclined at $\alpha = 48^\circ$, where the primary vortex and the initial secondary vortex is shown to have developed by $Re = 10$ and the alleyway flow to have formed from separating the primary vortex away from the cylinder surface by $Re = 15$. Flow separation about the trailing edge of the cylinder is

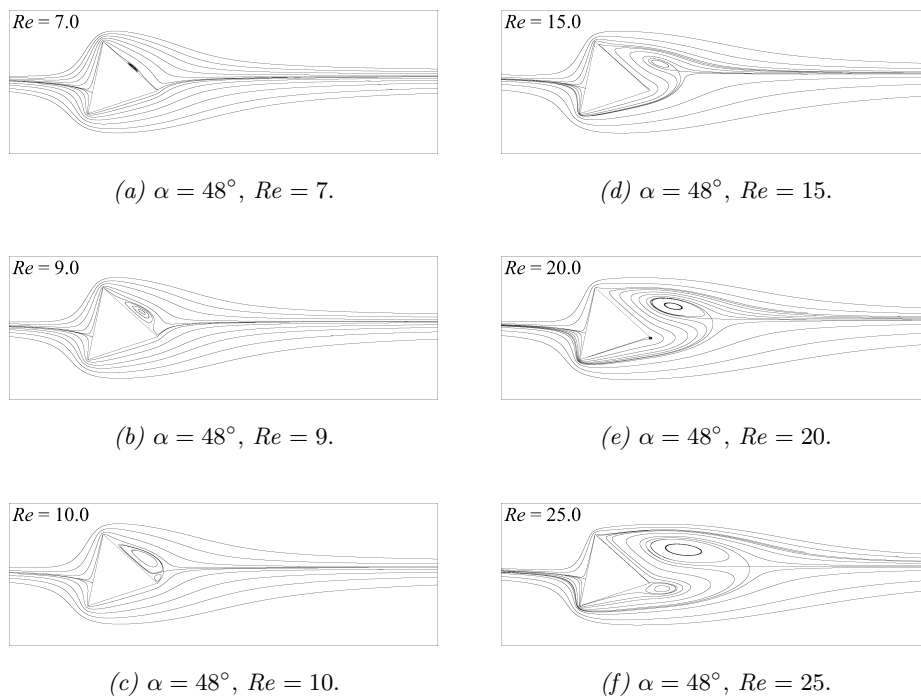


FIGURE 3.2: Streamlines of the separated flow past the cylinder inclined at $\alpha = 48^\circ$ at Reynolds numbers as labelled.

observed at $Re = 20$, with the steady secondary vortex being well observed by $Re = 25$. For either process by which the steady secondary eddy develops, a strong similarity to the starting vortices of aerofoils in establishing the Kutta condition is observed as both the aerofoil and the cylinder here present a sharp trailing edge. The presence of the alleyway flow through all asymmetric cylinder inclinations might find utility in heat exchanger applications where the convective heat transfer could be improved.

To determine the separation Reynolds numbers Re_s for the various cylinder inclinations, flow solutions are obtained for a range of low Reynolds numbers, and the variation in a characteristic length of the steady recirculation region is used to estimate the Reynolds number of its incipience. A common measure for this recirculation length is defined as the streamwise distance between the cylinder surface and the rear stagnation point in the wake, and has been used in Sen *et al.* (2009), Paul *et al.* (2014), amongst others. Unfortunately, this measure is not the most reliable in the present study. The stagnation point in the wakes of the cylinder at non-symmetric inclinations remain attached to the cylinder even after the primary eddy has formed, only growing away from the surface after the secondary eddy forms. This recirculation length

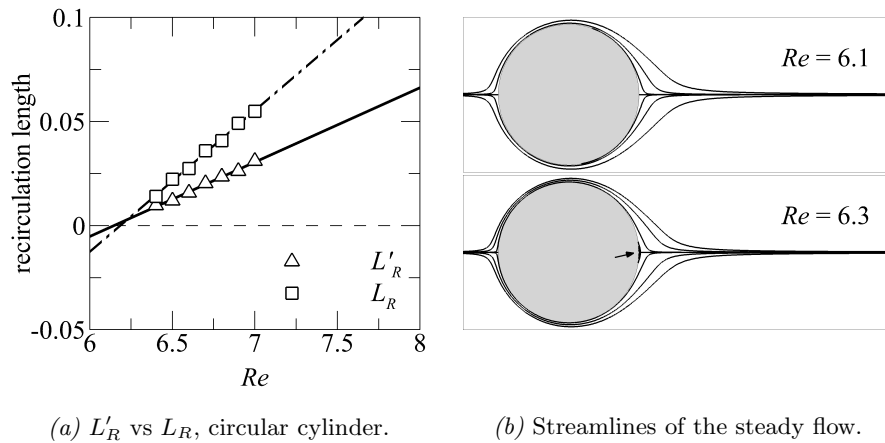


FIGURE 3.3: Prediction of the separation Reynolds number Re_s for flows past a circular cylinder. (a) A comparison of the L'_R (\triangle) and L_R (\square) measures of the length of the steady recirculation region, along with the line of best fit through these data points used for extrapolation. (b) Streamlines of the flow immediately past the cylinder at Reynolds numbers $Re = 6.1$ and $Re = 6.3$ (as labelled in the figure), the latter showing that the recirculation region has formed. The streamlines of the flow at $Re = 6.2$ was not shown here since the length of the recirculation region was too small, having some noise contaminating the streamlines due to a lack of resolution.

measure (denoted as L_R) thus produces a result of $L_R = 0$ up until the secondary eddy forms. As such, a modified length measure is used (denoted as L'_R) to aid in estimating Re_s , measuring the streamwise distance of the center of the primary eddy (corresponding to a center fixed point, $\mathbf{U} = 0$) from the cylinder.

The capacity of this measure in predicting the separation Reynolds number is first tested using the wakes of the circular and inclined elliptical cylinders. For the circular cylinder wake (results shown in figure 3.3), the prediction of the separation Reynolds number from the L_R and L'_R measures were $Re_s = 6.14$ and $Re_s = 6.18$, respectively, the difference here likely being resolution dependent (both values here also comparing well against the value of $Re_s = 6.29$ reported in Sen *et al.*, 2009). For the elliptical cylinder test case, a cylinder geometry with an aspect ratio of 0.8 inclined at 60° clockwise about the downstream flow direction was chosen owing to its lack of a geometric symmetry about the flow centreplane while still possessing a continuous surface for the flow to separate from as opposed to the sharp vertices the triangular cylinder presents to the flow. The onset of flow separation observed here develops through the single eddy as expected, with the L_R and L'_R measures predicting separation Reynolds numbers of

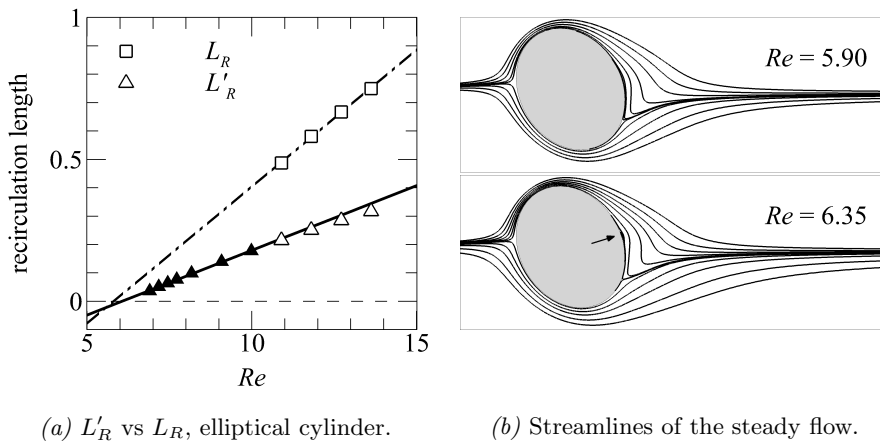


FIGURE 3.4: Prediction of the separation Reynolds number Re_s for flows past an elliptical cylinder of aspect ratio 0.8 with its major axis inclined at 60° clockwise from the horizontal. (a) A comparison of the L'_R (\triangle) and L_R (\square) measures of the length of the steady recirculation region, along with the line of best fit through these data points used for extrapolation. Solid data markers indicate that only a single steady vortex was observed in the streamlines, while the hollow data markers indicate that two steady eddies can be observed (not necessarily symmetric). (b) Streamlines of the flow immediately past the cylinder at Reynolds numbers $Re = 5.90$ and $Re = 6.35$ (as labelled in the figure), the latter clearly showing the recirculation region.

$Re_s = 5.80$ and $Re_s = 6.06$, respectively, as shown in figure 3.4. This shows that the estimate based on the modified length measure is within 4.5% of the conventional L_R measure. The L'_R measure, however, is shown to depart from the initial linear fit corresponding to the single bubble case upon the formation of the secondary bubble, and a linear fit through the points for the secondary bubble results in a predicted separation Reynolds number of $Re_s = 6.14$. The flow field was ultimately used to determine the most accurate of these measures — streamlines of the flow at $Re = 5.90$ shows no observable flow separation thus invalidating the L_R measure, while the flow at $Re = 6.35$ shows a single separation bubble formed at the leeward surface of the elliptical cylinder.

Having established the reliability of the modified length measure in predicting the separation Reynolds number, the next stage of this study is then to determine the corresponding values for the inclined triangular cylinder. An example of an L'_R against Re plot used to determine the separation Reynolds number is shown in figure 3.5(a), demonstrating the almost perfectly linear dependence of the two parameters close to

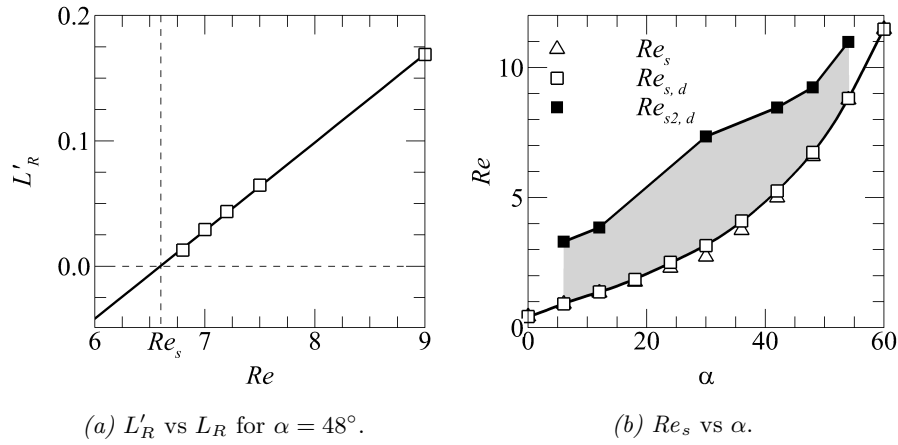


FIGURE 3.5: (a) Plot of L'_R against Re for the cylinder inclined at $\alpha = 48^\circ$. The solid line shows the linear function fitted to predict the separation Reynolds number Re_s . (b) Map of the separation Reynolds numbers, Re_s , scaled by the cylinder side length d (\square) and by the project height of the cylinder h (\triangle) as the incidence angle α of the cylinder is varied. The solid line through the data of $Re_{s,d}$ is described by equation (3.1). The $Re_{s2,d}$ points (\blacksquare) approximates the Re_d where the secondary vortex can initially be observed.

the onset of flow separation. Figure 3.5(b) summarises the separation Reynolds number for the various cylinder inclinations considered, showing that Re_s increases monotonically with α . An estimation of the Reynolds number at which the secondary vortex develops (made based on visualisation of the flow field) is mapped for several intermediate cylinder inclinations as also shown in figure 3.5(b). These Reynolds numbers for the emergence of the secondary eddy in the wakes of symmetric cylinder inclinations at $\alpha = 0^\circ$ and 60° were not determined as the former develops a symmetric wake rapidly past the initial separation while the latter inclination shows the flow separation scenario to occur through a symmetric pair of eddies at its onset; the separation Reynolds number Re_s and those for the emergence of the secondary eddy thus being approximately equal, if not equal. Intuitively, the increasing resistance to flow separation (and hence higher Re_s values) for increasing α was expected — the rear faces of the cylinder become less steeply inclined, leading to smaller impulsive decelerations and momentum losses in the flow around the sharp corner and thus also a smaller pressure drop. Increasing the Reynolds number past the onset of flow separation, the separation points on the cylinder were observed to move from its point of inception towards the vertices of the cylinder edge where it then remains fixed for any higher Reynolds number. In-

terestingly, the gradient of the Re_s data for increasing α is non-zero at both $\alpha = 0^\circ$ and 60° , despite the incidence angle smoothly continuing both to $\alpha < 0^\circ$ and $\alpha > 60^\circ$ for redundant inclinations already captured within $0^\circ \leq \alpha \leq 60^\circ$. Specifically, $\alpha = -1^\circ$ is simply a reflection of $\alpha = 1^\circ$ about the horizontal wake centreplane, and likewise $\alpha = 61^\circ$ is a reflection of $\alpha = 59^\circ$. Hence over a full 360° range of rotations, Re_s is a non-smooth continuous function of α with differentiability class C^0 , with discontinuous gradients every 60° (or when a triangle vertex points directly upstream or downstream) despite the D_3 dihedral group (symmetry) of the cross-sectional geometry.

$$Re_{s,d}(\alpha) = \sum_{k=0}^4 a_k \alpha^k. \quad (3.1)$$

a_0	4.45573×10^{-1}		
a_1	7.26661×10^{-2}	SSE	8.32771
a_2	4.75047×10^{-4}	R^2	0.99949
a_3	-1.29131×10^{-5}	\overline{R}^2	0.99915
a_4	5.97814×10^{-7}		

TABLE 3.1: Coefficients of the polynomial regression function in equation (3.1) shown on the left, and the goodness-of-fit statistics of the fitted function. SSE is the sum of squared error, R^2 is the coefficient of determination of the fit, and \overline{R}^2 is the modified coefficient of determination. The cylinder inclination α is taken in units of degrees ($^\circ$) as opposed to radians for niceness of the numbers.

The monotonic increase in the separation Reynolds numbers with increasing cylinder inclination indicates that a functional relationship may exist, for which a suitable expression is sought. As observed in figure 3.5(b), the data obtained for the separation Reynolds numbers re-scaled by the cylinder side length d , $Re_{s,d}$, shows a smoother variation than the values scaled by the projected area of the cylinder h particularly at intermediate cylinder inclinations of about $\alpha = 30^\circ$. A polynomial function was thus fitted to the $Re_{s,d}$ data to describe this trend, and is presented as equation (3.1), with the corresponding coefficients and goodness-of-fit statistics shown in table 3.1.

Several prior studies on the circular cylinder wake have shown that the size of the computational domain affects the reliability of the results when modelling unconfined flows, particularly on the evaluation of the force coefficients (Lange *et al.*, 1998; Kumar & Mittal, 2006; Posdziech & Grundmann, 2007; Sen *et al.*, 2009). In those studies, it was noted that the results appear to be increasingly affected at lower Reynolds numbers for a given computational domain. It then becomes essential to obtain an

α	M_0	DS_1	DS_2	DS_3
0°	0.434 (1.14%)	0.436 (0.68%)	0.438 (0.23%)	0.439
60°	11.503 (0.53%)	11.544 (0.17%)	11.560 (0.04%)	11.564

TABLE 3.2: Values of the separation Reynolds numbers, Re_s , with increasing computational domain sizes. The results for M_0 are for the default domain size used as reported in figure 3.5. The values in the parentheses quantify the percentage difference of the values relative to the results for DS_3 .

estimate of the domain truncation related uncertainties for the results of Re_s reported here. While the domain dependence study in § 2.5 has quantified the associated errors using a test case of $Re = 200$, the domain study here focused on the steady flow regime and bears importance to the credibility of the results in this section. Similar to Posdziech & Grundmann (2007), the initial mesh resolution was retained while the extent of the computational domain was increased by adding additional elements around it to reach the desired domain length. Three square computational domains of sizes $DS_1 = (100h)^2$, $DS_2 = (200h)^2$, and $DS_3 = (300h)^2$ were used to predict the separation Reynolds numbers of the flow past the cylinder at inclinations $\alpha = 0^\circ$ and 60° , the cylinder being centrally placed in each case. These two cylinder inclinations were chosen as they both possess the lowest and highest separation Reynolds numbers amongst the various cylinder inclinations tested. The uncertainties of each case quantified relative to the results of Re_s for DS_3 (shown in table 3.2) show little variation in the Re_s values predicted, being 1.14% at worst.

3.2 Unsteady flows

Most flows in the real world naturally possess some degree of unsteadiness or time-dependence. The following section aims to first identify the Reynolds number threshold of the two-dimensional steady- to unsteady flow transition, and then to demonstrate that the classical Kármán vortex street seen initially subsequently re-arranges itself to produce a visually different wake indicating that the Kármán vortex street arrangement of the two-dimensional flow may be is unstable at higher Reynolds numbers. Here, the characteristics of the various wake regimes are described, the variation of the vortex

shedding frequency with increasing Reynolds numbers elucidated, and the flow-induced forces on the cylinder by the two-dimensional flow quantified.

3.2.1 Transition to periodic flow

The first instability in the flow occurs at a critical Reynolds number (Re_c) above which the wake becomes oscillatory. From a dynamical systems standpoint, this instability occurs through a Hopf bifurcation of the steady base flow, and the evolution of the equivalent instability near its threshold in other bluff body wakes has been shown to be well-described by the Stuart–Landau equation (Mathis *et al.*, 1984; Provansal *et al.*, 1987; Sreenivasan *et al.*, 1987; Sohankar, 2007; Sheard *et al.*, 2004; Paul *et al.*, 2014). This equation models the amplitude evolution of a perturbation as described in the methodology chapter in § 2.3.4. To recap, the amplitude evolution equation is given as

$$\frac{d\Lambda}{dt} = (\sigma + i\omega) \Lambda - l(1 + ic) |\Lambda|^2 \Lambda + \mathcal{O}(\Lambda^5),$$

where Λ is the complex amplitude ($\Lambda = |\Lambda| \exp(i\phi)$), $|\Lambda|$ is the magnitude of the signal, ϕ the instantaneous phase of the signal, σ is the linear growth rate of the perturbation, l and c are real coefficients describing the nonlinear departure of the mode evolution from the linear regime, and ω the angular frequency of the signal in the linear regime. Retaining terms of $\mathcal{O}(|\Lambda|^3)$ and separating the equation into its real and imaginary components results in the equations

$$\begin{aligned} \frac{d \log |\Lambda|}{dt} &= \sigma - l|\Lambda|^2, \\ \frac{d\phi}{dt} &= \omega - lc|\Lambda|^2. \end{aligned} \quad (3.2)$$

The transition is thus supercritical if the l coefficient is positive and is an indicator of non-hysteretic transition behaviour, and subcritical if the l coefficient is negative which indicates the propensity of the transition to be hysteretic. A simple approach to predict the l coefficient for a given flow system is through the mode amplitude evolution equation (3.2), where a plot of $d \log |\Lambda|/dt$ against the square of the signal amplitude ($|\Lambda|^2$) yields the l coefficient as the negative of the linear gradient near the transition indicated by the axis intercept $|\Lambda|^2 = 0$. Likewise, the axis intercept of the linear function as $|\Lambda|^2 \rightarrow 0$ yields the linear growth rate of the disturbance (σ). The critical Reynolds number of the bifurcation (Re_c) can then be predicted through extrapolation to $\sigma = 0$ from analysis of several Reynolds numbers. This process is then repeated for each cylinder inclination.

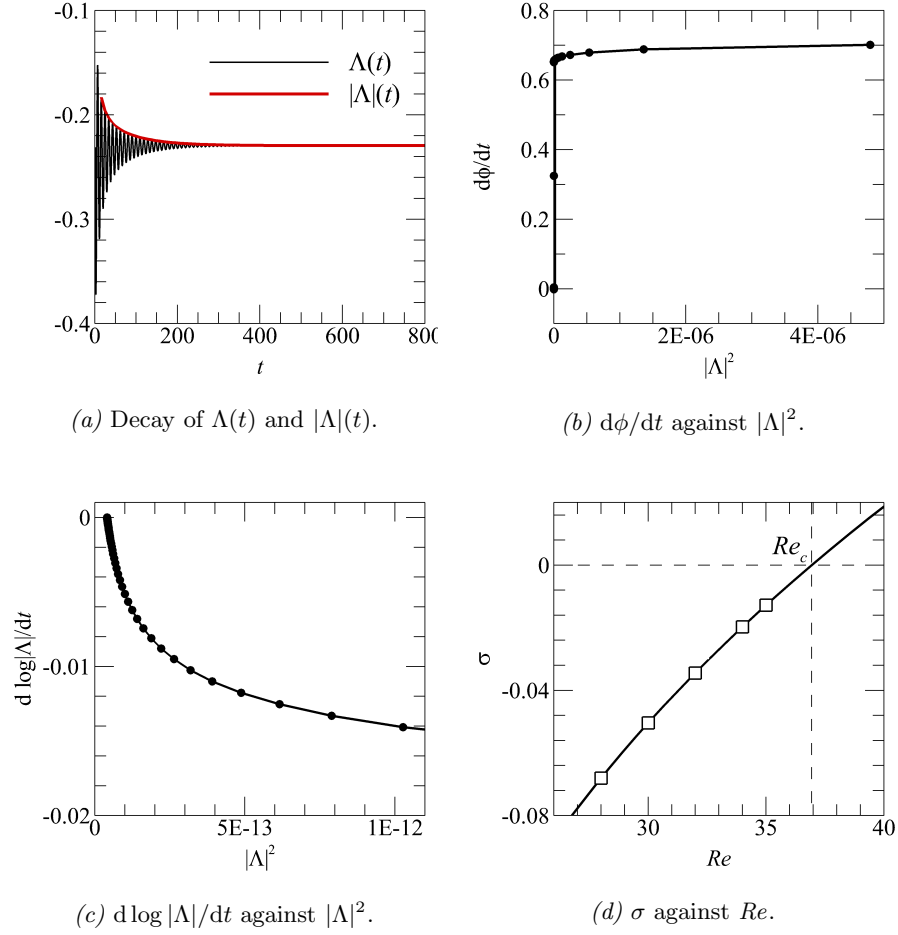


FIGURE 3.6: Typical plots of (a) the oscillatory lift force signal and the complex mode amplitude ($\Lambda(t)$, black line, and $|\Lambda|(t)$, red line), with time $t = 0$ corresponding to the instant the Reynolds number is impulsively reduced, (b) the rate at which the instantaneous phase evolves as the mode saturates ($d\phi/dt$ against $|\Lambda|^2$), (c) the rate of change of the mode amplitude near the bifurcation ($d \log |\Lambda|/dt$ against $|\Lambda|^2$), and (d) the linear growth rate of the perturbation against Reynolds numbers. In (b–c), the solid lines describe the fitted linear functions shown in equation (3.2), and in (d) the solid line represents the fitted inverse polynomial function while the thin dotted lines locate the zero growth rate threshold for the onset of the instability. The data points used for the extrapolation in (d) are indicated with square markers (\square). The data in these plots were obtained from wake of the cylinder inclined at $\alpha = 48^\circ$.

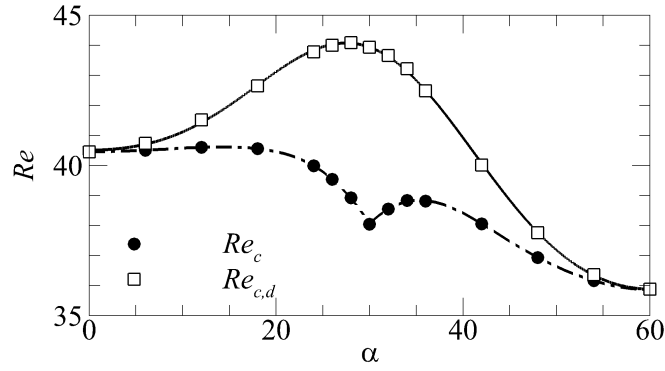


FIGURE 3.7: Plot of the critical Reynolds numbers scaled by the projected frontal height h (\bullet), and by the cylinder side length d (\square) as a function of the cylinder inclination. The solid line is described by the fitted Fourier function (equation 3.3), and the dash-dotted line describes equation (3.3) re-scaled by the projected frontal height h .

The approach taken for this analysis was to impulsively step the Reynolds number down to decay a time-periodic base flow and measure the resulting oscillatory response through the lift force exerted on the cylinder (Provansal *et al.*, 1987; Thompson & Le Gal, 2004). Base flow solutions at a Reynolds number of $Re = 50$ were used for all cylinder inclinations considering the critical Reynolds numbers were not known *a priori*. The truncation of any expansion function like those in equation (3.2) places a restriction on the range of values over which the truncated model is reliable. For all cases, the lower Reynolds number which the base flows were decayed to were confined within $0 < Re_c - Re \leq 10$ to aid with the validity of the analysis. An example of the results from this analysis is shown in figure 3.6. In all cases, the data obtained for the growth rates at various Reynolds numbers were not precisely linearly related as found in previous studies (Provansal *et al.*, 1987; Sreenivasan *et al.*, 1987), and as such inverse polynomial functions were fitted to the data to facilitate a more accurate extrapolation to zero growth rate corresponding to the critical Reynolds number. The l coefficients obtained through the least-squares regression were always positive demonstrating the supercritical nature of the bifurcation consistent with the wake of the circular cylinder as shown in Provansal *et al.* (1987) and Sreenivasan *et al.* (1987), amongst others.

The variation of the critical Reynolds numbers predicted with increasing cylinder inclination is summarised in figure 3.7. For the cylinder inclined at $\alpha = 0^\circ$, the critical Reynolds number was predicted to be $Re_c = 40.45$, comparing well against previously published values of 39.9 (De & Dalal, 2006), 39.6 (Zielinska & Wesfreid, 1995), and

approximately 40.4 (Prhashanna *et al.*, 2011), once again validating the computational setup. A discontinuity in the gradient of the $Re_c - \alpha$ plot was observed at $\alpha = 30^\circ$ corresponding to when the triangle vertex points vertically upward. This discontinuity arises from the $|\alpha - 30^\circ|$ term in the h/d relation described in equation (2.38). No such discontinuity was observed when the critical Reynolds number was re-scaled by the cylinder side length d as $Re_{c,d}$. This smoothness of the function, combined with the property that the data over $60^\circ \leq \alpha \leq 120^\circ$ will be a reflection of the data over $0^\circ \leq \alpha \leq 60^\circ$ invites the use of a Fourier series to describe the data. The fitted function is shown in equation (3.3) with its corresponding coefficients and goodness-of-fit statistics presented in table 3.3. The fitted function (3.3) recovers the original data to within 0.2% of the measured $Re_{c,d}$ values. The function describing the $Re_c - \alpha$ data can then be obtained by multiplying the fitted equation (3.3) with the h/d equation (2.38).

$$Re_{c,d} = \sum_{k=0}^4 a_k \cos\left(\frac{k\pi\alpha}{60^\circ}\right) \quad (3.3)$$

a_0	4.07437×10^1		
a_1	2.27251×10^0	SSE	0.02939
a_2	-2.86780×10^0	R^2	0.99973
a_3	3.90843×10^{-2}	χ^2	0.02939
a_4	3.22403×10^{-1}		

TABLE 3.3: Coefficients of the fitted function in equation (3.3) shown on the left, and the goodness-of-fit statistics of the fitted function on the right. SSE is the sum of squared error, R^2 is the coefficient of determination of the fit, and χ^2 is the standard chi-square goodness of fit test value. The cylinder inclination α is taken in units of degrees ($^\circ$) as opposed to radians for niceness of the numbers.

Several observations of the precritical steady flows are made to explain the trends of the critical Reynolds number in figure 3.7. Here, the steady flow solutions considered are those at $Re = 35$; further increases in the Reynolds number below Re_c changes only the length of the recirculation region without introducing any new features in the steady flow. In the case of the critical Reynolds numbers scaled by the cylinder side length d ($Re_{c,d}$), the instability is observed to be delayed the most when the cylinder is inclined at $\alpha \approx 28^\circ$, and is most susceptible in the flow when the cylinder is inclined at $\alpha = 60^\circ$. This is due to the projected height of the cylinder h being smallest about a cylinder inclination of $\alpha = 30^\circ$ compared to the other cylinder inclinations, thus causing the flow past the cylinder inclined at $\alpha \approx 30^\circ$ to apparently be more stable as it is a

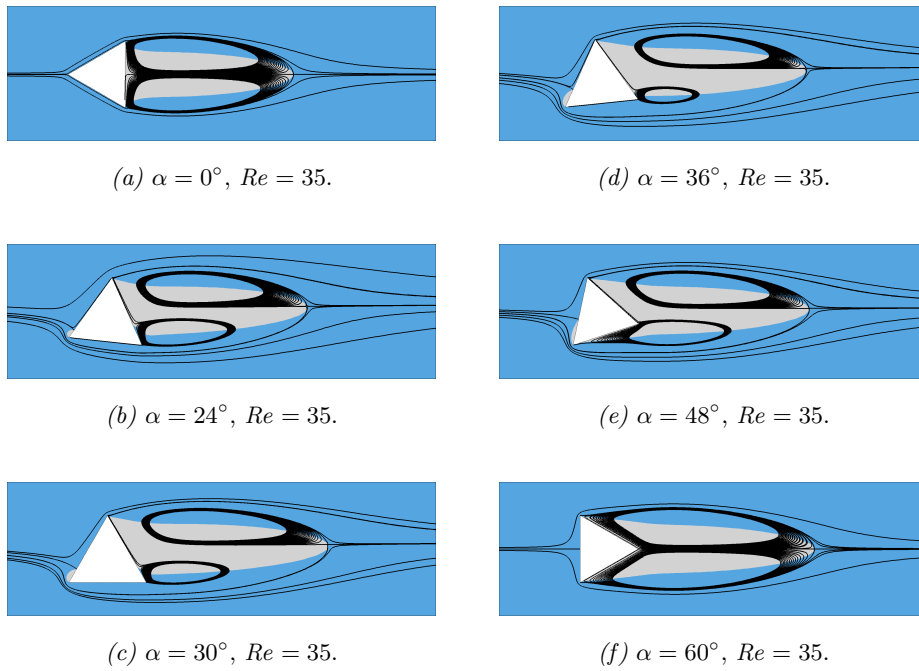


FIGURE 3.8: Streamlines and streamwise velocity contours of the steady flow at $Re = 35$ for cylinder inclinations as labelled. The light blue and grey regions denote negative and positive streamwise velocities, respectively.

‘smaller’ geometry. The Re_c curve, however, alludes to more complex dynamics within the range of cylinder inclinations. The following explanations are elucidated through figure 3.8. Over $0^\circ \leq \alpha \lesssim 18^\circ$, Re_c is observed to be almost independent of the cylinder inclination, with Re_c hovering about a value of $Re_c = 41 \pm 1.5$. Between cylinder inclinations $18^\circ \lesssim \alpha \leq 30^\circ$, the Re_c decreases rapidly, reaching a locally minimum value of $Re_c \approx 38$ at $\alpha = 30^\circ$. Over both these inclination ranges, the cylinder presents a single leeward surface to the flow. Observations of the pre-critical flows at $Re = 35$ for these cylinder inclinations show the recirculation region forming only over this single side, limiting the width of the steady recirculation region produced (and thus also its length), justifying the similar critical Reynolds numbers predicted for the flows past the cylinder at inclinations $0^\circ \leq \alpha \lesssim 18^\circ$. The drop in the critical Reynolds numbers for the cylinder inclined at $18^\circ \lesssim \alpha \leq 30^\circ$ is caused by the inception of a small negative streamwise velocity bubble on the steeper leading edge of the cylinder which acts as a disturbance to the impinging flow making these cases more susceptible to instability (see figure 3.8*b,c*). Over cylinder inclinations $30^\circ < \alpha \leq 60^\circ$, the cylinder presents

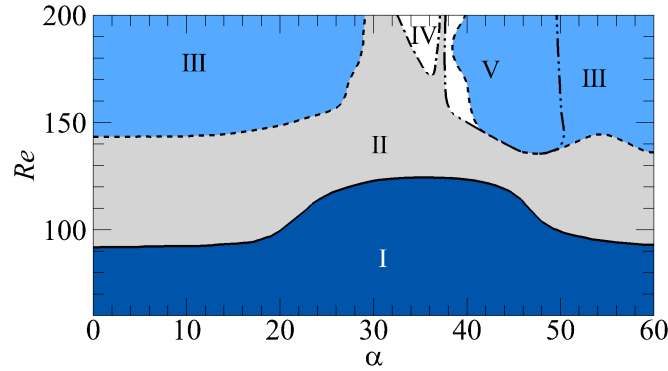


FIGURE 3.9: Map of the different vortex streets exhibited by the unsteady flow. Regime (I) is the Kármán vortex street, (II) is the bilayered wake arrangement, (III) bounded by the dotted lines correspond to the secondary vortex street, (IV) bounded by the dash-dotted line is the 2P mode, and (V) bounded by the dash-double-dotted line is the P+S mode.

two leeward surfaces to the downstream flow, and the trend of the critical Reynolds number exhibits a small local maximum at $\alpha \approx 34^\circ$. The difference in the flow on either side of this maximum is that over cylinder inclinations $30^\circ < \alpha \lesssim 34^\circ$, the recirculation region develops over only a single leeward surface of the cylinder, while those at cylinder inclinations $34^\circ \lesssim \alpha \leq 60^\circ$ develop over both leeward surfaces (see figure 3.8*d-f*). The wakes observed in the former range of inclinations are thus restricted to a smaller width compared to the latter range of inclinations whose wakes expand over both downstream facing cylinder surfaces, and hence a similar argument can be made that the effective wake Reynolds number for the $30^\circ < \alpha \lesssim 34^\circ$ cylinder inclination range is less than those for $\alpha \gtrsim 34^\circ$.

3.2.2 Variations of the two-dimensional vortex street

The instability whose onset was the focus of the previous section breaks the temporal invariance of the flow, and with sufficient increase in the Reynolds number, the classical Kármán vortex street comprising a dual row of alternately shed counter-rotating vortices can be observed. The vortex street can also subsequently re-arrange itself into a ‘new Kármán street’ of a larger dimension than that of the primary one (Taneda, 1956, 1959), indicating the propensity for various re-arrangements of the vortex street. The aim of this section is to elucidate and characterise as much as possible the variations in the vortex street encountered in the unsteady two-dimensional flows past the inclined triangular cylinder. To begin, a regime map delineating the $Re - \alpha$ regions

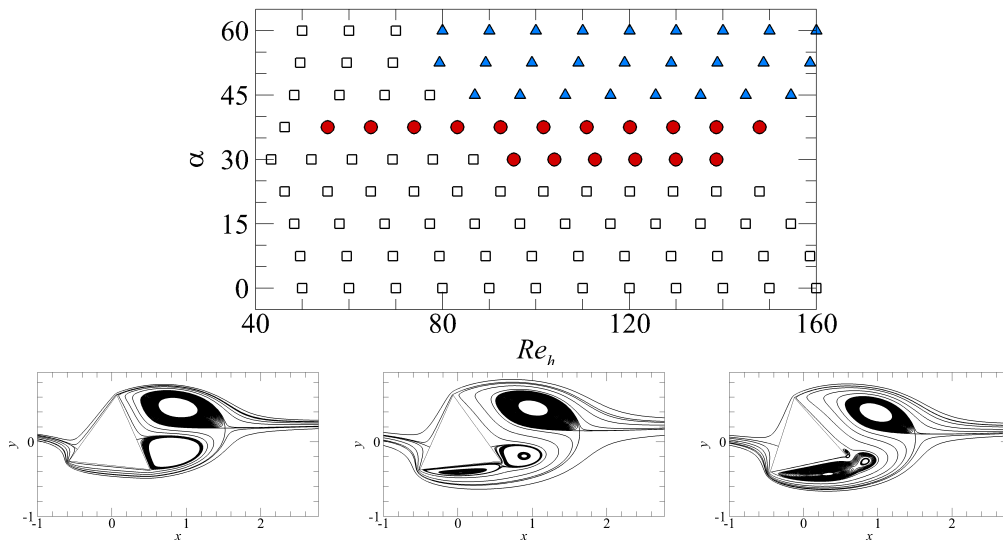


FIGURE 3.10: (*top*) Map of the vortex shedding topology in flows past the triangular cylinder reproduced from Tu *et al.* (2014) with permission from Elsevier. The values of α from the original plot have been altered to be consistent with the definition used in this thesis, and the Reynolds numbers rescaled from a length scale of d to h . The black square markers (\square) represent the main separation pattern (MS), red circles (\bullet) for the single secondary vortex (SSV) subpattern, and blue triangles (\blacktriangle) for the vortex merging pattern (VM). (*bottom*) Streamlines of the time-averaged flow showing the MS-, SSV-, and VM patterns from left to right. The flows in each panel corresponds to cylinder inclinations of $\alpha = 24^\circ$, 36° , and 42° , respectively, all at $Re = 100$.

where the different vortex street patterns were observed is presented in figure 3.9.

Tu *et al.* (2014) showed that the vortex shedding process in the wakes of inclined triangular cylinders can be characterised by its near wake topology as either of a main separation pattern (MS), a single secondary vortex sub-pattern (SSV), or a vortex merging pattern (VM), each of which occur over various ranges of cylinder inclinations. Their $Re - \alpha$ parameter space mapping these patterns are reproduced in figure 3.10, rescaling the Reynolds numbers using a length scale of h to remain consistent with those used in this study. The MS pattern (described in Yoon *et al.*, 2010) is the generic case for when the recirculation region of the time-averaged flow develops over the whole leeward surface(s) of the cylinder (or at least most of it), and possesses a primary recirculation region in the time averaged flow comprising two eddies. The SSV subpattern occurs when the flow separates from the windward edges of the cylinder but reattaches along an adjacent cylinder surface before separating again to form the shedding vortex. The region between the flow separation point at the windward edge of the cylinder and the

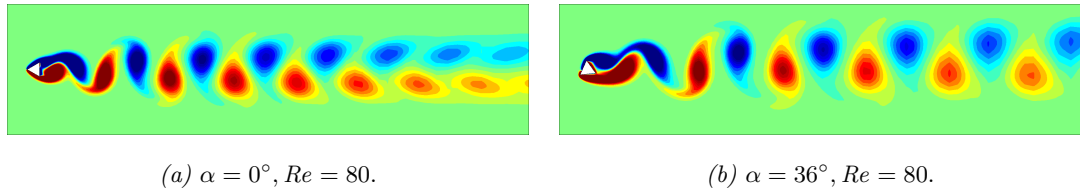


FIGURE 3.11: The Kármán vortex street in the wake of the cylinder at symmetric and asymmetric inclinations as labelled. Blue and red contours denote negative and positive vorticity values, respectively.

reattachment point forms the ‘secondary vortex’ in the mean flow characteristic of this pattern. The VM pattern is observed in flows where separate vortices form on each of the adjacent leeward cylinder surfaces which then merge to form the shedding vortex. Coincidentally, the range of cylinder inclinations where the SSV- and VM patterns can be observed is similar to that where complex regimes IV and V were found in this study (figure 3.9), broadly implying that the shedding topologies and the vortex street patterns are related. This will be discussed further in § 3.3 in relation to the shedding frequencies in the unsteady wake.

Regime I: The Kármán vortex street

Regime I corresponds to the classical Kármán vortex street, examples of which are shown in figure 3.11. Characteristic to this regime is the dual row of alternately shed counter-rotating vortices which decay as they advect downstream carried by the bulk flow. The flows in this regime are also periodic with a shedding period of T . This regime was observed for all cylinder inclinations at moderate Reynolds numbers, extending from the critical Reynolds number of the first instability to approximately $80 \lesssim Re \lesssim 90$ at a low cylinder inclination of $\alpha = 0^\circ$, a maximum of about $Re \approx 120$ when the cylinder is inclined at $\alpha \approx 30^\circ$, and to $90 \lesssim Re \lesssim 100$ approaching $\alpha = 60^\circ$. The threshold delineating regimes I and II presented in figure 3.9 is only approximate to within Reynolds numbers of ± 10 and was not resolved further as the onset of regime II can vary spatially (approaching the cylinder with increasing Reynolds number), and displays no distinct change specifying its onset. The purpose of introducing this threshold is to inform future studies that such a spatial transition may occur. The periodic nature of the flow in regime I is demonstrated through figure 3.12, where a fast Fourier transform (FFT) of the transverse velocity along the domain centreplane

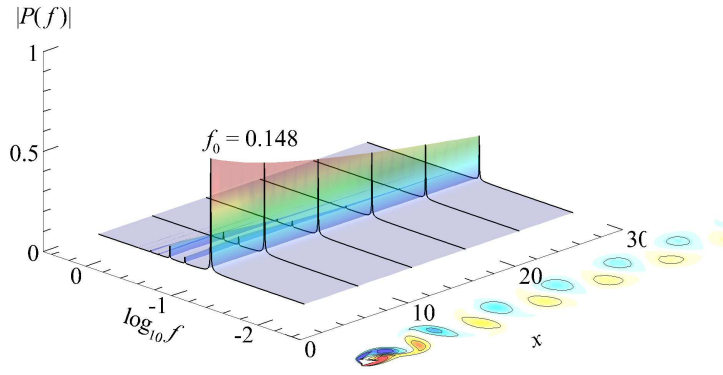


FIGURE 3.12: Fast Fourier transform of the transverse velocity signal taken at multiple downstream positions x at $y = 0$. The surface colour ranges from blue to green and to red for low (set as 0 here) to high spectral amplitude values. This plot demonstrates the dominance of the fundamental frequency f_0 in the wake throughout the domain, characteristic of the frequency responses expected of regime I. The flow used in this example corresponds to a cylinder inclination of $\alpha = 30^\circ$ at a Reynolds number of $Re = 80$.

($y = 0$) exhibits a single dominant spectral peak at the Strouhal frequency of the flow (the remaining peaks being harmonics of the fundamental frequency).

As it is in the wakes of the circular cylinder (for example, Marques *et al.*, 2004), the time-dependent solutions of the wakes of the cylinder at geometrically symmetric inclinations possess the spatiotemporal symmetry

$$\begin{aligned}
 U(x, y, t) &= U\left(x, -y, t + \frac{T}{2}\right) = U(x, y, t + T), \\
 V(x, y, t) &= -V\left(x, -y, t + \frac{T}{2}\right) = V(x, y, t + T),
 \end{aligned}$$

where a temporal translation by a half period of the flow and a reflection about the centreplane recovers the original solution (half-period-flip). The wakes of the cylinder at inclinations geometrically asymmetric to the wake centreplane instead shows that the vortex street drifts at a slight inclination in the near wake, and so its solution deviates slightly from this half-period-flip map.

Regime II: Decay or re-arrangement to a dual layer wake

Following from the previous regime, vortices comprising the Kármán vortex street are subject to vorticity diffusion amongst other processes leading to the decay of the vortex street. In some cases, this ultimately forms an almost time-invariant parallel shear layer structure far downstream, or at least re-arranges into two separate layers, each through

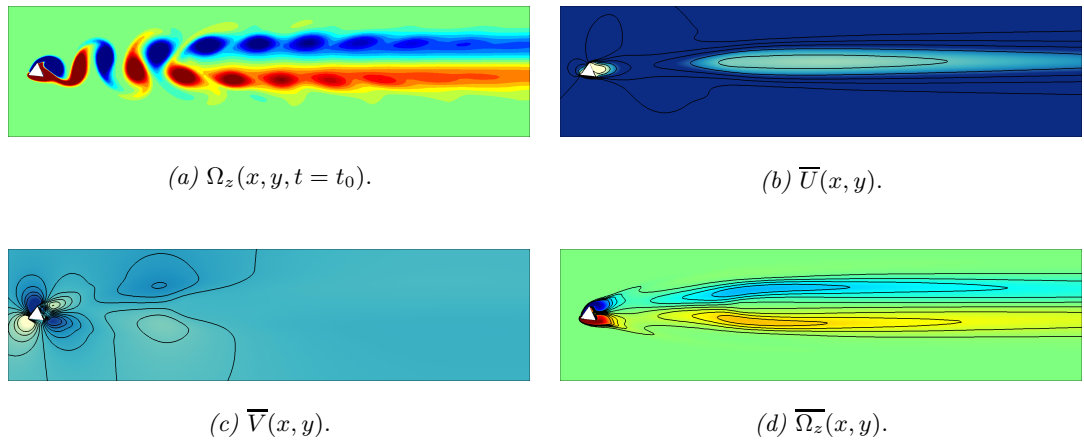


FIGURE 3.13: Visualisation of the dual layer wake, shown for the cylinder inclined at $\alpha = 24^\circ$ at a Reynolds number of $Re = 140$. In (a), the vortices are shown to have diffused sufficiently to an almost parallel shear layer. Panels (b–d) are the time-averaged U - and V -velocity fields (\bar{U}, \bar{V}) and the time-averaged vorticity field ($\bar{\Omega}_z$), respectively. Blue and red contours in plots of vorticity denote negative and positive vorticity values, respectively, while the light to dark coloured contours in plots of velocity denote low to high (or negative to positive) velocity values, respectively.

which like-signed vortices traverse. The regions of the $Re - \alpha$ space where this dual layer wake may be observed is presented in figure 3.9 as regime II, and an example of the wake in this regime is shown in figure 3.13. Experimental visualisations of this regime (usually termed the ‘vortex street breakdown’) can also be found in Taneda (1959), Zdravkovich (1969), and Cimbalá *et al.* (1988) for the circular cylinder, and also recently in Kim (2019). Durgin & Karlsson (1971) showed that the (longitudinal-to-latitudinal) vortex spacing ratio (h/a) plays a crucial role in the evolution of the vortex street comprising an array of small but finite sized vortices. Their calculations showed that exceeding a critical value of $h/a = 0.366$, the initially circular vortices strain into an elliptical form and begin to rotate about their axes where they can then be unstable to further secondary motions from the induced velocities. This spacing ratio is different to the value of $h/a = 0.281$ derived by von Kármán (1911) in his inviscid analysis of vortex street stability. Indeed, this vortex spacing ratio increases when subjected to viscous effects present in a real flow as demonstrated by Hooker (1936). Further works by Dynnikova *et al.* (2016) reconciled the existing data from Saffman & Schatzman (1982) and von Kármán (1911) by showing that the vortex street breakdown occurs within a region of vortex clustering or high dipole moment density whose wave velocity mismatch

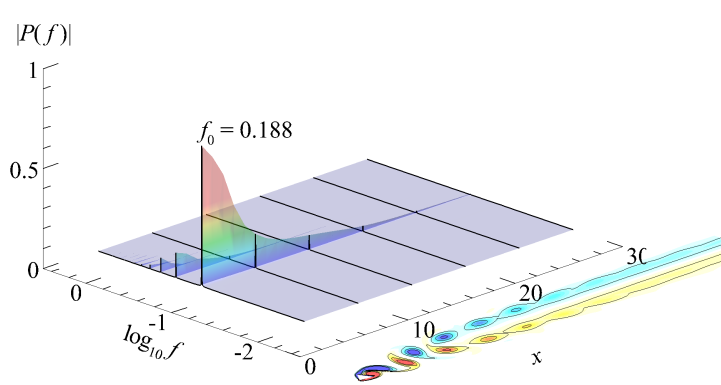


FIGURE 3.14: Fast Fourier transform of the transverse velocity signal taken at multiple downstream positions x at $y = 0$. The surface colour ranges from blue to green and to red for low (set as 0 here) to high spectral amplitude values. This plot shows the fundamental frequency f_0 to be dominant only in the near wake, but decays rapidly to an almost negligible state along the centreline in the far wake. This is characteristic of the frequency response of regime II. The flow used in this example corresponds to a cylinder inclination of $\alpha = 24^\circ$ at a Reynolds number of $Re = 150$.

with the vortex street advection speed induces a rearrangement of the vortex street. The formation of such vortex clusters likely originate from perturbations induced from the shedding process which in turn leads to the elliptical vortex deformation scenario described by Durgin & Karlsson. In all cases, the transition was modelled through an inviscid analysis of finite sized vortex arrangements, incorporating only the vorticity diffusion and ‘vortex aging’ mechanism derived through the viscid nature of the flow.

As pointed out in multiple previous studies, this vortex street breakdown develops spatially, and as such the delineation between the Kármán vortex street and this regime was only approximate — the spatial transition may possibly occur at lower even Reynolds numbers at further downstream distances since its onset approaches the cylinder with increasing Reynolds number, the finite outflow domain length then possibly precluding the observation of the vortex street breakdown. A critical element of the characterisation of this regime is that the wake response is also T -periodic, similar to that of the Kármán vortex street, but shows a rapid decay in its spectral amplitude in the streamwise direction. This is shown in the FFT plot in figure 3.14.

Regime III: Secondary vortex street wake

Another of these transitions in the sequence of increasing Reynolds number is the formation of a secondary vortex street. These vortex streets can appear to possess

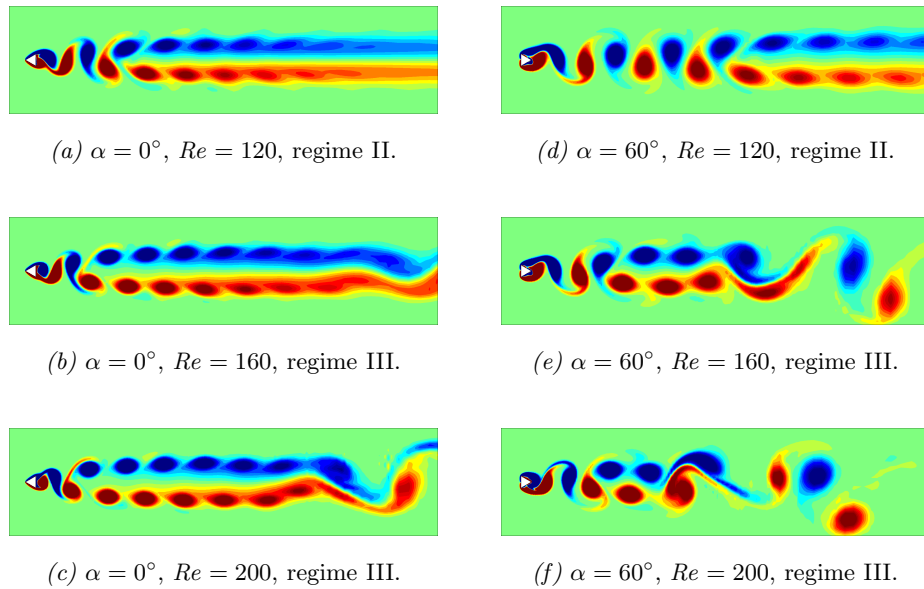
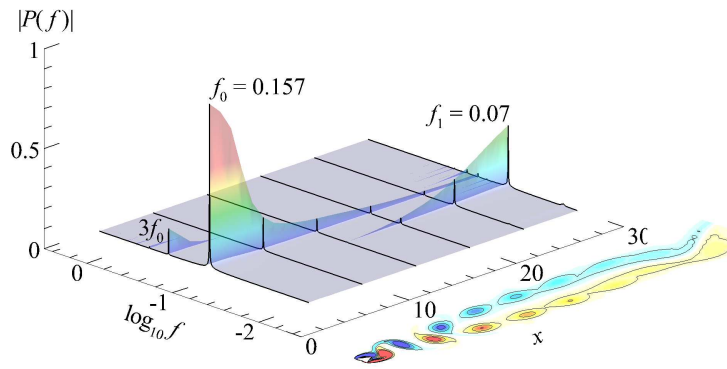
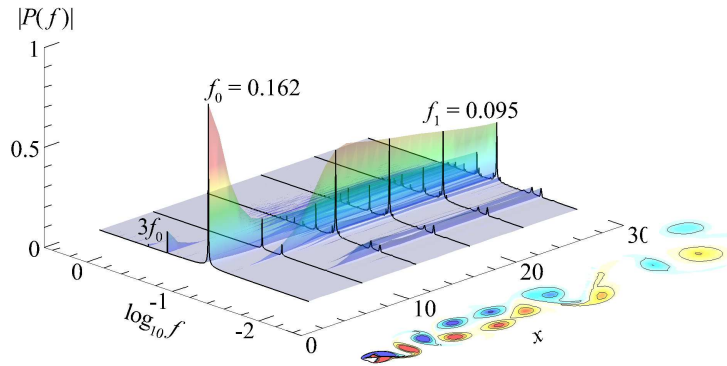


FIGURE 3.15: Visualisation of the secondary vortex streets in the wake of the cylinder inclined at $\alpha = 0^\circ$ on the left column, and $\alpha = 60^\circ$ on the right, both at increasing Reynolds numbers as labelled. Blue and red contours denote negative and positive vorticity values, respectively. In (a, d) , the flows are in regime II describing the dual layer wake structure developing downstream of the cylinder, and in (b, c, e, f) the secondary vortex street can be observed. In panels (b, c) , the secondary vortex street is observed to grow in the far wake out of the parallel shear layer wake, while in (e, f) , the secondary vortex street emerges rapidly nearer to the cylinder due to complex vortex interactions without the parallel shear layer being established.

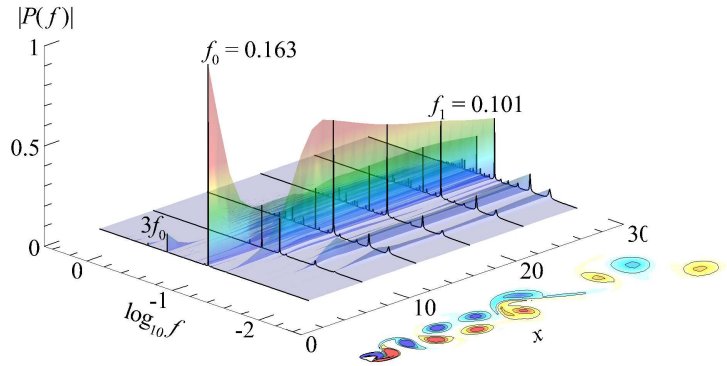
similar characteristics as the primary Kármán vortex street, but occurs at larger length scales and possesses wake structures with frequencies incommensurate with the primary shedding frequency. This corresponds to regime III in the $Re - \alpha$ parameter space shown in figure 3.9. Although this regime is usually encountered at higher Reynolds numbers above those where the parallel shear layer wake forms (figure 3.15a-c), the formation of the parallel shear layer wake itself not unnecessary (figure 3.15d-f). The sequence of images in figure 3.15(a-c) describes the development of the wake of the cylinder inclined at $\alpha = 0^\circ$ as it changes from regime II to III. Following the sequence in the figure from top to bottom, the parallel shear layer wake at $Re = 120$ is observed to have developed the secondary vortex street by $Re = 160$. For $\alpha = 60^\circ$ in figure 3.15(d-f), the vortex street breakdown is observed at $Re = 120$, but forms the secondary vortex street by $Re = 160$ without establishing the parallel shear layer.



(a) $\alpha = 60^\circ$, $Re = 140$, regime III.



(b) $\alpha = 60^\circ$, $Re = 180$, regime III.



(c) $\alpha = 60^\circ$, $Re = 200$, regime III.

FIGURE 3.16: FFT of the transverse velocity signals in the cylinder wake for cases as labelled, with captions following that for figure 3.12. A strong spectral peak at the fundamental frequency f_0 is observed in the near wake in all cases, but rapidly decays. In (a), the emergence of the secondary vortex street spatially is realised in the FFT plot as a non-harmonic frequency f_1 whose amplitude grows in space. Incommensurable frequencies then permeate the frequency response of the wake at higher Re .

Cimbala *et al.* (1988) conducted a thorough examination of the frequency spectra and velocity distribution in the far wake of the circular cylinder. They described the rapid deamplification of the spectral peak corresponding to the Strouhal frequency of the initially dominant Kármán street as the vortices traverse further downstream, and that the energies of a broad spectrum of frequencies subsequently amplify from where the secondary vortex street commences. The spatial profile of the frequency response of the flows within this regime is shown in figure 3.16, the plots agreeing with the observations by Cimbala *et al.* (1988). A pertinent feature of these FFT plots with increasing Reynolds number is that the spectral peak of the fundamental frequency in the near wake corresponding to the Strouhal frequency of the Kármán street decays significantly between measured downstream positions of $x = 5h$ and $x = 10h$. For the flow at $Re = 140$, secondary meanderings of frequency f_1 can be detected in the transverse velocity signal by $x = 20h$ as noted by the onset of some waviness in the vortex street. It is important to note that the secondary frequency f_1 measured here is not a harmonic of the fundamental f_0 . Similar rapid deamplification of the spectral peak corresponding to the Kármán street and subsequent formation of the secondary vortex street is observed at $Re = 180$ and 200 , but shows a range of incommensurable frequencies to have permeated the transverse velocity signals, as reflected by the increasing complexity of the flow.

In Kumar & Mittal (2012), the secondary vortex street observed from numerical simulations of flows past the circular cylinder was only transient at moderate Reynolds numbers but becomes more permanent with increasing Reynolds number. This differs from those observed here which are permanent features of the flow even at moderate Reynolds numbers. This does not, however, preclude the possibility that this regime is also convectively unstable at even lower Reynolds numbers.

Regime IV: The 2P mode

The vortex street types described in the previous sections appear to be consistent with a generic scenario for most bluff body flows as covered in the literature review. In contrast, the following two vortex street regimes appear to manifest only within the wakes of strongly asymmetric bluff bodies such as those for the inclined flat plate in Zhang *et al.* (2008).

The first of these wakes possesses a structure reminiscent of the 2P mode observed

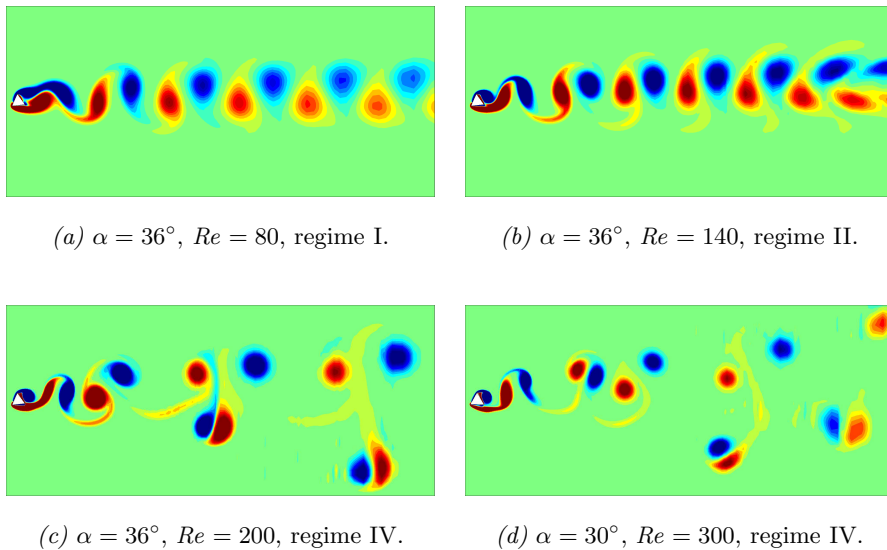


FIGURE 3.17: Evolution of the Kármán vortex street to the 2P vortex street in the wake of the cylinder at parameters as labelled. Blue and red contours denote negative and positive vorticity values, respectively. In (b), the vortex street breakdown is just visible on the right end of the panel.

in the wakes of oscillating cylinders as detailed in Williamson & Roshko (1988), and corresponds to regime IV marked on the $Re - \alpha$ space in figure 3.9. Specifically, this wake structure was only observed for cylinder inclinations $30^\circ \lesssim \alpha \lesssim 38^\circ$. For this range of cylinder inclinations, the vortex street was observed to develop slightly differently — the Kármán vortex street was observed to extend much further downstream before the vortex street breakdown than those wakes in which secondary vortex street development was observed, and so it exhibited much lower vorticity diffusion. The street also propagated at a slight angle away from the centreline through the cylinder axis, drawing some similarity to the P mode described by Williamson & Roshko (1988). The usage of the term ‘vortex street breakdown’ is also noted to be tenuous here since the wake never truly diffused sufficiently to a parallel shear layer wake, but the term is used here since the scenario still roughly follows that described for the parallel shear layer in § 3.2.2 where the vortices re-align at some spatial location through elliptical deformations of the vortices.

At sufficiently high Reynolds numbers, the wake abruptly transitions to the 2P mode (shown in figure 3.17) comprising two counter-rotating pairs of vortices, both propelling away from the wake centreline. As described in Zhang *et al.* (2008) for the wakes of

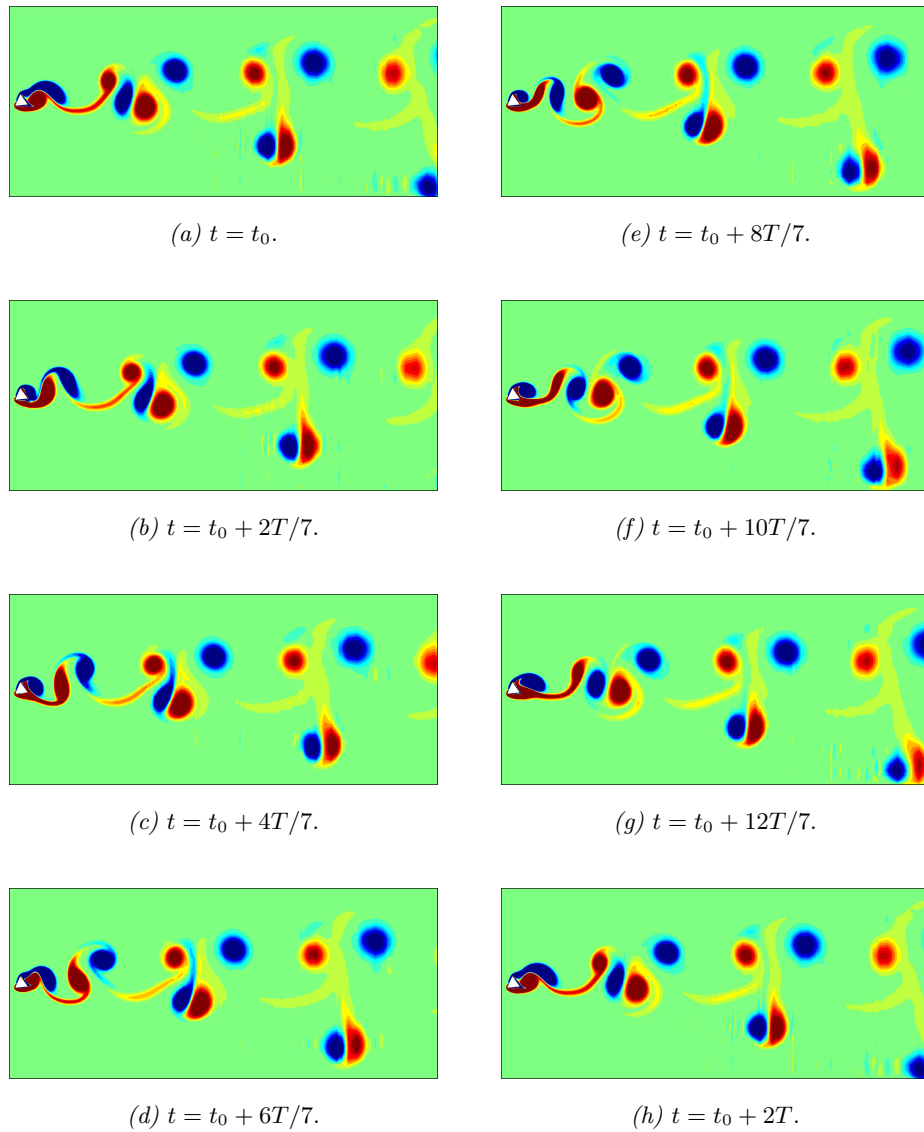


FIGURE 3.18: Evolution of the 2P mode over one $2T$ -periodic shedding cycle, shown for the flow at $Re = 200$ past the cylinder inclined at $\alpha = 36^\circ$. Blue and red contours denote negative and positive vorticity values, respectively.

the inclined flat plate, this vortex shedding mode arises from vortex interactions in the near wake, similar to that for the oscillating circular cylinder but distinct only in the sequence or method by which the shed vortices form. For the 2P mode in the oscillating circular cylinder wake, a forming vortex near the instant of being shed is strongly interacted upon by the forming region of the counter-rotating vortex due to the synchronisation of the cylinder oscillation frequency and the vortex shedding frequency. This causes a simultaneous shedding of the vortex along with an induced

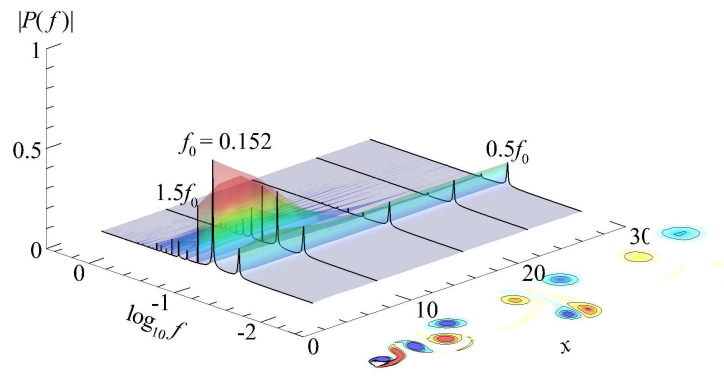


FIGURE 3.19: Fast Fourier transform of the transverse velocity signal in the 2P mode at $Re = 200$ flow past the cylinder inclined at $\alpha = 36^\circ$, with the velocities sampled at multiple downstream positions x at $y = 0$. The surface colour ranges from blue to green and to red for low (set as 0 here) to high spectral amplitude values. Distinct to the other regimes, the near wake of this mode shows a multi-frequency response. Most of these frequencies are harmonics of the fundamental frequency f_0 , but possesses only one subharmonic frequency $0.5f_0$, the latter being the distinguishing feature of this regime in terms of its frequency response.

splitting of said shed vortex, and is hence almost a pair vortex shedding (Williamson & Roshko, 1988; Govardhan & Williamson, 2000; Blackburn *et al.*, 2001). This results in a pattern of two like-signed vortices shed consecutively per half cycle, each propelling itself away from the wake centreline. The 2P mode in the static triangular cylinder wakes here on the other hand shows these interactions of the forming vortices to occur at a much earlier phase, straining the forming vortices and splitting them from the formation region, thus prematurely forcing the completion of the vortex pair. This is elucidated in figure 3.18. In fact, if conforming strictly to the nomenclature used for oscillating cylinder wakes, this regime would perhaps be more appropriately labelled as a 4S mode, or even a P+2S mode considering that a pair of counter-rotating vortices are shed within a very short time frame. These terminologies, however, are not usually applied in static cylinder wakes, and so this regime was termed 2P for its structural similarity to that found in the oscillating cylinder wake. Upon shedding, the pairs of opposite-signed vortices propel away from some apparent wake centreline, but differs to that for the oscillating circular cylinder in that the pair propelling away comprises counter-rotating vortices of every alternately shed pair.

A crucial feature of this resonant-like wake mode is the $2T$ periodicity of the wake structures. The frequency response across the wake confirms this (as shown in fig-

ure 3.19), describing the fundamental wake frequency corresponding to the vortex shedding frequency to be dominant only within the near wake, and a subharmonic frequency response pervading through the wake. At the upper limit of $Re = 200$, the flow past the cylinder inclined at $\alpha = 30^\circ$ exhibited the deflected Kármán street mode which was found to be a precursor leading to the 2P mode at higher Reynolds numbers. A quick check of the asymptotic solution of the flow field at $Re = 300$ showed that the flow has evolved to a complex wake resembling the 2P mode. This is shown in figure 3.17(d).

Regime V: The P+S mode

At larger incidence angles of $39^\circ \lesssim \alpha \lesssim 48^\circ$, the vortex street takes an appearance similar to the parallel shear layer wake in regime II, but is distinguished through several key features, and is labelled as regime V in figure 3.9. Firstly, the cross-wake vortex spacing appears to be much larger than those in regimes I and II, fully separating the dual rows of opposite-signed vortices even in the near wake. Like the parallel shear layer wake in regime II, the vortex street in this regime was also observed to be further susceptible to secondary meanderings in the downstream regions of the wake. The most crucial feature for this distinction, however, is in the observation of a small single vortex ‘riding’ along one of the rows of vortices in the wake. This is elucidated in figure 3.20.

This vortex street form bears a remarkable resemblance to the P+S mode again observed in the wakes of an oscillating circular cylinder (Williamson & Roshko, 1988; Govardhan & Williamson, 2000). Closer examination of the time-evolution of the vortex street shows that this mode forms through the same description for the P+S mode provided by Williamson & Roshko (1988) and Govardhan & Williamson (2000) wherein the vortices on the verge of being shed takes on such a strained form causing it to be susceptible to splitting when proximate to the previously shed opposite-signed vortex. In the case of the oscillating circular cylinder, the strain was induced by the oscillatory motion of the cylinder, stretching the forming region in its wake and hence straining the vortex. In contrast, the vortices in the case of the static triangular cylinder derives this strain from the asymmetric form of the cylinder cross-section. The vortex shed from the upper half of the cylinder in this case forms over a single edge of the cylinder and thus forms normally. The vortex shed from the lower half of the cylinder on the other hand first separates from the windward edge, but is subsequently subjected to a strong reversal into the wake immediately behind the upper leeward surface. As this positive

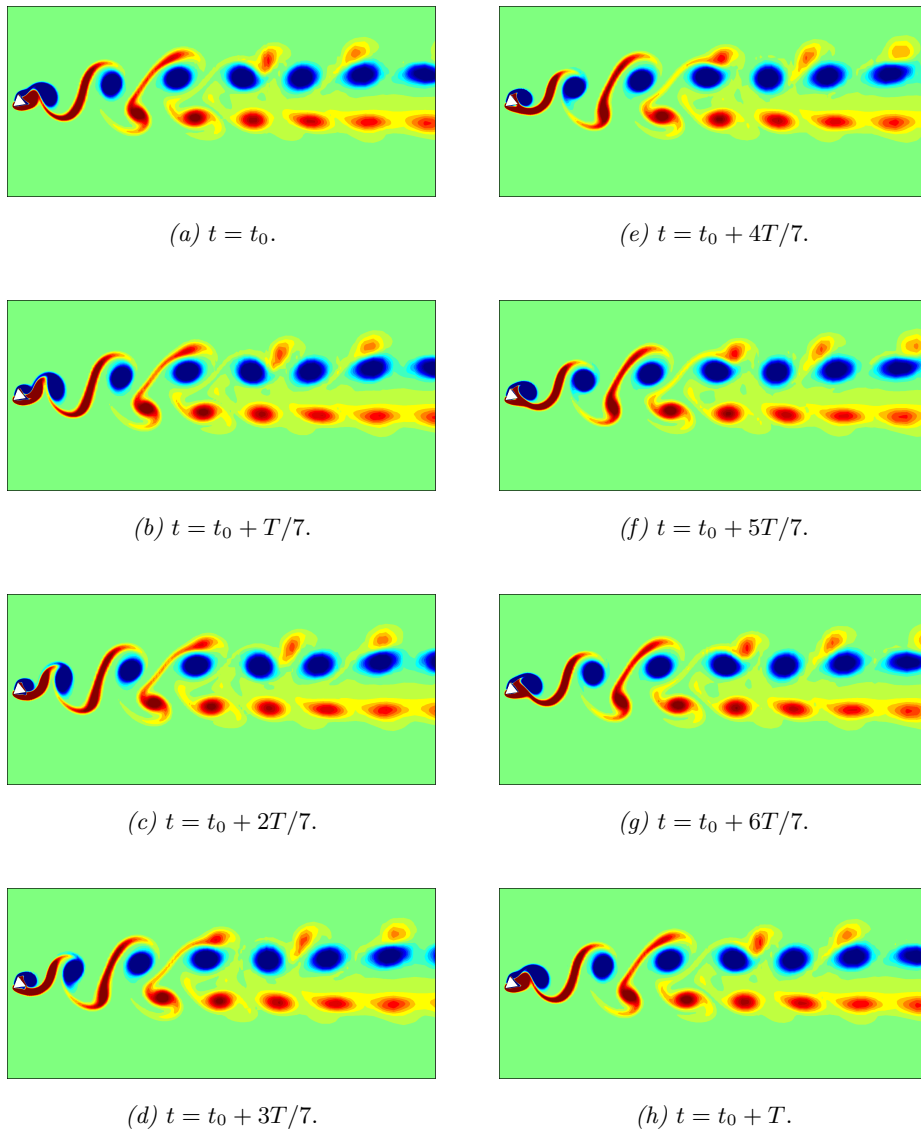
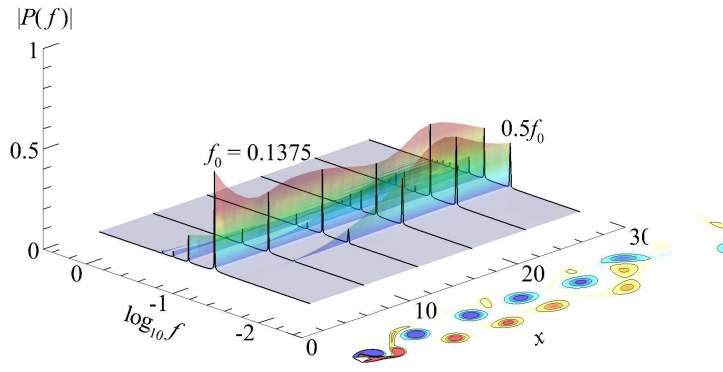
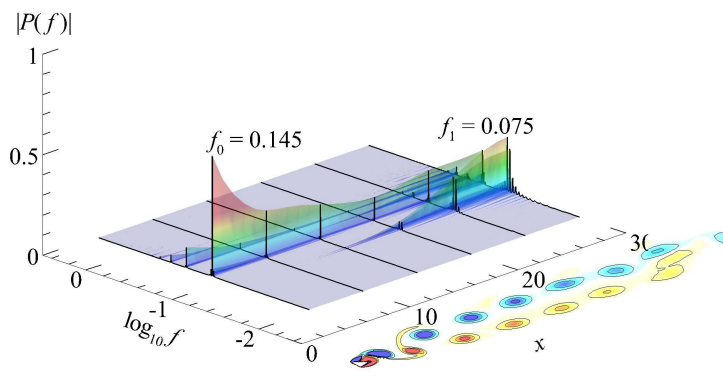


FIGURE 3.20: Evolution of the periodic P+S mode over one T -periodic shedding cycle, shown for the flow at $Re = 200$ past the cylinder inclined at $\alpha = 39^\circ$. Blue and red contours denote negative and positive vorticity values, respectively.

vorticity region forms, the negative forming vortex rapidly interacts with it, splitting it away from the cylinder surface. This induces a strong strain on the vortex, which then splits to form the smaller riding vortex on the upper row of vortices in the street while the larger portion of the split positive vortex remains in lower half of the vortex street. The smaller vortex possesses a smaller vorticity magnitude and is thus observed to ‘ride’ the vortex street, while the larger remnants of the split vortex experiences a lag (clockwise speed shift for the negative vortices). The local circulation imbalance in



(a) Periodic P+S: $\alpha = 45$, $Re = 240$.



(b) Aperiodic P+S: $\alpha = 48$, $Re = 200$.

FIGURE 3.21: FFT of the transverse velocity signal of the P+S mode for flows at $Re = 240$ past the cylinder inclined at $\alpha = 45^\circ$, and $Re = 200$ for the cylinder inclined at $\alpha = 48^\circ$ — the former showing the two-dimensional flow to be periodic, while the latter remains aperiodic. The surface colour ranges from blue to green and to red for low (set as 0 here) to high spectral amplitude values. In both cases, the far wakes show multi-frequency components to have been introduced into the wake response, and that in the periodic case, these multi-frequencies are coincidentally subharmonic/harmonic to the fundamental.

the vortex street arising from this vortex splitting increases further down the domain (due to the lead/lag of the negative vortices), which then causes the vortex street to lose stability in its point vortex arrangement (von Kármán, 1911), causing the far wake meandering observed.

Several cases within this regime exhibited a $2T$ periodicity at specific Reynolds numbers, but remained aperiodic otherwise. These isolated periodic cases were coincidentally resonant to some underlying flow feature. This is demonstrated through an FFT of the transverse velocity signal taken along the centreplane as shown in figure 3.21(a), where the $2T$ -periodic case possesses a frequency coincidentally subharmonic to the fundamental throughout the domain. The FFT plot of another case exhibiting the P+S mode instead shows a broadband of frequencies to be excited in the far wake as shown in figure 3.21(b), the most dominant of which is a non harmonic response.

Further discussion on the 2P and P+S modes

As observed in the regime map in figure 3.9, as the Reynolds number is increased, the vortex streets beyond the onset of the first instability adopts the familiar form of regime I through the periodic array of vortices. For all cylinder inclinations, the far wake of the vortex street is subsequently subjected to a spatial re-arrangement to regime II, regardless of whether the vortices completely diffuse to form a dual parallel shear layer. From this state, the vortex street develops into either the secondary vortex street, the 2P mode, or the P+S mode, depending on the cylinder inclination. It appears that the factor deciding the formation of either the 2P- or the P+S mode in the vortex street lies in the extent of the formation of the strained positive vortex on the cylinder surface prior to an interference by the negative vortex sweeping into the low pressure region, and if the forming vortices interact with the attached boundary layer on the rear side of the cylinder prior to being shed. This broadly corresponds to the vortex merging pattern described by Yoon *et al.* (2010). The evolution of the 2P- and P+S modes over a periodic cycle are elucidated in figures 3.18 and 3.20, respectively.

In both cases, the merging of the forming positive vortex with the attached boundary layer on the upper leeward cylinder surface introduces a lag into its shedding, and also significantly strains the vortex. The timing of this merging ultimately distinguishes the two modes. For the P+S mode, this merging occurs at a similar phase at every pair of counter-rotating vortices shed (figure 3.20a–e). After being shed from the cylinder, the

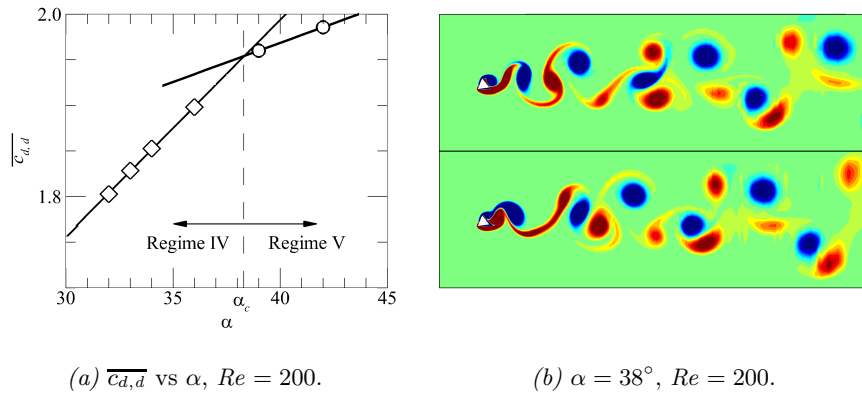


FIGURE 3.22: (a) Plot of the time-averaged drag coefficients scaled by the cylinder side length d , $\overline{c_{d,d}}$, against the cylinder inclination α at a Reynolds number of $Re = 200$. The solid lines are linear functions—one fitted through the data for the 2P mode (\diamond) and the other fitted through the data for the P+S mode (\circ), while the dashed line marks the estimated threshold for the 2P–P+S mode changeover. (b) Vorticity contours of the $Re = 200$ flow past the cylinder inclined at $\alpha = 38^\circ$ showing the wake in an intermediate state between the 2P and P+S modes. Blue and red contours denote negative and positive vorticity values, respectively. The lower image occurs one counter-rotating vortex pair apart from the top image.

strained positive vortex is further affected by the action of the adjacent negative vortex downstream causing it to split, thus leading to the observation of a pair of positive (like-signed) unequal-strength vortices about a single negative vortex (second positive vortex in the wake in figure 3.20a–g). For the 2P mode, this interaction between the forming positive vortex and the attached boundary layer is delayed in the shedding of a positive vortex causing it to be more appropriately formed, while the following pair of vortices is subjected to a similar straining described for the P+S mode (figure 3.18a–c). This leads to the two vortex pair periodicity of the 2P mode.

The evolution from the 2P- to P+S mode at a fixed Reynolds number is next investigated. For this, the drag coefficient induced on the cylinder by a flow at $Re = 200$ for $30^\circ \leq \alpha \leq 48^\circ$ was considered to predict the inclination angle where the pattern switching occurs (α_c). This is shown in figure 3.22. A fixed Reynolds number was chosen here to observe only the qualitative features of the flow field as the vortex pattern changes, foregoing a quantitative analysis since the critical angle changes with the Reynolds number. For the flow at $Re = 200$, the mode switching between the 2P and P+S modes is predicted to occur at an incidence angle of $\alpha \approx 38^\circ$. At this incidence angle, the wake develops with features consistent with both modes. This is elucidated in

figure 3.22. Over the shedding cycle, the vortex street forms identically to the 2P mode, but a strained positive vortex subsequently splits in the wake similar to that in the P+S mode. This results in the complex vortex pattern observed. Increasing the incidence angle further presumably alters the timing of the interaction of the shedding vortices, thereby suppressing the 2P mode leading to the onset of the P+S mode. Extra care was taken to ensure the flows were evolved to a saturated state, precluding the possibility that the different patterns in the vortex streets observed are transient features of the flow.

It is recognised at this point that the flow in some of the regimes mapped out in this study may in fact be inherently three-dimensional. Experiments by Luo & Eng (2010) on the wakes of a downstream pointing isosceles triangular cylinder reported that the flow is three-dimensional with a pattern consistent with mode *A* in the wake of a circular cylinder (Williamson, 1988b) at Reynolds numbers of $Re \geq 164$. Also, numerical simulations of the 2P mode in the wake of an oscillating circular cylinder by Blackburn *et al.* (2001) appeared three-dimensional in nature.

Regardless, the two-dimensional planes showed that spanwise vortex loops resembling the 2P mode persists, agreeing with various experimental visualisations showing the mode (Williamson & Roshko, 1988). As such, the 2P mode found in this study could perhaps be three-dimensional as well, along with several other regimes mapped in figure 3.9. It will later be shown in chapter 4 that in fact the flow becomes unstable to infinitesimal three-dimensional perturbations at Reynolds numbers ranging from approximately 100 to 140.

3.3 *St–Re* variations with cylinder inclination

Having elucidated the different vortex street configurations in the two-dimensional flow at Reynolds numbers up to $Re = 200$, an attempt was next made to understand how the dominant frequency in the wake varies with cylinder inclination and also with the Reynolds number. These frequencies were quantified for each case using two different datasets: the fluctuating lift signals induced on the cylinder (c_l), and the fluctuating cross-stream velocity (V) signals in the wake. The lift force measurement being taken on the cylinder itself means that its frequency correlates directly to the vortex shedding frequency (the Strouhal number St in the dimensionless sense), and is a near-wake-accurate measurement. The transverse velocity signal on the other hand provides

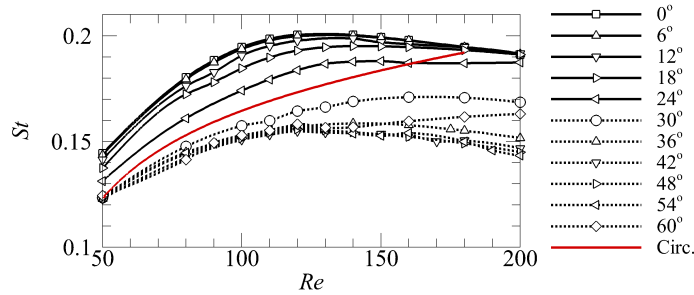


FIGURE 3.23: Plot of the Strouhal number St against the Reynolds number Re for various cylinder inclinations as indicated in the legend. Plots drawn with solid lines through the data markers are for the wakes of cylinder inclinations $\alpha < 30^\circ$, while those drawn with dashed lines are for cylinder inclinations $\alpha \geq 30^\circ$.

an estimate of the local oscillation frequency in the unsteady wake of the cylinder which is useful to demonstrate any spatial development of the vortex street. The latter measure was used in several figures earlier in § 3.2.2 to elucidate the development of the various vortex street patterns through the spatial variation of the wake frequencies (figure 3.16 for example). Since pairwise vortex shedding was not observed in any of the two-dimensional vortex street regimes for $Re \leq 200$, the dominant wake frequency obtained from the transverse velocity signal in the near wake is expected to match that obtained from the fluctuating lift coefficient. This was demonstrated in § 3.2.2 for all wake regimes where the frequency spectra in the near wake of each regime shown in figures 3.12, 3.14, 3.19, and 3.21 are consistently dominated by the primary frequency f_0 before the development or amplification of any secondary frequencies. For periodic wakes, the Strouhal numbers of the vortex shedding were obtained directly from the flow periods. For wakes with incommensurate or subharmonic frequencies, the vortex shedding frequencies were estimated using an FFT of the oscillatory lift coefficients. The measured Strouhal numbers for the vortex shedding are shown in figure 3.23.

As observed in figure 3.23, the Strouhal–Reynolds number profiles for these wakes appear to concentrate about two branches, one for cylinder inclinations $\alpha < 24^\circ$, and the other for $\alpha > 30^\circ$, with the St – Re profiles for the cylinders at $\alpha = 24^\circ$ and 30° bridging the two branches. For the circular cylinder wake, the Roshko number

$$Ro = St Re = \frac{U d f d}{\nu U} = \frac{f d^2}{\nu},$$

relates linearly to the Reynolds number within various intervals of the Reynolds number itself — the circular cylinder wake reported in Roshko (1954) shows that two linear

functions of Re within $50 < Re < 150$ and $300 < Re < 2000$ quite accurately describe the experimentally attained Strouhal numbers (for the linear function at higher Reynolds numbers of $300 < Re < 2000$, the agreement was within 1%). However, the Strouhal numbers showed a strong scatter in the intermediate range of Reynolds numbers of $150 < Re < 300$, and so it fit neither linear functions. Tritton (1959) and Gerrard (1978) associated the scatter in the $St-Re$ data with non-uniformities in the vortex rollers, with Williamson (1988a, 1989) later reconciling the scatter through correction of end conditions induced by finite-length cylinders. This led to a collapse of the scattered data onto a universal $St-Re$ curve at Reynolds numbers where the flow was two-dimensional, and a least-squares curve fit of the data showed this universal curve to be well described by the quadratic function

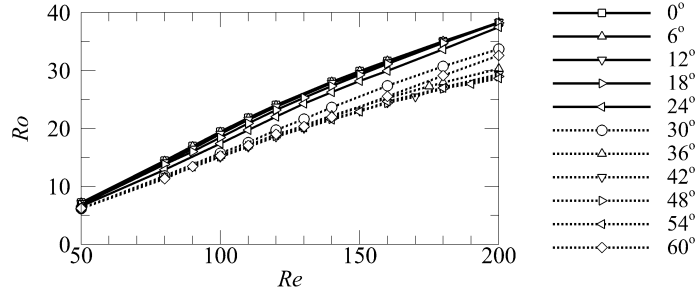
$$\begin{aligned} St &= a_2 Re + a_1 + \frac{a_0}{Re}, \\ \therefore Ro &= a_2 Re^2 + a_1 Re + a_0, \end{aligned} \quad (3.4)$$

where a_2 , a_1 , and a_0 are the regression coefficients, slightly improving on the linear $Ro-Re$ relation by Roshko (1954).

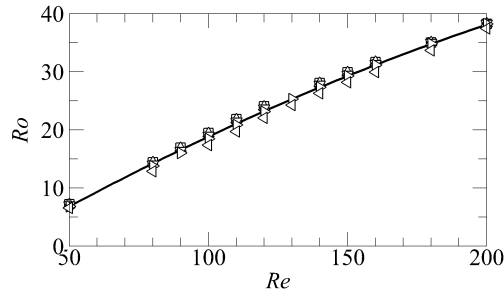
$\alpha(^{\circ})$	a_2	a_1	a_0	R^2
0	-4.0912×10^{-4}	0.3102	-7.4587	0.9997
6	-3.9629×10^{-4}	0.3077	-7.4127	0.9997
12	-3.4611×10^{-4}	0.2965	-7.1142	0.9996
18	-2.8735×10^{-4}	0.2832	-6.8218	0.9997
24	-1.9351×10^{-4}	0.2563	-6.0218	0.9994
30	-1.2349×10^{-4}	0.2179	-4.6398	0.9994
36	-2.5135×10^{-4}	0.2265	-4.7327	0.9997
42	-2.7139×10^{-4}	0.2229	-4.3583	0.9998
48	-3.1919×10^{-4}	0.2335	-4.8601	0.9997
54	-3.5668×10^{-4}	0.2419	-5.2448	0.9991
60	-3.6249×10^{-5}	0.1845	-2.9366	0.9995
Circular cylinder	-1.600×10^{-4}	0.1818	-3.3265	

TABLE 3.4: Coefficients of the polynomial function shown in equation (3.4) describing the $Ro-Re$ profile over a Reynolds number range $50 \leq Re \leq 200$ for each cylinder inclination α . The R^2 value is included as a goodness-of-fit statistic. The coefficient values for the wake of the circular cylinder reported in Williamson (1989) is included for comparison.

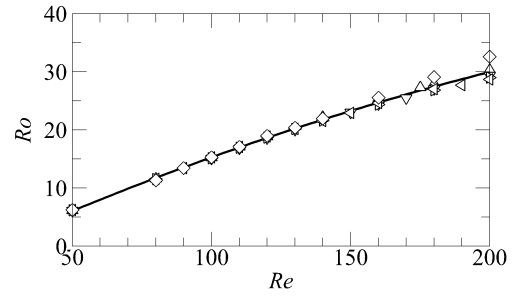
Following these studies, the Roshko numbers for the inclined triangular cylinder wakes were calculated and a least-squares regression was used to determine the corresponding a_0 , a_1 , and a_2 coefficients. The results from this analysis are summarised



(a) $Ro-Re$, all α .



(b) $Ro-Re$, $\alpha < 30^\circ$.



(c) $Ro-Re$, $\alpha > 30^\circ$.

	branch I (upper)	branch II (lower)
a_2	-3.167×10^{-4}	-2.512×10^{-4}
a_1	2.878×10^{-1}	2.223×10^{-1}
a_0	-6.778×10^0	-4.434×10^0
R^2	0.9952	0.9931
$\max St - St_{\text{est}} $	0.0168	0.0131

FIGURE 3.24: (a) Plot of the Roshko number Ro against the Reynolds number Re for various cylinder inclinations as shown in the line legend. Plots drawn with solid lines through the data markers are for the wakes of cylinder inclinations $\alpha < 30^\circ$, while those drawn with dashed lines are for cylinder inclinations $\alpha \geq 30^\circ$. Plots (b, c) are similar to (a), each focusing only on one of the upper and lower branches. The data markers in (b, c) follow those in (a), while the solid line through each plot are the ‘generalised’ $Ro-Re$ fitted curves described by the coefficients in the subsequent table. The bottom table shows the regression coefficients of the generalised $Ro-Re$ curve for each of the upper and lower branches, along with some goodness-of-fit and accuracy statistics.

in figure 3.24, and the fitted coefficients for each cylinder inclination α are given in table 3.4. The results show that the quadratic function (3.4) fitted the $Ro-Re$ data for each cylinder inclination to a good accuracy, as justified through their R^2 values which are 0.9991 at worst.

Similar to the $St-Re$ curves, the $Ro-Re$ curves shown in figure 3.24 appear to follow two general branches except for the cylinder inclined at 30° (triangle pointing transverse to the flow). These two branches correspond to cylinder inclinations $0^\circ \leq \alpha < 30^\circ$ for the upper branch, and $30^\circ < \alpha \leq 60^\circ$ for the lower branch; the distinguishing feature of the geometry between these inclination ranges is the number of windward and leeward cylinder surfaces it presents to the flow. This possibly causes the ‘universal curve’ of the shedding frequency of the $\alpha = 30^\circ$ inclined cylinder case to differ from the two other general branches, recalling that the $h/d(\alpha)$ function in equation (2.38) is non-smooth about this inclination angle. It is also the only case which presents a single cylinder surface to both the upstream and downstream directions of the flow, the remaining surface being parallel to the flow. Also, coincidentally, the two branches in the $Ro-Re$ profile shown in figure 3.24 separately agree with cylinder inclination ranges where the MS pattern and the VM- or SSV patterns are observed in the two-dimensional wakes. These results suggest that the shedding frequency itself (through the Roshko number) might be affected by the vortex shedding topology and the distribution of recirculation regions of the time-mean flow more so than it is by the cylinder inclination itself, and that the Roshko–Reynolds number relationship may be generalisable for cylinders with typical cross-sectional geometries under specific conditions.

3.4 Flow induced forces

The magnitude of the force coefficients reported in this section have been re-scaled to use the cylinder side length d as the length scale to facilitate a comparison with the results from Bao *et al.* (2010), unless specifically mentioned otherwise. At low Reynolds numbers where the flow is steady, the lift forces obtained were negligible relative to the drag forces induced on the cylinder. This is shown in the inset of figure 3.25(a). In such a laminar state, and despite the geometric asymmetry of the cylinder cross-section at most inclinations, the transverse momentum imparted into the flow by the cylinder is rapidly dissipated, leading to the low lift coefficients described. The drag coefficients induced on a circular cylinder is known to be approximately

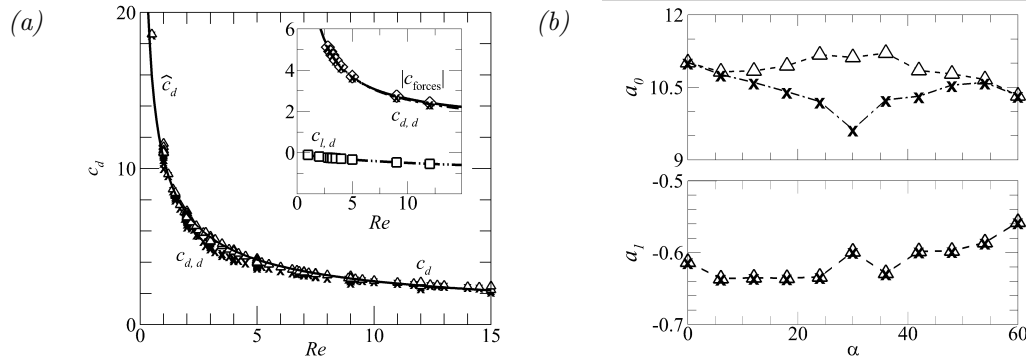


FIGURE 3.25: (a) Plot of the drag coefficients scaled by the projected height of the cylinder h (Δ) and by the cylinder side length d (\times) against the Reynolds number. The solid line describes the fitted function $\hat{c}_d(Re)$. (inset) Plot of the lift- (\square), drag- (\times), and resultant- (\diamond) force coefficients, all scaled by the cylinder side length d at the low Reynolds number range when the cylinder is inclined at $\alpha = 30^\circ$. (b) Plots of the a_0 and a_1 coefficients from equation (3.5) for various cylinder inclinations α . The coefficients marked by (Δ) are obtained for the drag coefficients scaled by h , and (\times) for the data scaled by d .

inversely proportional to the Reynolds number at low Reynolds numbers (Stokes, 1851; Oseen, 1910; Lamb, 1911) — non-dimensionalisation of the Stokes drag formula shows that $c_d = 24/Re$. Neglecting the transverse forces (lift) induced on the cylinder, the functional relationship between the drag coefficient and the Reynolds number (shown in figure 3.25a) was sought for the low Reynolds number regime in the form of

$$c_d = a_0 Re^{a_1}, \quad (3.5)$$

where a_0 and a_1 are coefficients of a power law. For this regression, data over Reynolds numbers $Re \lesssim 15$ is used. The coefficients a_0 and a_1 predicted for each cylinder inclination are summarised in figure 3.25(b). The data in figure 3.25(a) suggests that the drag coefficients are minimally affected by the cylinder inclination at these Reynolds numbers, and so a general fit to the data was also performed ($\hat{c}_d = \hat{a}_0 Re^{\hat{a}_1}$). The predicted coefficients of this general fit are $\hat{a}_0 = 10.6316$ and $\hat{a}_1 = -0.5817$, and is shown in figure 3.25(a) to reproduce the measured data quite accurately.

At moderate Reynolds numbers, the time-averaged lift coefficients of the cylinder exhibited a similar trend where the maximum lift coefficient occurred at $\alpha \approx 30^\circ$, and increases only in magnitude with the Reynolds number as shown in figure 3.26. The geometric asymmetry of the cylinder inclined at $\alpha = 30^\circ$ is largest, explaining the maximum mean lift coefficients found at these angles. Following the same reasoning,

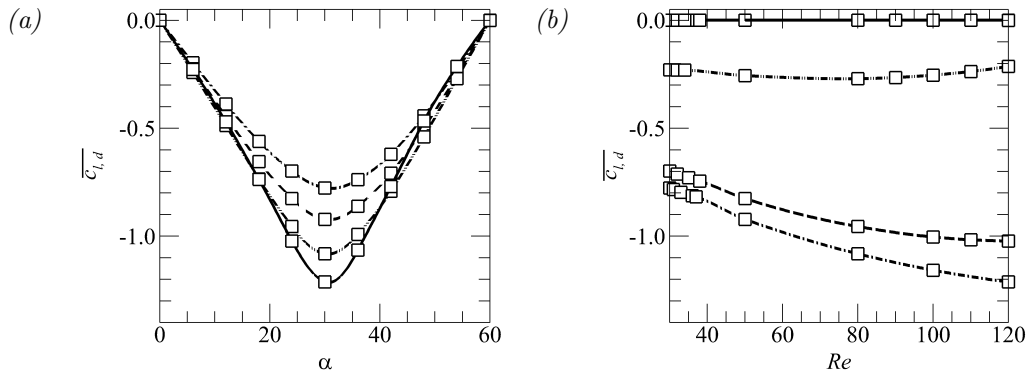


FIGURE 3.26: Variation of the mean lift force coefficient $\overline{c_{l,d}}$ with (a) α , and (b) Re . In (a), dash-dotted line is for $Re = 30$, dashed line $Re = 50$, dash-double-dotted line $Re = 80$, and the solid line $Re = 120$. In (b), the dashed line is for $\alpha = 24^\circ$, dash-dotted line $\alpha = 30^\circ$, dash-double-dotted line $\alpha = 54^\circ$, and the solid line $\alpha = 60^\circ$. For both plots, the data obtained are marked with (\square) data markers.

symmetric cylinder inclinations $\alpha = 0^\circ$ and 60° show negligible time-averaged lift coefficients for all Reynolds numbers reported. The figure also demonstrates the change in the trends of the lift coefficients about the transition at Re_c (ranging $30 < Re \lesssim 40$).

The variation of the time-averaged drag coefficient with both cylinder inclination and Reynolds number shown in figure 3.27 consistently reaches a minimum when the cylinder is inclined at $20^\circ \lesssim \alpha \lesssim 30^\circ$ for most Reynolds numbers, appearing consistent for both the steady-state regime (shown for $Re = 30$) and the unsteady flow regimes. For all Reynolds numbers shown, the time-averaged drag coefficients for the symmetric cylinder inclination $\alpha = 60^\circ$ are observed to be much larger than those for the symmetric cylinder inclination $\alpha = 0^\circ$, which is a consequence of the broader wakes produced by the cylinder inclined at $\alpha = 60^\circ$ compared to those for the cylinder inclined at $\alpha = 0^\circ$. A similar observation was reported by Iungo & Buresti (2009) in their experiments of flows past a finite-span triangular cylinder conducted at a Reynolds number of $Re_d = 1.2 \times 10^5$. The transition from steady- to unsteady flows again noticeably alter the trends in the mean drag coefficients as shown in figure 3.27(b). The mean drag coefficients for a flow at $Re_d = 100$ reported by Bao *et al.* (2010) are also included in figure 3.27(a) for comparison. Directly comparing the values of the mean drag coefficients at $\alpha = 0^\circ$ and 60° between the present study and Bao *et al.* (2010) ($Re = Re_d = 100$ at these two angles) shows a difference of approximately 0.85% and 3.5%, respectively. These differences may possibly stem from the smaller computational domain utilised

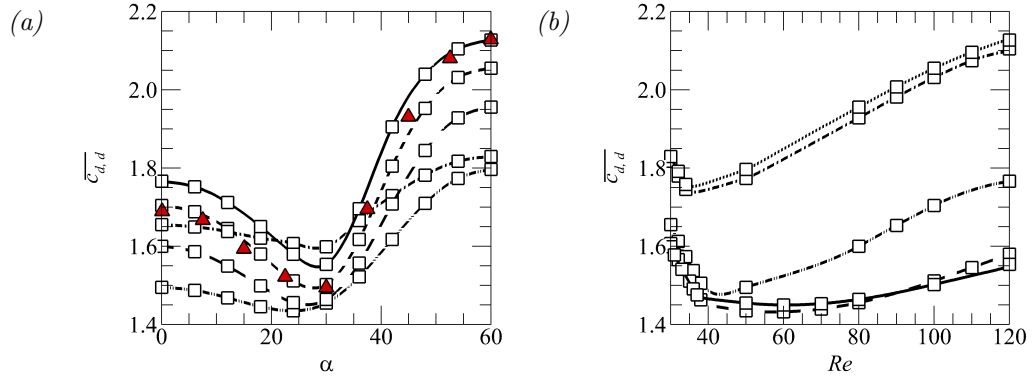


FIGURE 3.27: Variation of the mean drag force coefficient $\overline{c_{d,d}}$ with (a) α , and (b) Re . In (a), dash-dotted line is for $Re = 30$, dash-double-dotted line $Re = 50$, dashed line $Re = 80$, dotted line $Re = 100$, and the solid line $Re = 120$. In (b), the dash-double-dotted line is for $\alpha = 0^\circ$, dashed line $\alpha = 24^\circ$, solid line $\alpha = 30^\circ$, dash-dotted line $\alpha = 54^\circ$, and the dotted line $\alpha = 60^\circ$. The (\blacktriangle) data in (a) are results for the flow at $Re_d = 100$ reported in Bao *et al.* (2010). For both plots, the data obtained are marked with (\square) data markers.

by Bao *et al.* (2010) along with the towing tank boundary conditions they employed on the transverse boundaries. These factors along with the fact that higher cylinder inclinations produce broader wakes suggest that domain truncation uncertainties may account for the differences observed at higher cylinder inclinations.

Figure 3.28 describes the time-averaged force coefficients, the corresponding root-mean-square (r.m.s.) values about the time-averaged quantities, and the fluctuation extremes as the Reynolds number is increased for flows past the cylinder inclined at $\alpha = 0^\circ, 36^\circ, 42^\circ$, and 60° . Generally, the r.m.s. values are observed to follow the trends of the time-averaged force coefficients as the Reynolds number is increased. However, this quantity fails to follow the sudden increase in the fluctuations of the force coefficients at $Re \approx 170$ for the cylinder inclined at $\alpha = 36^\circ$ corresponding to the transition to the 2P wake. A change in the slope of the time-averaged drag force coefficient is observed at $Re \approx 110$ for the cylinder inclined at $\alpha = 0^\circ$, $Re \approx 135$ for the cylinder inclined at $\alpha = 42^\circ$, and $Re \approx 120$ for the cylinder inclined at $\alpha = 60^\circ$, occurring at Reynolds numbers unrelated to the change from regime I to regime II (i.e. from the Kármán vortex street to the dual shear layer wake). While the time-averaged lift coefficients for symmetric cylinder inclinations are negligible, the fluctuations for these cases are significant, with the cylinder inclined at $\alpha = 60^\circ$ exhibiting the largest fluctuation in the force profiles.

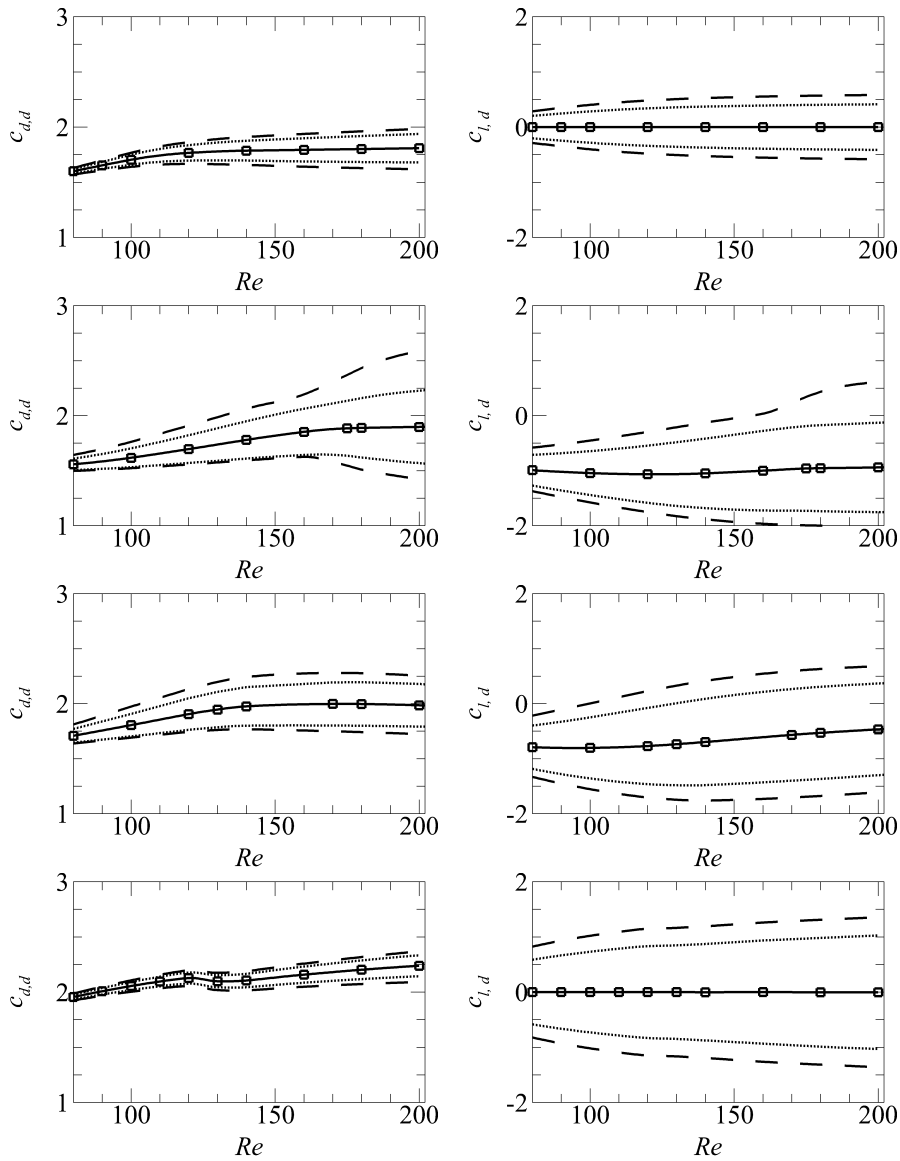


FIGURE 3.28: Force profiles for the cylinder inclined at $\alpha = 0^\circ, 36^\circ, 42^\circ$, and 60° from top to bottom, with plots on the left and right panels showing the variations in the mean drag coefficients $\overline{c_{d,d}}$ and mean lift coefficients $\overline{c_{l,d}}$ with increasing Reynolds number, respectively. Solid lines through the computed data (\square) show the trends of the mean coefficients, dashed lines show the fluctuation extrema (min and max of the data time history), and the dotted lines show the root-mean-squared values of the data centred about the mean.

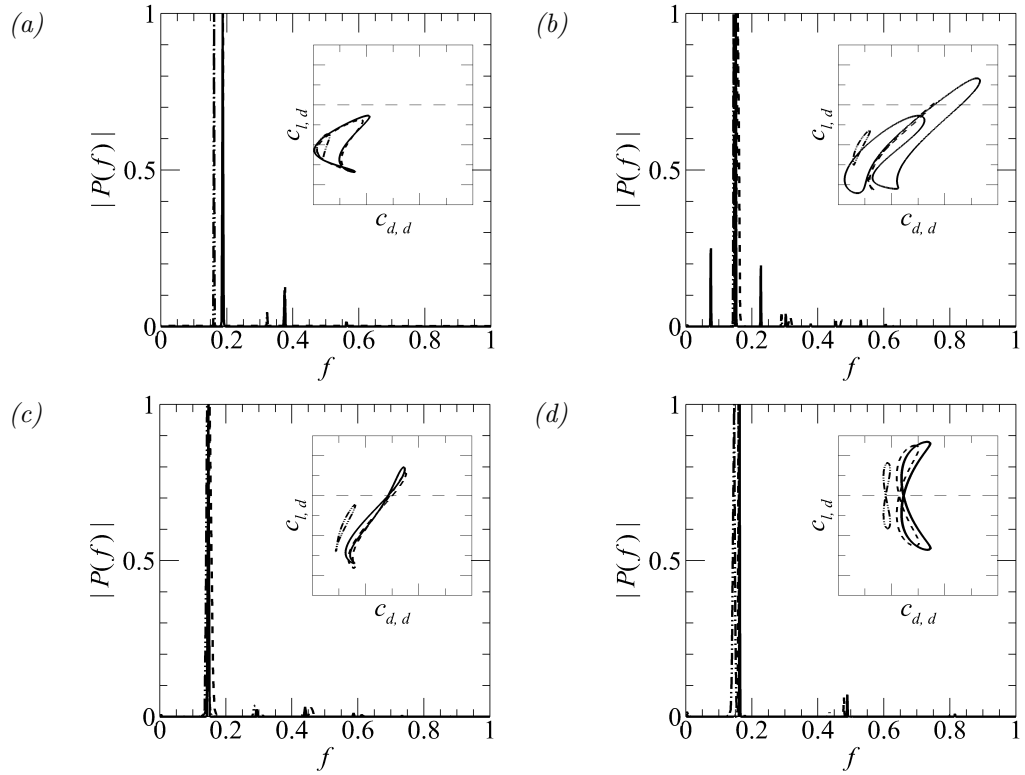


FIGURE 3.29: Power spectral densities of the lift coefficients for the cylinder inclined at (a) 24° , (b) 36° , (c) 42° , and (d) 60° , each at Reynolds numbers of $Re = 80$ (dash-dotted lines), $Re = 160$ (dashed lines), and $Re = 200$ (solid lines). The amplitudes in each case are normalised by that of the peak response at each Reynolds number. (*inset*) Corresponding phase portraits of the force coefficients. The plot axes are limited as $-2.5 \leq c_{l,d} \leq 1.5$ and $1.5 \leq c_{d,d} \leq 3.0$.

Spectral analysis of the lift coefficients of cylinder at various Reynolds numbers ($Re = 80, 160$, and 200) reveal the different frequency responses of the unsteady force time histories in the various wake regimes. These are shown in figure 3.29. For the cylinder inclined at $\alpha = 24^\circ$ and 60° (for the transition from the Kármán vortex street to the secondary vortex street), and also for the cylinder inclined at 42° (for the transition to the P+S mode), the frequency spectra appear highly similar through all wake regimes as expected due to the dominance of the vortex shedding frequency in the near wake of the cylinder. This follows the results demonstrated previously in figures 3.16 and 3.21. It is only in the transition to the 2P mode shown for the flow past the cylinder inclined at $\alpha = 36^\circ$ that the frequency spectra changes noticeably. For $Re = 200$ in the 2P case, the dominant frequency measured was again due to the vortex shedding with $f_0 = 0.151$, but the spectra now showing non-negligible subharmonic responses of $0.5f_0$

and $1.5f_0$.

3.5 Chapter summary

The characteristics and development of a two-dimensional flow past the cylinder across a range of inclinations and Reynolds number have been described. For a steady flow, the steady recirculation region for cylinders that present asymmetrically to the uniform flow develops asymmetrically through a detached eddy scenario. The separation Reynolds number where the flow first separates from the cylinder was found to increase from $\alpha = 0^\circ$ to 60° .

It was shown that the transition from a steady to an unsteady wake for the triangular cylinder occurs through a supercritical Hopf bifurcation for all cylinder inclinations, consistent with the results from Provansal *et al.* (1987) and Zielinska & Wesfreid (1995), amongst others. The critical Reynolds number for this transition was quantified for each cylinder inclination. For cylinders inclined at $\alpha < 30^\circ$, the presence of a small streamwise velocity reversal along the windward cylinder surface acted to disturb the flow, causing the critical Reynolds number to decrease at inclinations where this was observed. For flows past the cylinder at $\alpha > 30^\circ$, the lower critical Reynolds numbers obtained compared to the other inclination range were associated with the formation of a broader wake.

At Reynolds numbers past the transition, the familiar Kármán vortex street was first observed in all cases but was found to become unstable to various other wake patterns at higher Reynolds numbers. The first variation in the vortex street was associated with the vortex street breakdown, forming a dual row of vortices which may subsequently diffuse into a parallel shear layer. This was denoted regime II. The distinction between the Kármán vortex street and this regime is the formation of a layer of irrotational fluid between the two rows of vortices. This regime can then develop spatially in the far wake to form the secondary vortex street through the formation of non-harmonic wake structures. Within a narrow range of cylinder inclinations ($30^\circ \lesssim \alpha \lesssim 38^\circ$) and with increasing Reynolds numbers, the vortex street abruptly transitions into a complex wake pattern resembling the 2P mode of oscillating circular cylinder wakes. In this regime, a subharmonic frequency was observed to dominate the periodic response of the wake globally. At cylinder inclinations $38^\circ \lesssim \alpha \lesssim 54^\circ$ and also at higher Reynolds numbers, regime II is observed to develop differently, forming the P+S mode of oscillating circular

cylinders.

The vortex shedding frequencies of these two-dimensional flows were also quantified. The shedding frequencies in the cylinder wake showed two general branches characterising the frequency responses with increasing Reynolds numbers for most cylinder inclinations, except for the wake of the cylinder inclined at $\alpha = 30^\circ$. The forces induced on the cylinder were also quantified, and its relation to the various wake patterns were explored.

The two-dimensional solution branch has now been characterised. The next question pertains to when and how these flows might transition to a three-dimensional flow. This is addressed in the following chapter through a global linear stability analysis of these wakes.

Chapter 4

Stability of the cylinder wake

The cases investigated in the previous chapter spanned Reynolds numbers beyond where the flow is anticipated to become three-dimensional. Investigations on the wake transitions behind circular and square cylinders report the flows to become three-dimensional through either modes A or C, with the latter being the preferred mode when the flow experiences some asymmetry owing to the cylinder shape (Williamson, 1988b; Robichaux *et al.*, 1999; Sheard *et al.*, 2009, amongst others). Those studies show that the initial three-dimensional manifestation of the flow occurs at Reynolds numbers ranging over $115 \lesssim Re_A \leq 190$ in both the circular and square cylinders. Mode switching to various other modes such as mode B (Williamson, 1988b, amongst others), the quasi-periodic mode QP (Blackburn & Lopez, 2003), or to mode C (Sheard *et al.*, 2003) can also be observed at higher Reynolds numbers in certain cases. Knowing now that the subharmonic mode C arises due to an asymmetry in the wake (Sheard *et al.*, 2003, 2009; Blackburn & Sheard, 2010), it is then of interest to investigate the extent through which this asymmetry plays a role in the bifurcation scenario. The current setup provides a means to vary the level of asymmetry introduced into the flow through the cylinder inclination since flow separation at high Reynolds numbers are fixed to the sharp cylinder edges (vertices of the cross-section). This chapter presents the results from a linear stability analysis of the two-dimensional wakes to infinitesimal two- and three-dimensional perturbations. This approach has the appeal over direct three-dimensional computations in that it elucidates the structure of the dominant instability modes leading to three-dimensional flow. The characteristics of these three-dimensional modes are first discussed in § 4.1, followed by those of the two-dimensional mode in the time-averaged wake in § 4.2 motivated by a lack of understanding of the hyper-Kármán vortex street. Some of the results included in this chapter appears in Ng *et al.* (2018).

4.1 Stability of two-dimensional time-periodic wakes

The evolution of an infinitesimal perturbation on a base flow can be posed as an eigenvalue problem as shown in § 2.3.1. In this analysis, the two dimensional base flow is time periodic and the problem is thus of a Floquet type whose solution may be expressed as

$$\hat{\mathbf{u}}(t_0 + T) = \mu \hat{\mathbf{u}}(t_0),$$

where T is the period of the base flow, μ is the (complex) Floquet multiplier, and σ is the characteristic exponent such that $|\mu| = \exp(\sigma T)$. This analysis necessarily requires the base flow to be periodic, thus placing a restriction on the range of Reynolds numbers at which it can be performed here since flows at higher Reynolds numbers for most cylinder inclinations tend to become susceptible to incommensurable secondary frequencies (associated with the formation of the secondary vortex street and also the P+S modes at higher Reynolds numbers). In general, except for the small range of cylinder inclinations exhibiting the two dimensional 2P mode, the Reynolds number used for this study is restricted to $Re \lesssim 140$.

Prior studies on the stability of flows past cylinders of various cross-sections have associated the various predicted instability modes with the complex characteristic multipliers obtained from the stability analysis as follows: both regular modes A and B observed in the wakes of circular cylinders (Barkley & Henderson, 1996; Sheard *et al.*, 2003), square cylinders (Robichaux *et al.*, 1999; Sheard *et al.*, 2009), and bluff rings (Sheard *et al.*, 2003), amongst other geometries become unstable through a positive real multiplier, indicating that the perturbations grow synchronously with the periodic base flow. Modes A and B can then be discerned through their structure and spatio-temporal symmetries — mode A retains the underlying Z_2 symmetry of the two-dimensional base flow, while mode B breaks it with a spanwise translation leading to a continuous streamwise vortex tube. At higher Reynolds numbers, Blackburn & Lopez (2003) and Blackburn *et al.* (2005) showed that a quasi-periodic mode becomes unstable through a pair of complex-conjugate multipliers simultaneously crossing the unit circle $|\mu| = 1$. For the square cylinder in Blackburn & Lopez (2003), the transition occurs at a Reynolds number of about $Re_{QP} \approx 200$, while that for the circular cylinder in Blackburn *et al.* (2005) occurs at a Reynolds number of $Re_{QP} = 380$. It was demonstrated in Marques *et al.* (2004) that flows possessing the symmetries of the Kármán vortex street, which for the circular cylinder is a system of codimension-one,

can only exhibit three generic symmetry-breaking bifurcations described by the modes above. In increasing the dimensionality of the problem, various studies (including Sheard *et al.*, 2003; Carmo *et al.*, 2008; Sheard *et al.*, 2009) find a subharmonic mode with a period-doubling bifurcation in their systems. This mode (mode C) is shown to become increasingly prevalent in the wakes of bluff bodies which obstruct the flow at an increasingly asymmetric sense — in the wakes of rings, the asymmetry is induced through a choking effect the flow experiences when passing through the ring aperture as opposed to around the ring exterior; in the staggered circular cylinders, the asymmetry is induced by offsetting the cylinders from a symmetric streamwise configuration when placed in proximity; and then for the square cylinder, this asymmetry is induced by inclination of the cross-section to the flow similar to the present study.

The subsequent sections will demonstrate that the periodic wakes of the triangular cross-section cylinder is susceptible to both the synchronous mode A, and also the subharmonic mode C, both occurring at different ranges of cylinder inclinations. The results from the stability analysis will be analysed using the Floquet exponents σ , the real part of which corresponds to the instability growth rates, in preference to the Floquet multipliers themselves, considering that the present analysis investigates the flows over a range of Reynolds numbers and cylinder inclinations, each possessing a different base flow period. The eigenspectra of these wakes are presented in § 4.1.1 and the structure of the dominant eigenmodes are elucidated in § 4.1.2. Deviations in the spatiotemporal symmetries of the base flow are then described in § 4.1.3 and are then related to the emergence of the subharmonic mode branch in the eigenspectra. In all cases, the modes are characterised by their near wake spatio-temporal symmetry, recalling that the far wake of the base flows tend to deviate from the classical Kármán vortex street symmetry.

4.1.1 Instability growth rates and neutral stability

For cases investigating the first transition to three-dimensionality (generally at Reynolds numbers $Re < 150$), the eigenspectra obtained conformed to one of several generic profiles, drawing some similarities to those reported for the square and circular cylinders. For cylinder inclinations ranging from $0^\circ \leq \alpha < 24^\circ$ and also at $\alpha = 60^\circ$, a single local maximum comprising positive real Floquet multipliers in the eigenspectra was observed (shown in figure 4.1a), the dominant wavenumbers being consistent with those found

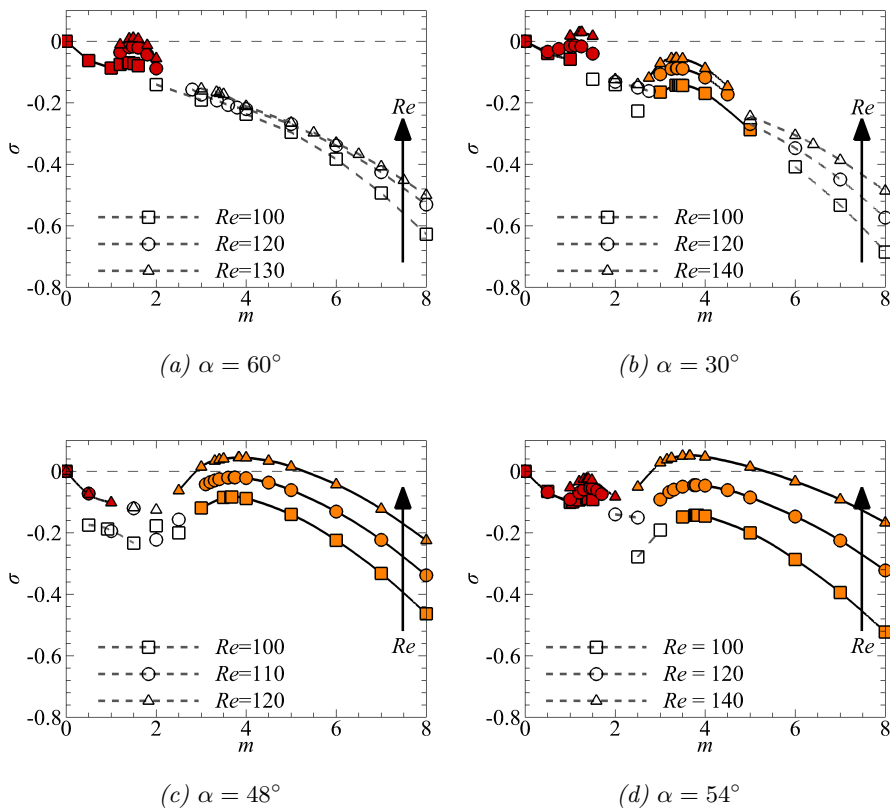


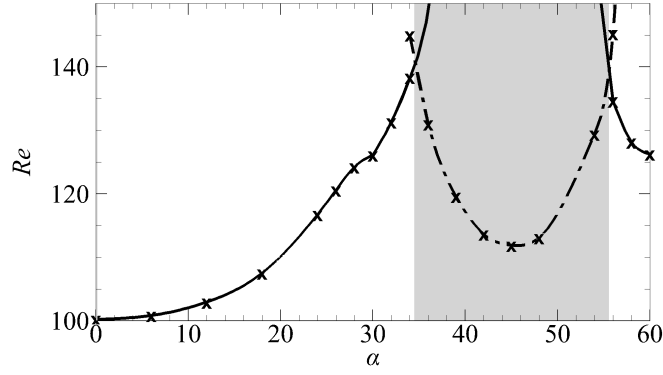
FIGURE 4.1: Generic forms of the eigenspectra of the cylinder wakes at Reynolds numbers about where a three-dimensional mode is first unstable (exceeds $\sigma = 0$). The profile shown in: (a) shows the mode A branch of solutions alone, with no mode C solutions obtained, (b) shows both modes A and C solution branches, but with the mode C branch remaining stable through a negative peak growth rate at increasing Reynolds numbers, (c) shows the mode C branch of solutions alone, with no mode A solutions obtained, and (d) is similar to that in (b), but with the reverse true where the mode A solution branch remains stable. Positive real eigenvalues are shown as red data markers, negative real eigenvalues as orange data markers, and complex-pair eigenvalues as hollow data markers.

for mode A in flows past circular and square cylinders. Negative real Floquet multipliers indicative of subharmonic modes were not obtained at these inclinations within the available range of Reynolds numbers. At cylinder inclinations $18^\circ < \alpha < 34^\circ$, the regular mode is observed to develop similarly to the lower range of inclinations, but a second local maximum composed of subharmonic eigenvalues emerges, as shown in figure 4.1(b). The subharmonic mode branches here are consistent with mode C through their negative multipliers/subharmonic synchronisation with the base flow, and also through their symmetries and wavelengths which will be elucidated subsequently.

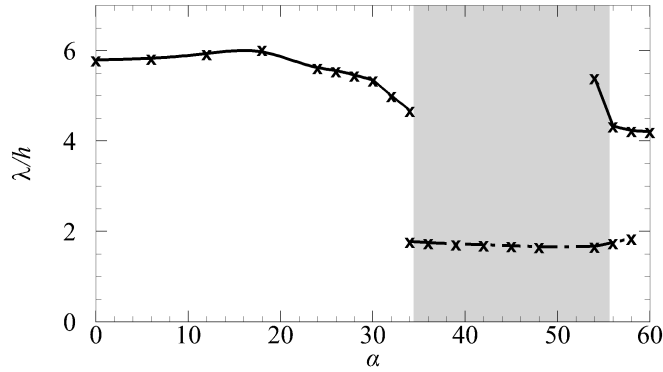
Trends of the peak growth rates versus Reynolds number for the subharmonic modes obtained within this range of inclinations describe a local maximum having negative values, indicating that the subharmonic mode here remains stable. At higher cylinder inclinations ranging $36^\circ \lesssim \alpha \lesssim 54^\circ$, a single local maximum consisting of negative real Floquet multipliers is observed; the regular mode being almost entirely absent from the perturbation growth rate profiles (shown in figure 4c). Figure 4(d) shows a scenario limited to cylinder inclinations $\alpha \approx 36^\circ$ and $\alpha \approx 54^\circ$ about which the dominant instability mode is expected to switch to (or from for the latter inclination) mode C with increasing Reynolds number. Only a small range of cylinder inclinations ($\alpha \approx 34^\circ$, and $54^\circ < \alpha < 60^\circ$) demonstrated the potential for mode C to become unstable beyond mode A, and these possess eigenspectra similar to that shown in figure 4(b), except that a positive local maximum is attainable for the subharmonic mode. As mode C for these cases is predicted to occur beyond the point of mode A becoming unstable, the flows could be sufficiently altered through nonlinear processes by the initial transition such that the onset of mode C might be observed differently (or not at all).

Figure 4.2(a) shows the neutral stability thresholds for modes A and C across the range of inclination angles. Pleasingly, neutral stability always occurs where the two-dimensional flow is periodic, and thus occurs within the range of Reynolds numbers where the stability analysis could be performed at. Across cylinder inclinations $0^\circ \leq \alpha \lesssim 34.6^\circ$, three-dimensional transition is predicted to occur via mode A, with its transition Reynolds number (Re_A) increasing monotonically from $Re_A = 100.2$ when $\alpha = 0^\circ$, to $Re_A = 126.1$ when $\alpha = 30^\circ$, and to $Re_A = 138.3$ when $\alpha = 34^\circ$ — the primary instability is predicted to switch to the subharmonic mode beyond this inclination. The rate at which Re_A increases with increasing cylinder inclination ($dRe_A/d\alpha$) shows a small shift at a cylinder inclination of approximately $\alpha = 30^\circ$, which remains even after rescaling Re_A by the cylinder side length d . The stability analysis predicts that mode A resumes as the dominant instability mode for $\alpha \gtrsim 55.4^\circ$ as the flow recovers some sense of symmetry, with $Re_A = 134.7$ at $\alpha = 56^\circ$, decreasing to $Re_A = 126.3$ when $\alpha = 60^\circ$. Within $34.6^\circ \lesssim \alpha \lesssim 55.4^\circ$, mode C is predicted to be the first-occurring three-dimensional mode. The transition Reynolds number for mode C (Re_C) decreases from $Re_C = 131.0$ at $\alpha = 36^\circ$ to reach a local minimum at $\alpha \approx 45^\circ$ with $Re_C = 111.9$, and increases again to $Re_C = 129.4$ when $\alpha = 54^\circ$.

The variation in the spanwise wavelengths of the predicted instability modes at



(a) Transition Re vs α



(b) Critical wavelengths vs α

FIGURE 4.2: (a) Neutral stability map across the range of cylinder inclinations, and (b) the corresponding critical wavelength of the instability mode at its onset. Solid lines describe the neutral stability threshold for the regular mode A, while dash-dotted lines mark that for the subharmonic mode C. Symbols (\times) mark cylinder inclinations where the stability analysis was performed.

transition are shown in figure 4.2(b). Similar to figure 4.2(a), two distinct branches corresponding to mode A are observed to be separated by the mode C branch, with the two distinct mode A branches exhibiting different ranges of wavelengths (mode A having wavelengths consistently two to three times larger than mode C). To disambiguate, the mode A branch over $0^\circ \leq \alpha \lesssim 34.6^\circ$ will be referred to as mode A_1 , and over $55.4^\circ \lesssim \alpha \leq 60^\circ$ as mode A_2 . The critical spanwise wavelengths (λ_A) of the branch corresponding to mode A_1 vary quite noticeably with the cylinder inclination, increasing from $\lambda_A = 5.80h$ at $\alpha = 0^\circ$ to $\lambda_A = 5.97h$ when $\alpha = 18^\circ$ (approximate inclination for which the wake shows the largest critical spanwise wavelengths for mode A_1), and

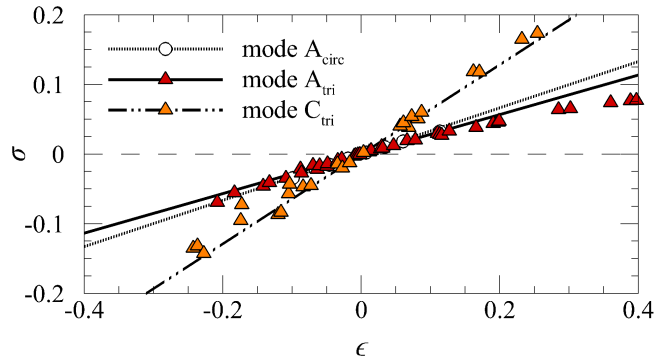


FIGURE 4.3: Variation of the peak instability growth rates with ϵ about the predicted transition Reynolds number. Red triangles (Δ) mark peak mode A growth rates, orange triangles (Δ) mark peak mode C growth rates, and hollow circles (\circ) mark those for the circular cylinder’s mode A. The lines through the data are the fitted linear approximations for each predicted instability mode: the solid line for mode A in this study, dash-dotted lines for mode C, and the dotted line for mode A in the circular cylinder wake.

decreasing thereafter. In this vicinity, a gradient discontinuity in $d\lambda_A/d\alpha$ is seen at $\alpha = 30^\circ$ mirroring the discontinuity seen in figure 4.2(a). Upon mode A_2 resuming as the dominant instability mode after the subharmonic mode branch, the critical spanwise wavelengths decrease with increasing cylinder inclination from $\lambda_A = 4.34h$ at $\alpha = 56^\circ$ to $\lambda_A = 4.21h$ at $\alpha = 60^\circ$. The mode C instability at inclinations $34.6^\circ \lesssim \alpha \lesssim 55.4^\circ$ shows an approximately consistent critical spanwise wavelength, varying from $\lambda_C = 1.75h$ at $\alpha = 36^\circ$ to $\lambda_C = 1.68h$ at $\alpha = 45^\circ$, and increasing to $\lambda_C = 1.67h$ at $\alpha = 54^\circ$. As a comparison, the critical spanwise wavelength of mode A_1 ranges between $5.34h \leq \lambda_A \leq 5.97h$ for $\alpha \leq 30^\circ$, appearing consistent with the values reported for mode A in the wakes of square cylinders in Sheard *et al.* (2009) (approximately $5d-6d$), while mode A_2 becomes unstable at wavelengths ranging $4.21h \leq \lambda_A \leq 4.34h$ which compares well with the $4h-5h$ wavelengths reported for mode A in the circular and elliptical cylinder wakes (Barkley & Henderson, 1996; Williamson, 1996a; Thompson *et al.*, 2014) as well as the square cylinder at lower inclinations (Sheard, 2011). The critical spanwise wavelengths of mode C are slightly lower than the approximately $2d$ wavelength reported for inclined square cylinders at incidence in Sheard *et al.* (2009).

To determine any generality in the growth of the linear instability modes, the variation of the growth rates with a distance parameter ϵ was determined, where

$$\epsilon = \frac{Re - Re_k}{Re_k}$$

and Re_k is the transition Reynolds numbers corresponding to modes $k = A, C$. The results are plotted in figure 4.3. Near the transition point, the function may be approximated using a linear function while enforcing that $\sigma(\epsilon = 0) = 0$. For data within $|\epsilon| \leq 0.1$, the growth rates of mode A for all cylinder inclinations collectively aggregate about $d\sigma/d\epsilon = 0.2840$, while separately, mode A_1 appears to follow $d\sigma/d\epsilon = 0.2712$ and mode A_2 follows $d\sigma/d\epsilon = 0.3461$ ($R^2 \geq 0.98$ for all cases). As a comparison, a similar function fitted through the peak growth rates of the mode A instability in the wake of the circular cylinder computed at Reynolds numbers ranging $170 \leq Re \leq 210$ is found to be $d\sigma/d\epsilon = 0.3322$. In contrast to mode A, the mode C data showed a larger scatter about the linear trend through the intercept, yielding a linear function following $d\sigma/d\epsilon = 0.6434$ with a correlation coefficient of $R^2 = 0.984$. The scatter of these points about the linear trend can be attributed to the effect of the different cylinder inclinations, which gives rise to slightly different base flows which ultimately affect the dynamics of the system. It is then interesting that the peak mode A growth rates for all cylinder inclinations aggregated strongly about a common linear trend, indicating that the different cylinder inclinations, and to a certain extent the cylinder geometry, have little effect on the growth of the mode A instability with increases in Reynolds number at low ϵ . These results also demonstrate that mode C generally develops more rapidly with increasing Reynolds number than mode A, increasing at approximately twice the rate. Despite the mode C scatter, the peak growth rates at each individual cylinder inclination still vary monotonically with Reynolds number.

4.1.2 Mode structure and symmetry

Further evidence of the regular instability modes reported in the previous section being consistent with the mode A instability in the wake of a circular cylinder, aside from the nature of the Floquet multiplier itself, can be observed through the structure of the eigenmode. In the visualisations of the perturbation field presented in this section, the dominant eigenmode predicted from the stability analysis of these wakes are superimposed on their corresponding two-dimensional base flows.

Perturbation fields are shown for cylinder inclinations $\alpha = 0^\circ, 30^\circ$, and 60° for the regular mode in figure 4.4, elucidating the three-dimensional structure of modes A_1 and A_2 . The instability is observed to develop primarily within the cores of the two-dimensional vortex loops (the translucent spanwise-oriented structures), which alludes

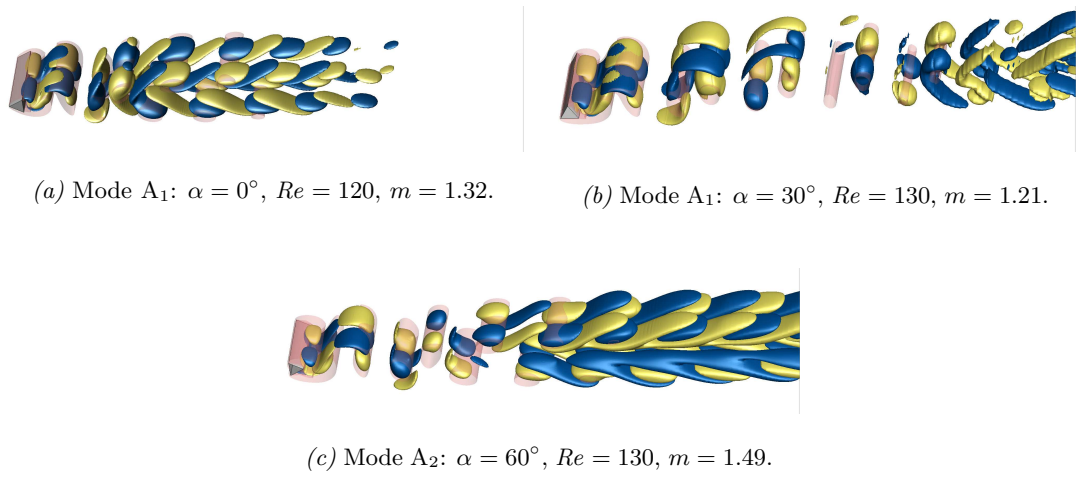


FIGURE 4.4: Superposition of the two-dimensional base flow and the three-dimensional instability mode showing the mode A structure. The flow direction is from left to right. Images are shown for cylinder inclinations (a) 0° , (b) 30° , and (c) 60° at Reynolds numbers and wavenumbers as labelled. Blue and yellow isosurfaces are the positive and negative streamwise perturbation vorticities at arbitrary levels, respectively, and the translucent red isosurfaces identify the two-dimensional vortex loops at $|\Omega_z| = 1$.

to the elliptical instability mechanism suggested by Leweke & Williamson (1998) and Thompson *et al.* (2001). A feature distinguishing mode A_1 from mode A_2 is the region where the perturbations are observed to develop strongly. For mode A_1 , the perturbation structures appear to develop more intensely in the near wake of the cylinder, decaying in strength as it moves downstream, and is consistent with mode A in the circular cylinder wake. Mode A_2 instead shows strong vortical structures developing in the downstream regions of the wake where the vortex street begins to form a dual row of like-signed vortices (corresponding to regime II discussed in § 3.2.2). For mode A_2 , the strong vortical structures in the far wake finds similarity to mode A in the wakes of the inclined square cylinder (see figure 13b in Sheard *et al.*, 2009).

The perturbation vorticity fields of mode C are shown for the cylinder inclined at $\alpha = 36^\circ$ and $\alpha = 45^\circ$ in figure 4.5. For all cylinder inclinations whose flow becomes unstable through this mode, the perturbations manifest strongly in the near wake and decays rapidly as it is advected downstream.



(a) $\alpha = 36^\circ$, $Re = 140$, $m = 3.66$.

(b) $\alpha = 45^\circ$, $Re = 120$, $m = 3.82$.

FIGURE 4.5: Mode C structure, shown for the wakes of the cylinder at inclinations (a) 36° and (b) 45° at Reynolds numbers and wavenumbers as labelled. Isosurfaces and colours are as described in figure 4.4.

4.1.3 Quantifying deviations from the Kármán vortex street symmetry

Prior studies on the stability of the wakes of various cylindrical configurations have shown the prevalence of mode C to be intrinsically linked to the geometric asymmetry about the horizontal centreline. Sheard *et al.* (2009) and Rao *et al.* (2017) showed that mode C takes over as the dominant instability when the cylinder is generally most non-symmetrically aligned. As such, it was surprising to note that mode C in this study becomes unstable at incidence angles $\alpha > 30^\circ$, despite the cylinder at an inclination of $\alpha = 30^\circ$ possessing the largest geometric asymmetry, as observed through the maximum lift coefficients incurred on the cylinder (hence having the largest flow asymmetry about the body) about this incidence angle (Ng *et al.*, 2016). Mode symmetry studies by Marques *et al.* (2004) and Blackburn *et al.* (2005) have described the generic bifurcations for wakes possessing spatio-temporal symmetries consistent with the ideal Kármán vortex street, with Blackburn & Sheard (2010) further showing a smooth transition from the generic quasi-periodic mode to one of a subharmonic nature as the wake symmetry was gradually broken beyond a small finite level. Indeed, in studies by Sheard *et al.* (2003) and Carmo *et al.* (2008) who respectively investigated the stability of the wakes of rings of varying slenderness and staggered cylinders, mode C was observable only at specific parameter values where the flow field generally produces *enough* of an asymmetric form. Considering that the stability of these wakes are entirely described from the characteristics of their base flows, the results obtained from the present stability analysis then pose a question regarding the extent to which the two-dimensional base flow can be asymmetric before mode C takes over as the preferred instability over mode A, and whether a robust measure of this asymmetry

exists. Experiments on flows past a circular cylinder with a trip wire by Yildirim *et al.* (2013b) elucidated the mode C structure similar to Zhang *et al.* (1995), but further attempted to characterise the three-dimensional mode. They showed an imbalance in the streamwise flow fluctuations about the wake centreline, and also showed the unequal strengths of counter-rotating spanwise vortices at a position $10d$ downstream. The present study extends this idea of asymmetry by first proposing and quantifying several measures alluding to a deviation in symmetry, and further attempts to draw a connection from these deviations in ideal symmetries to the observed instability modes from the stability analysis. The results for the remainder of this section are computed for the two-dimensional flows at the transition Reynolds number where they are linearly unstable to three-dimensional perturbations, such that $\epsilon = (Re - Re_k)/Re_k = 0$.

The ideal Kármán vortex street possesses the spatio-temporal symmetry

$$\begin{aligned} U(x, y, t) &= U(x, -y, t + T/2) = U(x, y, t + T), \\ V(x, y, t) &= -V(x, -y, t + T/2) = V(x, y, t + T), \\ P(x, y, t) &= P(x, -y, t + T/2) = P(x, y, t + T), \end{aligned} \quad (4.1)$$

where $(U, V, P)(x, y, t)$ are the streamwise and transverse velocity fields and the pressure field, respectively, and T is the time period of the base flow. The spanwise vorticity ($\Omega_z = \partial V/\partial x - \partial U/\partial y$) thus exhibits the symmetry

$$\Omega_z(x, y, t) = -\Omega_z(x, -y, t + T/2) = \Omega_z(x, y, t + T). \quad (4.2)$$

Denoting the peak vorticity of the counter-clockwise and clockwise rotating vortices as

$$\begin{aligned} \Omega_z^+(x) &= \Omega_z(x, y^+(x), t^+(x)), \\ \Omega_z^-(x) &= \Omega_z(x, y^-(x), t^-(x)), \end{aligned} \quad (4.3)$$

where the spatial and temporal trajectory of these peak vorticities are traced by $y^\pm(x)$ and $t^\pm(x)$, then, ideally, $y^+(x) = -y^-(x)$, $t^+(x)/T = t^-(x)/T + 1/2$, and $|\Omega_z^+(x)| = |\Omega_z^-(x)|$. Indeed, these relations are observed to hold in the laminar wakes of the circular cylinder. However, the wakes of the two-dimensional base flows for non-reflection-symmetric cylinder inclinations in this study exhibit small deviations, as expected.

4.1.3.1 Deviation of the wake centreline

In exploiting the symmetry conditions in (4.1) and (4.2) to quantify the degree of asymmetry in the flow, it became apparent that these only hold for cases where the

flow is reflection symmetric about the wake centreplane, which will only arise in cases where the body is aligned symmetrically to the oncoming flow. Increasing the cylinder inclination here quite rapidly caused the wake centreline to deviate from the centreplane $y = 0$. Further to this, a phase bias in the periodic signal was observed at intermediate (non-symmetric) cylinder inclinations, such that temporal events in the two-dimensional base flow are not reflection symmetric about $T/2$ like those for the circular cylinder. Re-arranging the spatiotemporal symmetry expressions in (4.1) and (4.2) leads to the following deviation measures:

$$\begin{aligned}\Delta U &= \left| U(x, y, t) - U\left(x, -y, t + \frac{T}{2}\right) \right|, \\ \Delta V &= \left| V(x, y, t) + V\left(x, -y, t + \frac{T}{2}\right) \right|, \\ \Delta\Omega_z &= \left| \Omega_z(x, y, t) + \Omega_z\left(x, -y, t + \frac{T}{2}\right) \right|.\end{aligned}\quad (4.4)$$

This deviation of the wake from the half-period-flip mapping is demonstrated in figure 4.6. The sequence of images show the discrepancy fields ΔU , ΔV and $\Delta\Omega_z$ for the wakes of the cylinder at asymmetric inclinations of $\alpha = 30^\circ$ and 45° and symmetric inclination of $\alpha = 60^\circ$.

Immediately noticeable is that the deviation fields of the asymmetric cylinder orientations shown are quite substantial since the vortex streets of the cylinder wake at these incidence angles tend to traverse at a slight angle away from the horizontal (as described in the previous chapter). Applying the reflection map on these cases is therefore unhelpful; the symmetry of these flow fields cannot be so simply represented. It was then of interest to understand how much the cylinder inclination affects the degree of this deviation, a question which has received little attention in the literature. For the circular cylinder, the wake centreline (denoted as y_c for brevity) of the two-dimensional flow conveniently traces through the points of the:

1. maximum streamwise velocity defect in the mean flow ($\max |\overline{U} - U_0|$),
2. zero transverse velocity in the mean flow ($\overline{V} = 0$),
3. maximum transverse velocity fluctuations ($\max |V'|$),

which all equally reside at $y_c = 0$. However, this was not the case for asymmetric triangular cylinder inclinations where the centreline traced out based on $\max(|V'|)$ was found to be consistently a small amount higher than that determined by the maximum

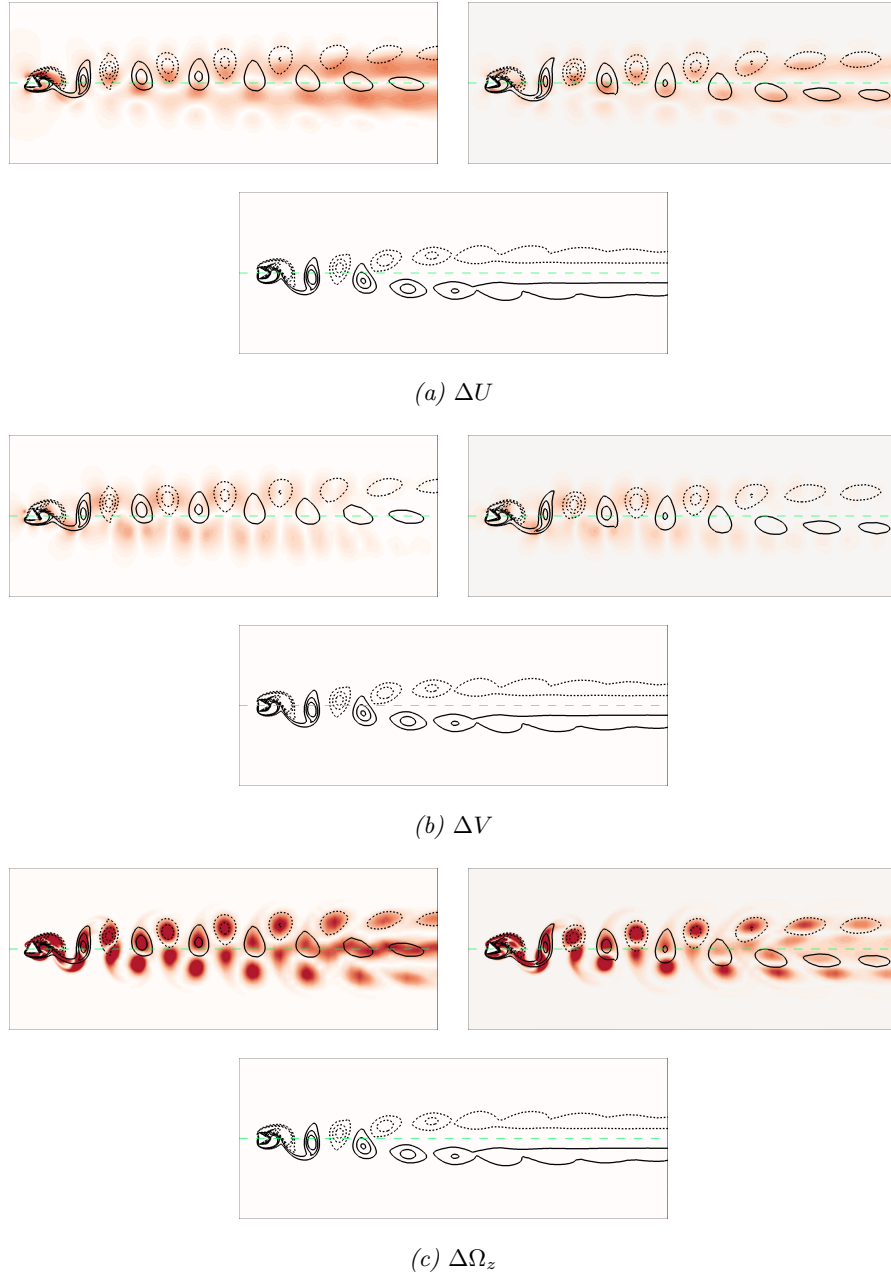
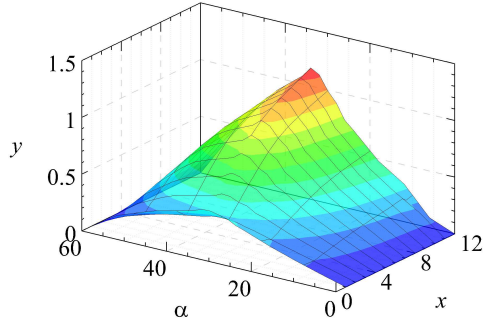
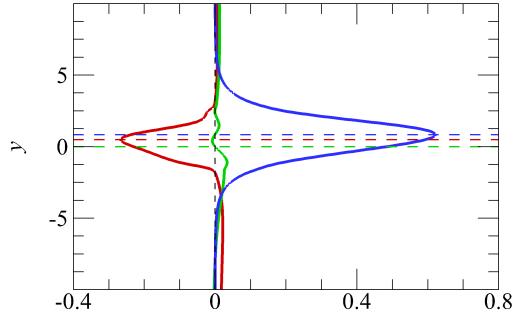


FIGURE 4.6: Plot of the deviation fields (a) ΔU , (b) ΔV , and (c) $\Delta\Omega_z$ for the wakes of the triangular cylinder inclined at (clockwise from top left of each panel) $\alpha = 30^\circ$, 45° and 60° . The contours change from white to red with increasing error magnitudes with the black solid and dashed lines marking the positive and negative values of $\Omega_z(t_0)$ at select equispaced levels describing the two-dimensional vortex street at an arbitrary time t_0 for guidance, and the green dashed line describing the ‘centreline’ $y = 0$.



(a) Variation of the wake centreline for the flow at $Re \approx Re_c$.



(b) Profiles of the $\alpha = 36^\circ$ cylinder wake at $x/h = 5$.

FIGURE 4.7: (a) Variation of the wake centreline (y_c) of the two-dimensional vortex street estimated using the $\max(|V'|)$ criteria — the wake centreline measured using this criteria was consistently at a larger deflection from the horizontal centreline for all cylinder inclinations α and positions x measured, and so it can be taken as a ‘worst-case’ scenario for lack of a clear prior definition. (b) Profiles of the mean streamwise velocity defect ($\overline{U} - U_0$) (red line), mean transverse velocity \overline{V} (green line), and r.m.s. of the transverse velocity V' (blue line), taken at a position $x = 5h$ downstream of the cylinder inclined at $\alpha = 36^\circ$, at a Reynolds number $Re = 140$. Matching coloured dashed lines are drawn at the y_c value predicted from each method.

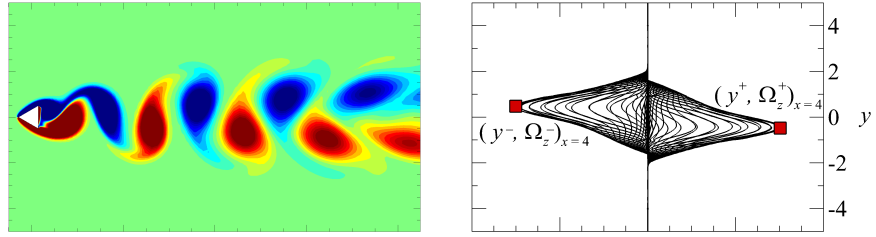
streamwise velocity deficit. The centreline of the wake of the cylinder inclined at 36° was observed to be deflected the most from all measures, with only symmetric inclinations $\alpha = 0^\circ$ and 60° possessing a $y_c = 0$ wake centreline. These are elucidated in figure 4.7. These wake centrelines also vary with the Reynolds number, but the extent of which was not investigated here.

4.1.3.2 Measures of global asymmetry

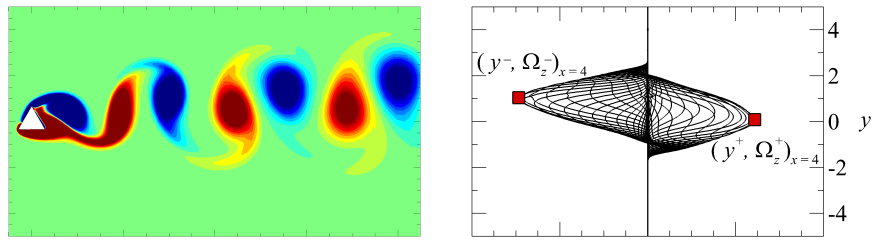
Given that a ‘half-period’ in a T -periodic wake should correspond to $T/2$ where, *ideally*, $T/2 = t^+ - t^-$, and that the magnitudes of the peak vorticities in each vortex core should ideally be equal at the same streamwise position, alternative means of measuring the deviations from the Kármán vortex street symmetry could be posed as

$$\begin{aligned} \epsilon_t(x) &= \left| \frac{t^+ - t^-}{T} - \frac{1}{2} \right|, \\ \epsilon_\Omega(x) &= \left| \Omega_z^+ + \Omega_z^- \right|, \end{aligned} \quad (4.5)$$

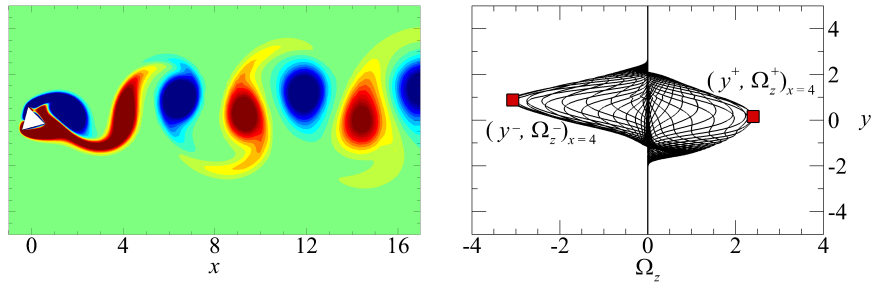
where ϵ_t estimates the imbalance in the anti-phases of the consecutive counter-rotating vortices, and ϵ_Ω measures the imbalance in the peak vorticity within each shedding



(a) $\alpha = 0^\circ$



(b) $\alpha = 30^\circ$



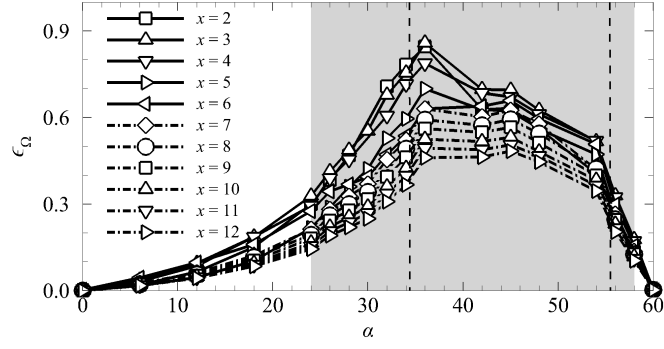
(c) $\alpha = 45^\circ$

FIGURE 4.8: (Left) Contours of spanwise vorticity (Ω_z) for the cylinder inclined at (a) 0° , (b) 30° , and (c) 45° , each of which are at a Reynolds number where the first three-dimensional mode is predicted to become unstable. Red and blue contours indicate positive and negative vorticity values, respectively. (Right) Profiles of the spanwise vorticity (Ω_z) in the cross-flow (y) direction, taken at a downstream position of $x = 4h$ at 52 equispaced time intervals over one shedding cycle, each corresponding to the flows in the left images. The red squares (■) indicate peak vorticity values Ω_z^+ ($x = 4h, y^+, t^+$) and Ω_z^- ($x = 4h, y^-, t^-$) as labelled.

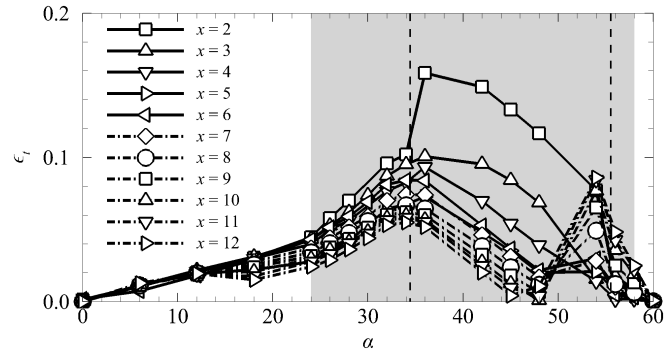
cycle, both being functions of the streamwise position x . In both measures, the flow has a perfect half-period-flip map when ϵ_t and ϵ_Ω are both 0. Measures based on the symmetry deviations of the (U, V) two-dimensional velocity fields were not utilised due to the lack of a planar wake centreline for non-symmetric cylinder inclinations. An issue that might be anticipated with these measures is that consecutive counter-rotating vortices in the two-dimensional base flow differ in size and shape spatially in the wake, and consequently in their peak strength. This is demonstrated in figure 4.8, the left frames showing instantaneous snapshots of the two-dimensional base flow vorticity field, and the corresponding plots on the right showing the temporal variation of the vorticity distribution at $x = 4h$. For the cylinder inclined at 0° shown in the top row, the cylinder presents symmetrically to the uniform flow, resulting in a vorticity profile that obeys (4.2) as expected. The following two rows of the figure correspond to the wakes of the cylinder inclined at 30° and 45° . For these asymmetric cylinder inclinations, the vorticity profile shows that the peak vorticity of the positive vortex is less in magnitude than that of the negative vortex ($|\Omega_z^+| < |\Omega_z^-|$), and that the positive vortex (as it passes the sampling position) has a broader vorticity distribution than that of the negative vortex (variation in the kurtosis of the distribution, ultimately conserving circulation). Taking these factors into consideration, the ϵ_Ω measure might be improved to account for the variability of the vortices by considering the accumulation of vorticity over a shedding cycle at various streamwise positions in the wake, as given by

$$\epsilon_\Gamma(x) = \int_t^{t+T} \int_{-\infty}^{\infty} \Omega_z(x, y, t) dy dt. \quad (4.6)$$

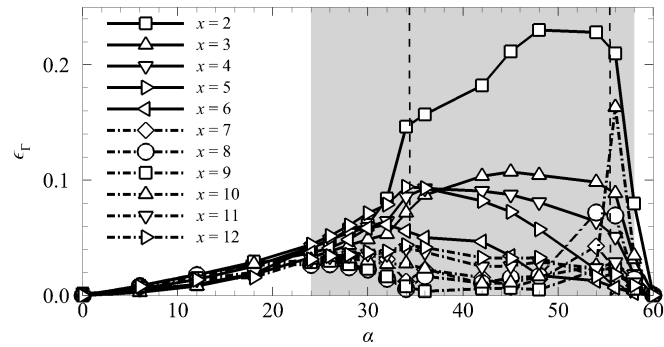
Figure 4.9 shows the variation of these asymmetry measures with cylinder inclination, obtained for flows at Reynolds numbers where the three-dimensional modes are neutrally stable. The ϵ_Ω asymmetry measure in figure 4.9(a) shows that the discrepancy in the peak vorticity of consecutive counter-rotating vortices increases with cylinder inclination, reaching a maximum at $\alpha \approx 36^\circ$, and having negligible magnitudes at reflection-symmetric inclinations. This trend is in approximate agreement with the variation of the lift force coefficient with cylinder inclination, but lacks a clear correlation with the emergence of the mode C branch besides the higher ϵ_Ω levels within the corresponding range of incidence angles (shaded region in figure 4.9). The ϵ_t levels of the two-dimensional base flows instead (shown in figure 4.9b) show a stronger correlation to the emergence of mode C, demonstrating that consecutive counter-rotating vortices in the base flow possess noticeably larger deviations in phase in the near wake



(a) ϵ_Ω



(b) ϵ_t



(c) ϵ_Γ

FIGURE 4.9: Variation of (a) ϵ_Ω , (b) ϵ_t , and (c) ϵ_Γ with cylinder inclination α . Solid lines weave through deviation values for $x/h \leq 7$, while dash-dotted lines connect deviation values for $x/h > 7$ where some wakes exhibit a change in their two-dimensional structure. The shaded region spans cylinder inclinations where the subharmonic mode branch can be observed from the stability analysis (figure 4.1b, d), while the region enclosed within the vertical dashed lines ($\alpha \approx 34^\circ$ and 54°) covers cylinder inclinations where the three-dimensional flow transition is predicted to occur via mode C (figure 4.1c).

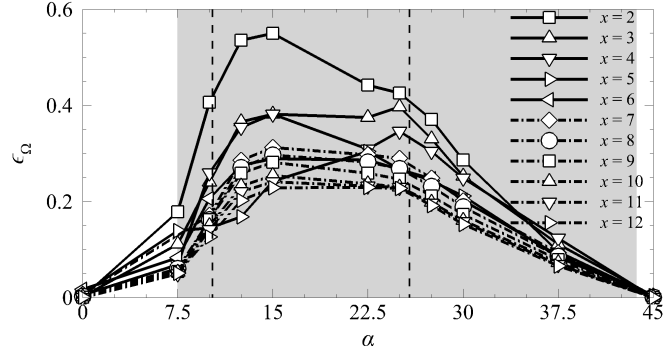
which rapidly decreases downstream within the range of inclinations where mode C can be observed. These variations in asymmetry levels for ϵ_t and ϵ_Ω may be related to the vortex shedding dynamics in the wake. For all cylinder inclinations, flow separation from the upper half of the cylinder remains fixed at the upper edge where the vortex forms. Flow separation from the underside of the cylinder experiences two different scenarios depending on the cylinder inclination. For $\alpha < 30^\circ$, flow separation and vortex formation occur similarly to the upper half of the cylinder, leading to an approximately similar vorticity distribution across both vortices. The commensurate increase in the magnitude of ϵ_Ω with increasing α then arises primarily from the difference in strengths of the flow reversal into the wake about the two rear edges of the cylinder (vertices in the cross-section), leading to increasingly unequal peak vorticities. The arrangement of vortices in the vortex street will then presumably be affected to maintain its stability, leading to the observed increase in ϵ_t . For $30^\circ \leq \alpha \lesssim 60^\circ$, the flow initially separates at the forward cylinder edge, but reattaches to the cylinder and undergoes a subsequent separation about the rear edge where the underside vortex is shed. In the latter case, the abrupt secondary separation of the already strained shear layer induces a stronger suction into the cylinder wake, entraining a proportion of the forming vortex into the upper region of the cylinder near wake. This broadens the vorticity distribution of the counter-clockwise rotating vortex, resulting in a lower peak vorticity Ω_z^+ as the vortex is shed, and thus a larger ϵ_Ω magnitude. The secondary separation and reversal about the rear cylinder edge also introduces a lag in the shedding of the underside vortex, resulting in larger ϵ_t magnitudes in the near wake.

The ϵ_Γ measure (shown in figure 4.9c) also shows a similar increase in asymmetry in the near wakes of cylinders at inclinations where mode C is observed. However, the variation of ϵ_Γ with streamwise position appears significant where the subharmonic mode branch can be detected from the stability analysis (shaded region in all plots of figure 4.9). Wakes becoming unstable through mode A show ϵ_Γ magnitudes to remain fairly constant spatially, without necessarily possessing $\epsilon_\Gamma = 0$. This implies that the flow can be asymmetric but yet remain unstable through mode A provided that the asymmetry levels (ϵ_Γ and to a certain extent ϵ_t) are consistent globally where the Kármán vortex street exists. Curiously, the rapid decay of ϵ_Γ in the wake of the cylinder for the mode C range of incidence angles correlates with the perturbation structures of the eigenmodes of mode C obtained from the stability analysis wherein the

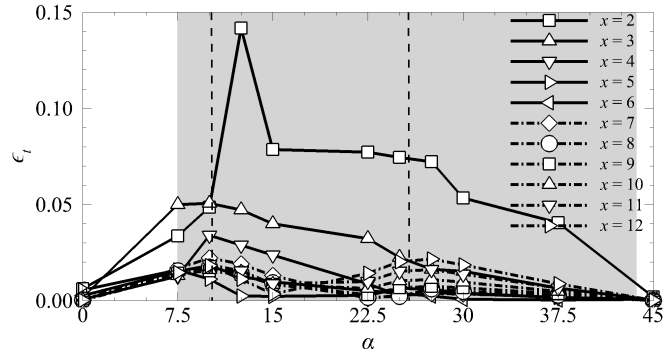
perturbations appear most intensely closest to the cylinder where the ϵ_Γ asymmetries are largest, and are almost unobservable where levels of ϵ_Γ appear low (see figure 4.5). Perhaps these imbalances in the base flow give rise to mode C instead of mode A — the instability acting as a mechanism to compensate for the asymmetries.

It is important to note that the deviations quantified here focus primarily on the near wake where structures similar to the Kármán vortex street exists, ranging between positions $2 \leq x/h \leq 12$. Wakes of the cylinder at inclinations ranging $54^\circ \lesssim \alpha \lesssim 56^\circ$ develop a dual layer wake within this range of streamwise positions, with the approximate position of the onset of the dual layer wake at $x/h \approx 7$ affecting the corresponding values of ϵ_t and ϵ_Γ as observed through the sudden increase in the asymmetry measured (figure 4.9*b,c*).

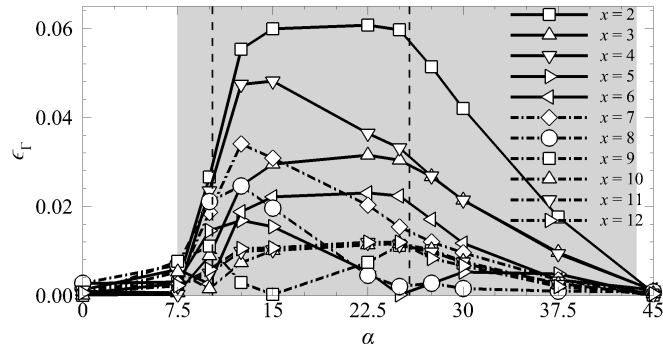
To test the predictive capacity of these asymmetry measures in more general wake flows, the measures were applied to the flows past an inclined square cylinder whose stability characteristics have been mapped and described in Sheard *et al.* (2009), Yoon *et al.* (2010), and Sheard (2011). In these studies, the first-occurring three-dimensional mode was observed to change as the inclination of the square cylinder was varied, starting with mode A when the cylinder presents a face normal to the flow (their $\alpha = 0^\circ$), changing to mode C at intermediate cylinder inclinations ($\alpha \approx 10.5^\circ - 26^\circ$), before mode A recovers as the first-occurring three-dimensional instability mode again at $\alpha \gtrsim 26^\circ$ as the cylinder orients towards a diamond shape. For these flows, ϵ_Ω , ϵ_t , and ϵ_Γ were obtained from the two-dimensional time-periodic base flows of the inclined square cylinder, generally at increments of 7.5° , and the results are shown in figure 4.10. The region enclosed within the vertical dashed lines in the figure highlights inclination ranges where linear stability analysis predicted mode C to be the first unstable mode (Sheard *et al.*, 2009; Yoon *et al.*, 2010; Sheard, 2011). Similar to the triangular cross-section cylinder wakes, the deviations obtained were larger in magnitude at cylinder inclinations where the flow becomes unstable through mode C. Both ϵ_t and ϵ_Γ for the square cylinder wake in figure 4.10(*b,c*) exhibit a similar rapid decay in space to the ϵ_Γ measure for the triangular cylinder. Since stability analysis of the wakes of the inclined square cylinder was not performed here, an estimate of the range of cylinder inclinations where the subharmonic mode branch might be observed was deduced from the spatial variation and magnitudes of ϵ_t and ϵ_Γ , and is represented by the shaded regions in figure 4.10 spanning incidence angles $7.5^\circ \lesssim \alpha < 45^\circ$. This range of cylinder inclinations



(a) ϵ_{Ω}



(b) ϵ_t



(c) ϵ_{Γ}

FIGURE 4.10: Variation of (a) ϵ_{Ω} , (b) ϵ_t , and (c) ϵ_{Γ} with cylinder inclination α for the square cylinder. Solid lines weave through deviation values for $x/h < 7$, while dashed lines connect deviation values for $x/h \geq 7$.

predicted purely from the deviations of the two-dimensional base flows from the Kármán vortex street symmetry show a strong agreement with those reported in Sheard *et al.* (2009) and Yoon *et al.* (2010) which report a range of $7.5^\circ \lesssim \alpha \lesssim 37.5^\circ$. These results are also consistent with those for the three-dimensional wake of a circular cylinder with a trip wire, where Yildirim *et al.* (2013a) describes the difference in strengths of consecutive spanwise vortices (similar to the present ϵ_Γ measure) 10 cylinder diameters downstream. The difference between the present measurements and those reported in Yildirim *et al.* (2013a) being that the present work quantifies these deviations and makes predictions of the stability characteristics purely from the two-dimensional base flows instead of requiring the full three-dimensional flow.

4.1.4 Linear instability modes in the 2P mode base flow

At higher Reynolds numbers past the onset of the first three-dimensional instability discussed in the previous section, the cylinder wake may undergo further transitions through secondary three-dimensional modes prior to the flow becoming fully turbulent. A classical example of this is the mode B transition in the circular cylinder wake which becomes linearly unstable at a Reynolds number of $Re_B = 259$ (Barkley & Henderson, 1996), a value consistent with the Reynolds number range of $230 < Re < 260$ where this mode is observed experimentally (Williamson, 1988b).

In the present study, the rapid onset of the vortex street breakdown and the subsequent development of the secondary vortex street at most cylinder inclinations preclude further linear stability analysis at higher Reynolds numbers. The 2P vortex street, however, remains periodic, and as such it is the focus of this subsection. Here, the stability analysis is performed for the wakes of cylinder inclined at $\alpha = 36^\circ$ at Reynolds numbers of $Re \leq 240$, noting that the wake of the two-dimensional flow abruptly transitions to the 2P mode at a Reynolds number of $Re_{2P} \approx 171$.

The results from the stability analysis of the 2P wake, shown in figure 4.11, show that three distinct modes can become unstable on this two dimensional base state. Two of these modes (which will be referred to as modes I and II, respectively) possess positive real Floquet multipliers, indicating that they remain synchronous to the 2P base flow, which is itself subharmonic to the original Kármán shedding frequency. The third mode (denoted mode III in this study) becomes unstable through a negative real Floquet multiplier, and as such, it is subharmonic to the 2P base flow. Mode I appears

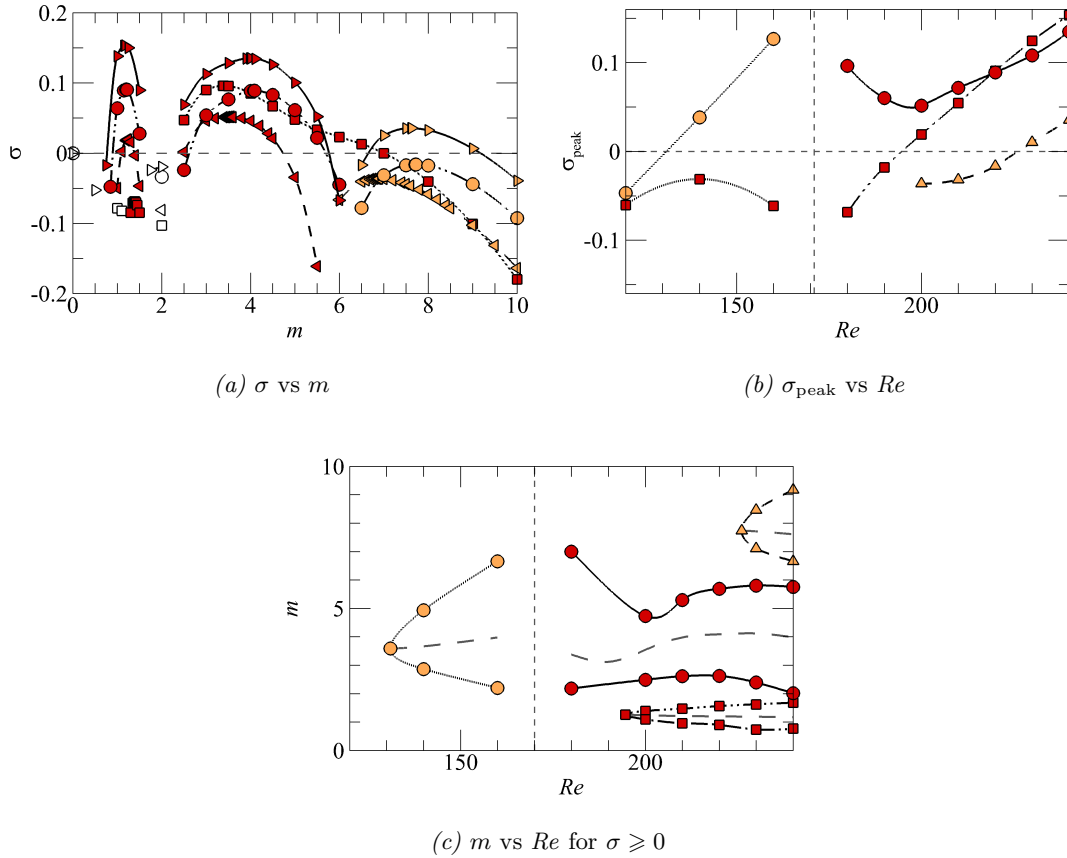


FIGURE 4.11: Plots summarising the linear stability of the 2P wake of the cylinder inclined at $\alpha = 36^\circ$. In (a), the eigenspectra shows the growth rates of the various wavenumber branches at $Re = 180$ (\square), $Re = 200$ (\triangleleft), $Re = 220$ (\circ), and $Re = 240$ (\triangleright). The plot in (b) shows the variation of the peak growth rates of each branch with the Reynolds number. For $Re \lesssim 170$, the two branches correspond to mode A (\square) and mode C (\circ), while above the 2P transition at $Re \gtrsim 170$, the three branches correspond to modes I (\square), II (\circ), and III (\triangle). The plot in (c) shows the map of unstable wavenumbers over the range of Reynolds numbers tested, with the marker symbols corresponding to those described in (b). For all plots, modes with positive real multipliers are coloured in red, negative real multipliers in orange, and complex multipliers as hollow markers.

at a band of wavenumbers similar to mode A as shown in figure 4.11(c), becoming unstable at a transition Reynolds number of $Re_I = 194.6$ with a critical wavenumber of $m_I = 1.26$. Mode II is instead found to be unstable over a band of wavenumbers consistent with those for mode C, and is already unstable at the Re_{2P} of the base flow, continuing on (almost) from mode C. The third mode, mode III, becomes critical at a transition Reynolds number of $Re_{III} = 226$ and a wavenumber of $m_{III} = 7.73$. Whether modes I and II are related to modes A and C is currently unclear — the streamwise

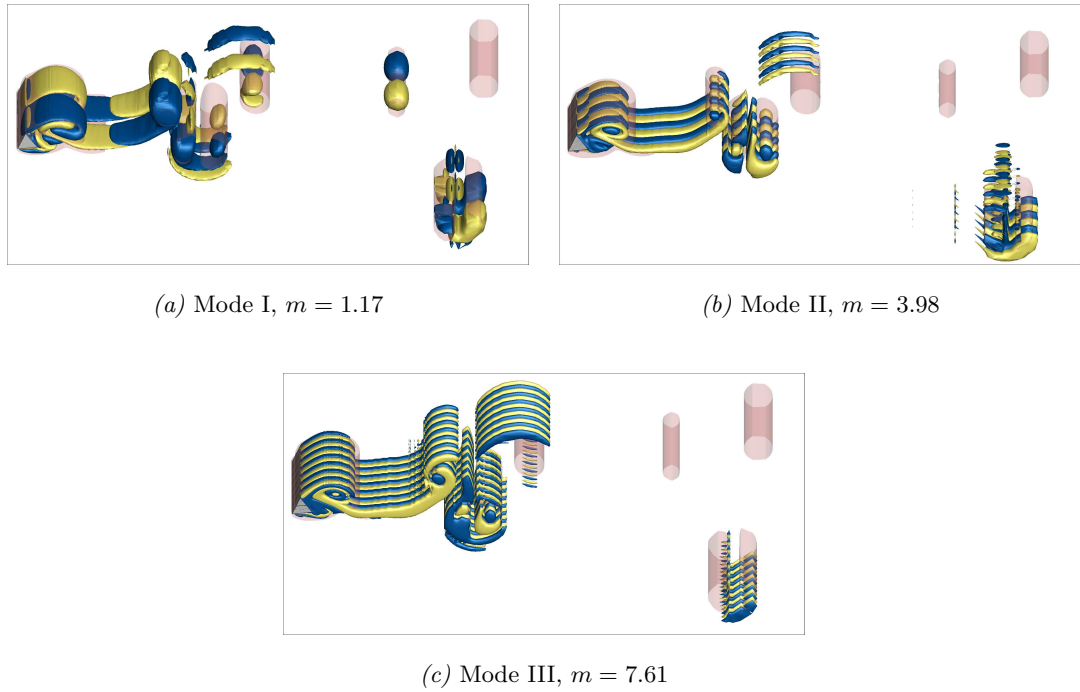


FIGURE 4.12: Streamwise perturbation vorticity fields for modes I, II, and III in the 2P wake of the cylinder inclined at $\alpha = 36^\circ$ at $Re = 240$ as labelled. The fields shown for modes II and III are duplicated by several wavelengths to show the spanwise periodicity of the structure at a similar out-of-plane length to mode I. The isosurfaces and colours are as described in figure 4.4.

perturbation vortices in both eigenmodes diffuse rapidly and the spanwise vortices of the two-dimensional base flow are strongly clustered as shown in figure 4.12, rendering the task of identifying their spatiotemporal symmetries difficult. Regardless, modes I and II are at least distinct from modes A and C since the base flows on which they develop possess different dynamics as discussed in the previous chapter. This argument applies to all three modes found here, and so the mode nomenclature was intentionally made different. This choice is further supported by the disconnect observed in the trends of the growth rates of the dominant mode about the 2P transition Reynolds number as shown in figure 4.11(c) — the function gradients appear discontinuous about Re_{2P} between mode C and mode II. It is worth noting at this juncture that Yang *et al.* (2013) have reported that a similar regular mode (mode D) becomes unstable in the wake of an inclined flat plate where the base flow has a complex structure similar to the 2P vortex street here, smoothly taking over the mode C branch with increasing Reynolds number. Mode D in the inclined flat plate wake is similar to mode II in the

present study through the similar band of wavenumbers continuing from mode C with increasing Reynolds numbers, the synchronous nature of the instability mode to the subharmonic base flow, and also through some similarity in the near wake perturbation vorticity structure.

The streamwise vorticity fields of these modes are shown in figure 4.12. For mode I, the perturbations grow strongly within the elliptic cores of the base flow vortices similar to mode A. The perturbations are also observed to decay rapidly in the wake. The perturbation field for mode II instead shows the perturbation vortices to develop strongly in the ‘braid’ regions of the flow between the base flow vortices, the vortex rollers past one shedding cycle lacking any perturbations within it unlike mode I. The perturbation structures for mode III are also concentrated to the braid regions of the base flow similar to mode II, but is structurally different.

Having characterised the linear stabilities of the two-dimensional time-periodic wakes to three-dimensional disturbances through all the time periodic wake regimes, the mechanics behind the formation of the various unsteady two-dimensional wake patterns described in chapter 3 is next investigated through a linear stability analysis of the mean flows.

4.2 Stability of the time-averaged wakes

While the previous section investigated the growth of three-dimensional perturbations on two-dimensional time-periodic base flows, this section redirects the focus back on the variety of vortex streets observed in the cylinder wake as described in § 3.2.2, investigating if two-dimensional modes of the linearised system play a role in the formation of the various vortex streets observed.

The technique of analysing the mean flow profile to deduce the stability characteristics is not new, with Cimbala *et al.* (1988) investigating the onset of the secondary vortex street through a stability analysis of the time-mean profile of the wake. Their study implemented a spatial local stability analysis in which the flow is assumed to be locally parallel (which the authors also conceded was not an accurate description of the mean wake itself), and demonstrated that a low frequency temporal mode is dominant in the far wake in contrast with the near wake’s shedding frequency corresponding to the Kármán shedding frequency. Their study used this as evidence that the secondary vortex street arises from an instability in the mean wake instead of originating through

a vortex merging mechanism. Barkley (2006), also considering the wake of a circular cylinder, further showed that the mean wake of the two-dimensional flow performed exceedingly well in global linear stability analyses, demonstrating that the predicted eigenfrequencies match the Strouhal numbers of the two-dimensional flow, and that spacings between the perturbation vorticity maxima match those from the underlying vortex street, both to a high accuracy compared to the eigenmodes obtained from stability analysis of the steady flow solutions. The only drawback observed in using this method was that the linear growth rates obtained from the mean flows were essentially zero at all Reynolds numbers tested, which Barkley explains as the modes being marginally stable states when viewed through the forced Navier–Stokes equations. Another study by Kumar & Mittal (2012) demonstrated that the linear mode in the time averaged wake of the circular cylinder causing the emergence of the secondary vortex street at $Re = 150$ is convective in nature — the perturbation kinetic energy in their control volume decreases abruptly as the disturbance wavepacket exits the domain in their time integration of the disturbance equations initialised with the dominant convective mode, and so the process is not self-sustaining.

The present section continues this investigation on the wakes of inclined triangular cylinders, performing global linear stability analysis on the wakes of the time-averaged flows in an inertial frame as opposed to a moving frame as implemented in the study by Kumar & Mittal — it is acknowledged that the instability of interest may be convective in nature, but the present focus is on the perturbation structures and growth rate trends at increasing Reynolds numbers instead of the wavespeeds observing the largest growth, as well as the plausibility for an absolute instability. For this study, cylinder inclinations of $\alpha = 0^\circ, 24^\circ$ and 60° were used to investigate the linear stability of the time averaged wakes to determine if any mode may be related to the secondary vortex street. The analysis was also extended to the time mean wakes of the cylinder inclined at $\alpha = 36^\circ$ and 42° to observe if any two-dimensional linear modes may help describe the formation of the 2P and P+S modes of the two-dimensional flow.

Discrete time averaging of the flow field was performed as the unsteady flow was evolved, such that

$$\bar{\mathbf{U}}_N = \frac{1}{N} \sum_{k=1}^N \mathbf{U}_k, \quad (4.7)$$

where N denotes the number of discrete time solutions used to obtain the average. Considering the nature of the solver employed, and the memory requirements of storing

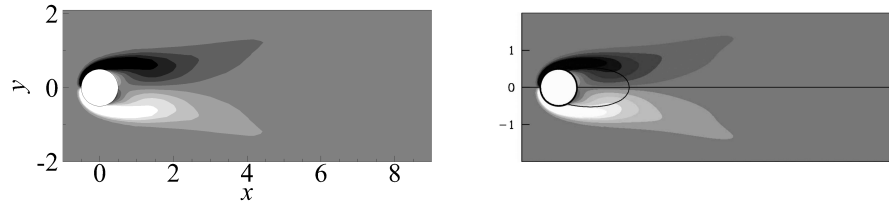
a large number of fields necessary to obtain a decent estimate of the mean flow field, (4.7) can be re-formed for the k^{th} update as

$$\bar{U}_k = \left(\frac{k-1}{k}\right)\bar{U}_{k-1} + \left(\frac{1}{k}\right)U_k. \quad (4.8)$$

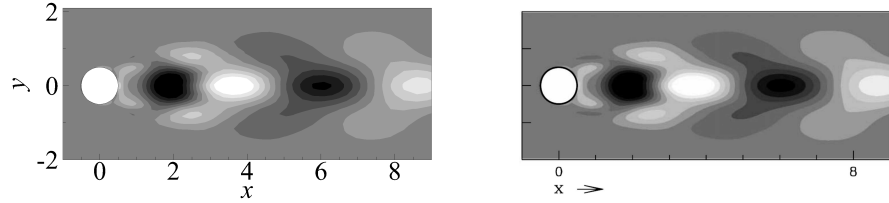
In this form, the mean flow field when including an additional snapshot can be obtained by updating the previous estimate of the mean. This enables the mean for a large number of discrete-time flow fields to be obtained while storing only one additional flow field during time integration. $(k-1)/k$ is then the scaling coefficient of the previous estimate of the time-averaged field, which in the current context can be interpreted as the amount that the mean flow field changes with each additional solution provided, and is thus useful as a crude convergence measure. In the present work, the time-averaged flow solution is obtained from evolving the unsteady flow over a span of dimensionless time $t = 1000$ using 144000 discrete snapshots of the flow (inclusion of additional snapshots of the solution affects the mean flow at a magnitude of less than $144000^{-1} \approx \mathcal{O}(10^{-6})$). Test cases using Reynolds numbers of $Re = 100$ and 200 past the cylinder inclined at $\alpha = 60^\circ$ was performed to assess the convergence of the time-averaged flow, comparing the mean flow solutions at $t = 1000$ and $t = 1050$. The domain integrated kinetic energies differed by $\mathcal{O}(10^{-8})$ and $\mathcal{O}(10^{-6})$ for the flows at $Re = 100$ and 200 , respectively. Convergence of the flow in the far wake was also considered, the maximum velocity difference being $\mathcal{O}(10^{-3})$ at $x = 30h$ for the $Re = 200$ case. These measures both suggest that the velocity fields of the mean flow are sufficiently time invariant.

For the stability analysis of these mean flows, appropriate boundary conditions are applied to ensure that those for the base flow satisfies the required boundary conditions described in § 2.5. A two-dimensional perturbation field having zero spanwise wavenumber is evolved using the linearised equations (2.21) to obtain the leading eigenmodes at each Reynolds number. Several tests were performed for the circular cylinder wake to validate the numerical setup. The time averaged flow of the circular cylinder at $Re = 100$ was linearly unstable with a growth rate of $\sigma = 0.002 \approx 0$ and an eigenfrequency of $f = 0.165$ which closely matched the two-dimensional shedding frequency of $St = 0.167$, and the perturbation vorticity field of the eigenmode was visually identical to that reported in Barkley (2006), as shown in figure 4.13.

The results obtained from the global stability analysis of the mean wakes at cylinder inclinations $\alpha = 0^\circ, 24^\circ$, and 60° predicts three different instability modes. Two of



(a) Plots of $\overline{\Omega_z}$

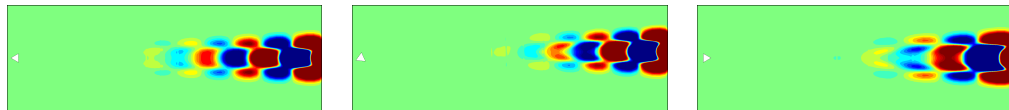


(b) Plots of $\hat{\omega}_z$

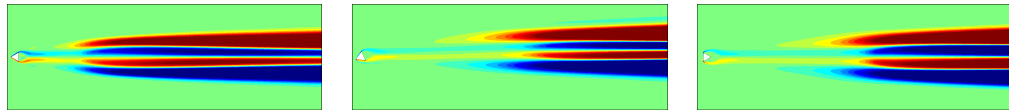
FIGURE 4.13: Validation of the time averaging and linear stability analysis using an $Re = 100$ flow past the circular cylinder. The mean wake is shown in (a) and its eigenmode from the stability analysis in (b), both colour matched to the corresponding plots from Barkley (2006) shown on the right panels. These plots on the right are reproduced from Barkley (2006) with permission from EDP Sciences.



(a) *BvK* mode



(b) *Sec* mode



(c) *Bil* mode

FIGURE 4.14: Spanwise perturbation vorticity fields ($\hat{\omega}_z$) of the *BvK*, *Sec*, and *Bil* modes as labelled. Figures from left to right are for the cylinder inclined at $\alpha = 0^\circ, 24^\circ$, and 60° , respectively. Blue and red contours indicate negative and positive perturbation vorticity values.

these modes are distinct complex pairs in competition over most of the higher Reynolds number range computed ($100 \leq Re \leq 200$), and the third mode occurs through a positive real eigenvalue. One of these complex modes is responsible for the Kármán vortex street, possessing perturbation structures concentrated in the near wake and resembling those reported for the circular cylinder in Barkley (2006) and Kumar & Mittal (2012), amongst others. A quick comparison of the frequency of this eigenmode against the Strouhal numbers obtained from the unsteady two-dimensional base flows (for cases where the base flow remained T -periodic) further confirms that this mode is indeed closely related to, if not responsible for, the primary instability, the shedding frequency obtained from the corresponding mode matching the Strouhal number of the flow to within 3%. The second of these complex modes again possesses perturbation structures reminiscent of those responsible for the Kármán street but manifests in the far wake and possesses perturbation structures of larger scales, similar to the dominant convective mode reported in Kumar & Mittal (2012) for the onset of the secondary vortex street in the circular cylinder wake. The third mode with a positive real eigenvalue shows a perturbation vorticity field which suggests its association with the vortex street breakdown to the parallel shear layer. For brevity, the first complex mode growing in the near wake is labelled the *BvK* mode, the second complex mode growing in the far wake the *Sec* mode, and the steady mode the *Bil* mode. The perturbation fields for each mode is depicted in figure 4.14.

The growth rates of the *BvK* and *Sec* modes for various Reynolds numbers are plotted in figure 4.15. For the mean wake of the cylinder inclined at $\alpha = 24^\circ$ and 60° , the plot shows that the *BvK* mode possesses a small growth rate across the computed Reynolds number range. These growth rates can be considered small enough to be consistent with the results reported by Barkley (2006). At $Re \gtrsim 120$, the mean wakes of the cylinder inclined at 0° predicts only the *Sec* mode. The lack of the *Bil*- and *BvK* modes can be attributed to the separation of the rows of vortices in the vortex street which precludes the formation of the typical Kármán street, and likewise the *BvK* mode. This separation of the rows of vortices can be clearly observed in figure 3.15 for the wake of the cylinder inclined at $\alpha = 0^\circ$ at $Re = 160$, and also in recent experimental visualisations by Kim (2019). Similarly, the *Bil* mode was not found to be amongst the leading eigenmodes at cylinder inclinations $\alpha = 24^\circ$ and 60° at $Re \gtrsim 120$, but in these cases the *BvK* eigenmodes were still found. The *Sec* mode branch for the cylinder inclined

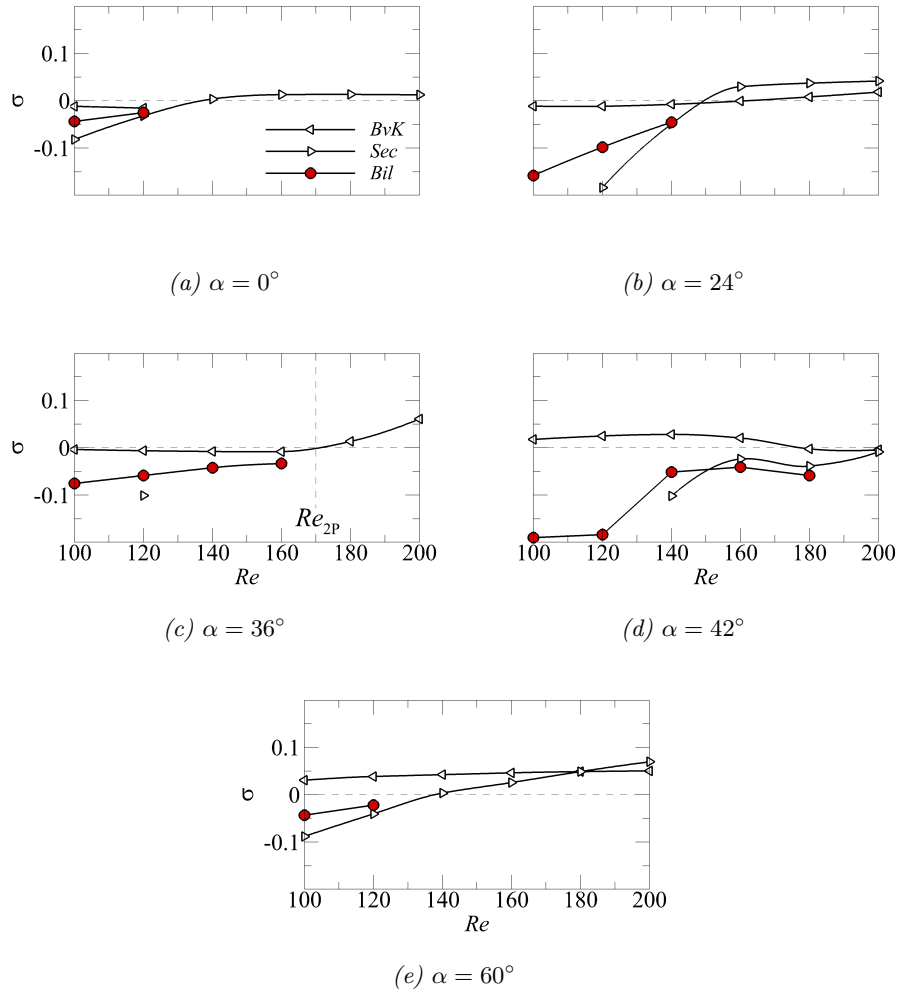


FIGURE 4.15: Variation of the linear growth rates of the leading eigenmodes in the mean wakes of the cylinder with increasing Reynolds numbers. Each plot corresponds to the case for the cylinder inclined at $\alpha = 0^\circ, 24^\circ, 36^\circ, 42^\circ$ and 60° as labelled, with the *BvK* mode marked with \triangleleft symbols, the *Sec* mode with \triangleright , and the *Bil* mode with \circ . Red filled symbols indicate positive real eigenvalues, while hollow symbols indicate complex eigenvalues.

at $\alpha = 0^\circ, 24^\circ$, and 60° generally appears to grow with increasing Reynolds numbers, and a polynomial interpolation through select data points predicts this secondary mode to become unstable in the mean flow ($\sigma = 0$) at transition Reynolds numbers of $Re_{t1}(\alpha = 0^\circ) \approx 137$, $Re_{t1}(\alpha = 24^\circ) \approx 150$, and $Re_{t1}(\alpha = 60^\circ) \approx 138$. Piecewise polynomial interpolation through the data points for the *BvK* and *Sec* modes at cylinder inclinations of $\alpha = 24^\circ$ and 60° further predicts the Reynolds number at which the *Sec* mode surpasses the *BvK* mode as the dominant instability ($\sigma_{BvK} \geq \sigma_{Sec}$) as $Re_{t2}(\alpha = 24^\circ) \approx 149$ and $Re_{t2}(\alpha = 60^\circ) \approx 180$. These predicted transition Reynolds

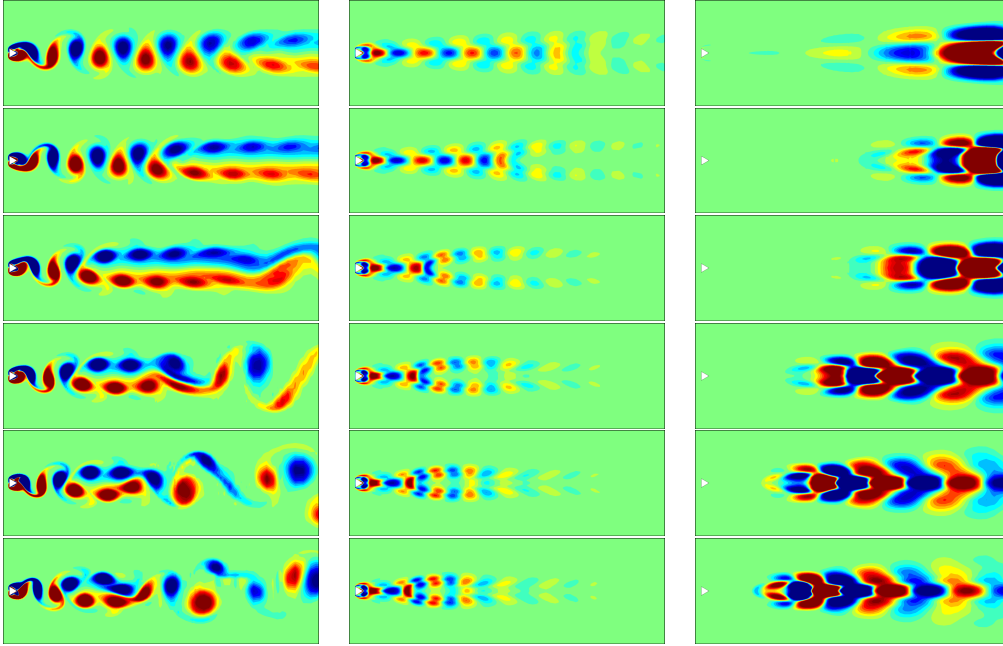


FIGURE 4.16: Variation of the *Sec* and *BvK* modes of the mean flows of the cylinder inclined at $\alpha = 60^\circ$ with increasing Reynolds numbers. Images in each column from left to right correspond to the unsteady two-dimensional base flow's vorticity field (Ω_z) and the perturbation vorticity fields ($\hat{\omega}_z$) for the *BvK*- and *Sec* modes, respectively, while each row corresponds to Reynolds numbers of $100 \leq Re \leq 200$ at increments of $\Delta Re = 20$. Blue and red contour levels denote negative and positive vorticity magnitudes, respectively.

numbers agree exceedingly well with visualisations of the unsteady two-dimensional flows, examples of which are shown in figure 4.16 for the cylinder inclined at $\alpha = 60^\circ$ — flows at Reynolds numbers $Re < Re_{t1}$ show no secondary meandering in the far wake, while those at $Re_{t1} < Re < Re_{t2}$ show that the organised dual rows of counter-rotating vortices still exist in the near wake, but also shows the spatial onset of the vortex street breakdown and the subsequent secondary meanderings in the far wake, and ultimately by $Re > Re_{t2}$ the secondary vortex street dominates the flow sufficiently that the ordered arrangement of the Kármán vortex street can no longer be properly discerned. The distance from the cylinder at which the *Sec* mode is excited decreases with increasing Reynolds number — observe the location of the perturbation vorticity field in figure 4.16 approaching the cylinder as the Reynolds number is increased.

This analysis was also performed for the wakes of the cylinder inclined at $\alpha = 36^\circ$ and 42° where the 2P and P+S modes can be observed in the unsteady wakes to understand if any meaningful linear modes of the mean flow are associated with these

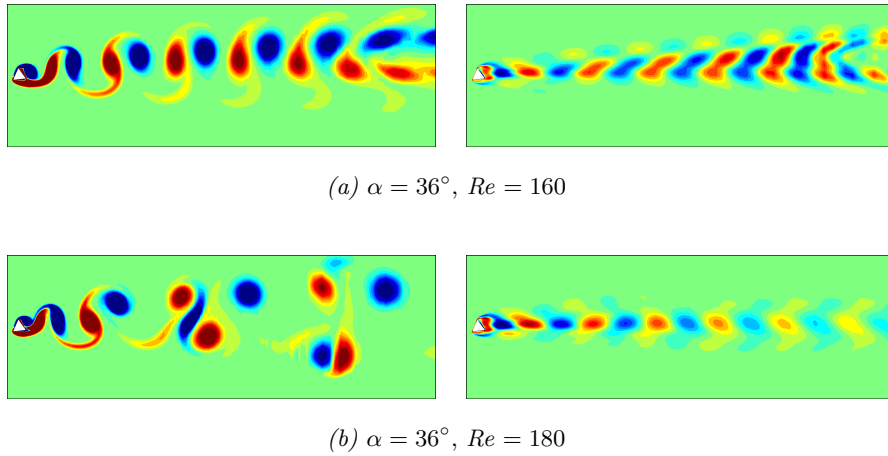
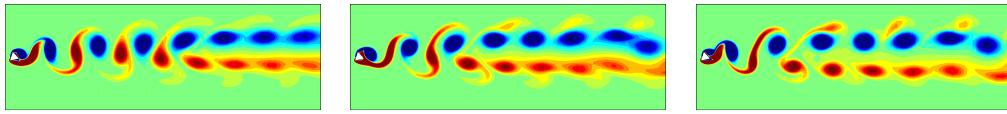
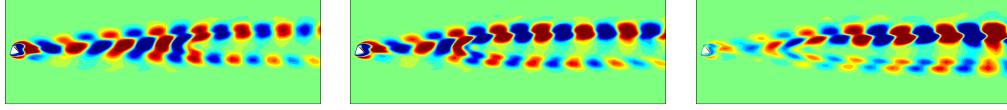


FIGURE 4.17: Plots of the unsteady two-dimensional base flow vorticity fields on the left and the *BvK* mode perturbation vorticity field on the right for the cylinder inclined at $\alpha = 36^\circ$. The top row is at a pre-2P base flow Reynolds number of $Re = 160$, while the bottom row is at a Reynolds number of $Re = 180$ where the 2P base flow can be observed. Blue and red contour colours denote negative and positive vorticity magnitudes, respectively.

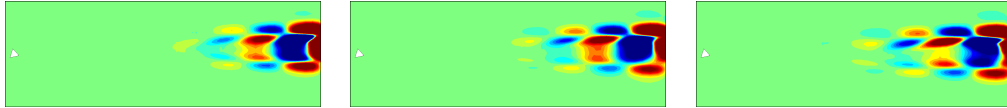
vortex street variations. While none were found, several peculiar features were observed in the eigenspectra of these cases. For the cylinder inclined at $\alpha = 36^\circ$, the *Sec* mode branch was absent within the range of Reynolds numbers tested ($Re \leq 200$), and the *Bil* mode branch was only observed up to a pre-2P mode Reynolds number of $Re = 160$. The *BvK* mode, however, was observed to grow strongly on the time averaged 2P base flow ($Re > 160$), differing from the *BvK* modes observed at other cylinder inclinations where the growth rates remain at a relatively low magnitude (≈ 0 in the circular cylinder wake as shown by Barkley, 2006). Piecewise polynomial interpolation of the growth rate data here predicts this mode to become unstable in the mean flow at $Re \approx 170$, which is consistent with the value predicted from interpolation of the force coefficients ($Re_{2P} \approx 171$) and from using the Stuart–Landau equation ($Re_{2P} \approx 172$). Despite the 2P transition changing the base flow drastically, the perturbation structures of the eigenmodes in the near wake of the cylinder remains similar as shown in figure 4.17, differing noticeably only in the far wake. The prevalence of the *BvK* mode in the near wake of the cylinder arises from the similarity of the mean recirculation region where the disturbances originate. The lack of another mode growing on the time mean wake of the 2P base flow can then be attributed to the lack of sufficient disturbance levels in the far wake to excite the growth of another mode like the *Sec*



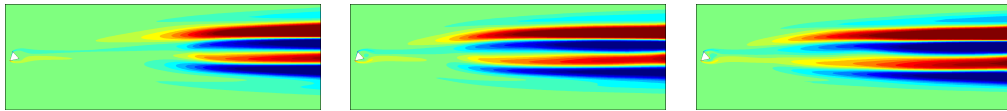
(a) Unsteady base flow vorticity field (Ω_z), $Re = 140, 160, 180$.



(b) *BvK* mode perturbation vorticity field ($\hat{\omega}_z$), $Re = 140, 160, 180$.



(c) *Sec* mode perturbation vorticity field ($\hat{\omega}_z$), $Re = 140, 160, 180$.



(d) *Bil* mode perturbation vorticity field ($\hat{\omega}_z$), $Re = 140, 160, 180$.

FIGURE 4.18: From top to bottom: plots of the two-dimensional base flow vorticity field Ω_z showing the P+S vortex street, and the perturbation vorticity fields for the *BvK*-, *Sec*-, and *Bil* modes ($\hat{\omega}_z$), respectively, with each column corresponding to flow Reynolds numbers of $Re = 140, 160$, and 180 , respectively.

mode, and also the lack of the parallel shear layer structure in the time mean wake to excite the growth of the *Bil* mode.

The time-mean flow of the cylinder inclined at 42° instead appears similar to the earlier cases for the cylinder inclined at $0^\circ, 24^\circ$ and 60° , but in this case, the growth rate of the *Sec* mode does not increase monotonically with the Reynolds number — the *Sec* mode branch appears to show a decrease in the growth rate at $Re = 180$ from $Re = 160$ before increasing again at $Re = 200$. A quick check of the unsteady base flow solutions reveal that the flows at Reynolds numbers of $140 \leq Re \leq 200$ (increments of $\Delta Re = 20$) are periodic *except* at $Re = 160$ whose flow solutions are aperiodic, and so the higher growth rate of the *Sec* mode at $Re = 160$ is reflective of it this aperiodicity. The perturbations of the *BvK* mode at $Re = 160$ and $Re = 180$ appear similar in form, but are weaker in the near wake at $Re \geq 180$, being almost unnoticeable at $Re = 200$.

The vorticity fields of the base flow and the different modes in this case are shown in figure 4.18. The growth rates of both the *BvK* and *Sec* modes are observed to be similar at $Re = 200$, indicating that an exchange of the dominant mode might occur at a higher Reynolds number. The growth rate of the *Bil* mode is also observed to feature at a comparable magnitude to that of the *Sec* mode at Reynolds numbers ranging $140 \lesssim Re \lesssim 160$. In this case, the magnitude of the *Bil* mode branch can be explained through the prominent separation of the dual rows of vortices about the apparent wake centreline.

Kumar & Mittal (2012) demonstrated that the *Sec* mode in the wake of the circular cylinder can be excited by inflow disturbances — their study reduced the time step used to march the governing equations forward in time and found that the transverse disturbance velocity fluctuations in the far wake occur at much smaller magnitudes over time. However, such magnitudes of disturbances arising from temporal or spatial resolution are easily introduced into any flow field of a physical flow from random effects — proof of this can be observed in the experimental visualisations of the vortex street breakdown and the secondary vortex street from Taneda (1959), Zdravkovich (1969), and Cimbala *et al.* (1988), the latter showing that the secondary vortex street persists far in the wake even when the smoke wire was placed far downstream to remove errors compounded by streakline memory effects.

4.3 Chapter summary

The transitions in the two-dimensional flows were investigated using linear stability analysis. Time-periodic two-dimensional flows have been found to become three-dimensionally unstable through mode A or C depending on the cylinder inclination. These modes correspond to those found in the wakes of the circular- and square cylinders. The development of the secondary vortex street in the two-dimensional flow introduces an aperiodicity in the solution, precluding analysis at higher Reynolds numbers, and so mode B was not observed in this study. The rate at which the linear growth rates increase with Reynolds number were generalised for modes A and C, finding that mode C develops faster than mode A upon detection in the eigenspectra with increasing Reynolds number. The structure and symmetry of these instability modes were then described.

Mode C has traditionally been associated with wakes which break the $Z_2 \times O(2)$

symmetry (Blackburn *et al.*, 2005; Blackburn & Sheard, 2010). The extent of this statement was investigated in this chapter. Several measures of wake asymmetries were quantified for the base flows at their corresponding three-dimensional transition Reynolds number. The wake asymmetry quantified through a half-period phase error and a local circulation imbalance demonstrated that mode C was indeed associated with deviations in the half-period-flip map. Specifically, mode C develops when the wake possesses large symmetry deviations locally in the near wake and when these wake asymmetries decay rapidly spatially in the wake. Mode A is the preferred transition mode when the wake asymmetries are approximately invariant in the wake, but can permit a finite asymmetry level regardless.

The linear stability of the 2P mode was also investigated. For the cylinder inclined at $\alpha = 36^\circ$, the 2P mode manifests at a Reynolds number of approximately 170, at which stage the time-periodic flow was already three-dimensionally unstable through mode C. At the onset of the 2P mode, the analysis predicted secondary instability modes I, II, and III, where modes I and II bore a resemblance to modes A and C. Here, modes I and II were synchronous to the $2T$ -base flow, while mode III was subharmonic. Theoretically, mode III might find interest owing to the period doubling bifurcations leading to it.

The next section of this chapter investigated the stability of the mean wakes of the cylinder. Prediction of the primary wake instability (the *BvK* mode here) from such a method have been established in the past (Barkley, 2006; Mittal, 2008). This study demonstrates the capacity of the same analysis in predicting the onset of the secondary vortex street in the two-dimensional base flow, and shows that the secondary vortex street in the wakes of the triangular cylinder in this study can be absolutely unstable on top of the convectively unstable predictions by Kumar & Mittal (2012) as evidenced by the positive growth rates of the *Sec* mode on the time-averaged base flow from the linear stability analysis as shown in figure 4.15, and also from direct two-dimensional flow computations as reported in chapter 3 where regime III (the secondary vortex street, which forms through the *Sec* mode reported here) is self-excited and self-sustaining.

Having identified the instability modes associated with the transitions in the flow, the next chapter investigates the energetics and structural sensitivity of the modes, aiming to identify the driver of the instability and its relation to the perturbation kinetic energy budget of the mode.

Chapter 5

Structural sensitivity and energetics of wake instabilities

In light of the stability results obtained from the previous chapter, it is of interest to attempt to investigate the characteristics of these instability modes to further understand their origins. Two common adjoint-based approaches used in prior works are (1) to investigate the transient energy growth of an instability mode to determine if significant energy amplification can be observed within a bounded time interval which may alter the route to instability predicted from the global stability analysis, and (2), to investigate the sensitivity of the flow to structural perturbations applied in the flow. Works by Abdessemed *et al.* (2009) and Cantwell & Barkley (2010) using transient growth analysis on the wake of a circular cylinder show that both primary and secondary instability modes predicted from the Floquet stability analysis are subjected to only modest energy amplification factors before recovering to the growth rates dictated by the stability analysis within a short time evolution. Considering this, and also since the linear modes in the current setup are not too dissimilar from those found in the wake of the circular cylinder, this chapter instead investigates the sensitivity fields of the linear instability modes which potentially locate the regions in the wake from where the instability modes may originate from (deriving from the concept of a wavemaker being the driver of the instability), as demonstrated by Giannetti & Luchini (2007). This is presented in § 5.1 of this chapter. In § 5.2, the sources of perturbation growth in the flow are investigated through the Reynolds–Orr equation, performing a perturbation kinetic energy budget of the instability to determine the terms contributing most significantly to its growth rate, and in doing so, identifying the regions from where the perturbations derive most of its growth.

5.1 Structural sensitivity of the linear instability modes

As mentioned by Luchini & Bottaro (2014), the idea of a localised region acting as the core of the instability driving the growth of a disturbance in the flow (the concept of a wavemaker) is crucial in the formulation of the concept of the sensitivity of the flow to structural perturbations. If one considers that such a localised wavemaker region exists in the flow and that the regions external to this act solely to amplify the disturbance wavepacket, then a localised forcing or modification to the flow within the wavemaker region should alter the eigenvalue of the problem most significantly, while a similar localised forcing in regions external to this should merely alter the amplitudes in the eigenvector field without affecting the eigenvalue significantly (and so they denote it the amplifier region). Giannetti & Luchini (2007) draws on this idea to derive the structural sensitivity tensor, demonstrating it on the primary instability in the wake of the circular cylinder. The spectral norm of the sensitivity tensor in that case agrees qualitatively with experimental results by Sreenivasan *et al.* (1987) on the control of the primary instability, the slight discrepancies arising from the velocity feedback of the structural perturbations onto the base flow itself. A similar analysis applied to the secondary instability in the wake of the circular cylinder is also described by Giannetti *et al.* (2010), demonstrating that the time-dependent sensitivity fields of modes A and B appear strongly localised in the near wake. Locating this wavemaker region finds significance within the flow control community where its identification may serve as an estimate of the optimal actuator placement (amongst other associated problems). The motivation for this study, however, is to develop a deeper understanding of the mechanism behind these instabilities.

For the primary instability in the wake of the circular cylinder, the regions in the flow with the highest sensitivity to structural modifications is located primarily in the recirculation region, being concentrated symmetrically about the wake centreline close to the rear stagnation point (Giannetti & Luchini, 2007). To extend those results to the wake of the triangular cylinder, the steady wakes are computed at a subcritical Reynolds number close to the predicted bifurcation parameter ($-0.15 < \epsilon < 0$ where $\epsilon = (Re - Re_c)/Re_c$) owing to the unsteady solver employed, and the spectral norm of the sensitivity tensor is then computed (method as described in § 2.3.3) — Giannetti & Luchini (2007) demonstrated that increases in the Reynolds number of the (forced) steady flow does little to affect the sensitivity field in the near wake qualitatively, thus

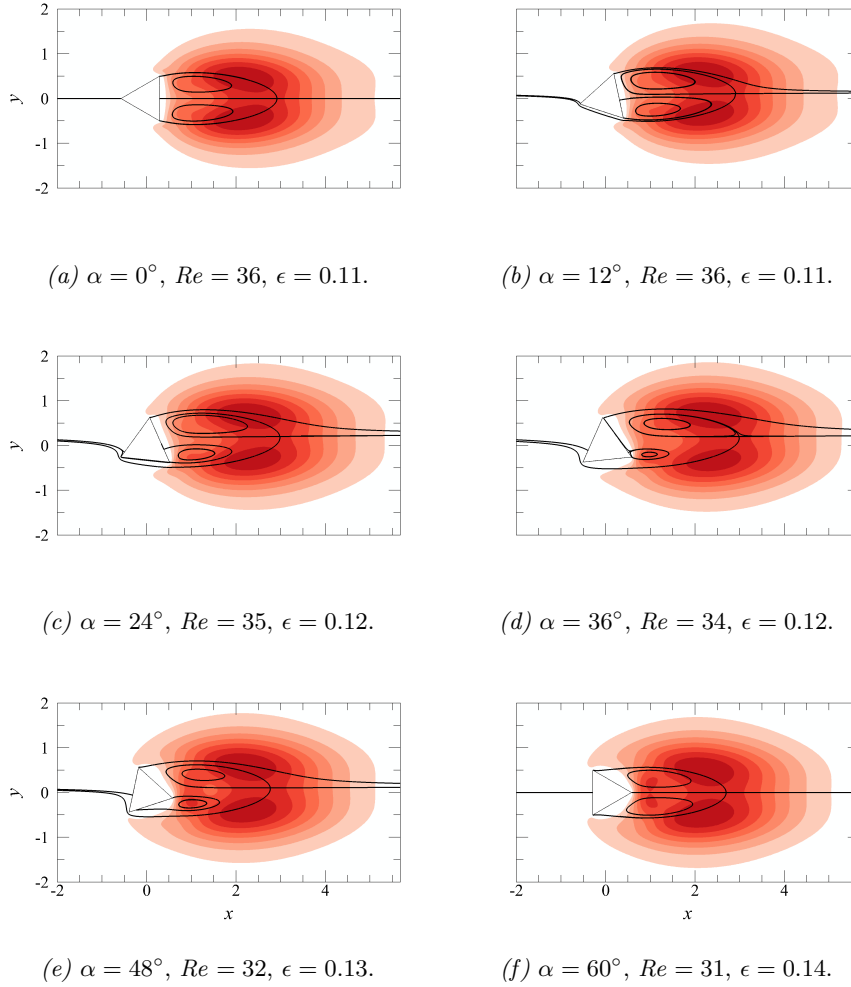
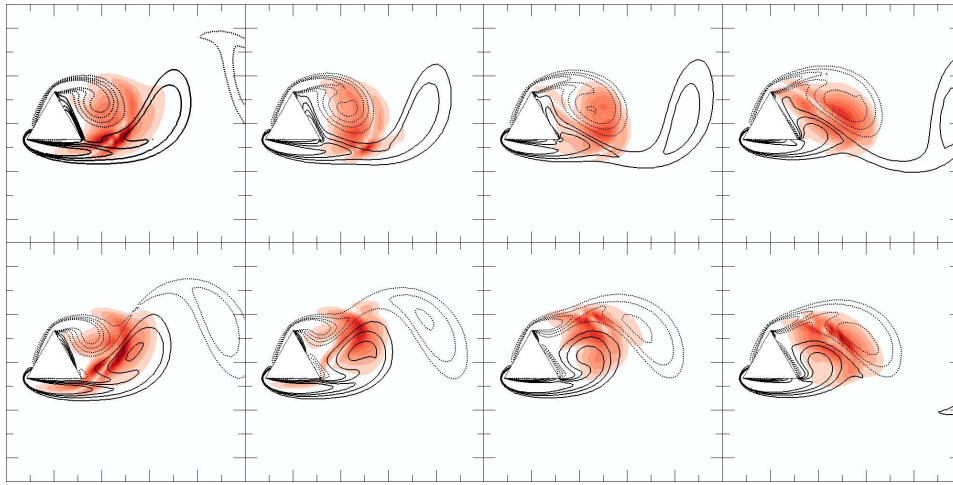


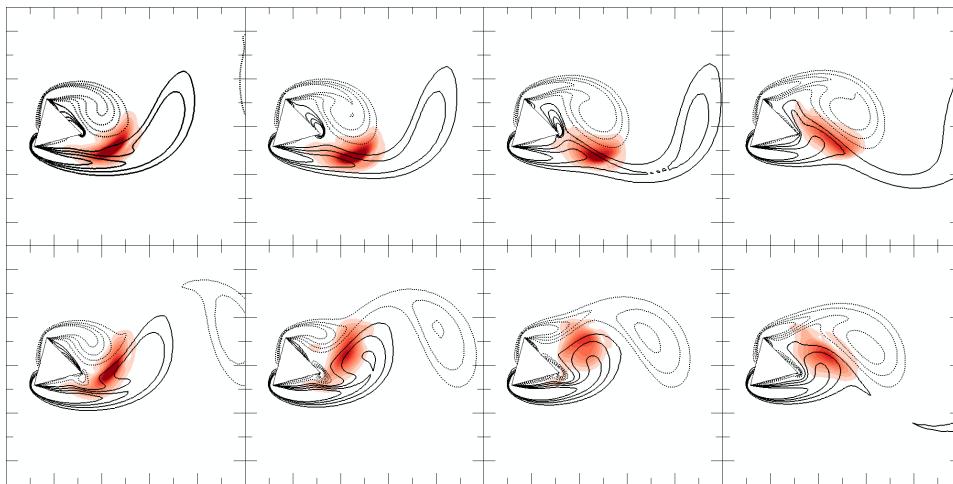
FIGURE 5.1: Spectral norm of the sensitivity tensor I for the primary instability mode in the wakes of the cylinder at various inclinations as labelled. Select streamlines are included to aid with flow visualisation. The corresponding map of I for the wake of the circular cylinder can be found in figure 2.9 and Giannetti & Luchini (2007).

lending credibility to the results obtained at the Reynolds numbers considered here.

Here, the norm of the sensitivity field obtained at all cylinder inclinations appear to be similarly distributed to that found for the primary instability in the wake of the circular cylinder, as shown in figure 5.1. Specifically, the sensitivity fields predicted generally extend from the upper flow separation point on the cylinder (the separation point on the lower side of the cylinder varies depending on the cylinder inclination — see § 3.2.1), and the regions of highest sensitivity acting as the wavemaker of the instability being located approximately symmetrically about the wake centreline near the rear stagnation point of the flow (the weak asymmetry in its distribution arises



(a) Mode A: $\alpha = 30^\circ$, $Re = 127$, $m = 1.183$.



(b) Mode C: $\alpha = 45^\circ$, $Re = 112$, $m = 3.730$.

FIGURE 5.2: Spectral norm of the instantaneous sensitivity tensor l at 8 equispaced time instants over a shedding cycle for modes A and C as labelled. The image sequence commences from the top left where base flow is at maximum lift, and proceeds in a clockwise direction. The solid/dotted lines correspond to contours of positive/negative base flow vorticity.

from the asymmetric flow field about the cylinder), akin to that found for the circular cylinder. This result was anticipated as the primary instability which manifests in the wake of the triangular cylinder is of the same mode found for the circular cylinder. Nevertheless, it was surprising how little the sharp corners and inclination variation of the cylinder here affects the sensitivity fields.

The spectral norm of the instantaneous sensitivity tensor (shown in figure 5.2) for the mode A instability similarly follows that of the same mode in the wake of the circular cylinder at similar phases of the shedding cycle shown by Giannetti *et al.* (2010), while that for mode C interestingly bears a strong resemblance to those reported for mode B. Specifically, the wavemaker for both modes A and C are localised to (and follows) the interface between the two forming counter-rotating vortices, with the sensitivity field for mode C being more concentrated within this region, while that for mode A is slightly more diffuse. Note that in all cases here, the sensitivity fields were calculated for flows where the modes have just become critical, such that $\epsilon = (Re - Re_k)/Re_k < 0.01$, where ϵ is a distance parameter to the bifurcation point, and Re_k is the transition Reynolds number predicted from the Floquet stability analysis where $k = A, C$. It was surprising how similarly the sensitivity field was distributed for these modes regardless of the cylinder inclination.

In all these cases, it was assumed that the force-velocity feedback acts purely on the disturbance field, leaving the base flow evolution equations unaltered. In reality, any structural modification applied to the disturbance field leading to such an eigenvalue drift would perturb the base flow as well. Marquet *et al.* (2008) and Luchini *et al.* (2009) demonstrated that such an effect was indeed significant to the overall eigenvalue sensitivity of the primary instability in the wake of the circular cylinder. A similar extension to the sensitivity analysis of the secondary wake instabilities incorporating perturbation feedback onto the base flow was recently derived and formalised by Giannetti *et al.* (2019). It would be interesting for future work to extend those techniques to the triangular cylinder studied here. It may be in this sensitivity of the eigenvalue to perturbation feedback onto the base flow itself where these fields truly reflect the effect of the cylinder inclination variation on the instability.

5.2 Perturbation kinetic energy budget of the linear instability modes

Another complementary study to the global stability analysis is in the consideration of the perturbation kinetic energy (PKE) equation (see § 2.3.2). The sensitivity analysis in § 5.1 reveals regions in the flow within which structural perturbations can most effectively and significantly alter the stability characteristics of the flow, and is akin to finding the core of the instability itself. The energy approach here instead maps the regions where the perturbation growth is being accelerated or inhibited, and reveals the source terms (from the PKE equation) from which these energy exchanges are derived. This perturbation kinetic energy equation (also the Reynolds–Orr equation) has, in past studies, been used for energy stability analyses of shear flows and boundary layers aiming to determine the energy Reynolds number of the system below which no perturbation energy amplification can be observed regardless of the disturbance amplitude (Schmid & Henningson, 2001). In contrast, the present study intends to determine the level of contribution of each individual term in the equation to the overall perturbation growth rate, the analysis being similar to those performed using the turbulence kinetic energy (TKE) equation. The difference between the TKE and PKE equations lie in the decomposition of the total flow — for the TKE equation, the Reynolds decomposition is used to separate the flow into its time mean and fluctuating components, and subsequent averaging retains the Reynolds stresses in both the Reynolds Averaged Navier–Stokes (RANS) and Reynolds Stress Transport (RST) equations, while for the PKE equation, the total flow decomposition into a base flow and perturbation field yields the nonlinear term (analogous to the Reynolds stresses) in the perturbation evolution equations (analogous to the RST equations) but not in the base flow equations (analogous to the RANS equations). This analysis is restricted to disturbances which are spatially periodic in the out-of-plane as a result of the spanwise-averaging simplification (see § 2.3.2), which in this context applies to flows whose characteristics are consistent with linear theory where the perturbation growth does not alter the basic state (this applies to three-dimensional flows prior to nonlinear effects dominating the flow or where nonlinearities are weak). For the remainder of this section, the analysis is conducted at the same Reynolds numbers for each cylinder inclination as those reported in § 5.1 (close to criticality), and the effect of varying the Reynolds numbers will be briefly discussed.

For convenience, the PKE equation (equation 2.25, § 2.3.2) is repeated here, introducing several new notations for brevity, such that

$$\frac{1}{E_k} \frac{dE_k}{dt} = \sum E_{\mathcal{T}} + \sum E_{\mathcal{P}} + E_{\mathcal{D}},$$

with each term on the right hand side of the equation defined as

$$\begin{aligned} E_{\mathcal{T}} &= \frac{1}{E_k} \int_{\Pi} \underbrace{-U \frac{\partial \langle k' \rangle}{\partial x}}_{\mathcal{T}_1} \underbrace{-V \frac{\partial \langle k' \rangle}{\partial y}}_{\mathcal{T}_2} d\Pi, \\ E_{\mathcal{P}} &= \frac{1}{E_k} \int_{\Pi} \underbrace{-\langle u' u' \rangle \frac{\partial U}{\partial x}}_{\mathcal{P}_1} \underbrace{-\langle u' v' \rangle \frac{\partial U}{\partial y}}_{\mathcal{P}_2} \underbrace{-\langle u' v' \rangle \frac{\partial V}{\partial x}}_{\mathcal{P}_3} \underbrace{-\langle v' v' \rangle \frac{\partial V}{\partial y}}_{\mathcal{P}_4} d\Pi, \\ E_{\mathcal{D}} &= \frac{1}{E_k} \int_{\Pi} \underbrace{-\frac{2}{Re} \langle \mathbf{s}'_{ij} \mathbf{s}'_{ij} \rangle}_{\mathcal{D}} d\Pi, \end{aligned}$$

where $k' = \mathbf{u}' \cdot \mathbf{u}'/2$ is the perturbation kinetic energy, E_k is the total PKE $\int_{\Pi} \langle k' \rangle d\Pi$, the notation E_i denotes the integral of the term i over the computational volume Π , \mathcal{T}_j are the terms quantifying the local transport of PKE by the base flow, \mathcal{P}_j are the terms quantifying the local production of PKE, \mathcal{D} quantifies the local viscous dissipation of PKE, and the terms in the angled braces $\langle \cdot \rangle$ denote spanwise averaged quantities. This equation can then be related to the Floquet exponent σ (the global growth rate of the instability) through

$$\sigma = \frac{1}{2} \left(\frac{1}{E_k} \frac{dE_k}{dt} \right).$$

For the primary instability in the wake of the cylinder, the map of each term appears qualitatively identical for all cylinder inclinations, an example of which is shown in figure 5.3. Since the instability here manifests through a complex eigenmode pair, the figure presents two instances of the map of the terms, one for an individual mode in the complex pair as shown in the left panels of figure 5.3(b-d), and the other for the combination of the complex modes as shown in the right panels. The contour levels in all panels are identical to facilitate comparison between the various terms. For the individual mode, the local transport rate ($\sum \mathcal{T}_j$) is observed to be the most significant contributor to the instability growth rate, the corresponding map of the term showing non-negligible growth in the wake past the region where the wavemaker is predicted to be, and increases in magnitude as the perturbations move downstream. This appears to incorporate both the wavemaker and amplifier regions of the perturbation growth shown

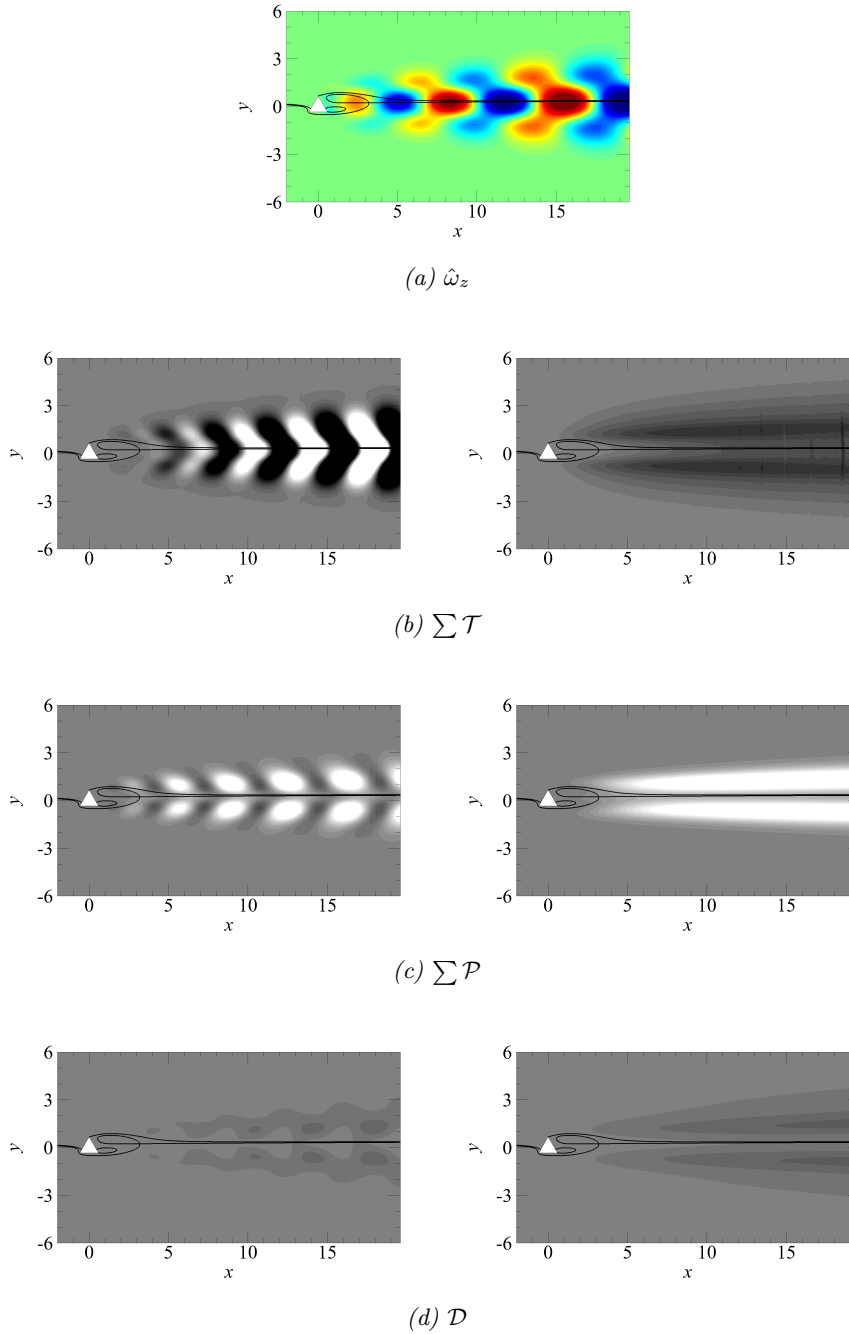


FIGURE 5.3: (a) Spanwise perturbation vorticity contours obtained for the primary instability mode at $\alpha = 30^\circ$ and $Re = 34$ (note that this mode has a complex-conjugate). (b–d) Map of the terms of the PKE equation for the primary instability in the cylinder wake, with light/dark contours corresponding to positive/negative values. The plots on the left panels are for the individual mode shown in (a), while those in the right panels are for the net contribution derived from both modes in the complex pair. In all plots, the contour levels used are identical for comparison, and select streamlines have been included to aid with flow visualisation.

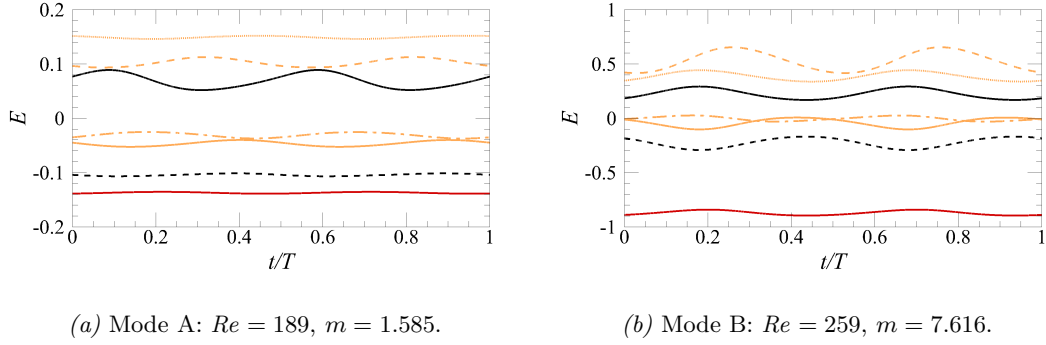


FIGURE 5.4: Plots of the time-varying magnitudes of the terms of the PKE equation over the shedding cycle for modes A and B in the circular cylinder wake as labelled. In each plot, the black continuous line (—) corresponds to term $E_{\mathcal{T}_1}$, the black dashed line (---) to $E_{\mathcal{T}_2}$, the orange continuous line (—) to $E_{\mathcal{P}_1}$, the orange dashed line (---) to $E_{\mathcal{P}_2}$, the orange dash-dotted line (—·) to $E_{\mathcal{P}_3}$, the orange dotted line (··) to $E_{\mathcal{P}_4}$, and the red continuous line (—) to $E_{\mathcal{D}}$.

in Barkley (2005) and Giannetti & Luchini (2007). The PKE production rate instead begins to increase from a location proximate to the instability wavemaker predicted from the sensitivity analysis, and shows periodically occurring regions of large PKE growth downstream of the recirculation region. When considering the action of both conjugate modes simultaneously, the local rate of transport of PKE remains negative throughout the wake indicating that it experiences an overall decrease as the disturbances are advected downstream. The production term on the other hand appears strongly positive in the wake region entirely, being largely contributed to by term $E_{\mathcal{P}_2}$ ($\langle u'v' \rangle dU/dy$). The PKE dissipation rate in either case appears low within the field of view shown in the figure, although its volume total is of the same order as the total PKE production rate ($\mathcal{O}(E_{\mathcal{D}}) = \mathcal{O}(\sum E_{\mathcal{P}})$). The maps shown in figure 5.3 agree exceedingly well with the corresponding plots by Mittal (2009) for the circular cylinder. Although the cases in the present study were computed at subcritical Reynolds numbers, the distribution of these maps are expected to remain qualitatively similar even at higher Reynolds numbers past the primary instability as demonstrated by Mittal (2009).

The next stage of this study was to then investigate the energetics of the secondary instabilities in the cylinder wake, an analysis which was curiously lacking in the bluff body wake literature except for a brief mention by Rocco (2014). For this reason, this analysis was also performed for instability modes A and B found in the wake of

the circular cylinder for comparison with the present results. The structure of this section is as follows: the time varying profiles of each term in the volume integrated PKE equation are first presented, followed by a discussion of the trends of their period averages, and finally the time-varying distribution of each term within the flow field is reported. The flows computed here were at the same Reynolds numbers used in § 5.1, being within 1% past the transition Reynolds numbers ($\epsilon < 0.01$) reported in § 4.1, and so the largest growth rates observed here were of $\mathcal{O}(10^{-3})$.

The time-varying magnitudes of each term in the PKE equation are described across figures 5.4–5.6, each corresponding to modes A and B in the circular cylinder wake, the mode A cases in the present study, and finally the mode C cases. For all mode A cases (figures 5.4a and 5.5), the only obvious similarity appears to be that the two most dominant production terms are $E_{\mathcal{P}_2}$ and $E_{\mathcal{P}_4}$ which are associated with the transverse base flow velocity gradients ($\partial_y \mathbf{U}$), and that viscous dissipation $E_{\mathcal{D}}$ acts most dominantly to inhibit the perturbation growth as anticipated. In contrast, plots of the terms for the mode C instability (figure 5.6) appear more synchronised across the various cylinder inclinations. The most dominant production terms for mode C are again the $E_{\mathcal{P}_2}$ and $E_{\mathcal{P}_4}$ terms, similar to the mode A cases. Also observe that for both modes B and C in figures 5.4(b) and 5.6, the two transport terms are always in exact opposition, and so $E_{\mathcal{T}_1} + E_{\mathcal{T}_2} = 0$ at all times. This can be attributed to the near wake localisation of these modes such that the perturbations decay before reaching the outflow boundary of the computational domain, and so the net transport of PKE within the domain is necessarily zero. Mathematically (for a two-dimensional incompressible base flow),

$$\begin{aligned} \sum \mathcal{T} &= U \frac{\partial \langle k' \rangle}{\partial x} + V \frac{\partial \langle k' \rangle}{\partial y} = (\mathbf{U} \cdot \nabla) \langle k' \rangle = \nabla \cdot (\langle k' \rangle \mathbf{U}), \\ \sum E_{\mathcal{T}} &= \int_{\Pi} \nabla \cdot (\langle k' \rangle \mathbf{U}) \, d\Pi = \int_{\Pi_b} (\langle k' \rangle \mathbf{U}) \cdot \mathbf{n} \, d\Pi_b, \end{aligned}$$

where Π is the computational domain and Π_b are the boundaries along the domain, and so since $\mathbf{u}' \approx \mathbf{0}$ along Π_b for modes B and C, $\langle k' \rangle \approx 0$, resulting in $\sum E_{\mathcal{T}} = 0$ as observed. The lack of such counteracting transport terms for mode A can thus be explained by a net perturbation outflow from the computational domain, as shown in figure 4.4, § 4.1.2. This analysis was repeated for mode A in the wake of the circular cylinder using an extended outflow domain length of $l_d = 300d$ to permit further decay of the perturbations (initially $l_d = 25d$ — see § 2.3.2 for mesh details), the results showing that the transport terms $E_{\mathcal{T}_1}$ and $E_{\mathcal{T}_2}$ finally negate each other. Another noticeable difference

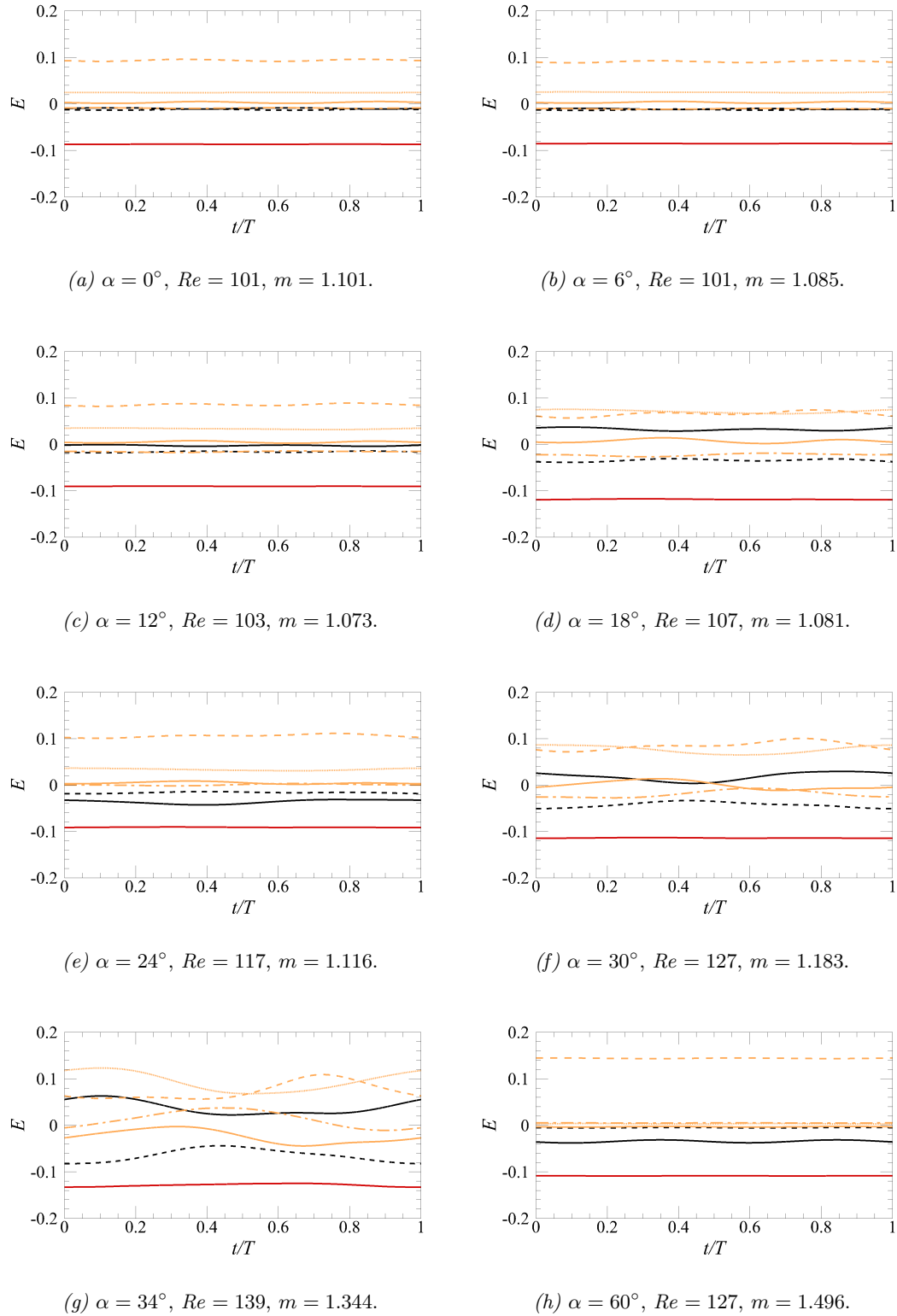
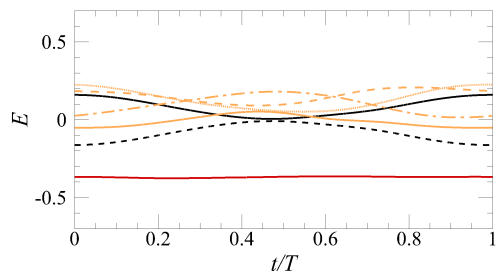
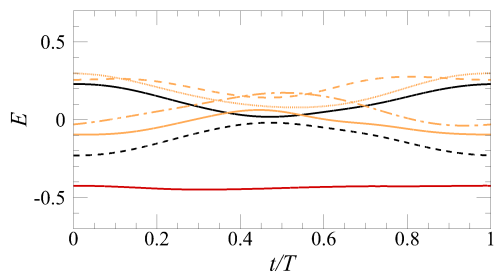


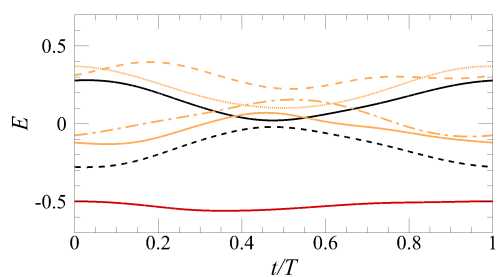
FIGURE 5.5: Caption follows that given in figure 5.4, but for the mode A cases in the triangular cylinder wake here.



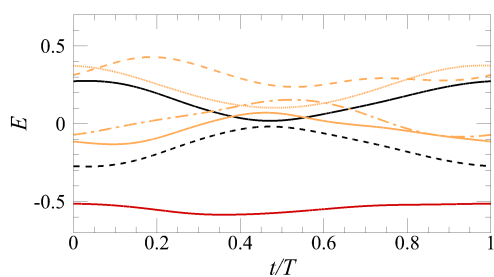
(a) $\alpha = 34^\circ$, $Re = 146$, $m = 3.539$.



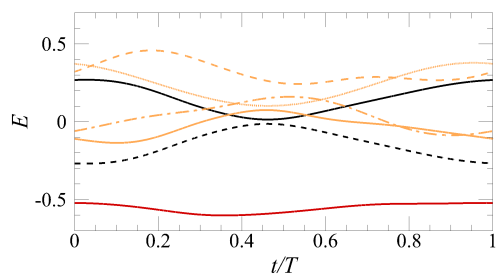
(b) $\alpha = 36^\circ$, $Re = 132$, $m = 3.590$.



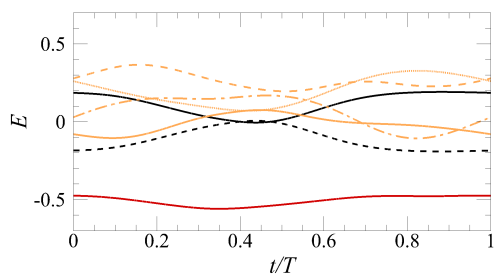
(c) $\alpha = 42^\circ$, $Re = 114$, $m = 3.684$.



(d) $\alpha = 45^\circ$, $Re = 112$, $m = 3.730$.

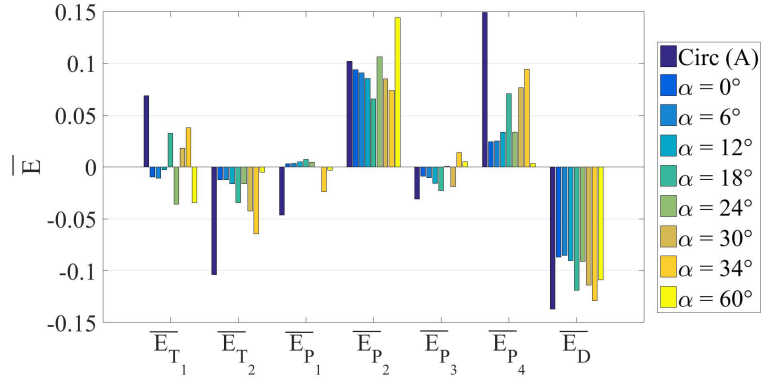


(e) $\alpha = 48^\circ$, $Re = 114$, $m = 3.782$.

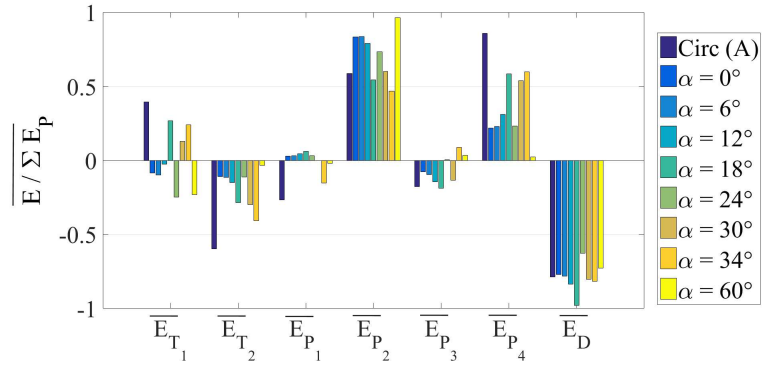


(f) $\alpha = 54^\circ$, $Re = 130$, $m = 3.757$.

FIGURE 5.6: Caption follows that given in figure 5.4, but for the mode C cases in the triangular cylinder wake here.



(a) Period-averages of terms \overline{E}_i .

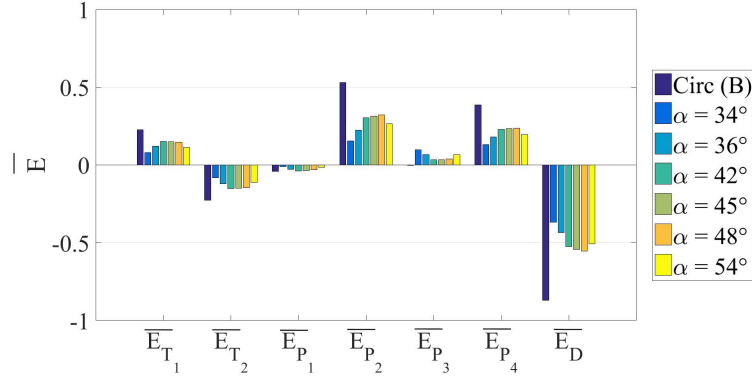


(b) Period-averages of terms $\overline{E}_i / \sum \overline{E}_P$.

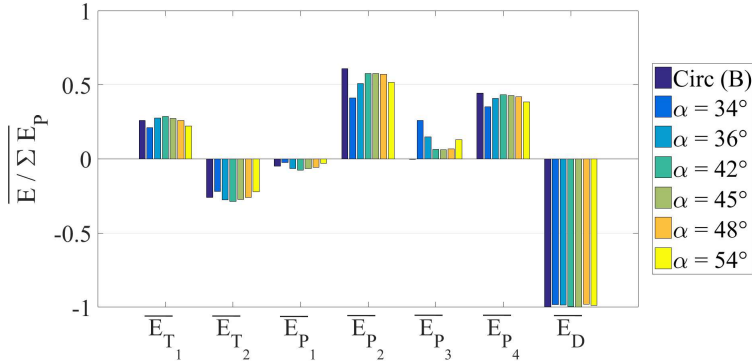
FIGURE 5.7: (a) Period-averages of the terms (\overline{E}_i) for the mode A cases. (b) Similar to the plot in (a), but with the \overline{E}_i values re-scaled by the mean total production rate $\sum \overline{E}_P$.

between the time-profiles of the PKE equation terms for the different instability modes is in the maximum magnitudes of the terms over the shedding cycle — all terms E_i for the mode A cases appear to be bounded within $|E_i| < 0.2$, the mode B case within $|E_i| \lesssim 1$, and the mode C cases within $|E_i| < 0.7$, conservatively.

The data contained within figures 5.4–5.6 is next summarised by considering the period averages of each term, the results of which are presented in figures 5.7(a) and 5.8(a). As similarly described earlier for the time varying plots, the period-averaged magnitudes of the terms, \overline{E}_i , for the mode A cases lack any clear distinguishing features across all cylinder inclinations (and also that for the circular cylinder wake) besides the fact that \overline{E}_{P_2} and \overline{E}_{P_4} are the most dominant contributors to the instability growth rate. The contribution of each term \overline{E}_i to the instability growth rate for the mode C cases



(a) Period-averages of terms \overline{E}_i .



(b) Period-averages of terms $\overline{E}_i / \sum \overline{E}_P$.

FIGURE 5.8: Caption follows that given in figure 5.7, but are for the mode C cases in the triangular cylinder wake. The data for mode B is also included in both plots (a,b) for comparison.

appear to be more consistent across the range of cylinder inclinations where mode C is the predicted transition mode. Under the argument that the transport terms are ultimately self-conserving at all times in all cases for a sufficiently large computational domain $\sum E_T = 0$, the magnitudes of \overline{E}_i were re-scaled as a percentage of the total production $\sum \overline{E}_P$, the results being shown in figures 5.7(b) and 5.8(b). The re-adjusted plots now clearly show that the magnitude of the mean total dissipation rate $|\overline{E}_D|$ for mode C (and also mode B which was included in the same figure as mode C) occurs at $\approx |\sum \overline{E}_P|$ — these cases being computed close to criticality of the modes lead to $\overline{dE_k/dt} \approx 0$, and because both transport terms counteract each other at all times for modes B and C, the PKE dissipation rate necessarily balances the total PKE production rate. Since the mode A cases were also computed close to criticality ($\overline{dE_k/dt} \approx 0$),

the discrepancy between the total PKE production rate and the PKE dissipation rate can be accounted for primarily by the net transport rate of PKE out of the domain: $\sum \overline{E_{\mathcal{P}}} + \overline{E_{\mathcal{D}}} = -\sum \overline{E_{\mathcal{T}}}$.

Having identified the terms of the PKE equation contributing most significantly to the instability growth rate, an assessment of the spatial distribution of the various terms locally within the wake is next conducted. For each mode, the maps of these terms in the wake appear to be qualitatively similar, regardless of the cylinder inclination or the cylinder cross-section geometry, and so only one representative case is shown for each mode. Figures 5.9–5.11 show the corresponding maps for modes A, B, and C, respectively, in each case showing 4 collections of terms corresponding to (a) $\sum \mathcal{T}$, (b) \mathcal{D} , (c) $\sum \mathcal{P}$, and (d) $\mathcal{P}_2 + \mathcal{P}_4$. The contour levels in all plots within each figure are all identically set to $\max_t \sum \mathcal{P}$ to enable direct comparisons across the terms.

For mode A, the net transport term $\sum \mathcal{T}$ is actively distributed throughout the wake following the base flow vortices, propagating the perturbations in the flow but contributes nothing to the instability growth rate globally. Observation of the net production terms ($\sum \mathcal{P}$) as well as the dominant production rate terms ($\mathcal{P}_2 + \mathcal{P}_4$) reveal regions where the instability growth is most aggressive. These regions possess a high PKE production rate and are observed to originate in the core of the forming vortices, intensifying within the elliptic core region as the vortex develops. These regions are then drawn out into the ‘tail’ of the shedding vortex, amplified primarily by a high strain rate. These production regions then diminish rapidly with strain after the vortex is shed and as it relaxes back into an unstrained form. Weak secondary regions of PKE production are observed to develop within the cores of the elliptical vortices further downstream, but remains at a low magnitude overall. Although not shown here, the secondary production regions which develop in the vortex cores appear to be associated with the \mathcal{P}_2 term: $\langle u'v' \rangle \partial U / \partial y$. The description of the path and movement of these production regions for mode A aligns well with the description of the co-operative elliptical instability mechanism explained by Leweke & Williamson (1998) and Thompson *et al.* (2001). Regions where the dissipation term (\mathcal{D}) act are generally found to be clustered about the interface between the forming vortices, and also in the strained ‘tail’ of the vortex as- and after it is shed. Weak PKE dissipation regions inhibiting the instability growth were also observed to accompany the vortices further downstream where the secondary production regions develop. In both primary

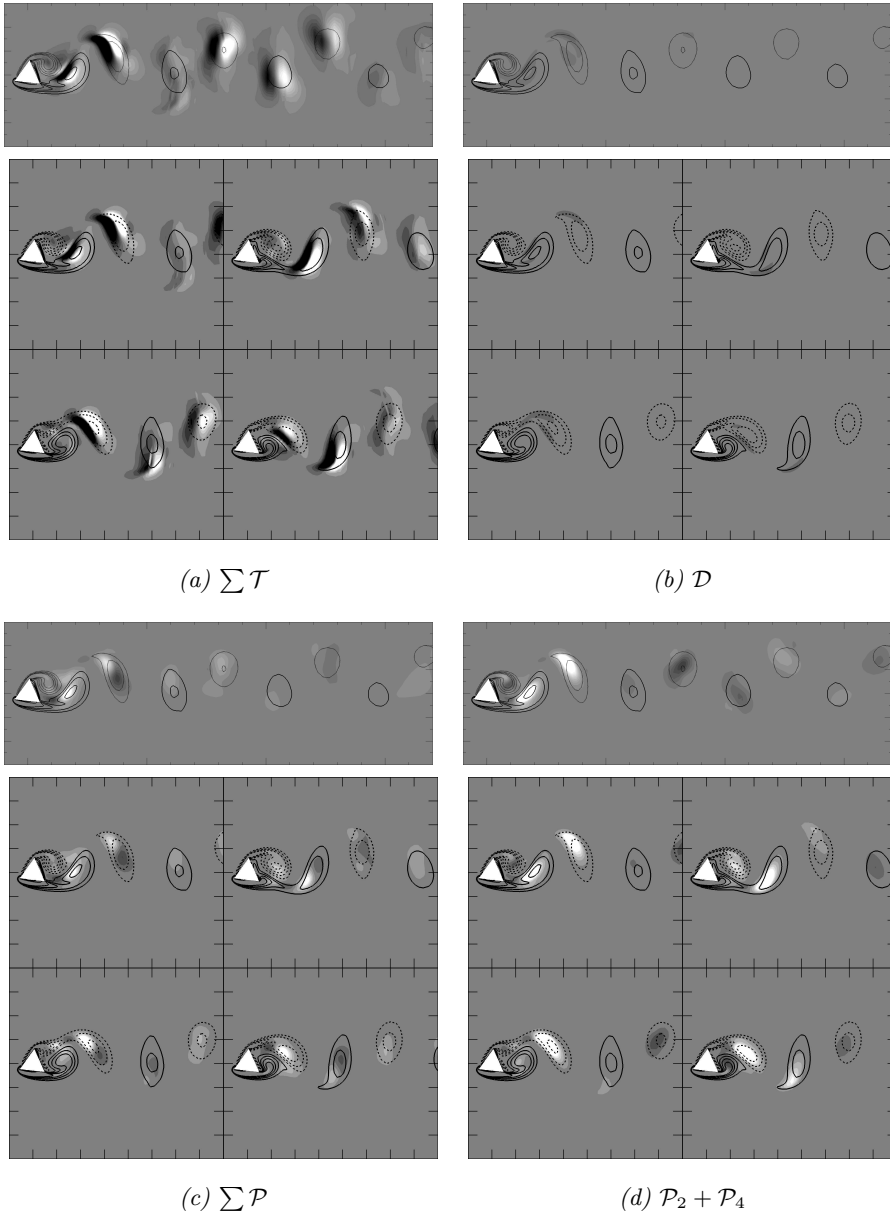


FIGURE 5.9: Map of the terms of the PKE equation (as labelled) for the mode A instability which is shown here for the cylinder inclined at $\alpha = 24^\circ$ and $Re = 117$, with light/dark contours corresponding to positive/negative magnitudes. In each panel, the top plot first shows the distribution of the term across the wake, while the bottom panel shows the time evolution of these terms at 4 equispaced time instances over a shedding cycle. In all plots, the contour levels used are identical for comparison, and the solid/dotted lines are contours of the base flow vorticity which are included to aid with flow visualisation.

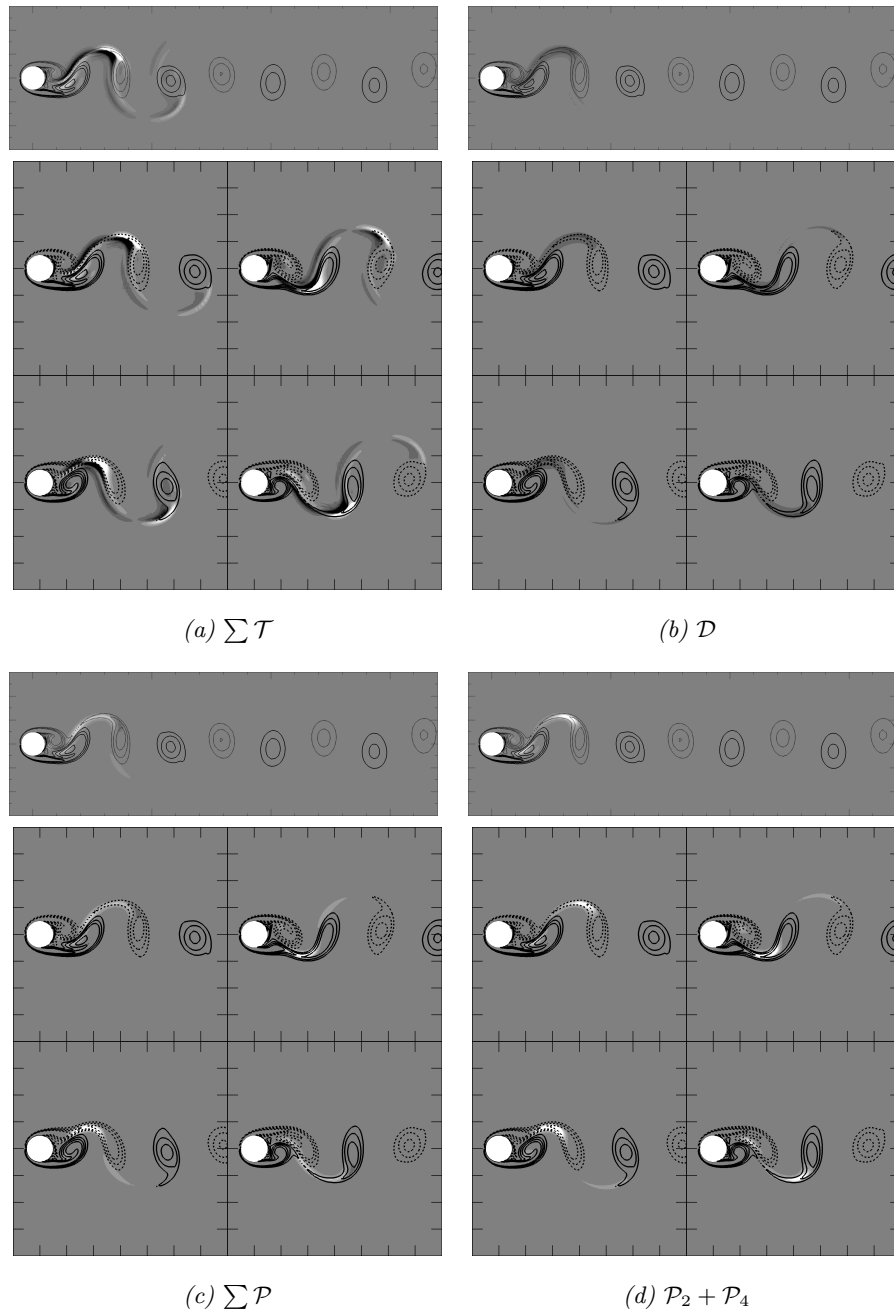


FIGURE 5.10: Caption follows that given in figure 5.9, but is for the mode B instability here shown for the wake of the circular cylinder at Reynolds numbers $Re = 259$.

and secondary regions, the local dissipation rate was observed to occur at an order of magnitude lower than those of the local transport and production terms.

The distribution of the terms of the PKE equation for modes B and C are shown in figures 5.10 and 5.11, respectively, both showing that the groups of terms appear to describe strongly similar processes over the shedding cycle, and as such both will be discussed together. The net transport terms in these cases are again observed in regions following the perturbation structure, developing strongly in the strained region of the shedding vortex, and dissipates within one vortex pair wavelength. The production regions for modes B and C here begin forming in a similar manner to those for mode A where a positive production region develops within the elliptical core of the forming vortex. However, the counter-rotating vortices in the forming region interact at an earlier phase of the vortex shedding, and the increased strain rate from it then causing the rapid development of a secondary production region. This secondary production region amplifies strongly within the strained braid region between the primary vortices, rapidly suppressing the initial production region within the vortex core. PKE growth is then observed to develop strongly within this braid region as the vortex is shed, and dissipates rapidly as the vortex relaxes back from its strained form to an elliptic form. Unlike the case for mode A, the shed vortices do not show any propensity for a further elliptical instability to develop. The production region within the strained layer of the shedding vortex from the underside of the cylinder for mode C extends back into the forming region, indicating that some feedback is established. Unlike mode B where this feedback occurs every half shedding cycle, the feedback for mode C in the triangular cylinder wake only occurs from the vortex shedding from the underside of the cylinder, once per shedding cycle. This continuance of the production regions are a consequence of the symmetry of the perturbation fields where a disconnect through $\langle k' \rangle = 0$ is necessary to permit any sign changes in the perturbation velocities. The broken feedback link in the upper-half plane for mode C in the triangular cylinder occurring once every shedding cycle thus effects the period-doubled symmetry for mode C as opposed to that for mode B, and has been demonstrated experimentally by Yildirim *et al.* (2013b) for the wake of the circular cylinder with a trip wire. Lastly, the regions where the dissipation rate \mathcal{D} was significant was largely coincident with those of the production regions, indicating that strain plays a dual role in accelerating the growth of these modes, and also in its inhibition. A quick comparison between the instantaneous

sensitivity fields l and the maps of the terms of the PKE equation for these secondary instabilities appear to show that regions with higher sensitivity norms l are generally contained within regions of positive PKE production within the near wake ($\sum \mathcal{P} > 0$), which was anticipated since these sensitive regions indicate the core from where the instability should emanate from. An example of this is shown in figure 5.12. Finally, it is anticipated that increasing the Reynolds number should not affect these results qualitatively since in each case the same mode type is being traced with increasing Reynolds number. Specifically, modes B and C which manifest in the near wake should show no distinguishable difference in the production and dissipation except through growing magnitudes of E_i owing to the non-zero instability growth rate, while mode A cases are anticipated to show an increasing imbalance between the transport terms using the same domain size on top of the increasing magnitudes of E_i . A pertinent point to note is that higher Reynolds number flows are unstable to a broader spectrum of wavenumbers, each of which contributes to the total PKE growth in the flow, and so its cumulative effect may need to be given due consideration.

5.3 Chapter summary

The first section of this chapter investigated the structural sensitivity of the wake instabilities found in chapter 4. For the complex mode responsible for the primary wake instability, the regions in the flow most sensitive to external disturbances appeared within two lobes in the cylinder wake, similar to those found for the circular cylinder (Giannetti & Luchini, 2007). Varying the cylinder inclination showed little impact on the sensitivity fields for this mode. The sensitivity fields for the three-dimensional modes in this study similarly resembled those for the circular cylinder (the sensitivity field of mode C in this study resembling that for mode B in the circular cylinder wake). Considering such similarities, the sensitivity properties of these wakes were not investigated further in this thesis.

The next section of this thesis considered the evolution of the perturbation kinetic energy (PKE) in the wake and its associate energy budget. The results for the primary wake instability follow those for the circular cylinder found by Mittal (2009). The application of this analysis to the secondary instabilities of the wake was, however, novel. In general, terms of the cross-flow gradients of base flow velocity ($\partial \mathbf{U} / \partial y$) were found to contribute most to the instability growth of modes A, B and C. The analysis

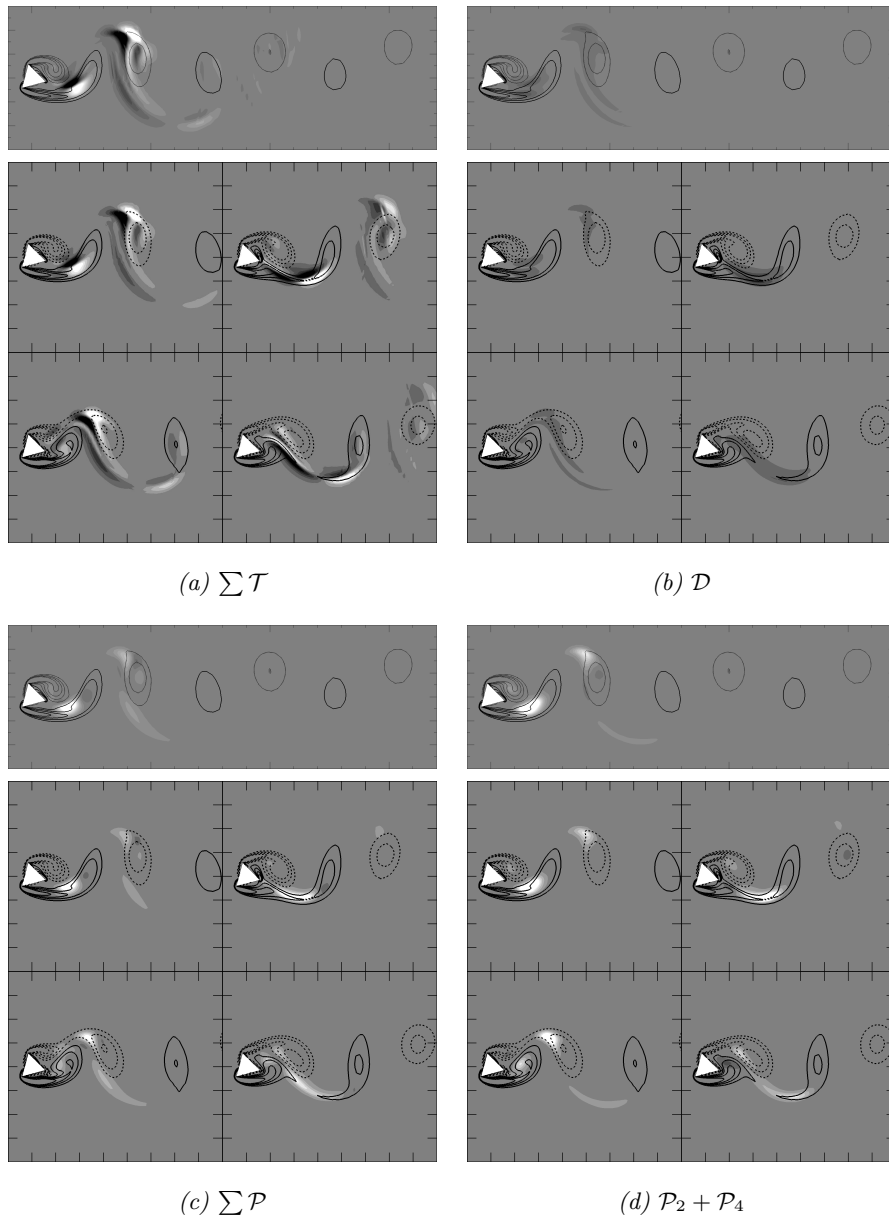
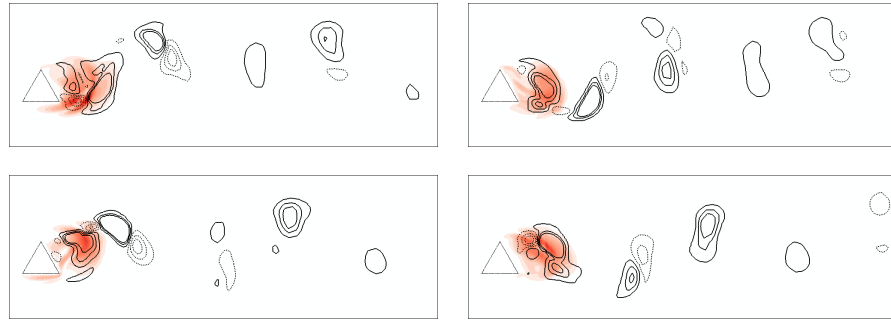
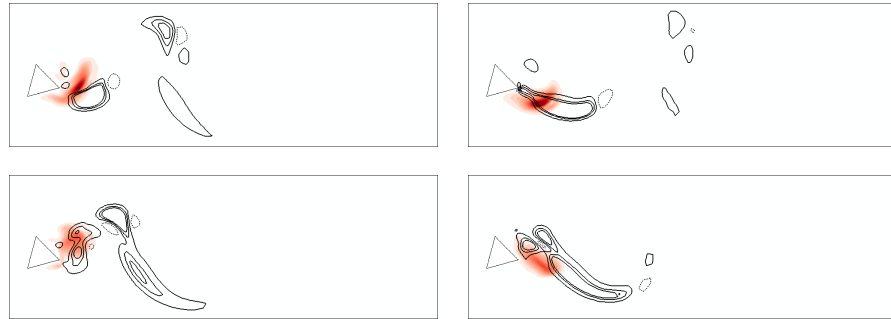


FIGURE 5.11: Caption follows that given in figure 5.9, but is for the mode C instability here shown for the wake of the cylinder at $\alpha = 45^\circ$ and $Re = 112$.



(a) Mode A: $\alpha = 30^\circ$, $Re = 127$



(b) Mode C: $\alpha = 45^\circ$, $Re = 112$

FIGURE 5.12: Contours relating the production regions $\sum \mathcal{P}$ with the sensitivity field I , shown at 4 equispaced time intervals in the shedding cycle (clockwise). Light to dark red-scale contours correspond to low to high magnitudes of I , while the solid and dashed lines correspond to positive and negative $\sum \mathcal{P}$ values.

finds that the slow dissipation of mode A structures in the wake affects the energy budget through the terms for the transport of PKE — computational domains that are insufficiently large for a full decay of mode A structures will possess an imbalance in these transport terms, the energetics of the instability however remaining the same. The local distribution of the PKE production terms were then considered, finding that the dominant production terms for mode A evolve according to the elliptical instability mechanism described by Leweke & Williamson (1998) and Thompson *et al.* (2001). The energy budget for modes B and C were again similar, indicating that the two modes may somehow be related.

Having investigated these properties of the instability modes, the remaining question now is to investigate the role of nonlinearities in three-dimensional flows as it evolves from these linear modes, and also the dynamics of the flows at higher Reynolds numbers beyond where the two-dimensional flow was periodic. Numerical simulations of the three-dimensional flows are conducted in the following chapter to address this question.

Chapter 6

Three-dimensional flows past the inclined cylinder

Having completed a thorough investigation on the characteristics of the two-dimensional wakes of the inclined cylinder, the linear modes underlying some of the transitions observed in the flow, as well as the energetics and sensitivity of these modes, the final results chapter of this thesis turns its attention to the fully three-dimensional wakes evolved using the Navier–Stokes equations. The purpose of this investigation is to understand the complex dynamics underlying the three-dimensional wakes with earlier imposed constraints being lifted — the two-dimensional flows computed in Chapter 3 reduced the dimensionality of the flow by assuming that the flow was homogeneous in the spanwise direction which is only appropriate where three-dimensionality is trivial, while the linearised eigenfields reported in Chapter 4 neglected the effects of nonlinear interactions in the flow as it is evolved and are hence only appropriate near the onset of the instability in the basic flow itself. This chapter instead focuses on the asymptotic solutions of the three-dimensional flow past the inclined cylinder and their transient developments to understand how nonlinear interactions alter the flow from its idealised eigenmodes to its final state.

The first part of this chapter in § 6.1 discusses the dynamics of the spanwise periodic modes in a three-dimensional flow near the transition (to within 10% past the transition Reynolds number), aiming to understand the nature of the three-dimensional transition and its propensity for hysteresis, and to also determine the differences between the linearised mode and the asymptotic solution of the three-dimensional flow within the same wavelength. § 6.2 then discusses the results obtained from flow evolution in an extended domain, and finally quantifies the forces induced on the cylinder.

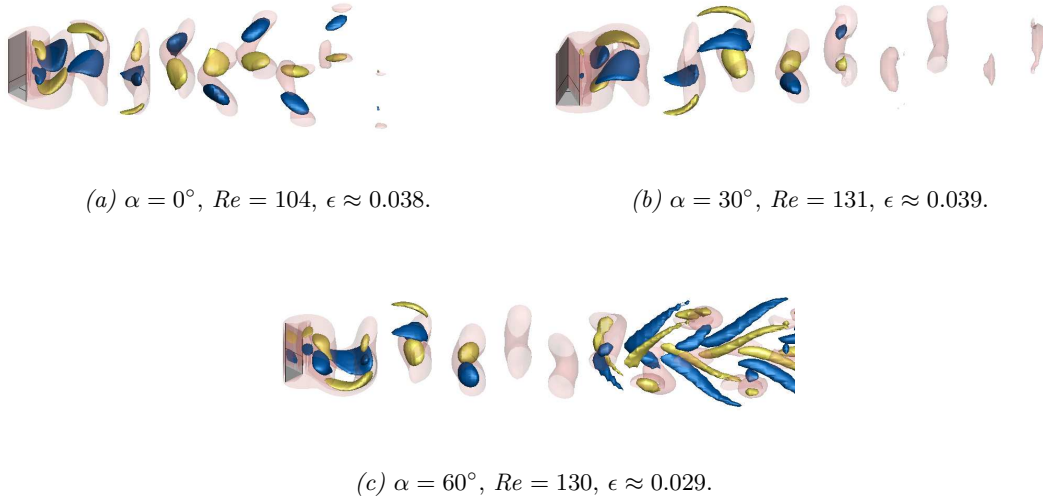


FIGURE 6.1: Visualisation of the mode A flow at its saturated state for select cases as labelled in each panel. Here, the blue/yellow isosurfaces highlight the streamwise vortices in the flow at an arbitrary ω_x level (equal magnitude, opposite signed), while the translucent red isosurfaces describe the spanwise vortex rollers (ω_z) in the wake. The flow is left to right in each frame.

6.1 Three-dimensional flow transition via the linear instability modes

While linear stability theory applied to these wakes is capable of predicting the form of the modes that may develop in the flows and their corresponding transition Reynolds numbers, nonlinearities in the total flow can be excited rapidly past the bifurcation, which can in turn alter the flow itself through self-excitation of the dominant mode or through couplings of the modes as they become non-negligible in size. This effect becomes expectedly worse at higher Reynolds numbers past the transition seeing that linear stability theory predicts broader bands of instability modes in the spectrum to be unstable. To characterise the nonlinear dynamics of these transitions, the three-dimensional flow was computed at Reynolds numbers just above the predicted transition. The cylinder inclinations chosen for this analysis were selected to cover a range of inclinations where the flow was predicted to become unstable through modes A_1 , C , and A_2 , and the spanwise domain for each computation was set to the wavelength of the leading mode predicted from the stability analysis in chapter 4 ($\Pi_z \in [0, l_z]$) where $l_z = 2\pi/m_{\text{peak}}$. The spectral-element–Fourier method naturally imposes a periodic boundary condition on the out-of-plane/spanwise boundaries, and so the choice of l_z



(a) $\alpha = 36^\circ$, $Re = 140$, $\epsilon \approx 0.069$.

(b) $\alpha = 45^\circ$, $Re = 120$, $\epsilon \approx 0.072$.

FIGURE 6.2: Visualisation of the mode C flow at saturation for cases as labelled. Isosurfaces and flow direction are as per figure 6.1.

here restricts the flow transition to only structures with spanwise wavelengths that are harmonics of the leading instability mode. The simulations were performed at Reynolds numbers within $\epsilon < 0.1$, such that

$$\epsilon = \frac{Re - Re_k}{Re_k},$$

where ϵ is a difference parameter relating the Reynolds number of the flow to the transition Reynolds number Re_k , with $k = A, C$. This same parameter was used in § 4.1.1 to demonstrate that mode C in the linearised flow system grew more aggressively than mode A, only that in this chapter $\epsilon > 0$ since the three-dimensional modes cannot be observed otherwise; the same parameter is used in Henderson (1997). The range of $\epsilon < 0.1$ (that is, to within 10% of the predicted transition Reynolds number) was chosen to limit the study to Reynolds numbers where the peak growth rates of the dominant modes predicted from the stability analysis vary linearly with ϵ as shown in figure 4.3. The initial condition used in these simulations comprises the unsteady two-dimensional base flow on the fundamental Fourier mode and a white noise perturbation across the modes at a maximum magnitude of $|\mathbf{u}'| \sim \mathcal{O}(10^{-4})$ — this provides a disturbance in the initially two-dimensional flow field to accelerate the onset of any instabilities without bias toward any particular mode. The flow is evolved until the solution envelope is approximately asymptotic (this will be termed as the ‘saturated solution’ for brevity).

A resolution study was conducted to determine the optimal number of Fourier modes necessary to resolve the dynamics of these three-dimensional flows. For the resolution study, cylinder inclination and Reynolds number combinations ($\alpha = 18^\circ$, $Re = 120$) and ($\alpha = 36^\circ$, $Re = 140$) were chosen as linear stability theory predicts that these cases possess amongst the larger instability wavelengths representative of the mode A and mode C transitions, respectively (discussed in § 4.1.1, figure 4.2b). For these test cases,

the time-mean kinetic energies per unit span of the total flow (\overline{E}_k), the fundamental mode (\overline{E}_0), and the leading Fourier mode (\overline{E}_1) at saturation were monitored for convergence, along with the averaged flow period at saturation (\overline{T}), and the exponential growth rate of the leading Fourier mode ($d \log |E_1| / dt$). The results are shown in table 6.1.

Case	N_F	\overline{E}_k	\overline{E}_0	\overline{E}_1	$d \log E_1 / dt$	\overline{T}
$\alpha = 18^\circ$ $Re = 120$ (mode A)	2	3918.1952 (0.116%)	3914.4393 (0.146%)	1.8780 (67.052%)	0.0538 (0.044%)	5.8924 (8.166%)
	4	3922.9734 (0.006%)	3920.4827 (0.008%)	1.0844 (3.539%)	0.0538 (0.021%)	5.4501 (0.046%)
	8	3922.7431 (< 0.001%)	3920.1638 (< 0.001%)	1.1240 (0.019%)	0.0538 (0.027%)	5.4475 (0.001%)
	16	3922.7405 (< 0.001%)	3920.1607 (< 0.001%)	1.1242 (< 0.001%)	0.0538 (0.033%)	5.4477 (0.002%)
	32	3922.7405	3920.1606	1.1242	0.0538	5.4475
$\alpha = 36^\circ$ $Re = 140$ (mode C)	2	3932.4981 (0.021%)	3932.2884 (0.023%)	0.1049 (26.103%)	0.0759 (0.087%)	6.3472 (0.324%)
	4	3931.5272 (0.004%)	3931.2244 (0.004%)	0.1484 (4.610%)	0.0759 (0.068%)	6.3706 (0.044%)
	8	3931.6726 (< 0.001%)	3931.3833 (< 0.001%)	0.1419 (< 0.001%)	0.0759 (0.130%)	6.3678 (< 0.001%)
	16	3931.6726 (< 0.001%)	3931.3833 (< 0.001%)	0.1419 (< 0.001%)	0.0760 (0.015%)	6.3678 (< 0.001%)
	32	3931.6726	3931.3833	0.1419	0.0760	6.3678

TABLE 6.1: Variation, with increasing number of Fourier modes (N_F), of the total (volume integrated) kinetic energy of the flow per unit span (\overline{E}_k), total kinetic energies per unit span possessed by the fundamental and dominant Fourier modes of the flow (\overline{E}_0 and \overline{E}_1 , respectively), and the mean shedding period of the flow (\overline{T}), all for the saturated flow solutions, as well as the growth rate of the leading mode during the exponential growth phase of the flow evolution ($d \log |E_1| / dt$). The two cases evaluated here are representative of flows which become unstable through modes A and C, respectively. The percentage difference of the measurements relative to that for the corresponding case at $N_F = 32$ (highest N_F tested here) are shown in the parentheses.

From these results, flow variable discretisation in the spanwise direction using 8 Fourier modes ($N_F = 8$) is noted to be sufficient for this study, showing a convergence to approximately 0.1% relative to the $N_F = 32$ case (highest tested). This is hence applied in conjunction with the $N_p = 8$ polynomial order shape function imposed in the two-dimensional spectral-element discretisation which was validated in

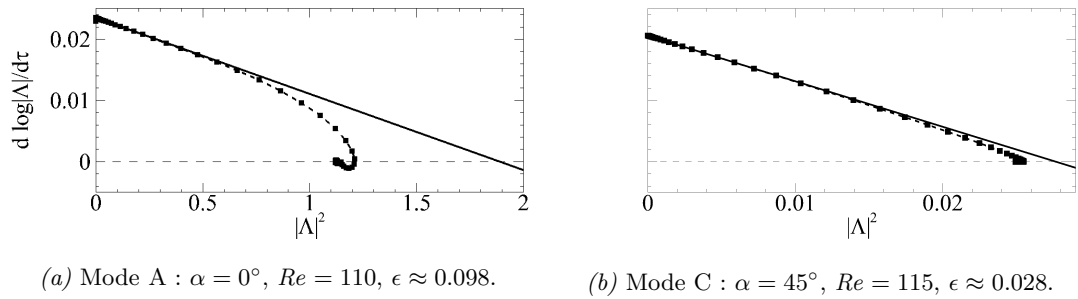


FIGURE 6.3: Examples of the growth of the predicted instability modes from the initially two-dimensional flow for cases as indicated in each panel. The dashed line through data points are the measured amplitude growths which crosses the $|\Lambda|^2$ -axis at the nonlinear saturated amplitude ($|\Lambda|_{\text{sat}}^2$), while the solid line describes the cubic-order truncation of the Stuart–Landau equation which crosses the $|\Lambda|^2$ -axis at the linearised ‘limiting’ amplitude ($|\Lambda|_{\text{lim}}^2$). The effect of nonlinear interactions in the flow is apparent through the departure of the amplitude of the flow solutions from the linearised model.

§ 2.5. Figures 6.1 and 6.2 show the vortical structures in the saturated flows near the corresponding transition Reynolds numbers, each of which becomes unstable through modes A and C (the cylinder inclinations here being chosen to mirror those showing the eigenmodes of the linearised system in figures 4.4 and 4.5), and so these figures act as a lead-in to the ensuing analysis. In comparing these vorticity fields against the eigenmodes of the linearised system shown in figures 4.4 and 4.5, it is observed that the saturated flows which become unstable through mode A showed noticeable deformations in the two-dimensional vortex rollers induced by the streamwise vortices compared to the spanwise invariant two-dimensional flow, thus deviating strongly from the linearisation assumptions. The saturated flows unstable through mode C instead shows small disturbances induced on the spanwise vortex rollers, and so it has not deviated significantly from its two-dimensional basic state despite these flow visualisations for the mode C unstable flow being at higher ϵ . This generates an interest to understand the evolution of the wakes and its responses as the flow transitions from its basic two-dimensional state, through its growth phase, and ultimately to its saturated state.

The nature of these secondary transitions can again be modelled using the Stuart–Landau equation described in § 2.3.4, which was used previously in § 3.2.1 to determine the critical Reynolds numbers at which the flow becomes unsteady, and in doing so also verifying that the primary transition itself was supercritical. A similar investigation is

conducted here for the secondary wake transitions through modes A and C, the analysis having been applied extensively in the past for similar bluff body wakes as reported in Henderson (1997), Sheard *et al.* (2004), Sheard *et al.* (2009), amongst others, and also in various other flow configurations such as those for confined channel flows (Sapardi *et al.*, 2017) and in confined rotating systems (Vo *et al.*, 2015). For the configuration in the present study, the total kinetic energy contained in the Fourier mode corresponding to the dominant mode predicted from the linear stability analysis was used as the complex amplitude measure, similar to Henderson (1997), and is given by

$$|\Lambda_k|(\tau) = \left[\int_{\mathcal{V}} |\hat{\mathbf{u}}_k(\tau)|^2 d\mathcal{V} \right]^{1/2},$$

where τ is the normalised time $\tau = (t_0 + nT)/T$ with n being an integer and t_0 an arbitrary starting time where the data sampling commenced, $|\Lambda_k|(\tau)$ is the magnitude of the oscillatory signal at time τ , and k corresponds to the dominant mode, and so this traces the evolution of the mode amplitude on the Poincaré section.

For all cylinder inclinations investigated, the transitions for both modes A and C were found to be supercritical through positive l coefficients predicted using the Stuart–Landau equation, indicating a hard bifurcation from the two-dimensional base state to the unstable three-dimensional modes without any discontinuities. Examples of these are shown in figure 6.3. Hence, the transition to three-dimensional flow is expected to occur at the predicted critical Reynolds number without any hysteretic behaviour. This is in contrast to the mode A transition observed in the wake of the circular cylinder where Henderson & Barkley (1996) and Henderson (1997) showed the transition to be subcritical using a similar analysis. Bridging these results are the corresponding bifurcations in the square cylinder wake where Sheard *et al.* (2009) reported the mode A transition to be either sub- or supercritical depending on the cylinder inclination, whereas the mode C transitions were always supercritical. The present results also show that the supercritical nature of mode A here differs from the hysteretic nature of the mode A transition found in the wake of a downstream-pointing isosceles triangular cylinder (Luo & Eng, 2010) where the two leeward faces of the cylinder in their study were longer than the normally oriented side at the fore of the cylinder, as opposed to the equilateral triangular cross-section cylinder investigated here. This demonstrates the possible sensitivity in predicting the nature of these transitions, which may be associated with the experimental set-up, similar to that reported for mode A in the circular cylinder wake as shown by Jiang *et al.* (2018).

A comparison of the l coefficients across the different cylinder inclinations shows that they adopt distinctly different values depending on whether they relate to mode A or mode C transitions, whereas the differences between values within each mode are relatively small. For mode A, these coefficients were measured to be $l_A \approx \mathcal{O}(10^{-2})$, while those for mode C were consistently higher, ranging $\mathcal{O}(10^{-1}) < l_C < \mathcal{O}(1)$ (figure 6.4). Thus, the transition through mode C is ‘more strongly’ supercritical than those through mode A, regardless of the Reynolds number for $\epsilon < 0.1$. This suggests that the l coefficient may find further utility in the classification of three-dimensional instability modes; this could be helpful experimentally in cases where fluid opacity precludes optical approaches for visualisation (such as laser-induced fluorescence) and velocimetry (such as particle image velocimetry).

Studies by Akbar *et al.* (2011) on the subcriticality of mode A in the circular cylinder wake, as well as by Jiang *et al.* (2018) on that for the square cylinder wake showed that the approach of evolving the flow in a periodic domain confined to a single wavelength of the instability mode might possibly lead to a difference in the nature of the transition — the latter study found that the mode A transition in the square cylinder wake was subcritical when evolving the flow in a computational domain with a large spanwise extent of $l_z = 15d$, while Sheard *et al.* (2009) found the bifurcation to be supercritical in the single mode domain. The results from the cited studies are acknowledged here, the implications of which might see the mode A transition in the triangular cylinder wake actually be subcritical through a small hysteresis loop (ΔRe) similar to that found by Jiang *et al.* (2018) for the square cylinder wake’s mode A transition, especially when taking into consideration the small magnitudes of the l coefficients predicted for mode A here. This may ultimately result in a small region of ΔRe where bistability may be observed.

As a consequence of the larger l coefficients predicted for mode C relative to those for mode A, the saturated amplitudes ($|\Lambda|_{\text{sat}}$) of the asymptotic state of the mode C flow remained small where $|\Lambda|_{\text{C,sat}}^2 \approx \mathcal{O}(\epsilon)$ as shown in figure 6.4(b), and showed a strong agreement with the limiting amplitudes ($|\Lambda|_{\text{lim}}$) predicted by the cubic-order truncation (linearised form) of the Stuart–Landau equation (the $|\Lambda|^2$ axis intercept in figure 6.3) such that $|\Lambda|_{\text{C,lim}}^2 \approx |\Lambda|_{\text{C,sat}}^2$ as shown in figure 6.4(c). This suggests that any coupling to the primary mode is weak near the onset of the mode C instability similar to that described for mode B by Henderson (1997). The saturated amplitudes of mode A

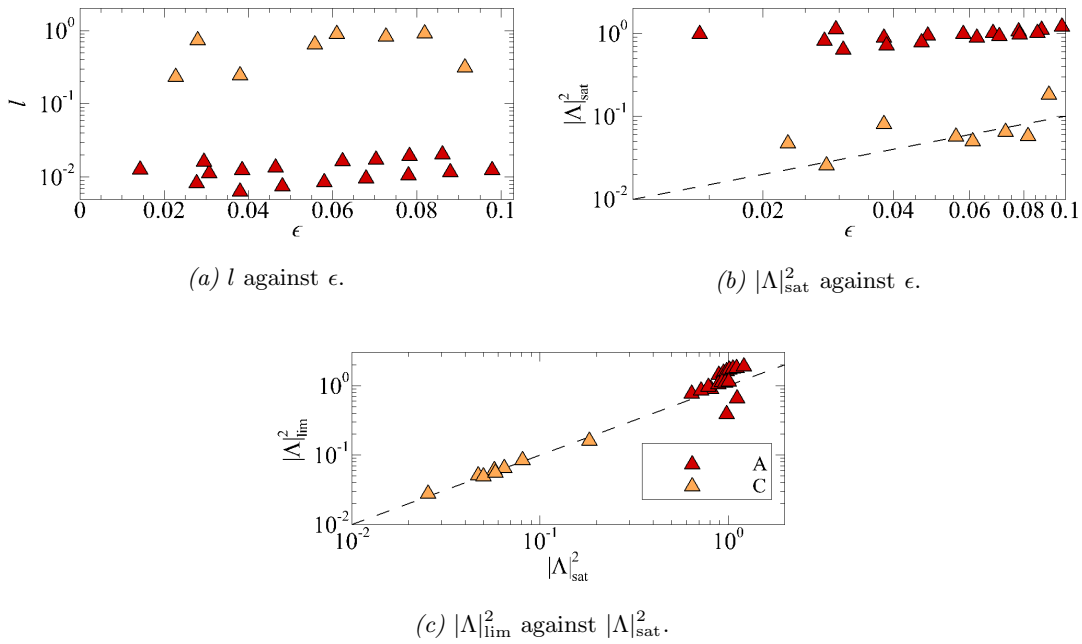


FIGURE 6.4: Plots of (a) the l coefficient against the distance parameter ϵ , (b) the squares of the amplitude at saturation of the mode ($|\Lambda_{\text{sat}}|^2$) versus ϵ , and (c) the squares of the predicted limiting amplitudes ($|\Lambda_{\text{lim}}|^2$) versus $|\Lambda_{\text{sat}}|^2$. For all panels, the red triangles (\blacktriangle) correspond to mode A simulations, while the orange triangles (\blacktriangle) correspond to mode C. The dashed lines in (b) and (c) map the linear functions $|\Lambda_{\text{sat}}|^2 = \epsilon$ and $|\Lambda_{\text{sat}}|^2 = |\Lambda_{\text{lim}}|^2$, respectively.

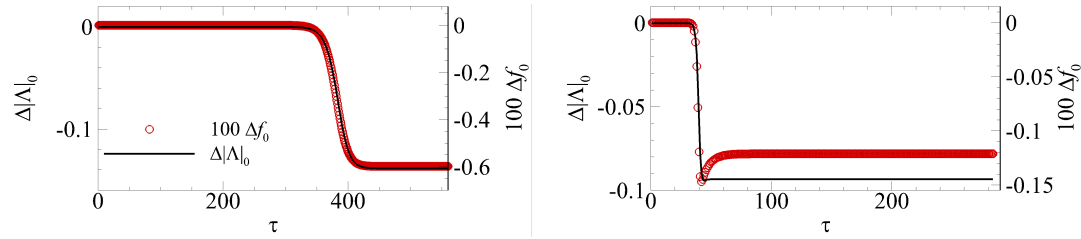
($|\Lambda_{A,\text{sat}}|$) instead consistently asymptote at a larger amplitude than mode C despite being within the same ϵ range (figure 6.4b), but still demonstrates a fair agreement with the predicted limiting amplitude ($|\Lambda_{A,\text{lim}}|$), such that $|\Lambda_{A,\text{sat}}|^2 = \mathcal{O}(|\Lambda_{A,\text{lim}}|^2)$ as shown in figure 6.4(c). The scatter of the mode C points about the $|\Lambda_{\text{lim}}|^2 = |\Lambda_{\text{sat}}|^2$ line in figure 6.4(c) was also found to be significantly smaller than that for mode A as quantified by the residual sum of squares error of these points, normalised by the number of points (akin to a variance measure). Flows unstable through mode C were also observed to reach their asymptotic state much more rapidly than mode A, which agrees with the results reported in § 4.1.1 where the peak growth rates of mode C increased at approximately twice the rate of those of mode A with increasing ϵ .

In the investigation on the evolution of nonlinearities in the circular cylinder wake, Henderson (1995) modelled the complex amplitude evolution of both transition modes A and B using essentially the same truncated model for the mode amplitudes, but quantified the frequency shifts through changes in the flow's frequency from consecutive

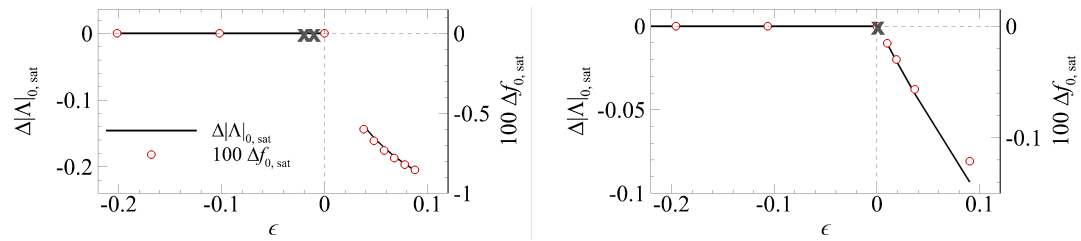
shedding periods as opposed to the flow’s instantaneous phase derived from the Hilbert transform of the complex signal. While both means arrive at the same conclusion, the evolution of the flow frequency presented by Henderson (1997) provides a more intuitive picture of the frequency drop. Here, the complex amplitude is measured from the oscillatory lift coefficient, and the flow period (T_n) is measured as the time between successive maxima of the signal,¹ such that the frequency can then be defined as $f_n = 1/T_n$. This analysis was performed for the three-dimensional wakes of the cylinder inclined at $\alpha = 0^\circ$ and 45° initialised from its two-dimensional base state, at various Reynolds numbers where $\epsilon < 0.1$ as mentioned previously.

The plots in panels (a,b) of figure 6.5 elucidate the shifts in the amplitudes and frequencies of the evolving flow from its initially two-dimensional state ($\Delta|\Lambda|_0$ and Δf_0), with each panel corresponding to the flow at $Re = 104$ past the cylinder inclined at $\alpha = 0^\circ$ ($\epsilon \approx 0.038$, which is the lowest ϵ case evolved here), and at $Re = 122$ past the cylinder inclined at $\alpha = 45^\circ$ ($\epsilon \approx 0.090$, which is the largest ϵ case evolved here such that $\epsilon < 0.1$). While both transitions from the two-dimensional base state to the saturated three-dimensional flow incur some changes in the frequency and amplitude response, the transition through mode A at $\alpha = 0^\circ$ showed a much larger drop in both amplitude and frequency even at the smallest ϵ compared to the mode C case at a much larger ϵ . The frequency and amplitude shifts for the mode A case drops by a similar form, akin to those for mode A in the circular cylinder wake as reported by Henderson (1997). The mode C case instead shows that the frequency shift overshoots from its stable solution, and so the frequency shift here is not commensurate with the amplitude drop. These results were consistent for the few Reynolds numbers the flow was computed at for both cylinder inclinations, and the final differences of the amplitudes and frequencies at saturation ($\Delta|\Lambda|_{0,\text{sat}}$ and $\Delta f_{0,\text{sat}}$) are summarised in panels (c,d) in figure 6.5. Here, the mode C unstable flow shows a smooth departure from the two-dimensional branch, with low order polynomial extrapolation of these amplitude and frequency shifts matching the predicted transition Reynolds numbers at $\epsilon = 0$. This was not the case for the mode A flow where the solution branch for the three-dimensional flow required the extrapolation of a least a fifth order polynomial

¹Henderson used the total kinetic energy in the fundamental Fourier mode of the flow at times where the instantaneous lift coefficient was zero. Although the lift coefficient value can be more accurately interpolated to zero rather than interpolating for the maxima, the waveform of the lift coefficients obtained in this study could have subharmonic frequencies excited which could affect the interpolation, and so the maxima measure is marginally more robust here.



(a) $\Delta|\Lambda|_0$ and Δf_0 against τ .



(b) $\Delta|\Lambda|_{0,\text{sat}}$ and $\Delta f_{0,\text{sat}}$ against ϵ .

FIGURE 6.5: Plots of (a) the amplitude and frequency shift ($\Delta|\Lambda|_0$ and Δf_0 , respectively) as the mode evolves from an initially two-dimensional state to saturation, and (b) of these differences at saturation (denoted with a subscript “sat”) with increasing ϵ about the predicted transition Reynolds number ($\epsilon = 0$). The panels on the left/right are for the $\alpha = 0^\circ/45^\circ$ cylinder inclination cases, with the top panels being for the flows at (left) $Re = 104$ ($\epsilon = 0.038$) for the mode A case and (right) $Re = 122$ ($\epsilon = 0.09$) for the mode C case. In all plots, the change in the amplitudes ($\Delta|\Lambda|_0$) and that of the frequency (Δf_0) are denoted by the solid black lines and red circles, respectively, and the frequency axis re-scaled to $100\Delta f_0$ to permit nice values. The amplitude measure used in these plots are derived from the maxima of the lift coefficients, and with the instantaneous shedding period being the time between consecutive lift maxima. The grey cross markers (\times) in the plots in (b) mark the bifurcation points predicted from quadratic and cubic extrapolation of polynomial functions fitted to the three-dimensional flow data.

function fitted to the data to obtain a bifurcation point on ϵ matching the predicted transition Reynolds number.

6.2 Three-dimensional flow dynamics in extended systems

Having characterised the nature of these transitions through evolution of the periodic mode by itself, the next stage of this project will consider the evolution of the three-dimensional flows in systems with a larger spanwise domain length (l_z/h) at higher Reynolds numbers, and attempts to quantify pertinent responses in the system such as the forces induced in the cylinder and some wake frequencies, finally drawing some comparison between these responses or measurements and those obtained from two-dimensional computations. Studies by Henderson (1997), Akbar *et al.* (2011), and Jiang *et al.* (2018) have demonstrated that the sub- or supercritical nature of the bifurcation may differ depending on the extent of the spanwise domain computed — a larger domain permits the excitation of a larger spectrum of wavenumbers, increasing the probability of intermodal interactions in the flow, and may rapidly lead to the onset of chaos, and that a smaller spanwise domain containing only the leading mode can perhaps misinform the hysteretic nature of the transition. These studies, along with that by Sheard *et al.* (2009) for the square cylinder wake have also shown that these flows computed in extended domains can exhibit three-dimensional vortical structures with some semblance of coherence consistent with the various modes (A, B, C) in the near wake, but also lead to a breakdown of coherent structures in the far wake marking the onset of spatio-temporal chaos. This section aims to shed some light on the dynamics of these flows as well as the onset of such breakdown phenomena. In all of the following computations in this section, a spanwise domain of $\Pi_z \in [0, l_z]$ with $l_z = 2\pi h/0.4 \approx 15.7h$ was chosen, and was discretised through at least 32 Fourier modes ($N_F \geq 32$) at the lowest Reynolds numbers tested here, increasing to $N_F = 64, 80$ or 128 where more resolution was necessary — while higher resolution is always desirable in these cases, the number of cases computed here and its associated computational cost was prohibitive, and so a resolution in the out-of-plane direction was chosen to ensure that the difference between the Fourier mode with the largest total kinetic energy and that with the lowest total kinetic energy at its asymptotic state were at least $\Delta E \sim \mathcal{O}(10^3)$, and so the force coefficients quantified would not be severely affected by resolution issues. The computations in this section were initialised using

the saturated two-dimensional base flow solution as the fundamental Fourier mode, and three-dimensionality in the flow was again instigated by introducing white noise into the initial flow field at a maximum magnitude of $\mathcal{O}(10^{-4})$. The following results and discussion generally proceeds in order of increasing Reynolds numbers past the three-dimensional transition threshold (increasing ϵ) to highlight how the dynamics of these flows change as they become increasingly unsteady/chaotic.

6.2.1 Modal growth, nonlinearities, and turbulence

Starting with flows at low ϵ , two cases were first considered: a flow at $Re = 130$ past the cylinder inclined at $\alpha = 60^\circ$ representing a mode A_2 case ($\epsilon \approx 0.03$), and an $Re = 120$ flow past the cylinder inclined at $\alpha = 45^\circ$ for mode C ($\epsilon \approx 0.07$). The choice of a larger ϵ for the mode C flow compared to the mode A flow was intentional to investigate how the results from the previous section regarding the supercriticality of the bifurcations might change in such an extended domain. In both these cases, the streamwise vortical structures in the asymptotic flow solutions shown in figure 6.6 resemble those of the streamwise perturbation vortices in their corresponding eigenmodes (figures 4.4–4.5) owing to the low ϵ values here. Despite this, the mode A_2 case here shows the spanwise vortex rollers to have been altered quite noticeably from its basic two-dimensional state particularly in the far wake where the disturbances grow most intensely — the undulations in the vortex rollers become substantial through self-induced motions leading to a noticeable breakdown of the vortex rollers in the far wake. Such breakages in the vortex rollers (or vortex dislocations) past the onset of mode A have also been observed in the wake of a circular cylinder (Williamson, 1996a). These vortex dislocations are observed in the near wake for mode A_1 cases (visualisation provided in a following section), showing better agreement to the mode A^* found in the circular cylinder wake (Williamson, 1996a; Henderson, 1997; Jiang *et al.*, 2016). While the vortex rollers in the mode C case are also altered through a similar mechanism, the induced waviness in its form is not sufficient to cause breakages or dislocations in the spanwise vortex rollers such as those in the mode A case despite the mode C case here being at a higher ϵ . This possibly justifies the difference between the asymptotic amplitudes of the three-dimensional flow from those predicted by the truncated Stuart–Landau equation for the mode A cases, as shown earlier in figure 6.3(a) and 6.4(c): modifications to the basic two-dimensional state of the flow reduces the validity of a linearised model (the cubic truncation of the

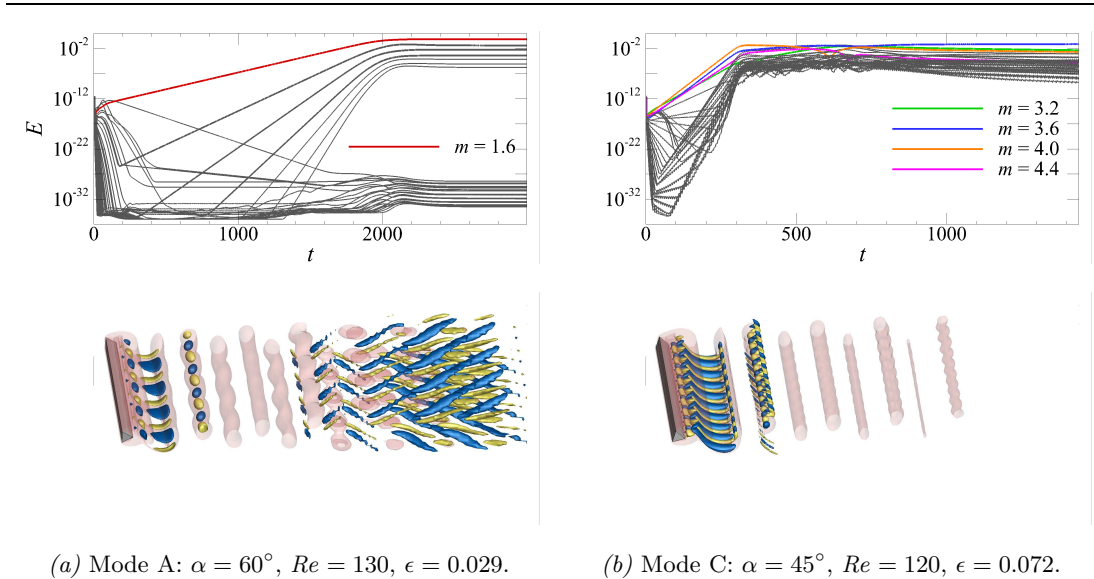


FIGURE 6.6: Examples of the evolution of the flow at low ϵ , shown for cases as labelled in the subfigures. (Top row) Plots of the growth of the total kinetic energies possessed by each Fourier mode describing the evolution of the flow from an initially two-dimensional state, through the exponential growth regime, and finally to saturation of the flow solution. The dominant Fourier modes during the exponential growth regime are highlighted as coloured lines here, with the corresponding wavenumber of these modes listed in the line legends inset. (Bottom row) Visualisation of the flow field at saturation. Here, the blue/yellow isosurfaces highlight the streamwise vortices in the flow at an arbitrary ω_x level (equal magnitude, opposite signed), while the translucent red isosurfaces describe the spanwise vortex rollers (ω_z) in the wake.

Stuart–Landau equation in this case), and so higher order terms in the expansion are necessary to resolve these changes.

At higher Reynolds numbers (maintaining $Re \leq 300$), a larger spectrum of unstable wavenumbers are excited simultaneously which accelerate the onset of nonlinear interactions in the flow. The focus here is to observe and understand how the flow evolves through the linear growth regime starting from a spanwise invariant state, and onward to nonlinear saturation. A smaller subset of cylinder inclinations were considered here owing to the prohibitive cost of these computations. As expected, the flow becomes three-dimensional through pattern forming modes, mostly similar to modes A and C, but also through several complex interactions which will be elucidated below. In the subsequent analyses in this section, the spatio-temporal symmetry of the flow in the wake of the cylinder is visualised through a space-time plot of the spanwise velocity signals (w -velocity) taken at an arbitrary point (x_0, y_0) in the near wake, the magnitudes

of which have been normalised through

$$w^*(x_0, y_0, z, t_n) = \frac{w(x_0, y_0, z, t_n)}{\max |w(x_0, y_0, z, t_n)|},$$

such that $|w^*| \leq 1$ at each time step t_n while still retaining its directionality. The space-time plots of the w^* -velocity at the point (x_0, y_0) in the wake thus highlights any modal structures in the evolving flow field over time without being obscured by the exponentially growing signal amplitudes. The breakdown of spatio-temporally coherent structures in the flow is further elucidated through an autocorrelation of the spanwise velocity signals at each time instance t_n . The autocorrelation coefficient, $R(\phi)$ is defined as

$$R(\phi) = \frac{\langle w'(z) w'(z + \phi) \rangle}{\langle w'(z) w'(z) \rangle},$$

where

$$\begin{aligned} \langle w(z) \rangle &= \frac{1}{l_z} \int_{\Pi_z} (w(z)) dz, \\ \langle w'(z) w'(z) \rangle &= \frac{1}{l_z} \int_{\Pi_z} \left(w(z) - \langle w(z) \rangle \right)^2 dz, \\ \langle w'(z) w'(z + \phi) \rangle &= \frac{1}{l_z} \int_{\Pi_z} \left(w(z) - \langle w(z) \rangle \right) \left(w(z) - \langle w(z + \phi) \rangle \right) dz, \end{aligned}$$

and ϕ represents the spanwise shift of the signal. In this representation, an autocorrelation coefficient of $R(\phi) = 1$ indicates that the signal is perfectly correlated to the same signal shifted in the out-of-plane direction by an amount ϕ , $R(\phi) = -1$ indicates that the signal is inversely correlated and so the signal is now in anti-phase with the original signal, and $R(\phi) = 0$ indicates that the given signal after a shift by ϕ lacks any distinguishable correlation. This measure can thus be utilised to observe the breakdown of large-scaled coherent structures found in the exponential growth regime as it becomes chaotic, and the recurrences of coherent structures in the asymptotic state. The Fourier expansion approach for discretising flow variables in the out-of-plane direction implemented in the solver naturally imposes a periodic boundary condition in the z -direction, and as such the autocorrelation when ϕ is an integer multiple of the spanwise domain size will always be perfectly correlated, so $R(\phi = 0) = R(\phi = l_z) = 1$. For most cases here, the spanwise velocity signals were measured at $(x_0, y_0) = (5, 0.5)$ — the vertical displacement from the centreline being included since the vortex streets observed from the two-dimensional flow computations generally follow an inclined tra-

jectory at most cylinder inclinations. For the symmetric cylinder inclinations $\alpha = 0^\circ$ and 60° , the point (x_0, y_0) was set as $(5, 0)$.

The first cases to be examined were flows at low ϵ to demonstrate how nonlinear interactions in such an extended domain alters the asymptotic solution of the three-dimensional flow close to the transition threshold, while also working as a benchmark to compare how strongly the asymptotic solutions differ from those at even higher Reynolds numbers as subsequently reported.

Here, flows at $Re = 110$ past the cylinder inclined at $\alpha = 0^\circ$ (and so $\epsilon \approx 0.098$), and at $Re = 120$ past the cylinder inclined at $\alpha = 45^\circ$ ($\epsilon = 0.072$) are reported, each respectively representing a case where mode A and mode C are the leading transition modes during the linear growth phase of the flow evolution. As described earlier, mode interactions in the mode A case induce strong undulations in the two-dimensional vortex rollers, eventually introducing dislocations in the vortex rollers which are then amplified through self-induced motions. The asymptotic solution of this case ultimately shows a markedly different solution in the extended domain compared to the single mode wavelength system reported in § 6.1 — the saturated solution here shows the flow to be strongly three-dimensional with some remnants of mode A structures with inherent dislocations (mode A*) even at low ϵ values while those in § 6.1 show the mode structure to remain even in the saturated flow solution. The mode evolution is elucidated here through the temporal w^* -velocity signal as well as its corresponding autocorrelation signal R as shown in figure 6.7 — notice the change in the coherence level of the signals as the growth of the leading mode is gradually arrested through excitation of the other modes in the flow. As the flow solution asymptotes, these signals show recurrences of mode A patterns in the near wake, which can also be observed in the saturated flow. The corresponding signal evolution for the mode C case (also shown in figure 6.7) lacks such a dramatic deviation between the asymptotic solution and the linear mode, showing that the three-dimensional mode C pattern remains salient in the flow even as the solution saturates. This supplements the results summarised in figures 6.3 and 6.4 of § 6.1 showing that flows unstable through mode C tend to asymptote with amplitudes close to that predicted from the cubic-order truncated Stuart–Landau equation.

In the present study, the transition to turbulence in the wakes of the cylinder inclined at 0° and 18° from their initially two-dimensional basic state exhibits a similar set and sequence of transitions as the Reynolds number is increased. This is perhaps generally

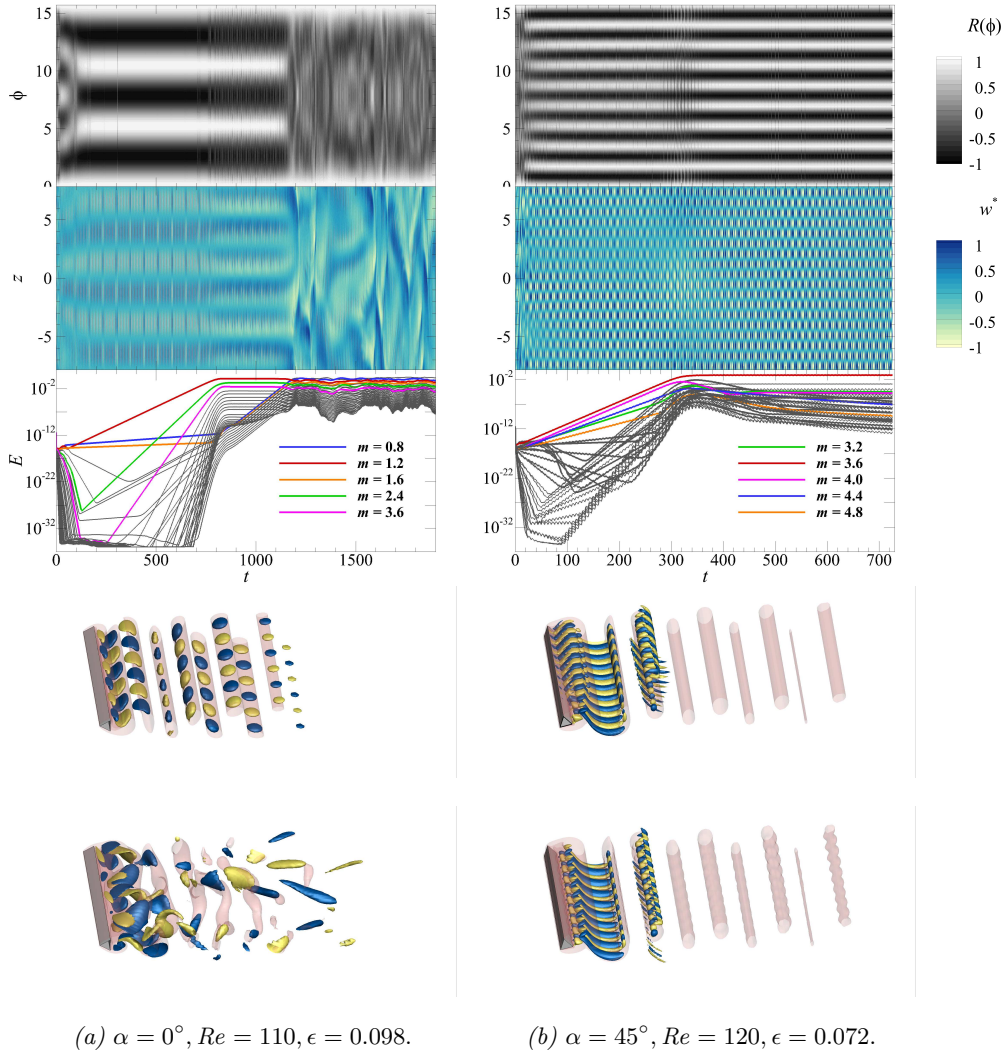


FIGURE 6.7: Evolution of the flow from an initially two-dimensional state to a saturated nonlinear state for the cases as labelled in each subfigure. From top to bottom, the figures correspond to: (i) the plot of the autocorrelation coefficients (R) of the w -velocity signal along the span corresponding to a spatial shift of ϕ , (ii) a space-time reconstruction of the w^* -velocity signals, (iii) the growth of the total kinetic energies within each Fourier mode, (iv) flow visualisation during the linear growth regime, and (v) flow visualisation of the asymptotic solution. In the $R(\phi)$ plot, white/black contours correspond to positive/negative R values within $|R| \leq 1$. Contours and isosurfaces in the flow visualisations here (iv–v) follow those captioned in figure 6.6.

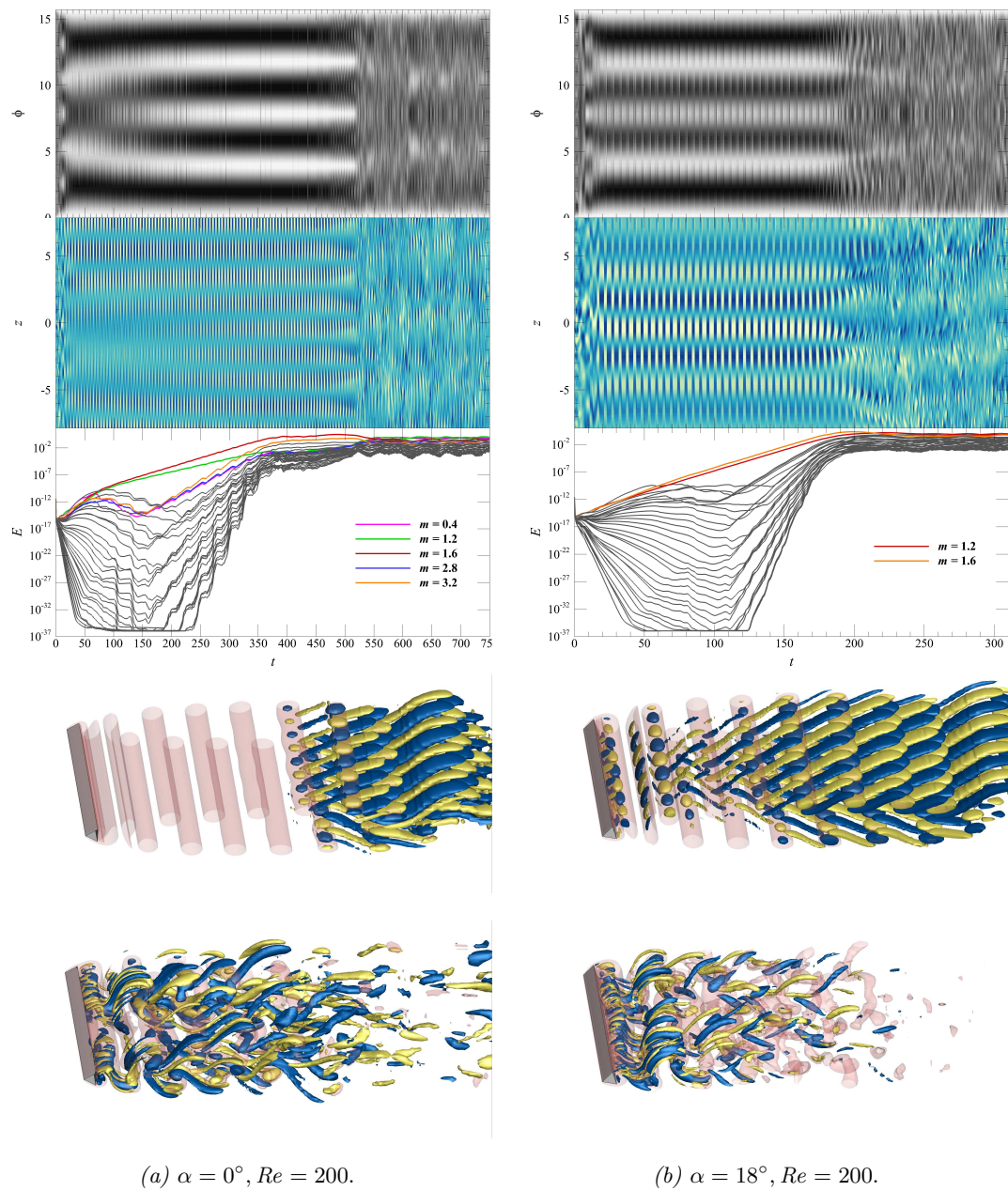


FIGURE 6.8: Captions follow that given in figure 6.7, but are for the flow cases labelled in each subfigure here.

true for $\alpha < 30^\circ$ since the two-dimensional flows at these cylinder inclinations are similar, but the exploration of additional intermediate cylinder inclination angles is beyond the scope of this work, so this remains an open question. For flows at Reynolds numbers of $Re < 240$ for the cylinder inclined at $\alpha = 0^\circ$ and $Re < 300$ for the cylinder inclined at $\alpha = 18^\circ$, the exponential growth regime in the flow from the initially two-dimensional state is dominated by mode A structures in the near wake with spanwise wavelengths ranging over $2\pi/1.2 \lesssim \lambda/h \lesssim 2\pi/1.6$, with the aperiodic vortex street observed in the two-dimensional flow remaining unaltered. The streamwise vortical structures in the three-dimensional flow at this stage (an example of which is shown in figure 6.8) takes a closer resemblance to mode A_2 obtained from the stability analysis where the perturbations are observed to grow more dominantly in the far wake where the rows of vortices show a massive separation. This is likely the preferred mode for this vortex street form — the separation of the rows of vortices in the nominally two-dimensional vortex street combined with the elongation and re-orientation of the spanwise vortices in the far wake appear to promote instability locally in the array of unequal strength co-rotating vortices. The rapid development of the dual layer vortex street (to within approximately one vortex pair downstream of the cylinder) introduces some difficulty in discerning the symmetry of the dominant mode in the near wake purely from visualisation of the flow field, and so the w^* -velocity signals in the near wake and its corresponding autocorrelation plots (shown in figure 6.8) were utilised to this end to reveal the half-period-flip symmetry of the linear mode A locally. As the flows reach an asymptotic state, the kinetic energies possessed by the various other modes are excited to a comparable level to the dominant mode, and the nonlinear interaction between modes then causing the breakdown of large scaled coherent structures in the flow. Structures resembling the linear mode A with inherent dislocations (the mode A^*) with wavelengths of $\lambda \approx 4h$ can still be observed intermittently in these wakes as elucidated in figure 6.8, despite the overall chaotic nature of the wake.

At a higher Reynolds number of $Re = 240$ for the cylinder inclined at $\alpha = 0^\circ$ and $Re = 300$ for the cylinder inclined at $\alpha = 18^\circ$, the random disturbance field of $|\mathbf{u}'| \sim \mathcal{O}(10^{-4})$ seeded into the two-dimensional (spanwise invariant) flow field at the start of the flow computations decay, causing the flows here to revert to their two-dimensional spanwise invariant states as the solution saturates. This case was re-computed using a different initial condition of the saturated three-dimensional flow solution at $Re =$

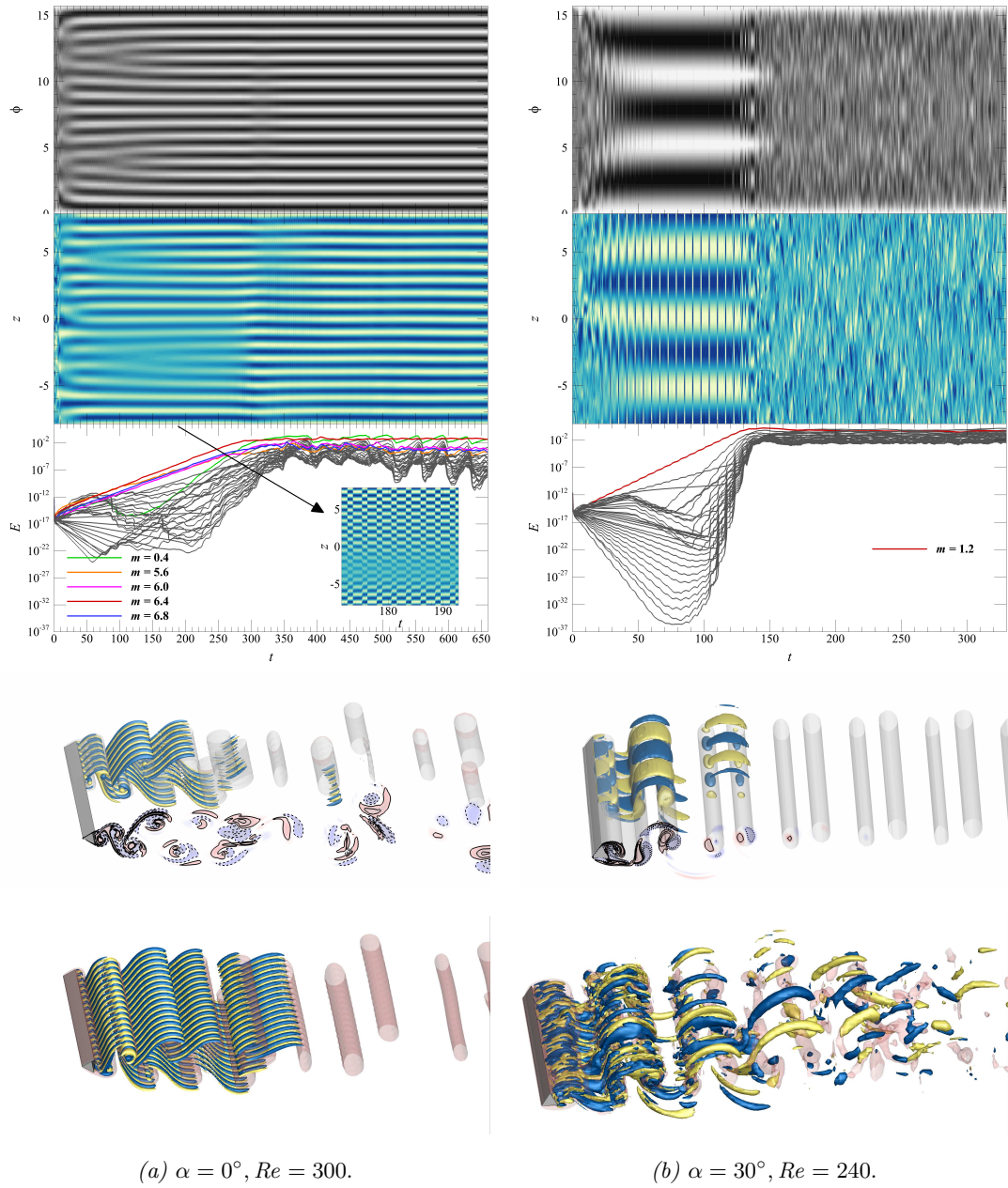


FIGURE 6.9: Captions follow that given in figure 6.7, but are for the flow cases labelled in each subfigure. The additional inset shown in panel (a iii) is the space-time plot of the w^* -velocity taken at a point $(x_0, y_0) = (1, 0)$ in the near wake to demonstrate the half-period-flip symmetry of the solution here. Visualisation of three-dimensional vortical structures in the flow during the exponential growth regime here (panel iv) is truncated to show only several repeats of modal structures along the span to permit the addition of two-dimensional line contours describing the spanwise vorticity perturbation field in the wake. For these line contours, solid/dashed lines correspond to positive/negative values of the spanwise vorticity perturbation.

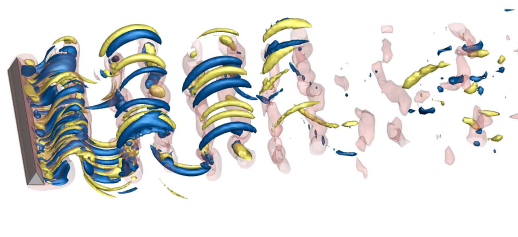
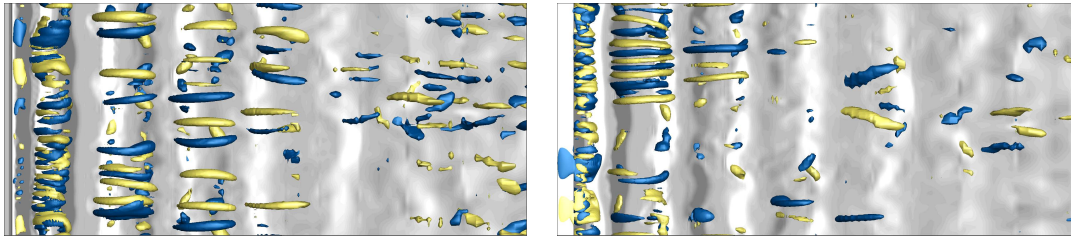
200 for the $\alpha = 0^\circ$ cylinder inclination to test for possible subcriticality of this two-dimensionalisation event, the results again showing that the three-dimensional flow field of the $Re = 200$ solution decays towards a two-dimensional state at $Re = 240$. While this result by itself cannot conclude if the two-dimensional transition is sub- or supercritical, it does pose sufficient evidence that the flow at $Re = 240$ here is absolutely stable to three-dimensional disturbances. A further transition mode was observed in the wake of the $Re = 300$ flow past the cylinder inclined at $\alpha = 0^\circ$ which can also be found in the wakes of low aspect ratio elliptical cylinders as reported by Thompson *et al.* (2014) who denoted it as mode AA. Here, mode AA was observed to possess a dominant wavelength of $\lambda \approx 2\pi h/6.4$ and a spatio-temporal symmetry similar to mode A, at least in the near wake before the separation of the rows of vortices (shown in the inset of figure 6.9a iii where the w -velocity was acquired at a point closer to the cylinder). Besides the different wavelengths, modes A and AA can be distinguished through the structure of the streamwise vorticity perturbation locally within the spanwise vortex loops: mode A has a radial mode number of 1 in a frame of reference moving with the vortex, while mode AA shows a radial mode number of 2 as shown in figure 6.9a iv. Even as the flow approaches an asymptotic state, the modal structure in the near wake observed through the w^* -velocity remains salient as shown in figure 6.9.

In fact, the mode $A \rightarrow 2D \rightarrow$ mode AA sequence of linear transitions from the two-dimensional time-periodic flow as the Reynolds number is increased agrees perfectly with the transitions found in the wakes of a normally oriented elliptical cylinder at low aspect ratios reported by Thompson *et al.* (2014). In that study, the elliptical cylinder with a minor-to-major axis aspect ratio of 0.25 shows mode A to become unstable at a transition Reynolds number of $Re_A = 88.2$ with a wavelength of $\lambda_A = 5.34d$ where d in their study corresponds to the length of the major axis of the cylinder, the suppression of mode A back to a two-dimensional state to occur at $Re \approx 125$, and the subsequent $2D \rightarrow$ mode AA transition to occur at a transition Reynolds number of $Re_{AA} = 185$ with a wavelength of $\lambda_{AA} = 1.3d$. The corresponding transition Reynolds numbers for the triangular cylinder wakes in this study were not determined, but generally occur at much higher Reynolds numbers compared to those found for the elliptical cylinder wake. For example, where in the case of the elliptical cylinder wake the transition to mode AA was predicted to occur at $Re_{AA} = 185$, the equivalent transition in the wake of the cylinder inclined at $\alpha = 0^\circ$ was expected to occur within $200 < Re < 240$. Now,

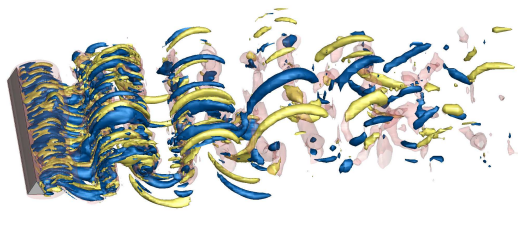
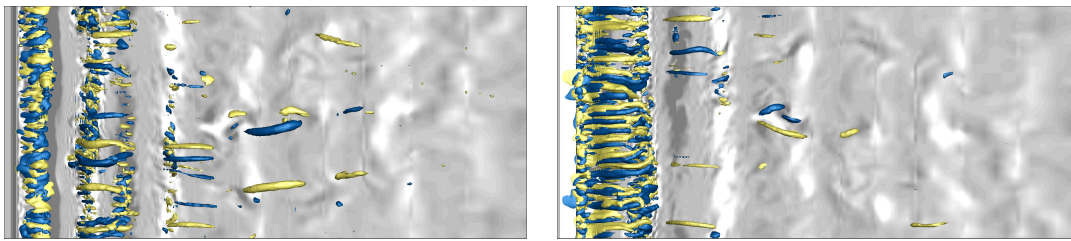
since similar transitions were observed in the wakes of the cylinder inclined at $\alpha = 18^\circ$, but at higher Reynolds numbers than those in the $\alpha = 0^\circ$ cylinder inclination wake, the mode AA transition can be expected to occur in the wake of the cylinder inclined at $\alpha = 18^\circ$ at a higher Reynolds number of $Re > 300$, which was not computed.

A different dominant linear mode was observed in the $200 \lesssim Re \lesssim 240$ flows past the cylinder inclined at $\alpha = 30^\circ$ (shown in figure 6.9) where in the exponential growth regime, three-dimensional structures with wavelengths of $2\pi/1.2 < \lambda/h < 2\pi/1.6$ (similar to mode A) were observed to develop strongly in the near wake, but its spatio-temporal symmetry shows a spanwise translation after a half period evolution as well as a reflection about the wake centreplane such that its spatio-temporal symmetry is similar to that of mode B in the circular cylinder wake (Barkley & Henderson, 1996). Despite this, the disturbance still appears to grow strongly within the elliptical cores of the spanwise vortex rollers much like mode A albeit in the near wake, with the spanwise vorticity perturbations being identical to that demonstrated for the elliptical instability in the vortex rollers found for mode A as reported in Leweke & Williamson (1998). For the asymptotic solution of the $\alpha = 30^\circ$, $Re = 200$ case (shown in figure 6.10), coherent streamwise structures at several different wavelengths can be observed intermittently. In the upper-half of the wake centreplane, counter-rotating streamwise vortex pairs with wavelengths ranging approximately $1h - 2h$ can be observed in the wake, while in the lower-half of the wake centreplane, streamwise vortex pairs with wavelengths of approximately $1h$ can be observed to develop in the near wake. The asymptotic state of the flow at a higher Reynolds number of $Re = 240$ shows a much more chaotic near wake compared to that at $Re = 200$, and also shows streamwise structures in the wake to decay rapidly as they move further downstream of the cylinder, presumably because of the breakdown of the spanwise vortex loop.

For the 2P base flow case at $Re = 240$ and $\alpha = 36^\circ$, the exponential growth phase of the three-dimensionally unstable flow again develops in agreement with the predictions from the stability analysis, with mode structures of wavelengths $\lambda \approx 2\pi h/1.2$ and $\lambda \approx 2\pi h/4$ becoming dominant over various phases of the periodic flow as shown in figure 6.11. These correspond to modes I and II reported in § 4.1.4, and the mode switching observed here arises from the similar linear growth rates of these two modes ($\sigma_I = 0.153$ and $\sigma_{II} = 0.135$). The subharmonic mode III of the 2P base flow predicted from the stability analysis was not observable in the flow field, which was likely due



(a) $\alpha = 30^\circ$, $Re = 200$.



(b) $\alpha = 30^\circ$, $Re = 240$.

FIGURE 6.10: Visualisation of the saturated flow solution for the cases labelled in each subfigure. The left/right panels in the top row of each subfigure describe three-dimensional flow structures in the upper/lower half of the wake, with the spanwise vorticity field shaded in the background. The flows here are from left to right with the cylinder aligned on the left edge of each panel, and the view here encompasses the entire span (z -) of the computational domain. The bottom panel in each subfigure shows the full view of the wake, and the contours and isosurfaces here follow the descriptions given in figure 6.6.

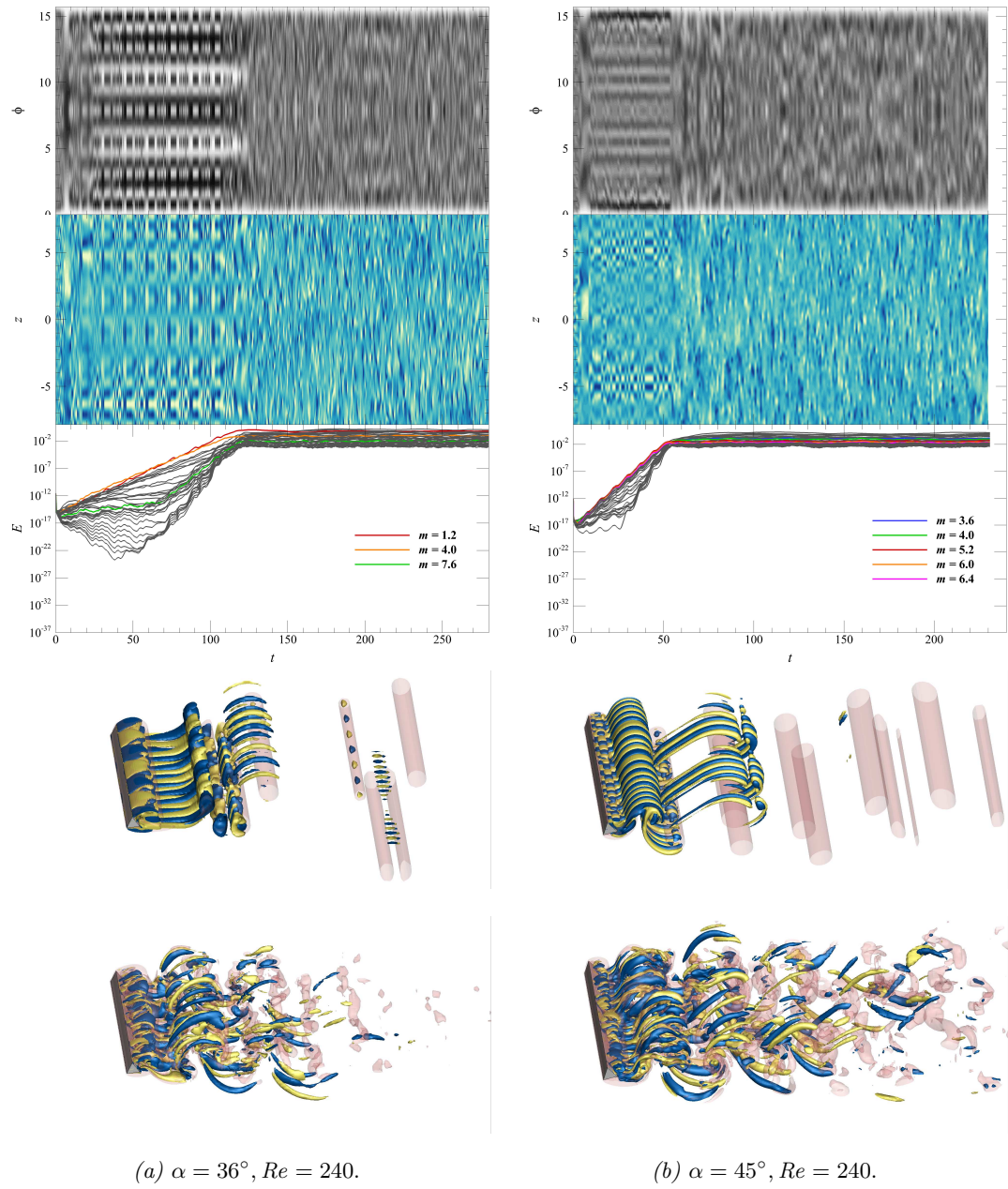


FIGURE 6.11: Captions follow that given in figure 6.7, but are for the flow cases labelled in each subfigure here.

to the smaller linear growth rates at which it is predicted to become unstable. When the disturbances have grown sufficiently and begin to alter the base flow, the 2P vortex street arrangement from the two-dimensional base flow is observed to break down, reforming vortex rollers similar to the Kármán vortex street, albeit with three-dimensional irregularities and distortions along the span of the vortex roller. This possibly implies that the 2P vortex street here, and likely those observed in static structural obstacles such as those in the two-dimensional wakes of an inclined flat plate (Yang *et al.*, 2013) are naturally unstable arrangements in a full three-dimensional flow, the 2P form destabilising back to the Kármán vortex street through the formation of three-dimensional structures.

For most other flows at even higher Reynolds numbers (higher ϵ), distinct transition modes become obscure owing to the large spectrum of wavenumbers that are simultaneously excited leading to the rapid onset of a chaotic flow in the cylinder wake. A representative example of this case is shown for the $Re = 240$ flow past the cylinder inclined at $\alpha = 45^\circ$ in figure 6.11. During the exponential growth phase of the flow evolution, multiple modes are observed to develop simultaneously with comparable growth rates as opposed to the earlier cases where a distinct dominant mode could be discerned within this regime. The flow field reflects this as well, showing three-dimensional streamwise vortices at multiple wavelengths to develop simultaneously in the near wake. The flow is then observed to saturate towards a chaotic solution, and the spanwise averaged flow field describes a vortex street which very crudely resembles the Kármán street array of vortices, deviating from the vortex street regimes predicted from two-dimensional flow computations. This has also been found to be the case in the wake of the normal flat plate reported by Najjar & Balachandar (1998). The deviation in the observed vortex street forms between the two- and three-dimensional flows can be justified through consideration of the term responsible for vortex stretching in the vorticity transport equation: $(\boldsymbol{\omega} \cdot \nabla) \mathbf{u}$. For a two-dimensional flow ($\partial/\partial z = 0$ and $w(x, y, z, t) = 0$ in the present study), the vortex stretching term becomes identically zero, and so the local rate of change of vorticity becomes solely dependent on the diffusion of vorticity which acts to spread the vorticity distribution. This presumably affects the stability of the vortex street arrangement, ultimately leading to the formation of the various two-dimensional vortex street modes. The inclusion of the vortex stretching term in a three-dimensional flow field permits the stretching of the initially

two-dimensional vortex and the amplification of its vorticity distribution which leads to a decrease in its cross-sectional size as it elongates to conserve angular momentum, besides also more pertinently allowing for the generation of streamwise and transverse vorticity (ω_x and ω_y). Note the contradicting actions of the vortex stretching and vorticity diffusion terms on the vortex size — the former narrows the size of the vortex while the latter broadens the vorticity distribution of the vortex. From visualisation of the computed three-dimensional flows (an example is shown in figure 6.11), it is clear that the vortices decrease in size as they advect downstream, and so the vortex stretching term from the vorticity transport equation plays a crucial role in destabilising the various two-dimensional vortex street modes.

6.2.2 Flow induced forces and shedding frequencies

An investigation into the characteristics of three-dimensional flows past a static structure (such as the cylinder in this project) would be incomplete without consideration of body forces and their temporal characteristics. The preceding sections in this chapter have established that the dynamics of the wakes at these Reynolds numbers can only truly be appreciated in a computational domain sufficiently large in the spanwise direction to account for nonlinear interactions in the flow — this section is nested under the results for the larger-span domains for this reason. As a recap, the results presented in this section were obtained from a computational domain with a spanwise length of $l_z = 2\pi h/0.4$ which accommodates the formation of multiple instances of modal structures in the wake, thus permitting nonlinear interaction either through self-excitation of individual modes or through intermodal interactions. The results presented in this section were obtained from the saturated three-dimensional flow solutions after nonlinear effects have fully developed, as estimated through the saturation of the total kinetic energy of the Fourier modes. Also, the dimensionless time values (t) in this section have been reset such that $t = 0$ corresponds to an arbitrary time when the three-dimensional flow solution has saturated, and so all results for $t \geq 0$ are for the saturated flow solutions. Only several cases were considered owing to the computational expense, and so the cylinder inclinations considered here were $\alpha = 0^\circ, 18^\circ, 30^\circ, 36^\circ, 45^\circ$, and 60° , all being computed to a maximum Reynolds number of $Re = 300$. Recall also that the lift and drag forces exerted on the cylinder have been non-dimensionalised and normalised as force coefficients per unit span, and so all subsequent references to these forces within

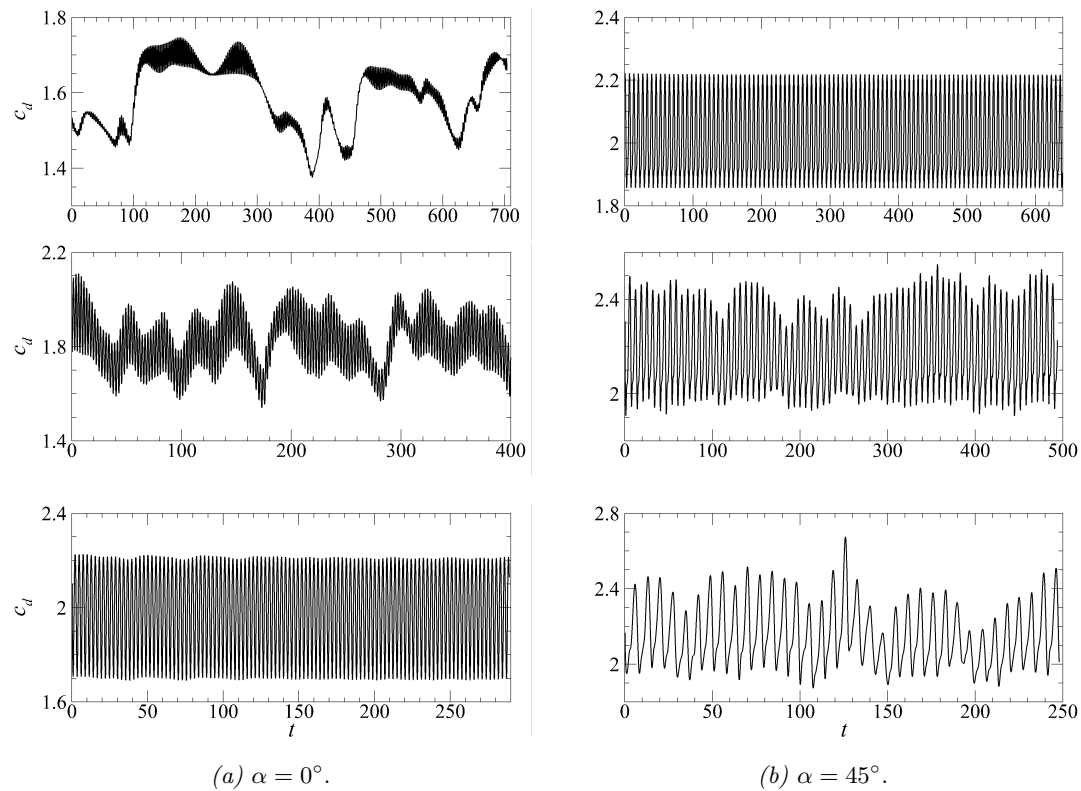


FIGURE 6.12: Time-history of the instantaneous drag coefficient of the cylinder inclined at (a) $\alpha = 0^\circ$ for flows at Reynolds numbers of $Re = 110, 200,$ and 300 from top to bottom, and at (b) $\alpha = 45^\circ$ for flows at Reynolds numbers of $Re = 120, 200$ and 300 from top to bottom. Recall that for the remainder of this section, $t \geq 0$ correspond to flow solutions in the saturated nonlinear state.

this section should be treated as such. Spectral analysis of the fluctuating lift force signals were also performed to obtain an estimate of the vortex shedding frequency — the lift coefficient being an integral measure of the flow field about the cylinder is less sensitive to turbulent or chaotic fluctuations in the wake while retaining effects from bulk fluid motion such as those generated during the vortex shedding process, and was thus determined to be the most suitable measure for this purpose.

Several observations are first made on the fluctuating force signals obtained from the cylinder. First, and as expected, the drag force exerted on the cylinder at any instance of time is derived primarily from the pressure drag, while the friction drag component remains small in magnitude. This effect becomes more pronounced with increasing Reynolds numbers. Examples of the lift and drag force signals are shown figures 6.12 and 6.13. The mean and r.m.s. of these quantities will be discussed shortly. A second

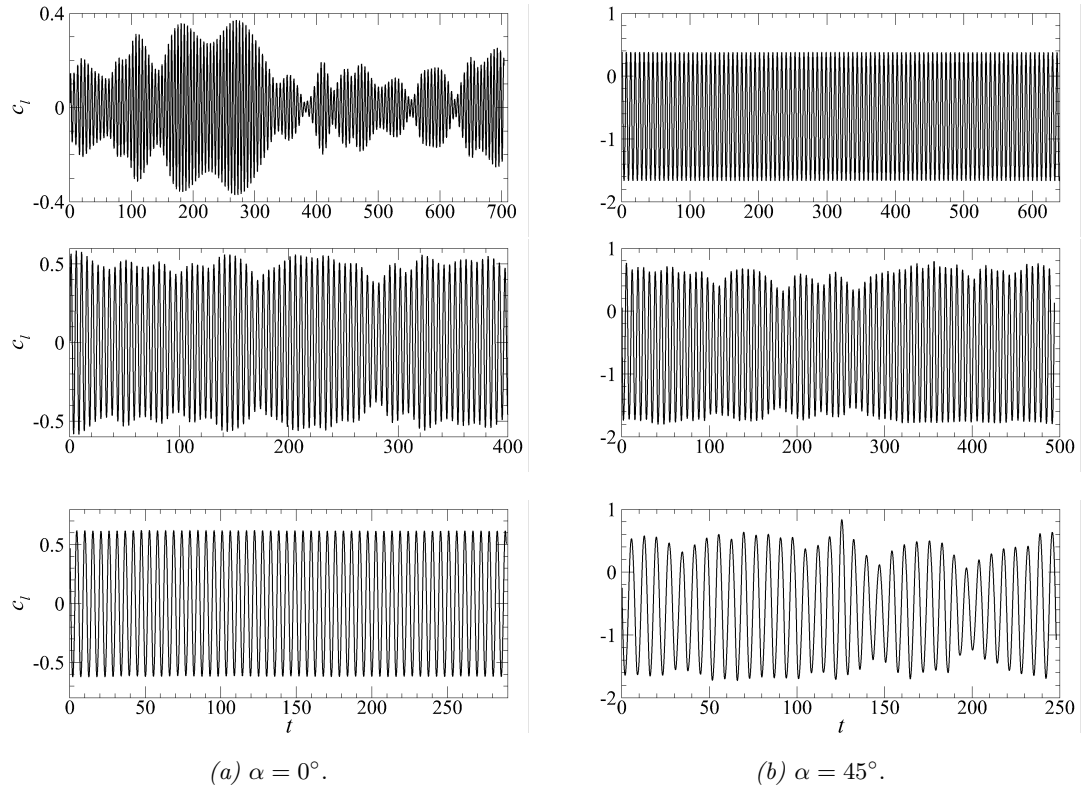


FIGURE 6.13: Captions follow that given in figure 6.12, but are instead for the instantaneous lift coefficients.

observation from these plots concerns the mode A* wake exemplified by the saturated solution of the $Re = 110$ flow past the cylinder inclined at $\alpha = 0^\circ$. Despite the symmetry of this system, the large-scale dislocations in the vortex street for mode A* inflicts cycles of high and low drag forces on the cylinder which may be detrimental to the structural integrity of the cylinder depending on the application. In these cases, the flows remain in the higher and lower drag states for extended periods of time which often persists for up to $\mathcal{O}(10)$ shedding cycles, while the transition between the states is fairly abrupt. The lift forces on the cylinder are also commensurately affected, manifesting as modulations to the oscillatory signal. Najjar & Balachandar (1998) and Jiang *et al.* (2016) have reported these states for the normal flat plate and circular cylinder wakes, respectively, demonstrating a correlation between the occurrences of these fluctuations in the lift and drag forces with the time-intervals where vortex dislocations can be observed. Figures 15–17 in Jiang *et al.* (2016) show these irregular fluctuations to decrease in frequency as mode B stabilises, particularly at $Re \gtrsim 265$. Flow visualisation of the mode A* cases in this study (shown in figure 6.14) agree with their results, showing

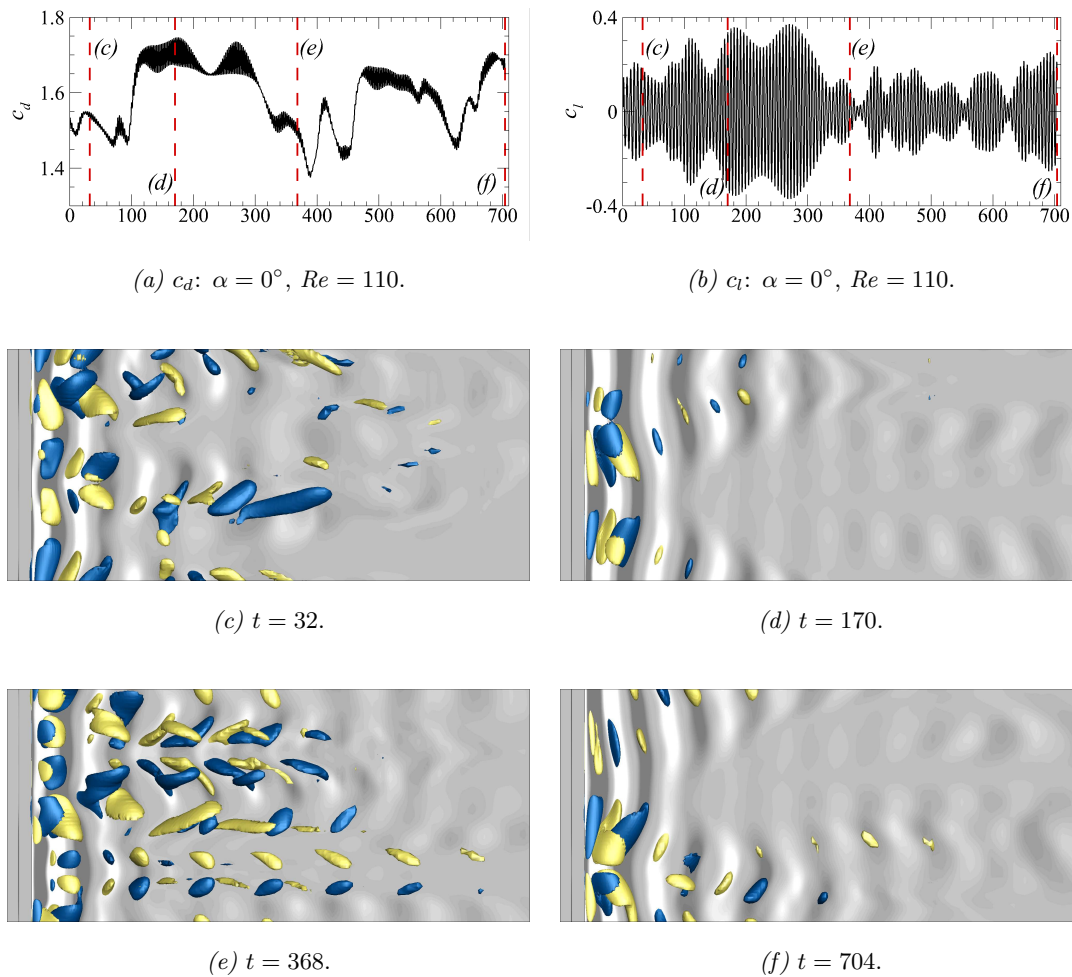


FIGURE 6.14: (a,b) Time histories of the drag and lift coefficients for the cylinder inclined at $\alpha = 0^\circ$ and $Re = 110$ similar to figures 6.12 and 6.13. The red dashed lines show the time instances corresponding to the flow visualisations in panels (c-f), each being representative of the flow in a higher- and lower drag state. (c-f) Visualisation of the flow in the upper half-plane of the wake at the time instances labelled in each panel. Blue/yellow isosurfaces mark the streamwise vortices in the flow at an arbitrary ω_x level (equal magnitude, opposite signed) to aid with visualisation, with the spanwise vorticity field in the wake-centreplane shaded in the background. The magnitudes of the streamwise vorticity isosurfaces and spanwise vorticity contours used to elucidate the wake structures were kept identical to permit direct comparisons of the flow field at various times. The flows in panels (c,e) are at time instances where the flow is in a lower drag state, while those in panels (d,f) are at time instances where the flow is in a higher drag state as shown in (a,b).

that the lower drag state is associated with the formation of large modal structures in the wake and stronger distortion to the spanwise vortex rollers, while the higher drag state is associated with the formation of streamwise structures with wavelengths similar to mode A, and with less distortions and dislocations to the spanwise vortex rollers. The forces measured on the cylinder inclined at $\alpha = 45^\circ$ in a flow at $Re = 120$, as well as at $\alpha = 0^\circ$ in an $Re = 300$ flow shows significantly cleaner oscillation signatures owing to the increased structural uniformity of the vortex rollers. These cases transition through linear modes C and AA, respectively, both of which have been shown to alter the spanwise vortex rollers quite minimally (§ 6.2.1) similar to mode B in the circular cylinder wake, most of which occur through (strongly) supercritical bifurcations from its two-dimensional basic state.

Results for the mean and r.m.s. force coefficients are shown in figures 6.15–6.18. From the available data, it was observed that the viscous drag exerted on the cylinders inclined at $\alpha < 30^\circ$ were always higher than that exerted on cylinders inclined at $\alpha \geq 30^\circ$, with the viscous drag in the former range of cylinder inclinations being of $\mathcal{O}(10^{-1})$ while those in the latter range were often found at magnitudes of $\mathcal{O}(10^{-2})$ or less. This can be observed in panels (a–f) in figure 6.15 where the pressure drag acting on the cylinders inclined at $\alpha = 0^\circ$ and 18° are noticeably less than the total drag computed whereas these values for the remaining cylinder inclinations $\alpha \geq 30^\circ$ appear almost identical, the viscous drag contribution being the difference of the pressure drag from the total drag. The mean drag for cylinder inclinations $\alpha \geq 30^\circ$ also appear to vary quite little with increasing Reynolds numbers up to $Re = 300$, while those for cylinder inclinations $\alpha < 30^\circ$ shows an increasing trend with increasing Reynolds numbers. For the latter range of cylinder inclinations, the increasing trend in the mean drag coefficient is likely caused by the presence of large scale dislocations in the spanwise vortex rollers as well as the existence several subsequent transition stages such as the mode AA, and so the wakes here are not truly at a Reynolds number independent or turbulent state as yet. The mean lift coefficients (shown in figure 6.16a) similarly show little dependence on the Reynolds number, except for when the flow transitions back to its two-dimensional state as observed in the wake of the $Re = 240$ flow past the $\alpha = 0^\circ$ cylinder and the $Re = 300$ flow past the $\alpha = 18^\circ$ cylinder. The mean lift coefficients of the cylinders at symmetric inclinations of $\alpha = 0^\circ$ and 60° were of $\mathcal{O}(10^{-4})$ or less for all Reynolds numbers tested here, which is essentially zero, as anticipated. The fluctuations of the

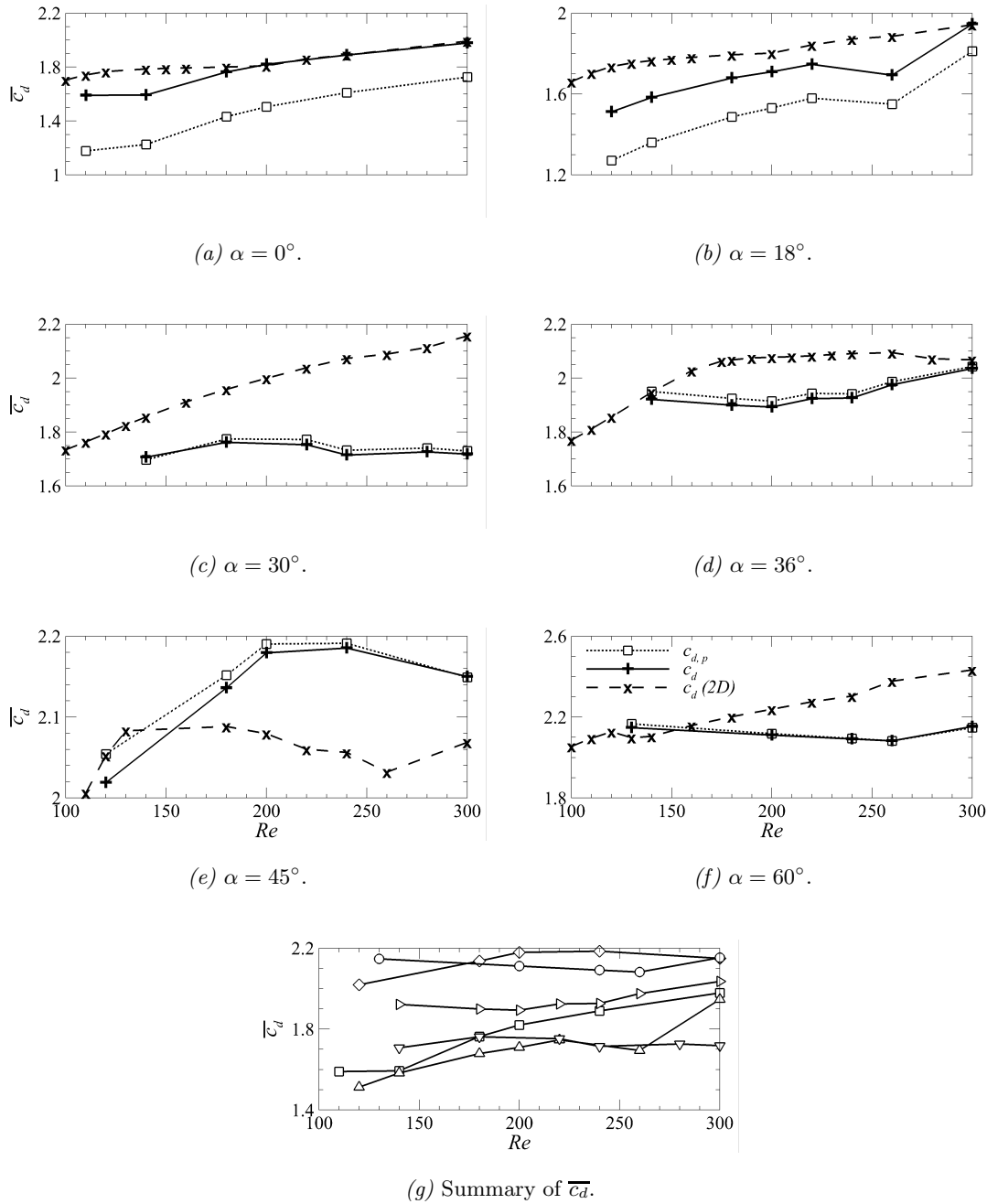


FIGURE 6.15: (a–f) Variation of the mean drag coefficient with increasing Reynolds numbers for cylinder inclinations as indicated in each panel. In each of these panels, the mean drag coefficients induced by the three-dimensional flows (\bar{c}_d) are marked by the solid line weaving through (+) markers, the pressure contribution to the mean drag coefficients ($\bar{c}_{d,p}$) by the dotted lines through the hollow square markers (\square), and the drag coefficients predicted from the two-dimensional flow ($\bar{c}_{d,2D}$) by the dashed lines connecting the (\times) markers. The plot in (g) summarises the results for the mean drag coefficients (\bar{c}_d), each cylinder inclination being denoted by: $\alpha = 0^\circ : \square$, $\alpha = 18^\circ : \Delta$, $\alpha = 30^\circ : \nabla$, $\alpha = 36^\circ : \triangleright$, $\alpha = 45^\circ : \diamond$, and $\alpha = 60^\circ : \circ$.

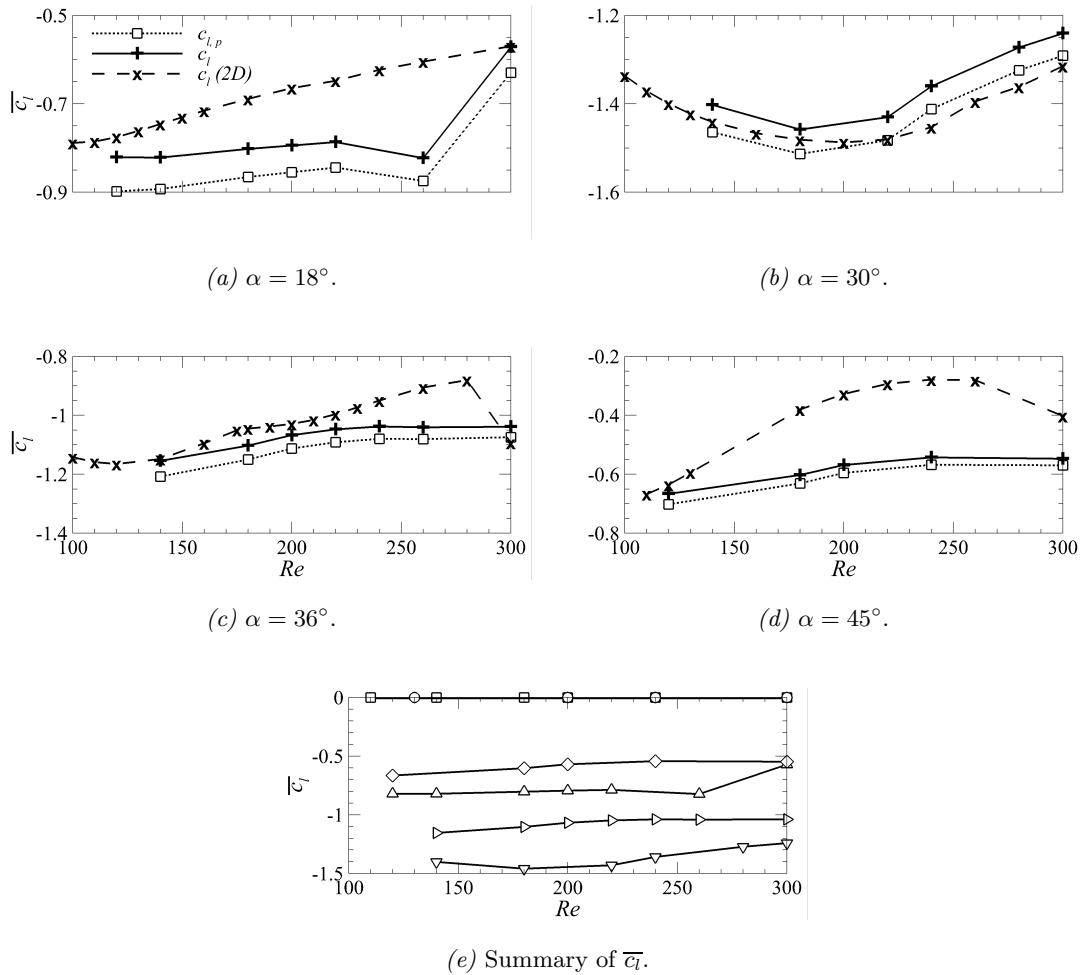


FIGURE 6.16: (a–d) Variation of the mean lift coefficient with increasing Reynolds numbers for cylinder inclinations as indicated in each panel. In each of these panels, the mean lift coefficients induced by the three-dimensional flows (\bar{c}_l) are marked by the solid line weaving through (+) markers, the pressure contribution to the mean lift coefficients ($\bar{c}_{l,p}$) by the dotted lines through the hollow square markers (\square), and the lift coefficients predicted from the two-dimensional flow ($\bar{c}_{l,2D}$) by the dashed lines connecting the (\times) markers. The plot in (e) summarises the results for the mean lift coefficients (\bar{c}_l), each cylinder inclination being denoted by: $\alpha = 0^\circ : \square$, $\alpha = 18^\circ : \Delta$, $\alpha = 30^\circ : \nabla$, $\alpha = 36^\circ : \triangleright$, $\alpha = 45^\circ : \diamond$, and $\alpha = 60^\circ : \circ$.

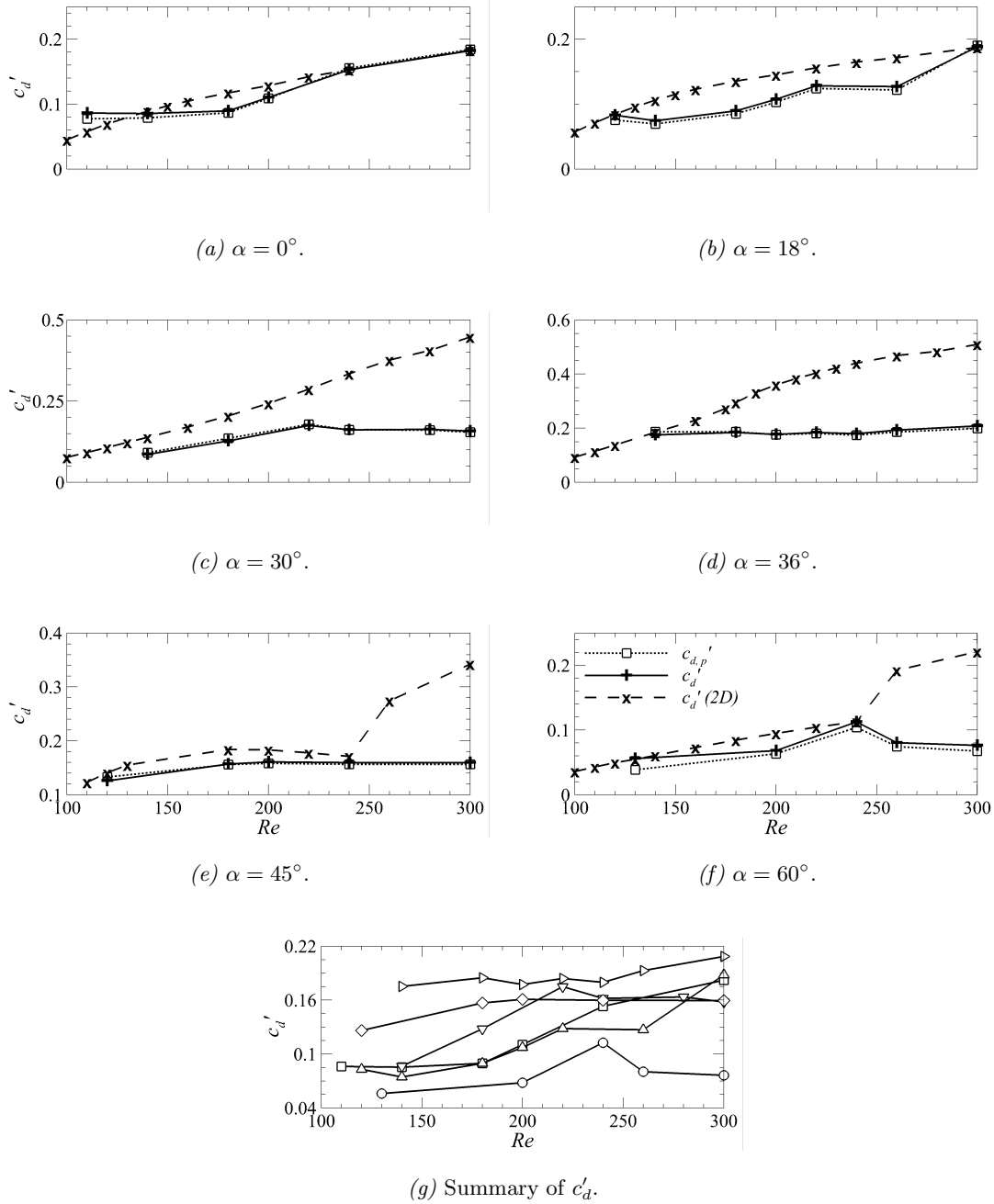


FIGURE 6.17: (a–f) Variation of the root-mean-squared (r.m.s.) drag coefficient with increasing Reynolds numbers for cylinder inclinations as indicated in each panel. In each of these panels, the r.m.s. drag coefficients induced by the three-dimensional flows (c'_d) are marked by the solid line weaving through (+) markers, the pressure contribution to the r.m.s. drag coefficients ($c'_{d,p}$) by the dotted lines through the hollow square markers (\square), and the r.m.s. drag coefficients predicted from the two-dimensional flow ($c'_{d,2D}$) by the dashed lines connecting the (\times) markers. (g) Summary of the results for the r.m.s. drag coefficients induced on the cylinder (c'_d), with each cylinder inclination being denoted by: $\alpha = 0^\circ$: \square , $\alpha = 18^\circ$: Δ , $\alpha = 30^\circ$: ∇ , $\alpha = 36^\circ$: \triangleright , $\alpha = 45^\circ$: \diamond , and $\alpha = 60^\circ$: \circ .

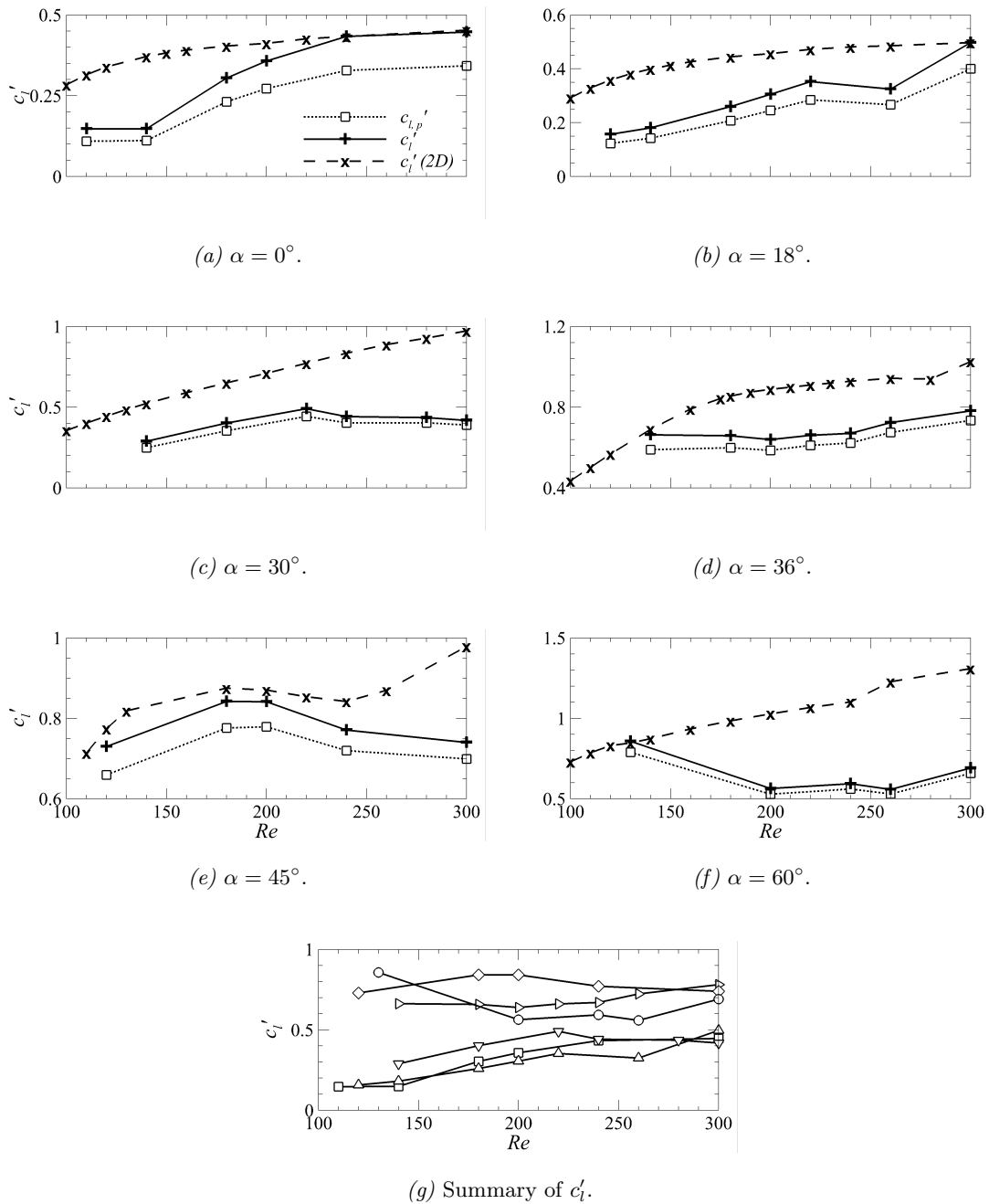


FIGURE 6.18: (a-f) Variation of the root-mean-squared (r.m.s.) lift coefficient with increasing Reynolds numbers for cylinder inclinations as indicated in each panel. In each of these panels, the r.m.s. lift coefficients induced by the three-dimensional flows (c'_l) are marked by the solid line weaving through (+) markers, the pressure contribution to the r.m.s. lift coefficients ($c'_{l,p}$) by the dotted lines through the hollow square markers (\square), and the r.m.s. lift coefficients predicted from the two-dimensional flow ($c'_{l,2D}$) by the dashed lines connecting the (\times) markers. (g) Summary of the results for the r.m.s. lift coefficients induced on the cylinder (c'_l), with each cylinder inclination being denoted by: $\alpha = 0^\circ$: \square , $\alpha = 18^\circ$: Δ , $\alpha = 30^\circ$: ∇ , $\alpha = 36^\circ$: \triangleright , $\alpha = 45^\circ$: \diamond , and $\alpha = 60^\circ$: \circ .

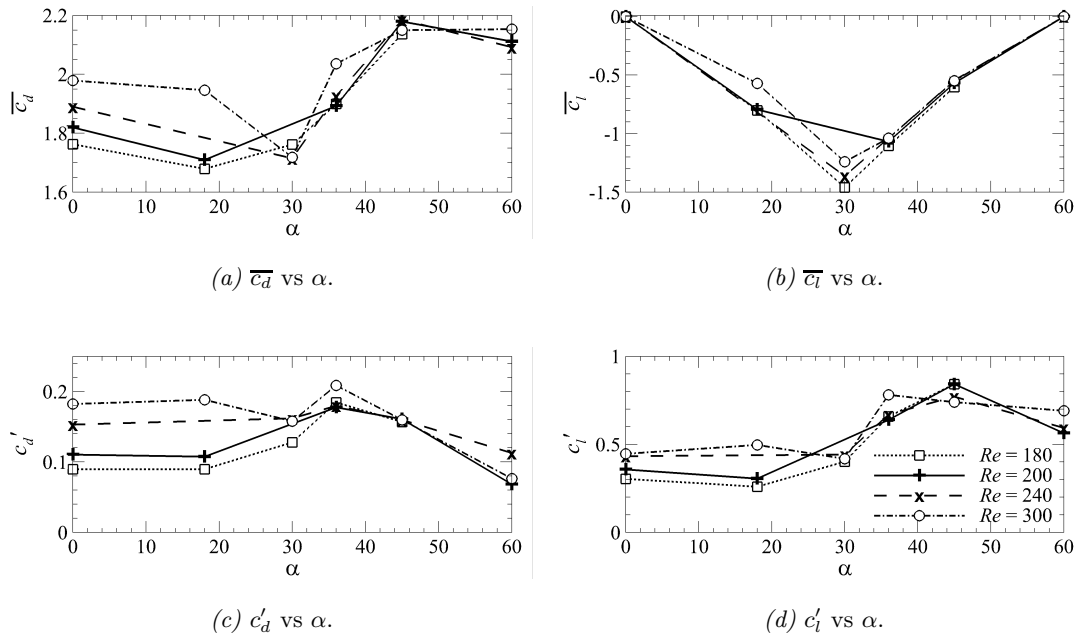


FIGURE 6.19: Variation of the mean and r.m.s. values of the lift and drag coefficients with cylinder inclination α for select Reynolds numbers. In all panels, the data obtained at Reynolds numbers of $Re = 180$ are indicated by square markers (\square) connected by dotted lines, $Re = 200$ by (+) markers connected by solid lines, $Re = 240$ by (\times) markers connected by dashed lines, and $Re = 300$ by circle markers (\circ) connected by the dash-dotted lines.

lift and drag coefficients were also quantified through the root-mean-square (r.m.s.) of the signals, the results showing that these fluctuations generally get more intense with increasing Reynolds numbers, as shown in figures 6.17–6.18. Figure 6.19 shows the variation of the mean and r.m.s. force coefficients with the cylinder inclination angle at select Reynolds numbers. From these plots, it can be observed that the mean drag coefficients as well as the r.m.s. of the lift coefficients are generally higher for cylinder inclinations of $\alpha > 30^\circ$, with the outlier at $\alpha = 18^\circ$, $Re = 300$ again corresponding to the two-dimensionalised flow state. The largest mean lift coefficients exerted on the cylinder generally occurred at an inclination of $\alpha = 30^\circ$ for all Reynolds numbers.

Comparing these results obtained from the nonlinear three-dimensional flows against those obtained from two-dimensional flow computations with increasing α , it is noted that the mean and r.m.s. of the force coefficients generally followed a similar trend to its two-dimensional counterpart, differing only in its magnitude (compare figure 6.19 here against figures 3.26–3.27 in § 3.4). In most cases, the three-dimensional flow computations predict lower mean drag coefficients and higher mean lift coefficient magnitudes

than those predicted from two-dimensional flow computations, as shown in figures 6.15–6.16. Intuitively, the higher mean drag coefficients predicted from two-dimensional flow computations might stem from the formation of various two-dimensional vortex street modes which produce large wake regions, thus increasing the drag forces acting on the cylinder. These two-dimensional vortex street modes have been shown (earlier in the previous section) to stabilise back to the Kármán vortex street mode in three-dimensional computations, and so the mean drag coefficients are generally lower owing to a narrower wake. A similar argument may be posed to justify the lower r.m.s. of the force coefficients found here compared to those found from the two-dimensional flow computations. Note that the mean lift and drag coefficients predicted for the two-dimensionalised flows as well as the mode AA flows in the wake of the cylinder inclined at $\alpha = 0^\circ$ and 18° are in agreement with those predicted from the two-dimensional flow. Although not computed in this study, a future direction of interest would be to investigate how the ‘drag crisis’ might manifest in these systems since flow separation is forced at the edges of the cylinder, and how the lift and drag coefficients in this system might change past the instability compared to those of the vortex shedding states here.

The shedding frequencies predicted from the spectral analysis reveal that a discontinuity exists between the shedding frequencies of the two-dimensional wakes and those for the saturated three-dimensional wakes with increasing Reynolds numbers crossing the transition Reynolds number for cylinder inclinations $\alpha \leq 30^\circ$, the three-dimensional flow transitions here occurring through the mode A instability. While this transition was predicted to be (weakly) supercritical as reported earlier in § 6.1, those results were predicted from a computational domain permitting only a single wavelength of the unstable mode thus restricting some nonlinear interactions, and concessions were made that these transition may well occur through subcritical bifurcations in extended systems as demonstrated by Akbar *et al.* (2011) and Jiang *et al.* (2018) for the mode A transition in the circular and square cylinder wakes, respectively. The flow past the cylinder inclined at $\alpha = 60^\circ$, while also becoming unstable through mode A at $Re_A = 127$, appears to remain non-hysteretic in agreement with the predictions made using the single-mode domain. Flows becoming unstable through mode C are also non-hysteretic with increasing Reynolds numbers. These are shown in the plots of the predicted shedding frequencies in figure 6.20, while the spectral amplitudes of the fluctuating lift signals for the flows past the cylinder inclined at $\alpha = 0^\circ$ and 36° are shown in figure 6.21.

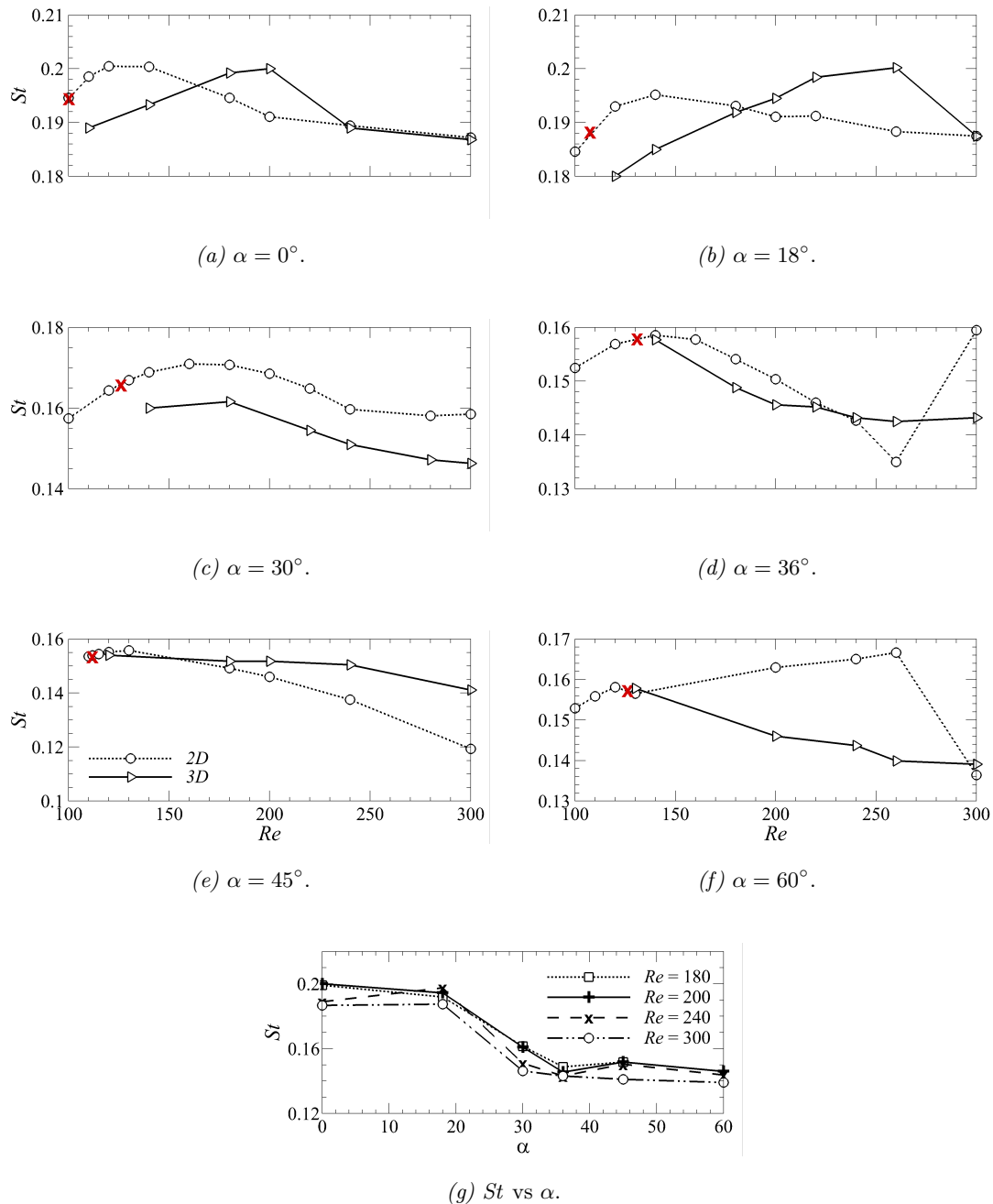


FIGURE 6.20: (a–f) Variation of the Strouhal number (St) with increasing Reynolds numbers for cylinder inclinations as indicated in each panel. In each of these panels, the Strouhal numbers of the three-dimensional wakes (St) are marked by the solid lines interconnecting triangular markers (\triangleright), the Strouhal numbers predicted from two-dimensional flow computations are marked by dotted lines through circle markers (\circ), and the critical Strouhal number at the transition is marked with a red cross (\times). (g) Plot of St against α at several Reynolds numbers as labelled in the inset line legend.

Increasing the Reynolds number of these three-dimensional flows appear to have little effect on the vortex shedding frequency at any given cylinder inclination as shown in figure 6.20(g). The shedding frequency is, however, dependent on the cylinder inclination similar to its two-dimensional flow predictions, appearing to possess similar St within ranges $0^\circ \leq \alpha < 30^\circ$ and $30^\circ < \alpha \leq 60^\circ$. In all cases computed here, the leading spectral peak was found at the Strouhal frequency, demonstrating the prevalence of vortex shedding in all these flows. Comparing the power spectra of the lift coefficients of the two cylinder inclinations in figure 6.21 (representative of most other cases), it was observed that the mode A transition case at $\alpha = 0^\circ$, $Re = 110$ showed some contamination in its response despite being at a low ϵ , which was an expected effect of the disturbances and dislocations introduced into the wake as characteristic of mode A*. The mode C case at $\alpha = 45^\circ$, $Re = 120$ instead shows a clean frequency response. Increasing the Reynolds number then generally broadens the band of frequencies excited in the wake or introduces incommensurate frequency bands, the exceptions being cases where the flow transitions back to a two-dimensional state or where the flow becomes unstable through mode AA.

Further investigations concerning the turbulent properties of the wake were not performed as it deviated from the scope of the present study. The computational cost associated with computing turbulent flows directly from evolution of the governing equations is substantial owing to the significantly higher spatial resolution required to resolve turbulent eddies and its dissipation, and also because of the long time evolution required to achieve a statistically stationary flow state necessary to perform any meaningful analysis on these turbulent states.

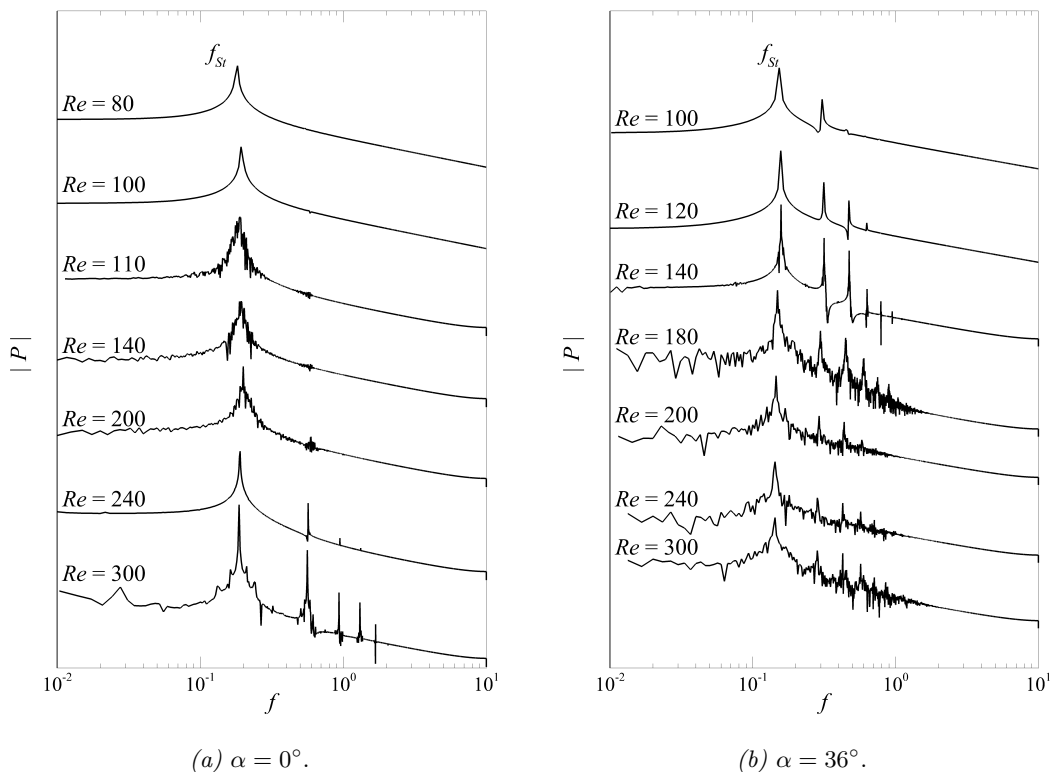


FIGURE 6.21: Power spectra of the lift coefficients with increasing Reynolds numbers demonstrating the salience of the vortex shedding process in the cylinder wake at these Reynolds numbers. In (a) for the cylinder inclined at $\alpha = 0^\circ$, the spectra corresponding to Reynolds number flows of $Re = 80$ and 100 are from two-dimensional flow computations since the first three-dimensional instability only manifests at $Re_A = 100.2$, the $Re = 240$ spectrum corresponds to the two-dimensionalised flow, and the $Re = 300$ spectrum corresponds to the mode AA flow. In (b) for the cylinder inclined at $\alpha = 36^\circ$, the spectra at $Re = 100$ and 120 are also obtained from two-dimensional flow computations since the flow transition is predicted at $Re_C = 131$.

6.3 Chapter summary

This chapter reports the results from three-dimensional numerical simulations of the flows past the inclined triangular cylinder. The wakes of flows unstable through mode A develop defects in the spanwise vortex rollers which rapidly lead to a breakdown of the mode pattern (mode A* in Williamson, 1996a, also ‘wake turbulence’ in Bloor, 1964) even at Reynolds numbers close to the predicted transition. Increasing the Reynolds numbers showed the asymptotic state of these wakes to become less coherent as expected. At low cylinder inclinations of $\alpha = 0^\circ$ and 18° here, these turbulent wakes showed a decay back into a two-dimensional state at Reynolds numbers $200 \lesssim Re \lesssim 300$, followed by the growth of a mode resembling mode AA in Thompson *et al.* (2014). The wakes of flows unstable through mode C remained coherent at nonlinear saturation of the flow near the transition, but also becomes turbulent when increasing the Reynolds number. The force coefficients of the cylinder at these Reynolds numbers were then quantified along with their shedding frequencies, and a comparison was made between these measured values and their two-dimensional flow counterpart.

Chapter 7

Conclusions

What started out as a curiosity concerning the variation of the dynamics of bluff body wakes as the flow symmetry is smoothly and systematically interfered with through structural or geometric modifications has revealed deep connections between the dynamics of the wakes of various canonical cylindrical structures, bridging the sometimes disparate observations of these wakes. The overarching message communicated by the results in this thesis is that even in seemingly simple systems such as those of moderate Reynolds number flows past the cylinder considered in this thesis, a diverse range of wake responses is excited through nonlinear interactions in the wake, which may then rapidly become turbulent. At moderate Reynolds numbers, however, these complex flows trace their origins to the growth of unstable wavepackets on a lower-dimensional basic state, and the transition modes associated with these bifurcations are shown to be strongly similar regardless of the cylinder cross-section geometry. This demonstrates that the instabilities which manifest in these systems are inherent to the flow while the body geometry merely acts to alter the flow symmetry which, in turn, promotes or suppresses the growth of various instability modes. Such a generalisation may find utility in the control of these wakes or the suppression of instabilities at moderate Reynolds numbers. These deductions have been drawn from the results presented over the preceding chapters of this thesis, conclusions from which are covered in the sections to follow.

7.1 Two-dimensional flow past an inclined cylinder

The first stage of this project considered the case of a two-dimensional flow in the plane of the cylinder without prior knowledge of the thresholds where any transitions may be observed in its wake. The primary purpose of this investigation was to map out the two-dimensional solution space and understand how the flow dynamics vary with the cylinder inclination relative to the oncoming flow, motivated by an apparent interest on flows past non-circular/non-smooth geometries within the framework of a two-dimension flow (Zhang *et al.*, 2008; Bao *et al.*, 2010; Yoon *et al.*, 2010; Yang *et al.*, 2012; Ganga Prasath *et al.*, 2014; Wang *et al.*, 2015, amongst others).

For steady flows, the steady detached eddy scenario is found to be the generic topology for flow separation wherein a streamtube can be drawn such that it always passes through the recirculation zone (denoted as an ‘alleyway’ flow in this thesis, consistent with Perry *et al.*, 1982). The steady recirculation regions are thus found in the two distinct eddies, with one being generally attached to the cylinder while the other ‘floats’ in the wake (the detached eddy), and the width of the alleyway flow between these eddies increase approximately proportionally with the geometric asymmetry of the cylinder about the wake centreplane. Closed recirculation zones containing two reflection-symmetric eddies about the wake centreplane are special cases for when the body cross-section is also symmetric. The Reynolds number at which flow separation occurs, Re_s , was also shown to increase monotonically with the cylinder inclination within $0^\circ \leq \alpha \leq 60^\circ$, and is non-differentiable about $\alpha = 0^\circ$ and 60° (or every 60° for a full range of rotations). Also, the separation Reynolds number for the cylinder inclined at $\alpha = 0^\circ$ was predicted to be $Re_s \approx 0$, and so a steady attached flow in this case is likely an unphysical outcome owing to the immense adverse pressure gradients that the flow experiences at the cylinder’s leeward vertex edges.

At the transition to a periodic flow, the instability manifests through a supercritical Hopf bifurcation, indicating that the equilibrium amplitude can be well predicted from a cubic order truncated amplitude equation. This is consistent with the transition from a steady to a periodic flow in the wakes of various other cylindrical geometries (Provansal *et al.*, 1987; Zielinska & Wesfreid, 1995, amongst others). Varying the cylinder inclination affects the stability threshold (the critical Reynolds number Re_c) either through the formation of a small flow reversal region at the windward faces of the cylinder which disturbs the flow before it reaches the separation points, or through the

shifting separation points as the steady recirculation zone spreads from forming across a single leeward cylinder face to both leeward faces — the former scenario occurring for cylinder inclinations $\alpha \leq 30^\circ$ while the latter being for $\alpha > 30^\circ$.

At even higher Reynolds numbers past the primary instability, the vortex street of the two-dimensional flow develops into various spatial forms. The first form observed was the Kármán vortex street comprising alternating counter-rotating vortices which decays in space due to viscosity and eddy diffusion, similar to that found in the wakes of the square and circular cylinders amongst other bodies. This form is periodic by definition set for this investigation, and was common across the entire range of cylinder inclinations. With sufficient increase in the Reynolds number, this vortex street adopts several topological changes. Most generically, like signed vortices in the Kármán street align to form a separated vortex street, which at even higher Reynolds numbers become unstable to a secondary vortex street characterised by large scale vortices formed through merging and non-harmonic vortex interactions, and whose frequency spectra shows peaks incommensurate to the Strouhal frequency. This secondary vortex street was also observed in the circular cylinder wake, being formed through convectively unstable wavepackets as shown by Kumar & Mittal (2012), and so it is a temporal feature there at $Re = 150$ which eventually re-stabilises to the Kármán street. The difference here is that this secondary vortex street in the present study appears as a fixed feature of wake, finding a stronger similarity to that found in the decelerated vortex streets reported by Durgin & Karlsson (1971) and also in various two-dimensional bluff body wakes such as those for the elliptical cylinder and flat plate (Johnson *et al.*, 2004; Zhang *et al.*, 2008, amongst others). Within a specific range of cylinder inclinations ($30^\circ \lesssim \alpha \lesssim 48^\circ$), harmonic interactions within the cylinder wake appear to dominate the response, the vortex street assuming a form resembling the 2P and P+S modes reported in the oscillating circular cylinder wake (Williamson & Roshko, 1988). Here, the 2P-like mode exhibits a spectral peak at a frequency subharmonic to that of the fundamental (the vortex shedding frequency), while the P+S-like mode was generally aperiodic except for specific combinations of α and Re where it is also subharmonic.

The final stage of this part of the project concerns the quantification of common wake properties. Here, the vortex shedding frequency of the two-dimensional flow past the cylinder was shown to be broadly similar across two cylinder inclination ranges $\alpha < 30^\circ$ and $\alpha \gtrsim 30^\circ$ through the Roshko number Ro . As for the forces induced on

the cylinder by the flow, the mean lift coefficient has the largest magnitude about a cylinder inclination of $\alpha = 30^\circ$ where the triangular cross-section is most geometrically asymmetric, regardless of the Reynolds number (within the range investigated). The mean drag coefficient instead appears to be largest at a cylinder inclination of $\alpha = 60^\circ$, and the larger mean drag coefficient found for the cylinder inclined at $\alpha = 60^\circ$ compared to that at $\alpha = 0^\circ$ demonstrates how severely an afterbody shape can affect the forces induced on the body. Besides that, the root-mean-squared measures of the flow-induced forces show that the onset of the 2P vortex shedding mode brings about a larger force fluctuation range.

7.2 Stability of the cylinder wake

Having characterised the two-dimensional flows, it was next of interest to determine how and when three-dimensional perturbations on these flows begin to grow. To this end, Floquet stability analysis of these two-dimensional flows was performed, and the most dominant modes in the eigenspectra identified. Overall, three-dimensionality in these cylinder wakes manifests through modes A or C across the possible cylinder inclinations, and the critical angles where both modes are simultaneously critical are $\alpha \approx 34.6^\circ$ and 55.4° . For mode A, the eigenvector field appears to vary from one where perturbations are concentrated in the near wake similar to those in the wake of a circular cylinder, to one where perturbations develop strongly in the far wake similar to those found in the wakes of the inclined square cylinder and flat plate (Sheard *et al.*, 2009; Thompson *et al.*, 2014). Regardless, both are consistent with the mode A description, having perturbations consistent with the elliptical instability mechanism forming in the vortex cores. The mode C perturbations instead appear consistent with those found in all other bluff body wakes where it exists, provided the flow symmetry about the cylinder is perturbed (Zhang *et al.*, 1995; Sheard *et al.*, 2003, 2009; Yang *et al.*, 2013; Yildirim *et al.*, 2013b). Specifically, the perturbations are concentrated in the near wake, having vortices that form with a bias towards one half of the wake about the centreplane. The generalised growth rates of the linear modes for near-critical systems show that mode C develops more rapidly than mode A, with its growth rate increasing with the Reynolds number distance parameter ϵ at almost twice the rate of mode A.

Several measures of the base flow's asymmetry about the wake centreplane were tested to isolate the key asymmetry feature in the underlying wakes inciting the sub-

harmonic mode. The results for most of these measures showed the asymmetry varying with streamwise position, but was particularly imbalanced in the near wakes of the cylinder at inclinations where mode C can be observed in the eigenspectrum obtained from the stability analysis. This suggests that the three-dimensional mode C acts as a correction mechanism through which the base flow attempts to recover some semblance of symmetry. The mode A cases instead did not require the asymmetry levels to be negligible at all points, but required an almost invariant degree of asymmetry in the streamwise direction.

Stability analysis was also performed on the periodic 2P base flows, despite mode C already having been predicted to become unstable at Reynolds numbers lower than those where the 2P vortex street transition takes place. The purpose of this was to investigate how the 2P vortex street might alter the stability characteristics of the preceding Kármán vortex street. It was found that mode C continues as the primary mode, but here referred to as mode II to make a clear distinction that the base flow differs and also that the eigenvalue is now positive real instead of negative real since the base flow itself is subharmonic to the vortex shedding frequency (and so the instability grows synchronous to the subharmonic base flow). Mode II here is also mode *D* in Yang *et al.* (2013) which grows through a positive real Floquet multiplier over a vortex street similar to the 2P mode. However, compared to the results of Yang *et al.* (2013), two various other modes are also observed to grow on this periodic base flow. Mode I is a synchronous long wavelength mode (wavelength at mode criticality $\lambda_I \approx 4.99h$ for cylinder inclination $\alpha = 36^\circ$), while mode III is a short wavelength mode subharmonic to the base flow which in itself is already subharmonic to the Kármán vortex street ($\lambda_{III} \approx 0.81h$ at mode criticality for cylinder inclination $\alpha = 36^\circ$).

Returning to two-dimensional states, the stability of the time-averaged two-dimensional flow was characterised to understand the formation of the various vortex street modes observed in the two-dimensional flow. Three generic modes were predicted through this analysis, each occurring at various ranges of Reynolds numbers. The most common of these modes was the complex *BvK* mode which forms primarily in the near wake, and the perturbation structures here resemble those found in the circular cylinder wake responsible for the Kármán vortex street. Even where the vortex street assumes an inclined trajectory, the alternating array of perturbation vortices (and its associated conjugate mode at a $\pi/2$ phase shift) can still be observed. In general, this

mode was the leading eigenmode at lower Reynolds numbers before the onset of any secondary instability or any spatial transitions in the vortex street.

Another of these modes was the steady *Bil* mode which develops further downstream in the wake, and appears to be associated with the vortex street separation into the dual row of like-signed vortices, regardless of whether the vortices diffuse into a two-layer vorticity sheet. This mode was generally superseded by the *Sec* mode, except for the wakes describing the 2P and P+S vortex streets. As for the complex *Sec* mode, the perturbation structures were similar to the *BvK* mode, but forms at larger spatial and temporal scales compared to that of the *BvK* mode and also manifests some distance downstream in the wake. This possibly implies that similar mechanisms underpin the formation of both the *BvK* and *Sec* modes.

The P+S vortex street forms from modes similar to the generic ones described above, except that within the range of Reynolds numbers where the P+S vortex street can be observed, all three *BvK*, *Sec* and *Bil* modes develop in the eigenspectra at similar Reynolds numbers, demonstrating the possibility of each becoming unstable over various subdomains in the flow at the same time. The particular cases with the 2P vortex street appear to show perturbation structures consistent with the *BvK* mode, lacking any prediction of the *Bil* or *Sec* modes. This was not surprising since the vortex shedding process remains similar in the near wake, and the time-mean wake shows no discernible features in the far wake since the counter rotating vortices negate each other over the shedding cycle (the other modes lack this negating effect owing to the *Bil* mode splitting the vortex rows). A recent report by Kim (2019) shows soap-film visualisations of vortex streets similar to those encountered in the present study despite the slightly different cylindrical cross-sections used to generate the wake at higher Reynolds numbers, lending physical credibility to these results. The extent of the realisation of these modes in a real flow, however, is uncertain since the basic state of the mean flow used in this analysis may have been modified through three-dimensional instabilities which generally occur at lower Reynolds numbers than most of these two-dimensional time-mean modes.

7.3 Perturbation characteristics of the instability modes

The next stage of this project set out to understand the characteristics of the eigenmodes accompanying the primary and secondary instabilities in the flow. Two approaches

were used here: in the first, the sensitivity of the eigenmode to force-velocity feedback was analysed, and in the next, the energetics of the eigenmodes were investigated. The former analysis was applied in an attempt to determine the core of the instability within which region any modifications to the flow will affect the eigenvalue of the problem most significantly, while the latter approach on the energetics of the mode aimed to determine the factors driving the growth of perturbations in the flow.

For the sensitivity analysis, the spectral norm of the sensitivity tensor (the sensitivity field) was considered (see Giannetti & Luchini, 2007). For the primary instability, the distribution of the sensitivity field in the cylinder wake was similar to that found for the circular cylinder wake reported by Giannetti & Luchini (2007), regardless of the cylinder inclination α . Varying the cylinder inclination only introduced a slight asymmetry in the sensitivity field about the wake centreline. For the secondary instability, the distribution of the sensitivity field in the cylinder wake for the mode A instability remained similar to that found for the circular cylinder as reported by Giannetti *et al.* (2010). Also, the sensitivity fields for mode C were qualitatively similar to those obtained for mode A, except being more localised to a region at any instance of time than those for mode A. This analysis was not pursued further owing to the similarities found between the sensitivity fields of the eigenmodes here and those in the case of the circular cylinder; for further discussion and analyses on this subject see Giannetti (2015) and Giannetti *et al.* (2019).

The next investigation of the mechanics of these instabilities turned to the consideration of their energetics, which can be directly related to the instability growth rates. For the primary instability through the BvK mode, regions of positive perturbation kinetic energy (PKE) production was observed in the wake past the recirculation region. This agreed well with the wavemaker position deduced from the sensitivity analysis in that the perturbation production upstream of the wavemaker remains negligible. Viscous dissipation was then observed to act increasingly strongly with distance from the cylinder to damp the instability growth.

For the secondary instability modes, the total (volume integrated) PKE transport terms were shown to be self-conserving, making no contribution to the total PKE growth rate (and also the instability growth rate). This was immediately obvious for modes B and C where the total transport terms cancel each other out at all times within the shedding cycle, and was a consequence of the near wake localisation of

the perturbations in the flow. For mode A, the imbalance between the total transport terms was associated with perturbation structures exiting domain at the outlet (without jeopardising any flow dynamics at play) — this imbalance was reconciled when the analysis was repeated for the circular cylinder mode A instability at $Re = 189$ with an extended outflow domain length of 300 cylinder diameters. In terms of the contribution of the total PKE production terms to the total PKE growth rate, the production terms involving base flow velocity gradients $\partial U/\partial y$ and $\partial V/\partial y$ were consistently the most dominant for all modes.

Scrutiny was next directed to the spatial distribution of the terms of the PKE equation to understand the local workings of each collection of terms as opposed to their global effect. For mode A, the PKE transport ($\sum \mathcal{T}$) was observed to extend quite a distance into the wake, demonstrating that the perturbations were being continuously amplified through its action as the vortex advects downstream, recalling that these terms do not affect the (global) instability growth rate at all times of the shedding cycle. Also for mode A, the distribution of the PKE production rate ($\sum \mathcal{P}$) within the domain was concentrated to within the base flow vortices. The primary contributors to the total PKE production ($\mathcal{P}_2 + \mathcal{P}_4$) show dominant positive production regions in the cores of the shedding vortices in agreement with the perturbation locations for an elliptical instability. The vortices further downstream in the wake subsequently develop a secondary positive PKE production region through \mathcal{P}_2 giving rise to the secondary regions of elliptical instability (Lewke & Williamson, 1998; Thompson *et al.*, 2001). For modes B and C, the map of the contribution through each term of the PKE evolution equation was qualitatively similar across most of the shedding cycle, implying that similar instability mechanisms likely underpin the dynamics of both. In these cases, all terms $\sum \mathcal{T}$, $\sum \mathcal{P}$, \mathcal{D} were concentrated in similar regions where the perturbation vortices develop. The net of the PKE production terms ($\sum \mathcal{P}$) assumed a strongly similar distribution to that obtained when only the dominant terms $\mathcal{P}_2 + \mathcal{P}_4$ were considered, which in both cases develop in the braid region as the base flow vortex was being shed. These production regions dissipated rapidly as the shed vortex relaxed back into an unstrained form. The dissipation rates in these modes were also shown to occur more intensely in regions where the perturbations manifest, in contrast to the weak dissipation regions found for mode A. The difference between modes B and C from an energetics perspective then lies in the continuity of the production regions over

the shedding cycle which possibly affects the symmetry of these modes — for mode B, the production regions remain continuous in the near wake through the shedding cycle, while for mode C, these production regions disconnect once per shedding cycle, which breaks the perturbation information feedback.

7.4 Three-dimensional flows past the cylinder

In the final results chapter, the weakly nonlinear characteristics of the modes associated with the flow about its transition was elucidated, followed by exposition of the fully three-dimensional (nonlinear) flow at higher Reynolds numbers. In the first case, the flows evolved in a domain matching a single wavelength of the leading mode predicted that the transitions were supercritical, although the magnitude of the Landau coefficient l obtained for all mode A cases were always much smaller than those calculated for mode C. Mode C was also shown to retain a stronger semblance to its two dimensional state, the perturbations growing over the spanwise vortices in the wake without introducing any severe deformations in it as a result of the rapid nonlinear saturation of the flow predicted through the large Landau coefficients.

The flows were next computed in an extended spanwise domain to understand how complex nonlinear mode interactions alter the wake from those predicted from the linearised system or the periodic mode domain. The general conclusion from this was that the wakes of these flows become strongly disorganised or even turbulent in its final state even at low increments past the transition Reynolds numbers for the onset of secondary instabilities in the flow. Several exceptions to this were the mode C cases *near the transition* where the asymptotic flow solution still resembled the predicted eigenmode (and so the flow is predictable for a larger range of Reynolds numbers), and the mode AA patterns which follow from a naturally retdimensionalised state that were both observed in the flows past the cylinder inclined within $0^\circ \leq \alpha \lesssim 18^\circ$. Another important observation is that the unique 2P and P+S vortex streets encountered in the two-dimensional flows restabilise back to one resembling the Kármán vortex street in these three-dimensional flow computations, the differences here explained through the action of vortex stretching (or the lack thereof for two-dimensional flows). Despite the turbulent appearance of most of these wakes at its asymptotic state, coherent structures were still intermittently identifiable in the wake, generally up to a Reynolds number of $Re \lesssim 200$. This is perhaps useful in the context of flow control — *if* a control strategy

can be executed reactively, one can exploit the fact that mode C can easily be tripped in the flow in preference over mode A (such is the case for the circular cylinder wake as accidentally demonstrated by Zhang *et al.* 1995 and later by Yildirim *et al.* 2013b) in conjunction with the results here showing that flows which transition through mode C remain more coherent for a larger range of Reynolds numbers than mode A does even at saturation to then *possibly* revert the flow back into a lower dimensional state. A caveat to this (amongst the multitude of other physical or experimental limitations¹) is that these mode C cases become turbulent abruptly at high enough Reynolds numbers, which in this project was found to be at about $Re \gtrsim 200$.

Finally, the forces acting on the cylinder induced by the flow were re-assessed to compare against the predictions made from two-dimensional flow computations. As expected, these values differ quite significantly, except for the cases where the flow re-laminarises into a two-dimensional state or where the mode AA structures emerge. Specifically, within the range of Reynolds numbers considered in this project, the two-dimensional flow predictions generally overpredict the mean and r.m.s. drag coefficients as well as the r.m.s. lift coefficient, but underpredicts the magnitudes of the mean lift coefficients. The variation of the force coefficients with the cylinder inclination angle was similar to those observed experimentally for a $Re = 1.2 \times 10^5$ flow (Iungo & Buresti, 2009) as well as those from two-dimensional flow computations, indicating that these and subsequent flow states affect only the magnitude of the forces predicted.

Potential avenues for future investigations

It has become clear that these instabilities are not beholden to any one transition mechanism, but are associated with a complex interaction of multiple drivers. Such was the case for mode A in the circular cylinder wake, for example, where Thompson *et al.* (2001) showed that the perturbations from the elliptic mode accounts for two-thirds of the global instability growth, or in Braza *et al.* (2001) who associated the nonlinear effects to a Craik–Leibovich shearing mechanism, and so a sole instability mechanism may not truly describe the dynamics of the mode in its entirety. However, the results found here demonstrate that some flow features are more universal and stable than previously thought, amongst which are the similarities found in the characteristics

¹Bear in mind that these results were obtained from flow computations where no irregularities would naturally arise except through truncation errors from either the computer or the numerical scheme.

between modes B and C, as well as the salience of the Kármán vortex street through all these transitions. It would be interesting for future research to investigate the sources behind the similarity of modes B and C, both of which appear less complex than their mode A counterpart. Also, the response of the wake to modifications in the flow should be investigated to determine the feasibility of control mechanisms, either active or passive, depending on the application.

Other directions for extending beyond this work could be to consider the free-vibration response of a triangular cylinder, considering that the force distribution about the cylinder is almost always asymmetric, and as such, a vibrational response may always be elicited. One may also consider the rotational or torsional response of the cylinder immersed in a flow. These investigations may find application in structural engineering, or in renewable energy technologies harvesting wind or wave energies. Several papers on these topics have emerged in recent years, but have primarily been afforded only two-dimensional computations in investigating the dynamics (Wang *et al.*, 2011; Alawadhi, 2013; Tu *et al.*, 2014; Wang *et al.*, 2015), with even fewer experimental attempts (Srigrarom & Koh, 2008; Seyed-Aghazadeh *et al.*, 2017). Considering the increasing interest in renewable energy sources, work of this nature may be prudent, if not essential.

Bibliography

- ABBASSI, H., TURKI, S. & BEN NASRALLAH, S. 2001 Numerical investigation of forced convection in a plane channel with a built-in triangular prism. *Int. J. Thermal Sci.* **40** (7), 649–658.
- ABDESSEMED, N., SHARMA, A. S., SHERWIN, S. J. & THEOFILIS, V. 2009 Transient growth analysis of flow past a circular cylinder. *Phys. Fluids* **21** (4), 044103.
- AKBAR, R., BOUCHET, G. & DUŠEK, J. 2011 Numerical investigation of the subcritical effects at the onset of three-dimensionality in the circular cylinder wake. *Phys. Fluids* **23** (9), 094103.
- ALAWADHI, E. M. 2013 Numerical simulation of fluid flow past an oscillating triangular cylinder in a channel. *J. Fluids Eng. Trans. ASME* **135**, 041202.
- ANDERSON, J. D. 2011 *Fundamentals of aerodynamics*, 5th edn. McGraw-Hill.
- BAO, Y., ZHOU, D. & ZHAO, Y.-J. 2010 A two-step Taylor-characteristic-based Galerkin method for incompressible flows and its application to flow over triangular cylinder with different incidence angles. *Int. J. Numer. Meth. Fl.* **62** (11), 1181–1208.
- BARKLEY, D. 2005 Confined three-dimensional stability analysis of the cylinder wake. *Phys. Rev. E* **71** (1), 017301.
- BARKLEY, D. 2006 Linear analysis of the cylinder wake mean flow. *Europhys. Lett.* **75** (5), 750–756.
- BARKLEY, D., BLACKBURN, H. M. & SHERWIN, S. J. 2008 Direct optimal growth analysis for timesteppers. *Int. J. Numer. Meth. Fl.* **57**, 1435–1458.
- BARKLEY, D. & HENDERSON, R. D. 1996 Three-dimensional Floquet stability analysis of the wake of a circular cylinder. *J. Fluid Mech.* **322**, 215–241.
- BEHARA, S. & MITTAL, S. 2010 Wake transition in flow past a circular cylinder. *Phys. Fluids* **22** (11), 114104.
- BÉNARD, H. 1908 Formation de centres de giration à l'arrière d'un obstacle en mouvement. *C. R. Acad. Sci. Paris* **147**, 839–842.

- BERGER, E. & WILLE, R. 1972 Periodic flow phenomena. *Annu. Rev. Fluid Mech.* **4** (1), 313–340.
- BLACKBURN, H. M., GOVARDHAN, R. N. & WILLIAMSON, C. H. K. 2001 A complementary numerical and physical investigation of vortex-induced vibration. *J. Fluids Struct.* **15**, 481–488.
- BLACKBURN, H. M. & LOPEZ, J. M. 2003 On three-dimensional quasiperiodic Floquet instabilities of two-dimensional bluff body wakes. *Phys. Fluids* **15** (8), L57–L60.
- BLACKBURN, H. M., MARQUES, F. & LOPEZ, J. M. 2005 Symmetry breaking of two-dimensional time-periodic wakes. *J. Fluid Mech.* **522**, 395–411.
- BLACKBURN, H. M. & SHEARD, G. J. 2010 On quasiperiodic and subharmonic Floquet wake instabilities. *Phys. Fluids* **22** (3), 031701.
- BLACKBURN, H. M. & SHERWIN, S. J. 2004 Formulation of a Galerkin spectral element-Fourier method for three-dimensional incompressible flows in cylindrical geometries. *J. Comput. Phys.* **197** (2), 759–778.
- BLOOR, M. S. 1964 Transition to turbulence in the wake of a circular cylinder. *J. Fluid Mech.* **19** (2), 290–304.
- BRAZA, M., CHASSAING, P. & HA MINH, H. 1986 Numerical study and physical analysis of the pressure and velocity fields in the near wake of a circular cylinder. *J. Fluid Mech.* **165**, 79–130.
- BRAZA, M., FAGHANI, D. & PERSILLON, H. 2001 Successive stages and the role of natural vortex dislocations in three-dimensional wake transition. *J. Fluid Mech.* **439**, 1–41.
- CANTWELL, C. D. & BARKLEY, D. 2010 Computational study of subcritical response in flow past a circular cylinder. *Phys. Rev. E* **82** (2), 026315.
- CARMO, B. S., SHERWIN, S. J., BEARMAN, P. W. & WILLDEN, R. H. J. 2008 Wake transition in the flow around two circular cylinders in staggered arrangements. *J. Fluid Mech.* **597**, 1–29.
- CHOMAZ, J. M., HUERRE, P. & REDEKOPP, L. G. 1988 Bifurcations to local and global modes in spatially developing flows. *Phys. Rev. Lett.* **60** (1), 25–28.
- CIMBALA, J. M., NAGIB, H. M. & ROSHKO, A. 1988 Large structure in the far wakes of two-dimensional bluff bodies. *J. Fluid Mech.* **190**, 265–298.
- COUTANCEAU, M. & BOUARD, R. 1977 Experimental determination of the main features of the viscous flow in the wake of a circular cylinder in uniform translation. part 1. steady flow. *J. Fluid Mech.* **79** (2), 231–256.

- DE, A. K. & DALAL, A. 2006 Numerical simulation of unconfined flow past a triangular cylinder. *Int. J. Numer. Meth. Fl.* **52** (7), 801–821.
- DRAZIN, P. G. & REID, W. H. 2004 *Hydrodynamic Stability*, 2nd edn. Cambridge University Press.
- DURGIN, W. W. & KARLSSON, S. K. F. 1971 On the phenomenon of vortex street breakdown. *J. Fluid Mech.* **48** (3), 507–527.
- DYNNIKOVA, G. Y., DYNNIKOV, Y. A. & GUVERNYUK, S. V. 2016 Mechanism underlying Kármán vortex street breakdown preceding secondary vortex street formation. *Phys. Fluids* **28** (5), 054101.
- EISENLOHR, H. & ECKELMANN, H. 1989 Vortex splitting and its consequences in the vortex street wake of cylinders at low Reynolds number. *Phys. Fluids A* **1** (2), 189–192.
- GANGA PRASATH, S., SUDHARSAN, M., VINODH KUMAR, V., DIWAKAR, S. V., SUNDARARAJAN, T. & TIWARI, S. 2014 Effects of aspect ratio and orientation on the wake characteristics of low Reynolds number flow over a triangular prism. *J. Fluids Struct.* **46**, 59–76.
- GERICH, D. & ECKELMANN, H. 1982 Influence of end plates and free ends on the shedding frequency of circular cylinders. *J. Fluid Mech.* **122**, 109–121.
- GERRARD, J. H. 1978 The wakes of cylindrical bluff bodies at low Reynolds number. *Philos. T. R. Soc. S-A* **288** (1354), 351–382.
- GIANNETTI, F. 2015 WKBJ analysis in the periodic wake of a cylinder. *Theoretical and Applied Mechanics Letters* **5**, 107–110.
- GIANNETTI, F., CAMARRI, S. & CITRO, V. 2019 Sensitivity analysis and passive control of the secondary instability in the wake of a cylinder. *J. Fluid Mech.* **864**, 45–72.
- GIANNETTI, F., CAMARRI, S. & LUCHINI, P. 2010 Structural sensitivity of the secondary instability in the wake of a circular cylinder. *J. Fluid Mech.* **651**, 319–337.
- GIANNETTI, F. & LUCHINI, P. 2007 Structural sensitivity of the first instability of the cylinder wake. *J. Fluid Mech.* **581**, 167–197.
- GOTTLIEB, D. & ORSZAG, S. 1977 *Numerical Analysis of Spectral Methods*. SIAM.
- GOUJON–DURAND, S., JENFFER, P. & WESFREID, J. E. 1994 Downstream evolution of the Bénard–von Kármán instability. *Phys. Rev. E* **50** (1), 308–313.

- GOVARDHAN, R. & WILLIAMSON, C. H. K. 2000 Modes of vortex formation and frequency response of a freely vibrating cylinder. *J. Fluid Mech.* **420**, 85–130.
- HENDERSON, R. D. 1995 Details of the drag curve near the onset of vortex shedding. *Phys. Fluids* **7** (9), 2012–2104.
- HENDERSON, R. D. 1997 Nonlinear dynamics and pattern formation in turbulent wake transition. *J. Fluid Mech.* **352**, 65–112.
- HENDERSON, R. D. & BARKLEY, D. 1996 Secondary instability in the wake of a circular cylinder. *Phys. Fluids* **8** (6), 1683–1685.
- HOOKE, S. G. 1936 On the action of viscosity in increasing the spacing ratio of a vortex street. *Proc. R. Soc. Lond. A* **154** (881), 67–89.
- HUERRE, P. & MONKEWITZ, P. A. 1990 Local and global instabilities in spatially developing flows. *Annu. Rev. Fluid Mech.* **22** (1), 473–537.
- INOUE, O. & YAMAZAKI, T. 1999 Secondary vortex streets in two-dimensional cylinder wakes. *Fluid Dyn. Res.* **25** (1), 1–18.
- IUNGO, G. V. & BURESTI, G. 2009 Experimental investigation on the aerodynamic loads and wake flow features of low aspect-ratio triangular prisms at different wind directions. *J. Fluids Struct.* **25** (7), 1119–1135.
- JACKSON, C. P. 1987 A finite-element study of the onset of vortex shedding in flow past variously shaped bodies. *J. Fluid Mech.* **182**, 23–45.
- JIANG, H., CHENG, L. & AN, H. 2018 Three-dimensional wake transition of a square cylinder. *J. Fluid Mech.* **842**, 102–127.
- JIANG, H., CHENG, L., DRAPER, S., AN, H. & TONG, F. 2016 Three-dimensional direct numerical simulation of wake transitions of a circular cylinder. *J. Fluid Mech.* **801**, 353–391.
- JOHNSON, S. A., THOMPSON, M. C. & HOURIGAN, K. 2004 Predicted low frequency structures in the wake of elliptical cylinders. *Eur. J. Mech. B-Fluids* **23** (1), 229–239.
- KARASUDANI, T. & FUNAKOSHI, M. 1994 Evolution of a vortex street in the far wake of a cylinder. *Fluid Dyn. Res.* **14** (6), 331–352.
- VON KÁRMÁN, T. 1911 Über den mechanismus des widerstandes, den ein bewegter körper in einer flüssigkeit erfährt. *Göttingen Nach. Math. Phys. Kl.* pp. 509–517.
- VON KÁRMÁN, T. 1954 *Aerodynamics: selected topics in the light of their historical development*. Cornell University Press.

- KARNIADAKIS, G. E., ISRAELI, M. & ORSZAG, S. A. 1991 High-order splitting methods for the incompressible Navier–Stokes equations. *J. Comput. Phys.* **97** (2), 414–443.
- KARNIADAKIS, G. E. & SHERWIN, S. J. 2005 *Spectral/hp element methods for computational fluid dynamics*, 2nd edn. Oxford University Press.
- KARNIADAKIS, G. E. & TRIANTAFYLLOU, G. S. 1992 Three-dimensional dynamics and transition to turbulence in the wake of bluff objects. *J. Fluid Mech.* **238**, 1–30.
- KERSWELL, R. R. 2002 Elliptical instability. *Annu. Rev. Fluid Mech.* **34** (1), 83–113.
- KIM, I. 2019 Separated rows structure of vortex streets behind triangular objects. *J. Fluid Mech.* **862**, 216–226.
- KOVASZNAY, L. I. G. 1948 Laminar flow behind a two-dimensional grid. *Mathematical Proceedings of the Cambridge Philosophical Society* **44** (1), 58–62.
- KUMAR, B. & MITTAL, S. 2006 Effect of blockage on critical parameters for flow past a circular cylinder. *Int. J. Numer. Meth. Fl.* **50** (8), 987–1001.
- KUMAR, B. & MITTAL, S. 2012 On the origin of the secondary vortex street. *J. Fluid Mech.* **711**, 641–666.
- LAMB, H. 1911 On the uniform motion of a sphere through a viscous fluid. *Philos. Mag.* **21** (121), 112–121.
- LAMB, H. 1932 *Hydrodynamics*, 6th edn. Cambridge University Press.
- LANDAU, L. D. & LIFSHITZ, E. M. 1976 *Mechanics*, 3rd edn. Pergamon Press.
- LANGE, C. F., DURST, F. & BREUER, M. 1998 Momentum and heat transfer from cylinders in laminar crossflow at $10^{-4} \leq re \leq 200$. *Int. J. Heat Mass Trans.* **41** (22), 3409–3430.
- LEHOUCQ, R., SORENSEN, D. & YANG, C. 1998 *ARPACK Users’ Guide*. Society for Industrial and Applied Mathematics.
- LEONTINI, J. S., LO JACONO, D. & THOMPSON, M. C. 2015 Stability analysis of the elliptic cylinder wake. *J. Fluid Mech.* **763**, 302–321.
- LEWEKE, T., LE DIZÈS, S. & WILLIAMSON, C. H. K. 2016 Dynamics and instabilities of vortex pairs. *Annu. Rev. Fluid Mech.* **48** (1), 507–541.
- LEWEKE, T. & WILLIAMSON, C. H. K. 1998 Three-dimensional instabilities in wake transition. *Eur. J. Mech. B-Fluids* **17** (4), 571–586.

- LUCHINI, P. & BOTTARO, A. 2014 Adjoint equations in stability analysis. *Annu. Rev. Fluid Mech.* **46** (1), 493–517.
- LUCHINI, P., GIANNETTI, F. & PRALITS, J. 2009 Structural sensitivity of the finite-amplitude vortex shedding behind a circular cylinder. In *IUTAM Symposium on Unsteady Separated Flows and their Control* (ed. M. Braza & K. Hourigan), pp. 151–160. Springer.
- LUO, S. C., CHEW, Y. T. & NG, Y. T. 2003 Characteristics of square cylinder wake transition flows. *Phys. Fluids* **15** (9), 2549–2559.
- LUO, S. C. & ENG, G. R. C. 2010 Discontinuities in the S-Re relations of trapezoidal and triangular cylinders. , vol. 7522, pp. 75221B–75221B–10.
- LUO, S. C., TONG, X. H. & KHOO, B. C. 2007 Transition phenomena in the wake of a square cylinder. *J. Fluids Struct.* **23**, 227–248.
- MARQUES, F., LOPEZ, J. M. & BLACKBURN, H. M. 2004 Bifurcations in systems with Z_2 spatio-temporal and $O(2)$ spatial symmetry. *Physica D* **189**, 247–276.
- MARQUET, O., SIPP, D. & JACQUIN, L. 2008 Sensitivity analysis and passive control of cylinder flow. *J. Fluid Mech.* **615**, 221–252.
- MATHIS, C., PROVANSAL, M. & BOYER, L. 1984 The Benard–Von Karman instability: an experimental study near the threshold. *J. Physique Lett.* **45** (10), 483–491.
- MATSUI, T. & OKUDE, M. 1983 Formation of the secondary vortex street in the wake of a circular cylinder. In *Structure of Complex Turbulent Shear Flow* (ed. R. Dumas & L. Fulachier). International Union of Theoretical and Applied Mechanics, Springer, Berlin, Heidelberg.
- MITTAL, R. & BALACHANDAR, S. 1995 Generation of streamwise vortical structures in bluff body wakes. *Phys. Rev. Lett.* **75** (7), 1300–1303.
- MITTAL, S. 2008 Global linear stability analysis of time-averaged flows. *Int. J. Numer. Meth. Fl.* **58**, 111–118.
- MITTAL, S. 2009 Stability of flow past a cylinder: energy budget of eigenmodes. *Int. J. Numer. Meth. Fl.* **63** (5), 533–547.
- MIZUSHIMA, J., HATSUDA, G., AKAMINE, H., INASAWA, A. & ASAI, M. 2014 Rapid annihilation of the Kármán vortex street behind a rectangular cylinder. *J. Phys. Soc. Jpn.* **83**, 014402.
- MONKEWITZ, P. A. 1988 The absolute and convective nature of instability in two-dimensional wakes at low Reynolds numbers. *Phys. Fluids* **31** (5), 999–1006.

- MUNSON, B. R., YOUNG, D. F., OKIISHI, T. H. & HUEBSCH, W. W. 2009 *Fundamentals of fluid mechanics*, 6th edn. John Wiley & Sons, Inc.
- NAJJAR, F. M. & BALACHANDAR, S. 1998 Low-frequency unsteadiness in the wake of a normal flat plate. *J. Fluid Mech.* **370**, 101–147.
- NAJJAR, F. M. & VANKA, S. P. 1995 Effects of intrinsic three-dimensionality on the drag characteristics of a normal flat plate. *Phys. Fluids* **7** (10), 2516–2518.
- NG, Z. Y., VO, T., HUSSAM, W. K. & SHEARD, G. J. 2016 Two-dimensional wake dynamics behind cylinders with triangular cross-section under incidence angle variation. *J. Fluids Struct.* **63**, 302–324.
- NG, Z. Y., VO, T. & SHEARD, G. J. 2018 Stability of the wakes of cylinders with triangular cross-sections. *J. Fluid Mech.* **844**, 721–745.
- NOACK, B. R., KÖNIG, M. & ECKELMANN, H. 1993 Three-dimensional stability analysis of the periodic flow around a circular cylinder. *Phys. Fluids* **5** (6), 1279–1281.
- NORBERG, C. 1994 An experimental investigation of the flow around a circular cylinder: influence of aspect ratio. *J. Fluid Mech.* **258**, 287–316.
- OSEEN, C. W. 1910 Über die stoke'sche formel und über eine verwandte aufgabe in der hydrodynamik. *Ark. Mat. Astr. Fys.* **6** (29), 1–20.
- PARK, D. & YANG, K.-S. 2016 Flow instabilities in the wake of a rounded square cylinder. *J. Fluid Mech.* **793**, 915–932.
- PARK, J. K., PARK, S. O. & HYUN, J. M. 1989 Flow regimes of unsteady laminar flow past a slender elliptic cylinder at incidence. *Int. J. Heat Fluid Flow* **10** (4), 311–317.
- PAUL, I., PRAKASH, K. A. & VENGADESAN, S. 2014 Onset of laminar separation and vortex shedding in flow past unconfined elliptic cylinders. *Phys. Fluids* **26** (2), 023601.
- PERRY, A. E., CHONG, M. S. & LIM, T. T. 1982 The vortex-shedding process behind two-dimensional bluff bodies. *J. Fluid Mech.* **116**, 77–90.
- PERRY, A. E. & FAIRLIE, B. D. 1975 Critical points in flow patterns. *Adv. Geophys.* **18**, 299–315.
- PONTA, F. L. 2010 Vortex decay in the kármán eddy street. *Phys. Fluids* **22** (9), 093601.

- POSDZIECH, O. & GRUNDMANN, R. 2007 A systematic approach to the numerical calculation of fundamental quantities of the two-dimensional flow over a circular cylinder. *J. Fluids Struct.* **23** (3), 479–499.
- PRHASHANNA, A., SAHU, A. K. & CHHABRA, R. P. 2011 Flow of power-law fluids past an equilateral triangular cylinder: Momentum and heat transfer characteristics. *Int. J. Thermal Sci.* **50** (10), 2027–2041.
- PROUDMAN, I. & PEARSON, J. R. A. 1957 Expansions at small Reynolds numbers for the flow past a sphere and a circular cylinder. *J. Fluid Mech.* **2** (3), 237–262.
- PROVANSAL, M., MATHIS, C. & BOYER, L. 1987 Bénard-von Kármán instability: transient and forced regimes. *J. Fluid Mech.* **182**, 1–22.
- RADI, A., THOMPSON, M. C., SHERIDAN, J. & HOURIGAN, K. 2013 From the circular cylinder to the flat plate wake: The variation of Strouhal number with Reynolds number for elliptical cylinders. *Phys. Fluids* **25** (10), 101706.
- RAO, A., LEONTINI, J. S., THOMPSON, M. C. & HOURIGAN, K. 2017 Three-dimensionality of elliptical cylinder wakes at low angles of incidence. *J. Fluid Mech.* **825**, 245–283.
- RAYLEIGH, L. 1915 XLVIII. æolian tones. *The London, Edinburgh, and Dublin Philosophical Magazine and Journal of Science* **29** (172), 433–444.
- REYNOLDS, O. 1883 An experimental investigation of the circumstances which determine whether the motion of water shall be direct or sinuous, and of the law of resistance in parallel channels. *Phil. Trans. R. Soc.* **174**, 935–982.
- ROBICHAUX, J., BALACHANDAR, S. & VANKA, S. P. 1999 Three-dimensional Floquet instability of the wake of square cylinder. *Phys. Fluids* **11** (3), 560–578.
- ROCCO, G. 2014 Advanced instability methods using spectral/*hp* discretisations and their applications to complex geometries. PhD thesis, Department of Aeronautics, Imperial College London.
- ROSHKO, A. 1954 On the development of turbulent wakes from vortex streets. Report 1191. National Advisory Committee for Aeronautics.
- ROSHKO, A. 1993 Perspectives on bluff body aerodynamics. *J. Wind Eng. Ind. Aerod.* **49**, 79–100.
- SAFFMAN, P. G. & SCHATZMAN, J. C. 1982 Stability of a vortex street of finite vortices. *J. Fluid Mech.* **117**, 171–185.
- SAHA, A. K. 2007 Far-wake characteristics of two-dimensional flow past a normal flat plate. *Phys. Fluids* **19** (12), 128110.

- SAHA, A. K., BISWAS, G. & MURALIDHAR, K. 2003 Three-dimensional study of flow past a square cylinder at low Reynolds numbers. *Int. J. Heat Fluid Flow* **24** (1), 54–66.
- SAPARDI, A. M., HUSSAM, W. K., POTHÉRAT, A. & SHEARD, G. J. 2017 Linear stability of confined flow around a 180-degree sharp bend. *J. Fluid Mech.* **822**, 813–847.
- SCHMID, P. J. & HENNINGSON, D. S. 2001 *Stability and transition in shear flows*. Springer–Verlag New York, Inc.
- SEN, S., MITTAL, S. & BISWAS, G. 2009 Steady separated flow past a circular cylinder at low Reynolds numbers. *J. Fluid Mech.* **620**, 89–119.
- SEN, S., MITTAL, S. & BISWAS, G. 2011 Flow past a square cylinder at low Reynolds numbers. *Int. J. Numer. Meth. Fl.* **67** (9), 1160–1174.
- SEYED-AGHAZADEH, B., CARLSON, D. W. & MODARRES-SADEGHI, Y. 2017 Vortex-induced vibration and galloping of prisms with triangular cross-sections. *J. Fluid Mech.* **817**, 590–618.
- SHEARD, G. J. 2011 Wake stability features behind a square cylinder: Focus on small incidence angles. *J. Fluids Struct.* **27** (5–6), 734–742.
- SHEARD, G. J., FITZGERALD, M. J. & RYAN, K. 2009 Cylinders with square cross-section: wake instabilities with incidence angle variation. *J. Fluid Mech.* **630**, 43–69.
- SHEARD, G. J., HUSSAM, W. K. & TSAI, T. 2016 Linear stability and energetics of rotating radial horizontal convection. *J. Fluid Mech.* **795**, 1–35.
- SHEARD, G. J., THOMPSON, M. C. & HOURIGAN, K. 2003 From spheres to circular cylinders: the stability and flow structures of bluff ring wakes. *J. Fluid Mech.* **492**, 147–180.
- SHEARD, G. J., THOMPSON, M. C. & HOURIGAN, K. 2004 From spheres to circular cylinder: non-axisymmetric transitions in the flow past rings. *J. Fluid Mech.* **506**, 45–78.
- SHEARD, G. J., THOMPSON, M. C. & HOURIGAN, K. 2005 Subharmonic mechanism of the mode C instability. *Phys. Fluids* **17** (11), 111702.
- SHERWIN, S. J. & KARNIADAKIS, G. E. 1996 Tetrahedral *hp* finite elements: algorithms and flow simulations. *J. Comput. Phys.* **124** (1), 14–45.
- SOHANKAR, A. 2007 Hopf bifurcation, vortex shedding and near wake study of a heated cylinder in cross flow. *Iran. J. Sci. Technol. Trans. B-Eng.* **31** (B1), 31–47.

- SOHANKAR, A., NORBERG, C. & DAVIDSON, L. 1997 Numerical simulation of unsteady low-Reynolds number flow around rectangular cylinders at incidence. *J. Wind Eng. Ind. Aerod.* **69–71**, 189–201.
- SOHANKAR, A., NORBERG, C. & DAVIDSON, L. 1998 Low-Reynolds-number flow around a square cylinder at incidence: study of blockage, onset of vortex shedding and outlet boundary condition. *Int. J. Numer. Meth. Fl.* **26** (1), 39–56.
- SOHANKAR, A., NORBERG, C. & DAVIDSON, L. 1999 Simulation of three-dimensional flow around a square cylinder at moderate Reynolds numbers. *Phys. Fluids* **11** (2), 288–306.
- SREENIVASAN, K. R., STRYKOWSKI, P. J. & OLINGER, D. J. 1987 Hopf bifurcation, Landau equation, and vortex shedding behind circular cylinders. In *Proceedings of the Forum on Unsteady Flow Separation* (ed. K. N. Ghia), , vol. 52, pp. 1–13. American Society of Mechanical Engineers.
- SRIGRAROM, S. & KOH, A. K. G. 2008 Flow field of self-excited rotationally oscillating equilateral triangular cylinder. *J. Fluids Struct.* **24** (5), 750–755.
- SRIKANTH, S., DHIMAN, A. K. & BIJJAM, S. 2010 Confined flow and heat transfer across a triangular cylinder in a channel. *Int. J. Thermal Sci.* **49** (11), 2191–2200.
- STOKES, G. G. 1851 On the effect of the internal friction of fluids on the motion of pendulums. *Trans. Cambridge Phil. Soc.* **9**, 8–106.
- TANEDA, S. 1956 Experimental investigation of the wakes behind cylinders and plates at low Reynolds numbers. *J. Phys. Soc. Jpn.* **11** (3), 302–307.
- TANEDA, S. 1959 Downstream development of the wakes behind cylinders. *J. Phys. Soc. Jpn.* **14** (6), 843–848.
- TANEDA, S. 1963 The stability of two-dimensional laminar wakes at low Reynolds numbers. *J. Phys. Soc. Jpn.* **18** (2), 288–296.
- THOMPSON, M., HOURIGAN, K. & SHERIDAN, J. 1996 Three-dimensional instabilities in the wake of a circular cylinder. *Exp. Therm. Fluid Sci.* **12** (2), 190–196.
- THOMPSON, M. C. & LE GAL, P. 2004 The Stuart–Landau model applied to wake transition revisited. *Eur. J. Mech. B-Fluids* **23** (1), 219–228.
- THOMPSON, M. C., LEWEKE, T. & WILLIAMSON, C. H. K. 2001 The physical mechanism of transition in bluff body wakes. *J. Fluids Struct.* **15** (3–4), 607–616.
- THOMPSON, M. C., RADI, A., RAO, A., SHERIDAN, J. & HOURIGAN, K. 2014 Low-Reynolds-number wakes of elliptical cylinders: from the circular cylinder to the normal flat plate. *J. Fluid Mech.* **751**, 570–600.

- TONG, X. H., LUO, S. C. & KHOO, B. C. 2008 Transition phenomena in the wake of an inclined square cylinder. *J. Fluids Struct.* **24**, 994–1005.
- TRITTON, D. J. 1959 Experiments on the flow past a circular cylinder at low Reynolds numbers. *J. Fluid Mech.* **6**, 547–567.
- TU, J., ZHOU, D., BAO, Y., HAN, Z. & LI, R. 2014 Flow characteristics and flow-induced forces of a stationary and rotating triangular cylinder with different incidence angles at low Reynolds numbers. *J. Fluids Struct.* **45**, 107–123.
- VERMA, A. & MITTAL, S. 2011 A new unstable mode in the wake of a circular cylinder. *Phys. Fluids* **23** (12), 121701.
- VO, T., MONTABONE, L., READ, P. L. & SHEARD, G. J. 2015 Non-axisymmetric flows in a differential-disk rotating system. *J. Fluid Mech.* **775**, 349–386.
- VOROBIEFF, P., GEORGIEV, D. & INGBER, M. S. 2002 Onset of the second wake: dependence on the Reynolds number. *Phys. Fluids* **14** (7), L53–L54.
- WANG, H., ZHAO, D., YANG, W. & YU, G. 2015 Numerical investigation on flow-induced vibration of a triangular cylinder at a low Reynolds number. *Fluid Dyn. Res.* **47**, 015501.
- WANG, S., ZHU, L., ZHANG, X. & HE, G. 2011 Flow past two freely rotatable triangular cylinders in tandem arrangement. *J. Fluids Eng. Trans. ASME* **133**, 081202.
- WEI, T. & SMITH, C. R. 1986 Secondary vortices in the wake of circular cylinders. *J. Fluid Mech.* **169**, 513–533.
- WESFREID, J. E. 2017 Henri Bénard: Thermal convection and vortex shedding. *C. R. Mec.* **345** (7), 446–466.
- WHITE, F. M. 2011 *Fluid mechanics*, 7th edn. McGraw Hill.
- WILLIAMSON, C. H. K. 1988a Defining a universal and continuous Strouhal-Reynolds number relationship for the laminar vortex shedding of a circular cylinder. *Phys. Fluids* **31** (10), 2742–2744.
- WILLIAMSON, C. H. K. 1988b The existence of two stages in the transition to three-dimensionality of a cylinder wake. *Phys. Fluids* **31** (11), 3165–3168.
- WILLIAMSON, C. H. K. 1989 Oblique and parallel modes of vortex shedding in the wake of a circular cylinder a low Reynolds number. *J. Fluid Mech.* **206**, 579–627.
- WILLIAMSON, C. H. K. 1996a Three-dimensional wake transition. *J. Fluid Mech.* **328**, 345–407.

- WILLIAMSON, C. H. K. 1996b Vortex dynamics in the cylinder wake. *Annu. Rev. Fluid Mech.* **28** (1), 477–539.
- WILLIAMSON, C. H. K. & PRASAD, A. 1993 Wave interactions in the far wake of a body. *Phys. Fluids A* **5** (7), 1854–1856.
- WILLIAMSON, C. H. K. & ROSHKO, A. 1988 Vortex formation in the wake of an oscillating cylinder. *J. Fluids Struct.* **2** (4), 355–381.
- WILLIAMSON, C. H. K. & ROSHKO, A. 1990 Measurements of base pressure in the wake of a cylinder at low Reynolds numbers. *Z. Flugwiss. Weltraumforschung* **14**, 38–46.
- YANG, D., PETTERSEN, B., ANDERSSON, H. I. & NARASIMHAMURTHY, V. D. 2012 Vortex shedding in flow past an inclined flat plate at high incidence. *Phys. Fluids* **24** (8), 084103.
- YANG, D., PETTERSEN, B., ANDERSSON, H. I. & NARASIMHAMURTHY, V. D. 2013 Floquet stability analysis of the wake of an inclined flat plate. *Phys. Fluids* **25** (9), 094103.
- YILDIRIM, I., RINDT, C. C. M. & VAN STEENHOVEN, A. A. 2013a Energy contents and vortex dynamics in Mode-C transition of wired-cylinder wake. *Phys. Fluids* **25**, 054103.
- YILDIRIM, I., RINDT, C. C. M. & VAN STEENHOVEN, A. A. 2013b Mode C flow transition behind a circular cylinder with a near-wake wire disturbance. *J. Fluid Mech.* **727**, 30–55.
- YOON, D.-H., YANG, K.-S. & CHOI, C.-B. 2010 Flow past a square cylinder with an angle of incidence. *Phys. Fluids* **22** (4), 043603.
- ZANG, T. A. 1991 On the rotation and skew-symmetric forms for incompressible flow simulations. *Appl. Numer. Math.* **7**, 27–40.
- ZDRAVKOVICH, M. M. 1968 Smoke observations of the wake of a group of three cylinders at low Reynolds number. *J. Fluid Mech.* **32** (2), 339–351.
- ZDRAVKOVICH, M. M. 1969 Smoke observations of the formation of a Kármán vortex street. *J. Fluid Mech.* **37** (3), 491–496.
- ZHANG, H.-Q., FEY, U., NOACK, B. R., KÖNIG, M. & ECKELMANN, H. 1995 On the transition of the cylinder wake. *Phys. Fluids* **7** (4), 779–794.
- ZHANG, J., LIU, N. S. & LU, X. 2008 Route to a chaotic state in fluid flow past an inclined flat plate. *Phys. Rev. E* **78** (3), 036320.

- ZIELINSKA, B. J. A., GOUJON-DURAND, S., DUŠEK, J. & WESFREID, J. E. 1997 Strongly nonlinear effect in unstable wakes. *Phys. Rev. Lett.* **79** (20), 3893–3896.
- ZIELINSKA, B. J. A. & WESFREID, J. E. 1995 On the spatial structure of global modes in wake flow. *Phys. Fluids* **7** (6), 1418–1424.